SGS HORIZON

VERMILION

Harlingen Subsidence Study

2014

DISCLAIMER

This report has been prepared for the exclusive use of Vermilion Oil and Gas Netherlands B.V., it is not intended to be published or otherwise made available to third parties under authorship of SGS Horizon B.V. and may not be reproduced, distributed, quoted or made available to any third party unless (the conditions of) such use is explicitly agreed beforehand in writing between SGS Horizon B.V. and Vermilion Oil and Gas Netherlands B.V.

SGS Horizon B.V. does not accept any liability towards third parties in connection with the contents of this report, nor does SGS Horizon B.V. in case of reproduction, distribution, quotation or otherwise making available of this report in whole or in part to third parties accept any responsibility or liability for the consequences thereof.

This report contains findings, analyses, interpretations, conclusions, recommendations and other work not only by SGS Horizon B.V., but also by NGI (Stiftelsen Norges Geotekniske Institutt[1]).

SGS Horizon B.V. shall not be liable or responsible for any loss, costs, damages or expenses incurred or sustained by any party as a result of any incorrectness in findings, analyses, interpretations, conclusions, recommendations represented in this report as a result of any decision or assessment made on the basis of such findings, analyses, interpretations, conclusions or recommendations (whether correct or incorrect).

The party who uses (the contents of) this report accepts that it shall have to indemnify SGS Horizon B.V. for any and all (alleged) liabilities, costs or expenses incurred as a result of claims made vis-a-vis SGS Horizon B.V. in connection with the use made of the (contents of the) report by such party.

Signed:

Barbara Schatz
Project Manager
Date: 27.10.2014

Danilo Bandiziol
Managing Director
Date: 27.10.2014

[1] Norwegian Geotechnical Institute

EXECUTIVE SUMMARY

The Harlingen Chalk gas field is located in the western part of the Leeuwarden concession in the province of Friesland, onshore northern Netherlands. It is located between the towns of Franeker and Harlingen. The crest of the chalk reservoir is at a depth of 1026 mTVDss and the maximum thickness of the gas bearing zone is some 30 m. The field's areal extent is 6 by 10 km and is notionally split into up to five sectors with varying amounts of connectivity based on different initial GWC and production performance information. The initial gas in place is estimated to be approximately $5x10^9$ Sm^3.

The field was brought on stream in November 1988. By July 2008, 9 wells had been brought on production and the cumulative gas recovery was $1.77x10^9$ Sm^3. Over time a subsidence bowl developed at the surface due to the gas extraction from the field. This subsidence bowel overlaps with a subsidence bowl resulting from deep solution salt mining in the nearby Barradeel concession to the north-west of the field. The entire area encounters ongoing natural (autonomous) subsidence of the shallow layers, which is unrelated to gas and salt extraction.

A degree of reservoir compaction and associated surface subsidence was predicted in the 2004 Winningsplan (10 cm +/- 20 %). However, by 2008 it was apparent that actual measured subsidence exceeded the originally predicted maximum subsidence by a factor two. This additional subsidence appeared to be due to gas extraction, however the underlying processes causing the observed discrepancy were not completely understood. This lack of understanding resulted in a shut-in of the Harlingen Chalk gas field in July 2008.

The objective of this study was to investigate the discrepancy between the forecast of subsidence above the Upper Cretaceous Harlingen Chalk gas reservoir and the actual subsidence measured over time. Focus was to understand and model gas production induced subsidence. In addition, having resolved this discrepancy, a further objective was to forecast future subsidence including uncertainty bands.

This technical work was carried out by SGS Horizon B.V. (SGSH) and the Norwegian Geotechnical Institute (NGI) for Vermilion Oil and Gas Netherlands B.V. (Vermilion) between 2008 and 2014. SGSH and NGI carried out the technical work in consultation with a technical committee (TCM). The members of the TCM were Vermilion, the Geological Survey of the Netherlands/Advisory Group of Economic Affairs (TNO-AGE) and the State Supervision of Mines (SodM). An intermediate progress report was issued in September 2010 and this report addresses the totality of the study.

Extensive laboratory testing and measurements carried out by NGI on Harlingen Chalk samples, combined with literature data on similar rock types, have provided better understanding of the physical mechanism controlling the compaction behavior of the reservoir rocks. A key result was the identification of a transition from elastic to plastic behaviour via pore collapse in the Harlingen Chalk, which was not anticipated in pre 2008 forecasts. It is the most important cause of the higher than expected compaction and surface subsidence.

Based on a 3D subsurface model and the NGI derived mechanical rock properties a new model for the calculation of compaction and subsidence was built. Rock mechanical parameters were fine-tuned based on comparison of the modelled results with the actual subsidence measurements in the area affected by the Harlingen Chalk gas production.

The compaction and subsidence modelling was performed for the production period 1988-2008. The current subsidence model shows, on average, a fit that falls within the uncertainty of the benchmark measurements in the area. The subsidence model indicates that the subsidence due to gas extraction was a maximum of 23 cm in the centre of the subsidence bowl at the time of field shut-in in 2008 and that the total maximum subsidence at that moment including salt induced (5 cm) and autonomous subsidence (2 cm) amounted to 30 cm. An analysis was performed to illustrate the modelling uncertainty in the area of the city of Franeker which resulted in a very similar subsidence map as the reference case, with a maximum uncertainty in gas induced subsidence of up to 4 cm.

During the field shut-in period (2008-2013), creep (continued time dependent deformation under zero stress change) dominates the reservoir compaction process. The amount of additional gas induced subsidence modelled for the shut-in period is a maximum of 5 cm, hence maximum total gas induced subsidence by 2014 is 28 cm. If the field had not been shut-in and gas production would have continued at late average gas production rates the maximum gas induced subsidence would have amounted to at least 32 cm.

The current subsidence model was used for forecasting subsidence for the period from 2014 onwards. In order to increase the robustness of the subsidence forecast an alternative approach was implemented to generate an estimate of the subsidence over a short/mid-term time period and to create upper and lower bound scenarios that take into account the measurement errors of the benchmark data. The alternative approach is a curve fitting, with a mathematical structure compatible with the physics underlying the creep/compaction behaviour, performed on the subsidence values derived from benchmark measurements in the post-production period at the benchmark locations.

The subsidence model and the fitting procedure are two different approaches to perform forecasting of the subsidence. Their differences can be used as an illustration of the modelling uncertainties related to the subsidence predictions. Additionally, the upper and lower bound of the fitting procedure represent a forecast of the measurement uncertainties, which should also be taken into account.

Forecasted maximum additional total subsidence, assuming no further gas offtake and no further salt extraction induced subsidence, is 12 cm ± 3 cm by 2030. Since the start of gas production in 1988, the maximum total subsidence (gas and salt production induced and natural subsidence) amounts to ~42 cm ± 3 cm in 2030 at the location of the deepest point of the subsidence bowl.

After 2030 subsidence is expected to continue with a rate higher than the autonomous subsidence rate, however by 2050 the natural subsidence is expected to be the dominant subsidence process in most areas the field.

The following table summarizes the subsidence over time (all values have two-sigma uncertainty).

Subsidence over time in cm					
	1988	**2008**	**2014**	**2030**	**2050**
Gas	0	23	28	33	35
Salt	0	5	5	5	5
Autonomous	0	2	2	4	6
Total	**0**	**30**	**35**	**42**	**46**

TABLE OF CONTENTS

LIST OF TABLES

LIST OF FIGURES

TERMS AND ABBREVIATIONS

BAS	Barradeel (salt) wells
CPI	Computer Processed Interpretation
FF	Formation Factor
FR	Franeker seismic profiles
FRA	Franeker wells
FWL	Free Water Level
GAPI	American Petroleum Institute Gamma radiation Units
GDT	Gas Down To
GIIP	Gas Initially In Place
GPS	Global Positioning System
GRF	Gaussian Random Function
GWC	Gas Water Contact
HM	History Match
HRL	Harlingen wells
InSAR	Interferometric Synthetic Aperture Radar
JCR	Joint Chalk Research
LAS	Log ASCII Standard
LMP	Last Measured Pressure
m	meter
mD	milli-Darcy (unit of permeability)
MD	Measured Depth
MWD	Measurements While Drilling
NAP	Normal Amsterdam Peil
NFA	No Further Action
NGI	Norwegian Geotechnical Institute
p*	Extrapolated shut-in Pressure
psi	pounds per square inch
PSI	Persistent Scattered Interferometry
PS-InSAR	Persistent Scatter Interferometric SAR technique
RTCM	Rate Type Compaction Model
SAR	Synthetic Aperture Radar
SEG	Society of Exploration Geophysicists
SGSH	SGS Horizon
T-IJH	Texel-Ijsselmeer High
TNO-AGE	Geological Survey of the Netherlands/Advisory Group of Economic Affairs
TVDss	True Vertical Depth Sub Sea (i.e. below mean sea level)
TWT	Two Way Time
VB	Vlieland Basin
WLL	WireLine Logging
WUT	Water Up To

1 INTRODUCTION

This is the technical report of the Harlingen Subsidence Study carried out by SGS Horizon B.V. (SGSH) and the Norwegian Geotechnical Institute (NGI) for Vermilion Oil and Gas Netherlands B.V. (Vermilion) between 2008 and 2014.

SGSH and NGI carried out the technical work in consultation with a technical committee (TCM). The members of the TCM were Vermilion, the Geological Survey of the Netherlands/Advisory Group of Economic Affairs (TNO-AGE) and the State Supervision of Mines (SodM).

1.1 THE HARLINGEN CHALK GAS FIELD

The Harlingen Chalk gas field is located in the western part of the Leeuwarden concession in the province of Friesland, onshore northern Netherlands, between the towns of Harlingen and Franeker (Figure 1-1).

The Harlingen field was discovered by the well HRL-01 in 1965. Two appraisal wells were drilled in 1965 and 1978 (HRL-02 and FRA-01, respectively) near the northern culmination of the structure.

Production of dry gas from the field started in 1988. Over time, a subsidence bowl started developing at the surface due to the gas extraction from the field. This subsidence bowl overlaps with a subsidence bowl resulting from deep solution salt mining in the nearby Barradeel concession, in the wells located to the north-west of the Harlingen field (Figure 1-1). Combined subsidence due to gas and salt extraction led to significant, and higher than originally anticipated, total surface subsidence. This additional subsidence appeared to be due to the gas extraction and the lack of understanding of the processes, causing the discrepancy, resulted in a shut-in of the Harlingen Chalk gas field in July 2008.

Initial gas in place (GIIP) in the Harlingen Chalk gas field was approximately $5x10^9$ Sm^3. At the time of shut-in, nine wells had produced a cumulative amount of $1.77x10^9$ Sm^3 of gas, with minor water production.

Initially, the reservoir gas pressure was 135 bar at a reference depth of 1084 mTVDss, which has dropped to an average of 76 bar in the area of major gas production at the end of the production period in 2008. This and some other key Harlingen reservoir data are summarized in Table 1-1.

The field is subdivided into a central, an eastern and a southern region, which show different fluid contacts (Section 5.2.3). Subsequently the central and the southern pool were further subdivided into two regions to account for petrophysical and dynamic data analyses findings.

The Harlingen field is the only chalk gas field in the Netherlands and it is also the southernmost hydrocarbon field in chalk reservoir in the North Sea area. Other hydrocarbon fields in the chalk in The Netherlands are the producing oil field Hanze and a recent oil discovery in offshore block F17a; otherwise the nearest fields are located in Denmark.

Table 1-1 Summary of some key Harlingen Chalk reservoir data

Parameter	Value
Depth to crest	1026 mTVDss
Hydrocarbon type	Dry gas with high methane content [35]
Reservoir pressure	135 bar at reference depth of 1084 mTVDss
Reservoir temperature	43°C at 1050 mTVDss
Maximum gas bearing thickness	~30 m

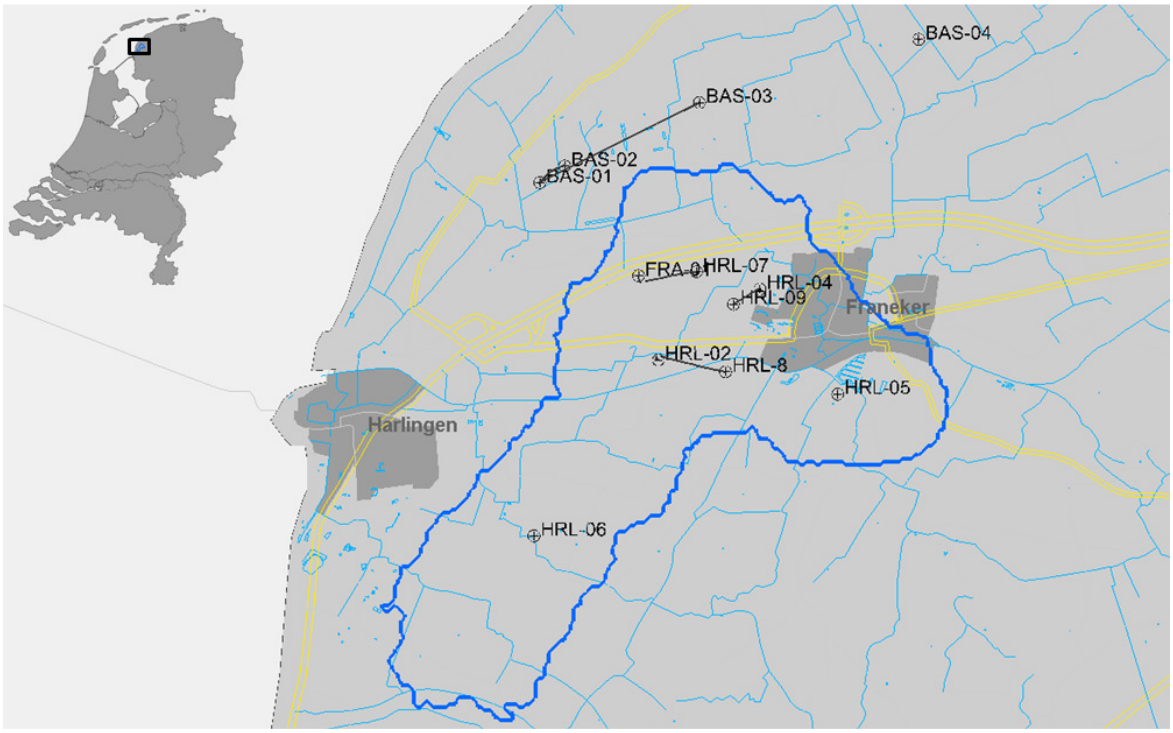

Figure 1-1 **Location of the Harlingen Chalk gas field (blue outline delineates Harlingen Chalk gas field, HRL are the Harlingen gas wells, BAS wells are the Barradeel salt wells).**

1.2 SUBSIDENCE HIGHER THAN EXPECTED

By 2008, observed surface subsidence over the Harlingen Chalk gas field was approximately two times higher than predicted.

In the extraction plan ("Winningsplan") the expected maximum subsidence due to gas extraction was predicted to be 10 cm ± 20 % (Total, 2004 [33]) and in later work (Vermilion, 2007 [41]) the expected maximum subsidence due to gas extraction by 2016 was estimated at 12-13 cm.

An analysis of observed data and subsequent mapping (Houtenbos, 2010 [11]), showed that gas extraction induced subsidence had reached 24.6 cm in the deepest point of the surface subsidence bowl above the gas field by 2009.

1.3 OBJECTIVE OF THE STUDY

The objective of this study was to investigate the discrepancy between the forecast of subsidence above the Upper Cretaceous Harlingen Chalk gas reservoir and the actual subsidence measured over time. Focus was to understand and model gas production induced subsidence.

In addition, having resolved this discrepancy, a further objective was to forecast future subsidence including uncertainty bands.

1.4 APPROACH

The most significant component of this study was a rock-mechanical laboratory study on samples from the Harlingen Chalk gas reservoir to determine its mechanical rock properties carried out by NGI. This led to an NGI-derived compaction model based on the Rate Type Compaction Model

(RTCM) (Van Ditzhuijzen, P.J.D. et al., 1984 [38], de Waal, 1986 [4], Smits, R.M.M. et al., 1988 [29]) for the Harlingen Chalk reservoir rock.

Building blocks for a 3D subsurface model included a seismic reinterpretation of the field and surrounding areas, the completion of a geological model and a model of porosity distribution. The subsequent dynamic model was fine tuned to obtain a match of the reservoir pressure history. In the dynamic model compaction at a reservoir scale was accounted for by embedding the associated pressure-porosity model in the dynamic model of the Harlingen Chalk gas reservoir.

Based on the 3D subsurface model and the NGI mechanical rock properties a new model for the calculation of compaction and subsidence was created, and rock mechanical parameters were fine-tuned based on comparison of the modelled results with the actual subsidence measurements in the area affected by the Harlingen Chalk gas production. Compaction and subsidence modelling was performed for the period 1988-2008 and the current model shows, on average, a fit that falls within the uncertainty of the benchmark measurements in the area. In addition, subsidence modeling was performed for the field shut-in period from 2008-2013, as well as forecast modelling for the period 2014 onwards.

1.5 DOCUMENTATION OF WORK

This technical report covers the work done since the start of the study in 2008.

Chapter 2 provides an introduction to the Harlingen Chalk gas field. Chapter 3 gives an overview of subsidence measurements available and Chapter 4 describes the rock mechanical studies conducted to determine compaction parameters and their key results. Chapter 5 describes the 3D subsurface model. The chapter includes the available data for building a 3D subsurface model, addresses the petrophysical evaluation, seismic interpretation, depth conversion and potential use of seismic attributes. Furthermore the static geological modelling and dynamic modelling to generate the input data required for the compaction and subsidence modeling work are addressed. Subsidence modelling for the production period of the field from 1988-2008 and the field shut-in period from 2008 to 2013 are addressed in Chapter 6. Forecast subsidence modelling for the period 2014 onwards and an alternative approach for subsidence forecasting, as well as a discussion of uncertainties, are discussed in Chapter 7. A summary and main conclusions are available in Chapter 8 and references are listed in Chapter 9.

2 OVERVIEW OF HARLINGEN CHALK GAS FIELD

2.1 FIELD STRUCTURE

Structurally, the Harlingen Chalk gas field, which is at a crestal depth of 1026 m, is a low curvature anticline (Figure 2-1) located on the edge of the Vlieland Basin, to the north-east of the inverted Texel-IJsselmeer High (Figure 2-2, Van den Bosch, 1983 [35], Van der Molen et al., 2007 [37]).

The Vlieland Basin and the Texel-IJsselmeer High are part of several intra-basinal highs and lows that characterized the Dutch North Sea area during the Late Jurassic to Early Cretaceous. The Vlieland Basin was inverted during the Late Cretaceous and later in the Oligocene through Middle Miocene, creating the current structure of the Harlingen Chalk field.

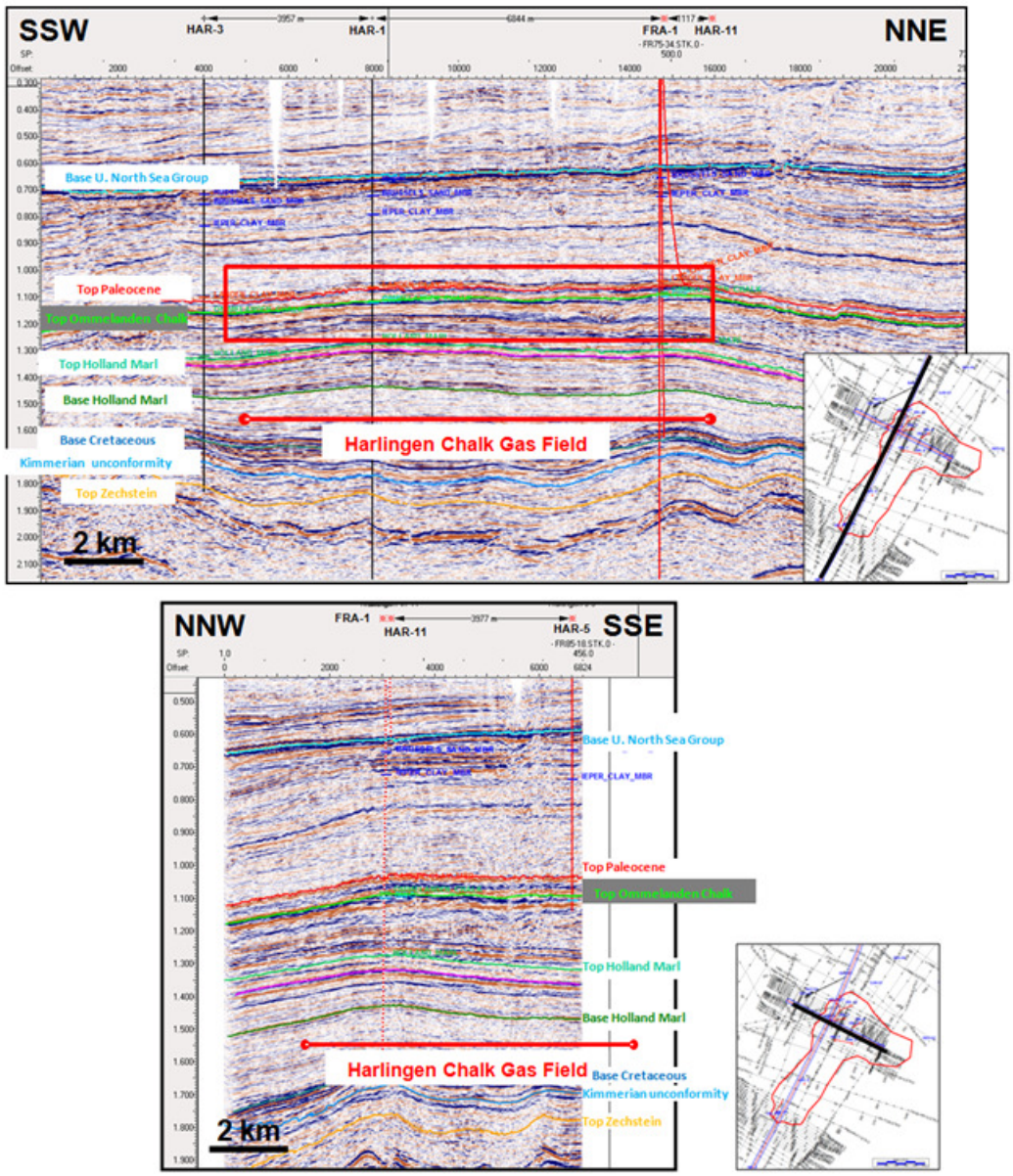

Figure 2-1 **2D seismic sections across the Harlingen Chalk gas field, red box indicates accumulation.**

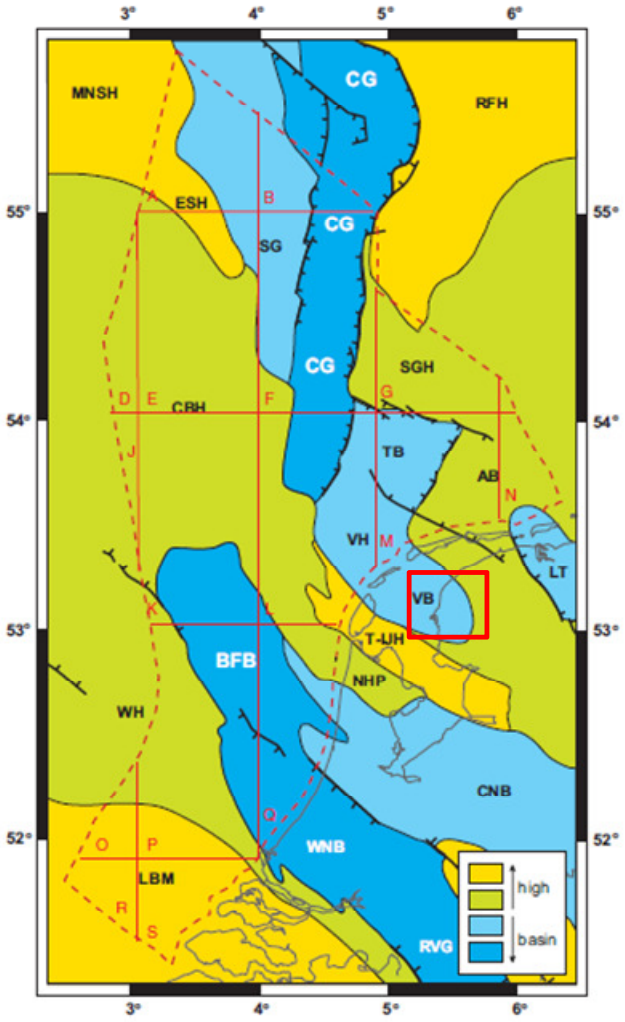

Figure 2-2 **Mesozoic structural elements of the Netherlands onshore and offshore. Bold red square marks approximate location of the Harlingen field. VB: Vlieland Basin. T-IJH: Texel-IJsselmeer High (after Van der Molen et al., 2007 [37]).**

2.2 STRATIGRAPHY

At Harlingen, the stratigraphic succession comprises sediments from the Carboniferous (Westphalian) coal-bearing clastics of the Limburg Group to Neogene clastics of the Upper North Sea Group (Figure 2-3).

The Chalk Group at Harlingen comprises the Cenomanian Texel Chalk Formation and the Turonian to Maastrichtian Ommelanden Chalk with a thickness ranging between 251 m and 638 m calculated from well information (Figure 2-4). The Upper Cretaceous Chalk section is not fully preserved in the Harlingen area. Also the equivalent of the Danian Ekofisk Chalk, which is present in various offshore wells, is missing in the Harlingen area. It was likely eroded during the Late Cretaceous inversion. The main reservoir at Harlingen is represented by the Upper Cretaceous Ommelanden Chalk.

The chalk section is generally recognized in the wells by its characteristic low gamma ray signature (Figure 2-5). The Texel Chalk is characterized by a clay-rich succession with a transitional basal contact with the underlying Upper Holland Marl. The Ommelanden Chalk is characterized by a consistently clean (low gamma ray) chalk succession (Figure 2-5).

Approximately 1000 m of Tertiary clays and sandstones of the North Sea Group constitute the overburden in the Harlingen area (Figure 2-5). The boundary between the Ommelanden Chalk and the overburden section is sharp, marking an abrupt lithology change; this is coinciding with the Late Cretaceous inversion unconformity (Figure 2-3).

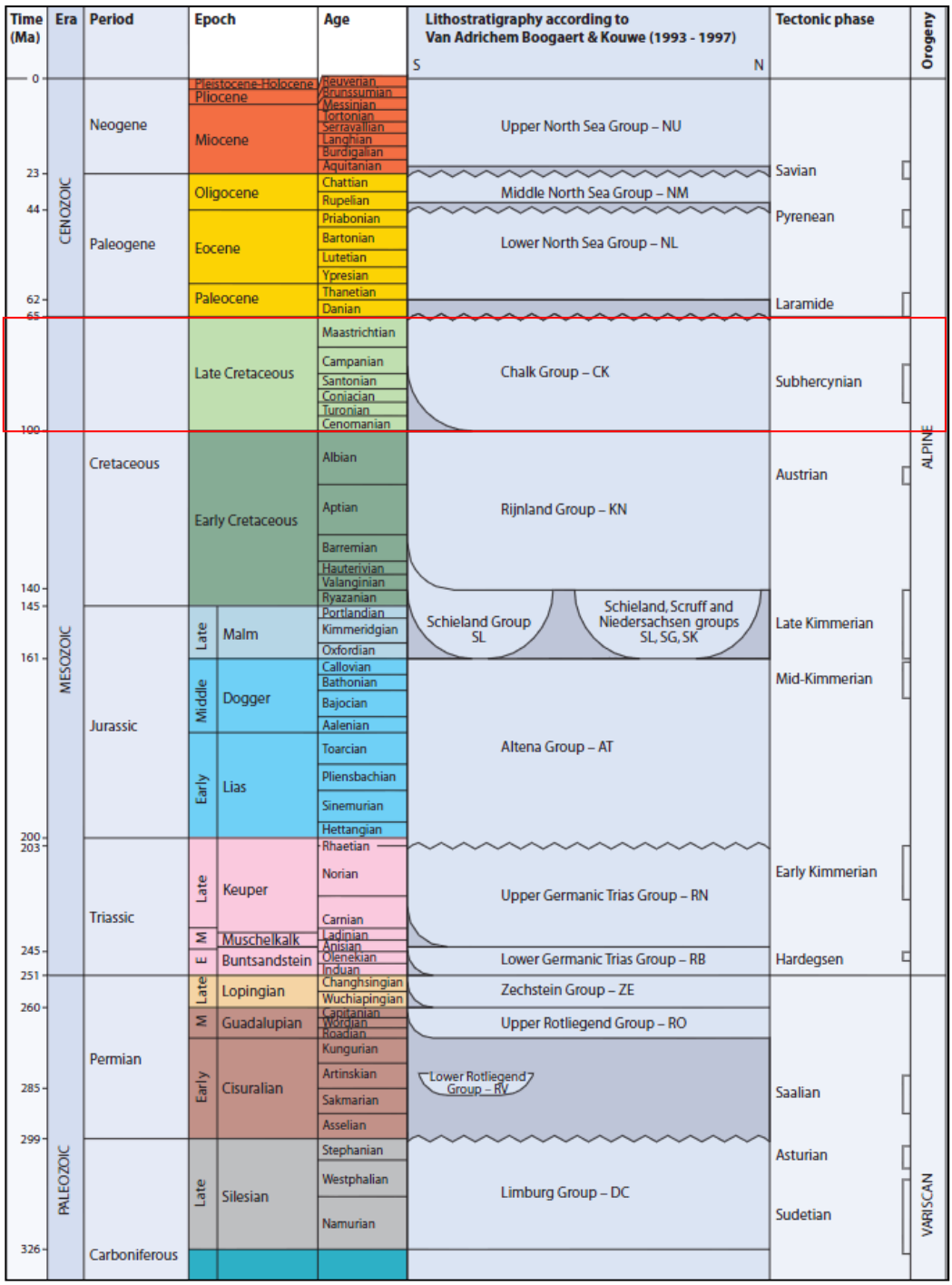

Figure 2-3 Geological time scale and lithostratigraphy in the Netherlands (after Duin et al., 2006 [5]).

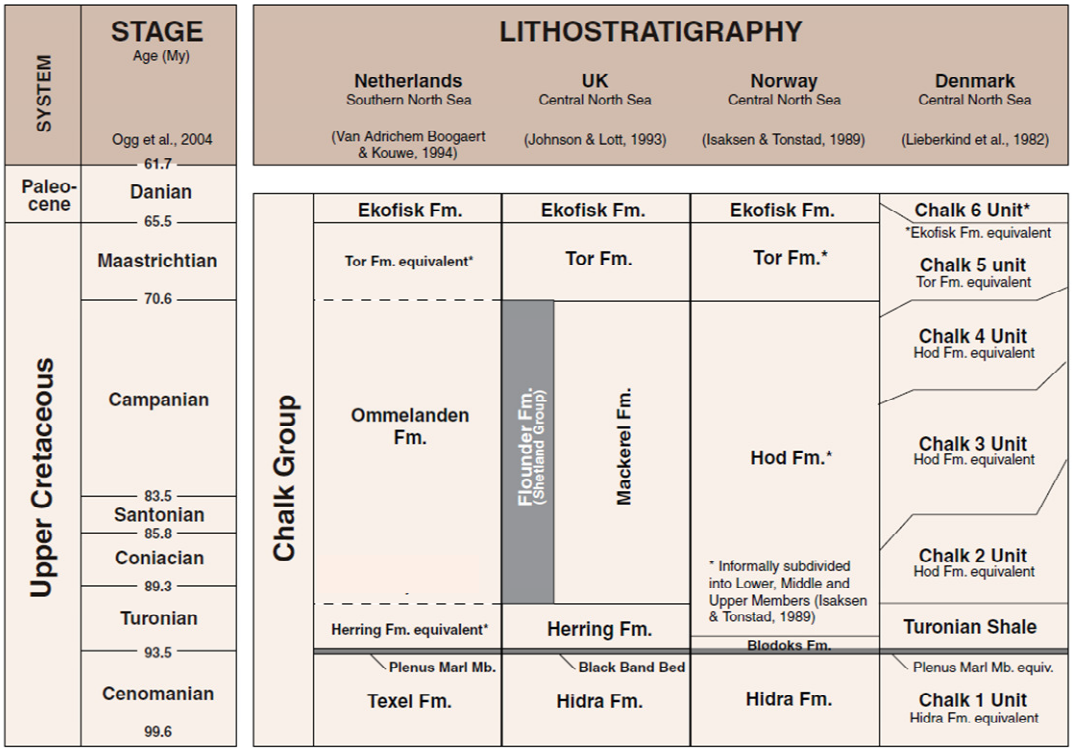

Figure 2-4 **Chalk lithostratigraphy in the Dutch, British, Norwegian and Danish sectors of the North Sea (Van der Molen et al., 2007 [37]).**

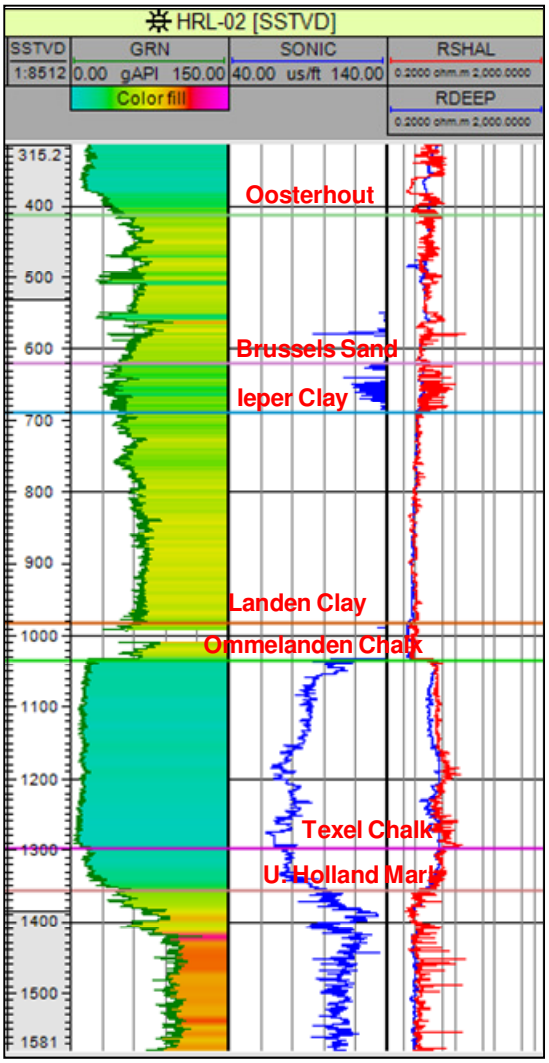

Figure 2-5 Harlingen type well.

2.3 CHALK RESERVOIR CHARACTERISTICS

The Ommelanden Chalk reservoir rocks were deposited in an open marine environment with depths ranging between 50 m to 150 m (Van der Molen, 2004 [36]). The main components of the chalk are coccoliths and foraminifera, which settled down from suspension in the water column (Van der Molen, 2004 [36]). Analyses of the reservoir chalk point to a geochemical composition of the reservoir rock of 96-99 % calcite, 1-4 % quartz and 0-2 % clay minerals (Van den Bosch, 1983 [35]). Good reservoir quality, with the highest porosity, is retained in the upper few meters of the reservoir. Porosity ranges from over 30 % in the reservoir to 24 % below the gas-water-contact (GWC), permeability is in the range of 1-2 mD (Orlic et al., 2006 [24]). Good reservoir quality is probably caused by early gas migration into the uppermost part of the Ommelanden Chalk section during the Oligocene (Van den Bosch, 1983 [35]). The presence of the overpressured gas prevented loss of porosity and permeability by diagenesis and compaction. The high amount of intact coccoliths described fits with this hypothesis (Van den Bosch, 1983 [35]). Below the GWC a higher amount of calcite crystals formed by recrystallization occur, which degrades the reservoir properties (Van den Bosch, 1983 [35]).

3 SUBSIDENCE: CONTRIBUTIONS AND MEASUREMENTS

Gas production from the Harlingen Chalk field caused surface subsidence in response to reservoir compaction upon pressure depletion of the field. The amount of reservoir compaction is mainly dependent on the amount of pressure drop in the reservoir, the porosity and thickness of the rock being depressurized, the depth of the compacting reservoir, and the strength of the reservoir rock itself.

Surface subsidence is not only influenced by the reservoir characteristics, but also depends on the elasticity (and therefore lithology) of the overburden layers. Furthermore, active salt production in the vicinity of the Harlingen Chalk gas field has also contributed to surface subsidence. Finally, autonomous subsidence contributes to the total surface subsidence.

As indicated in Section 1.2, the observed subsidence over the Harlingen Chalk gas field in 2008 was approximately two times higher than predicted. According to an analysis of benchmark levelling data by Houtenbos, 2010 [11], in 2009 gas extraction induced subsidence had reached 24.6 cm in the deepest point of the surface subsidence bowl above the gas field, close to the HRL-07 well location (Figure 3-1). The total subsidence in 2009 had reached up to 26 cm in the same location (Figure 3-2), while the contribution of salt mining-induced subsidence at that same point would have been in the order of 1.4 cm. Figure 3-3 shows the subsidence attributed to salt extraction. Muntendam-Bos et al., 2009 [15], reported a minimum estimate of total subsidence (26.5 cm) in the deepest point of the surface subsidence bowl above the gas field for the period 1988-2008, based on a combination of interpolated benchmark and satellite measurement data.

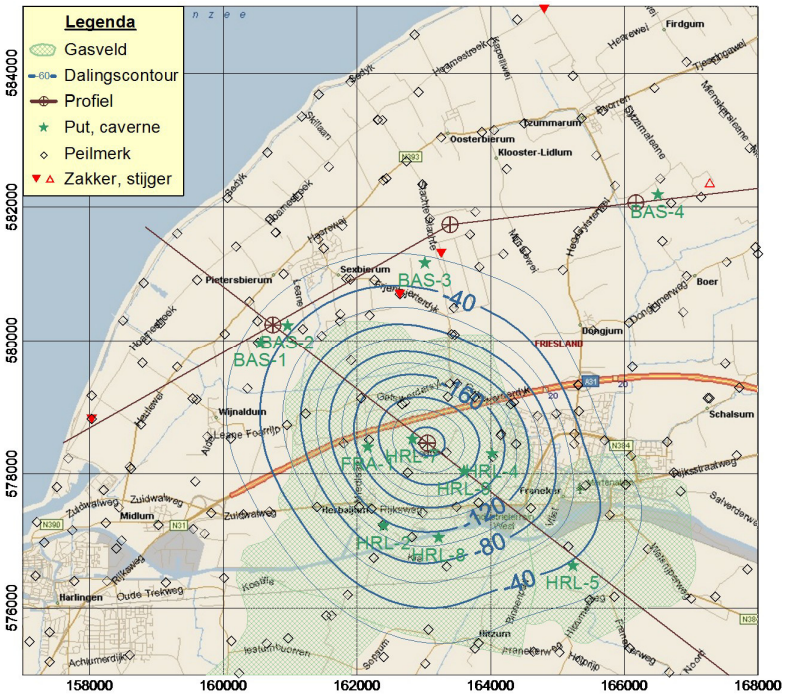

Figure 3-1 **Subsidence attributed to gas production over the period 1988-2009 [11]. Subsidence contours in mm.**

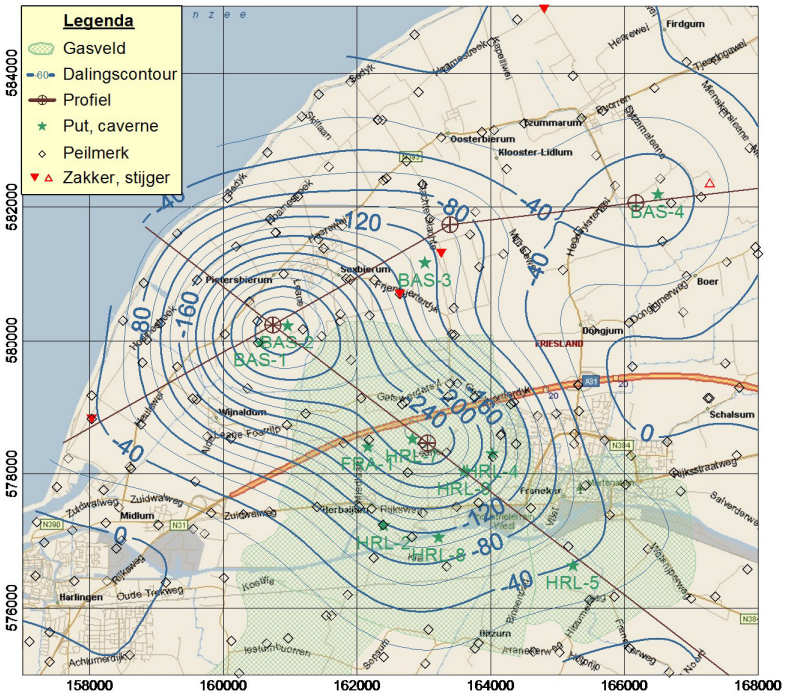

Figure 3-2 **Total subsidence in the Barradeel-Harlingen area over the period 1988-2009 [11]. Subsidence contours in mm.**

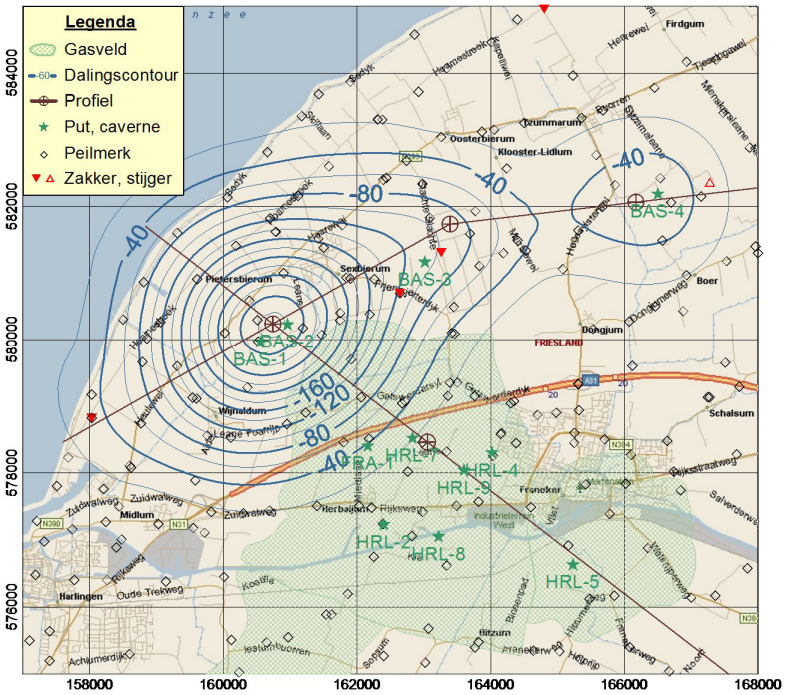

Figure 3-3 **Subsidence attributed to salt production over the period 1988-2009 [11]. Subsidence contours in mm.**

It should be noted that although providing a good indication of the relative contributions of the causes of subsidence, different models may lead to different maps and different relative contributions of the individual causes of subsidence.

SGSH uses surface subsidence measurements to evaluate the subsidence model. These measurements are collected across a grid of fixed benchmark points at which the vertical displacement is evaluated using levelling during measuring campaigns. The frequency of those campaigns has varied through the field life history and similarly the number of points that were included in each campaign has changed with time.

3.1 BENCHMARK DATA

3.1.1 LEVELLING SURVEYS

Elf Petroland B.V., Total, and later Vermilion Oil & Gas Netherlands B.V., have carried out regular levelling surveys of the fixed benchmark points across the area near Franeker since 1988. The benchmark network was expanded a few times to account for extended influence of subsidence. Since 2006 the network is shared with Frisia B.V. and includes the Barradeel area in which salt mining has taken place since 1995. The survey results are published in reports 'Meetregisters Leeuwarden-West' available on the website www.nlog.nl [43].

Since the initiation of the benchmark network ("nulmeting") in 1988 repeat measurements are available for 1992, 1997, 2000, 2003, 2006, 2007, 2008, 2009, 2010, 2011, 2012 and 2013. The extent of the network changed through time: points were added to cover an extended area of developing subsidence and some points were removed, e.g. because they were not available anymore. 'Meetplan Leeuwarden-West' contains a total of 340 points that have at least one repeat measurement between 1988 and 2013. The data are presented as height (meter) above NAP (Normal Amsterdams Peil) and the coordinates are determined either by GPS or by extracting data from a map which means accuracy ranges from less than a meter to a maximum of 50 meters. Although the latter accuracy is low it is not considered to have substantial influence on the modelling evaluation results. For this study, SGSH has used the integrated "differentiestaat" which is based on the above reports provided by Vermilion as shown in Appendix 1.

The benchmark measurements have an associated uncertainty and based on advice of the technical committee it is believed that the nature and magnitude of the uncertainties follow those described by Muntendam-Bos et al., 2012 [16]. The uncertainty associated with benchmark measurements consists of a fixed (instrument) measurement uncertainty, the fixed (instrument) measurement uncertainty of the reference station and a time-dependent (drift) uncertainty caused by instability of the benchmark point itself (Muntendam-Bos et al., 2012 [16]). According to Muntendam-Bos et al., 2012 [16], the fixed uncertainty (σ_{meas}) for each benchmark measurement and for the reference station (σ_{ref}) is 0.03 cm, respectively, and the drift is 0.025 cm/year for the time since the initiation of the benchmark network (1988). The total uncertainty on each benchmark measurement in a certain measurement campaign (year) is the statistical combination of these three error sources: $\sigma_{tot}(yr) = \sqrt{(\sigma_{ref}^2+\sigma_{meas}^2+((yr-1988)*drift)^2)}$.

Subsidence at the benchmark points is a combined effect of gas production, salt production in the nearby Barradeel salt mines and autonomous subsidence. To be able to evaluate the model for gas-production induced subsidence only, the benchmark data is corrected for the contribution of salt-induced and autonomous subsidence.

3.1.2 GPS

In addition to the levelling surveys subsidence measurements from GPS stations have become available in more recent years. Above the Harlingen Chalk field two stations have been installed to measure surface deformation since 2008, these are the height measurements at well locations HRL-04 and HRL-07 between 2008 and 2014.

The GPS measurements show large short term fluctuations but the average signal seems to display a stable trend. The accuracy of these subsidence measurements depends on the stability of the GPS station and of the reference station.

3.1.3 SATELLITE DATA

Satellite data, through the method of Persistent Scattered Interferometry (PSI) or PS-InSAR, can also provide a measure of surface deformation and hence of surface subsidence. A study by TNO (Muntendam-Bos et al., 2009 [15]), focused on the salt mining induced subsidence in the Barradeel and Harlingen areas. Although the accuracy of the satellite data is considered similar to the accuracy of the benchmark levelling surveys, this study highlighted the potential of PS-InSAR radar data to supplement levelling surveys in areas where benchmark data are sparse. This study uses PS-InSAR datasets from two time periods (1998-2000 and 2003-2006), which were processed by TU Delft. During these periods the satellite measurements show good agreement with the levelling surveys at the benchmark locations. Above the central part of Harlingen Chalk gas field the scatters show a moderate difference with the benchmark measurements (Muntendam-Bos et al., 2009 [15]).

Since then, Samieie-Esfahany et al., 2009 [27], highlighted the bias in the data due to the deformation measurement being in the line of sight direction of the satellite. A correction from line of sight deformation to vertical deformation could not be executed previously due to the absence of data on both the ascending and descending tracks of the satellite. They proposed a revised method for the correction of the data for the horizontal displacement of the scatter points and published an update of the difference maps in their publication. The differences above the Harlingen Chalk field between maps based on benchmark data combined with PS-InSAR data and benchmark data alone are less than 1 cm according to the corrected map (Samieie-Esfahany et al., 2009 [27]). The processed satellite data that are used to produce the difference maps were not available for this study and hence not used.

3.2 SALT MINING

Salt mining has occurred from four caverns in the Barradeel area, north-west of the Harlingen Chalk gas field: BAS-01,-02,-03 and -04. Figure 3-3 shows a map of subsidence attributed to salt production over the period 1988-2009 from Houtenbos, 2010 [11].

Though the focus of the study is related to the gas induced subsidence, it is required be to able to account for the contribution of the salt induced subsidence to the total subsidence above the Harlingen Chalk field in order to correct the benchmark data accordingly.

Gaussian fit parameters for the subsidence bowls due to salt-production are made available by Frisia B.V. (e.g. BECi, 2007 [1]). BAS-01 and BAS-02 are modelled as one due to their proximity. The parameters have resulted from the fitting of a Gaussian subsidence bowl to the measured levelling data where only the data that are considered to be influenced by salt extraction are used in the analysis. The bowl is defined by two shape parameters and by the position and depth of the deepest point. According to these Gaussian fit parameters, subsidence above the Harlingen Chalk gas field is mainly influenced by the BAS-01 and BAS-02 bowl, to a limited extent by the BAS-03 bowl and not influenced by the BAS-04 bowl.

Salt mining in BAS-01 and -02 started in 1995 and continued for approximately 10 years. Activities at the other localities started in 2003 (BAS-03) and 2006 (BAS-04). Annual salt-induced subsidence Gaussian fit parameter updates between 1995 and 2009 have been made available to SGSH. To correct for salt-induced subsidence after 2009 it is assumed that the subsidence bowls did not change in shape and position. The total depth for the bowls in this period has been extrapolated after correlation with permanent GPS measurements at the localities (available online: www.nlog.nl [43]). The BAS-01 and BAS-02 fit bowl, which is the main subsidence contributor above the Harlingen gas field, did not change in shape and depth from 2008 onwards according to this extrapolation.

Additionally TNO-AGE supplied differences between the Frisia modelled subsidence and outputs from their own salt-induced subsidence model at the benchmark locations. TNO-AGE's model calculates compaction based on the mined salt volumes, and translates this to surface subsidence with the Van Opstal method, 1974 [39]. The main difference between the two approaches is a difference in shape of the subsidence bowl: the TNO-AGE model results in a bowl which is wider

and hence less steep on the flanks than the bowl resulting from the Frisia Gaussian fit. The maximum difference between the two approaches above the gas field is 2.6 cm.

3.3 AUTONOMOUS SUBSIDENCE

In order to evaluate for gas-production induced subsidence only, the benchmark data has to be corrected for autonomous subsidence also.

Autonomous subsidence, e.g. due to compaction of shallow layers, was investigated by comparing subsidence at specific benchmark points with foundations in deeper subsurface layers to surrounding data points (Oranjewoud, 2007 [23]). A total of six available measurements between 1988 an 2006 above and near the Harlingen Chalk field, indicate autonomous subsidence is highly varying (Table 3-1 and Figure 3-4), making it difficult to apply a correction to all benchmark data.

Table 3-1 Autonomous subsidence at deeply founded benchmark points (data taken from Table 3 in [23])

Benchmark	Estimated autonomous subsidence 1988-2006 (cm)	Estimated autonomous subsidence rate (cm/yr)
000A2748	-0.2	-0.01
000A2750	-2.8	-0.16
000A2752	-1.4	-0.08
000A2756	-0.8	-0.04
000A2758	-0.7	-0.04
000A2760	-1.6	-0.09

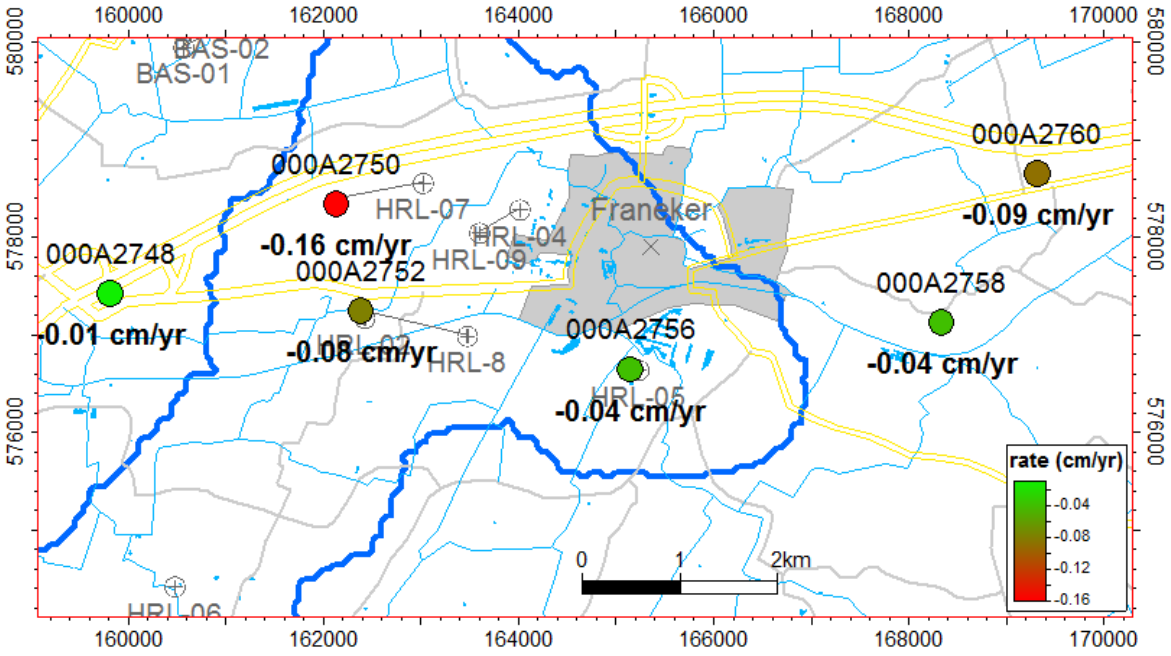

Figure 3-4 Estimated autonomous subsidence rates (based on Oranjewoud, 2007 [23]).

4 ROCK MECHANICAL STUDIES

Gas production without sustained pressure support supplied by an external source will lead to field pressure reduction. The change in reservoir pressure increases the effective stress in the reservoir and in the nearby rock formation. As a response to the increased effective stresses on the rock formation the rock deforms by compaction.

Chalk displays a particular susceptibility to deformation, more complex than many other rock materials; and strongly dependent on several factors such as the chalk porosity (van Ditzhuijzen et al., 1984 [38], Smits et al., 1988 [29], Collin, 2002 [3], Hickman, 2004 [10], NGI, 2007 [17], NGI, 2009a [18], 2011a [20], Schroeder et al., 2009 [28]), pore fluid composition and degree of saturation (Heggheim et al., 2005 [9], Madland, 2005 [14], Korsnes et al., 2006 [12], NGI, 2007 [17], Fabricius et al. 2010 [6], NGI, 2011a [20]), as well as loading rate (i.e. depletion/production rate) (Leroueil, 2006 [13], Hickman, 2004 [10], Pasachalk, 2004 [25], Priol, 2005 [26], NGI, 2009b [19], NGI, 2011a [20], NGI, 2013 [22], Smits et al., 1988 [29]). In case of the latter control parameter the current research performed within this project reveals that the effect of load rate may infer significant deformation even for relatively low porosities and moderate pressures for Harlingen and similar producing gas fields (NGI, 2009b [19], NGI, 2011a [20], NGI, 2013 [22]).

Compaction due to increased loading is described as elastic up to a certain effective stress limit which is determined by porosity, pore fluid and production rate. Beyond this limit the stress-strain behaviour is characterized by pore collapse, a plastic behaviour inducing significantly larger strain than in the elastic domain. Thus, the pore collapse threshold is a crucial parameter.

After production, when active depletion is terminated, the reservoir and surrounding formations typically exhibit continued compaction adding to the cumulative deformation and subsidence. This is an intrinsic time dependent behaviour related to the visco-plastic attributes of the chalk, and depends on its material properties and the loading history (from deposition to production and shut-in).

A laboratory testing program was launched to improve the rock mechanical understanding to bridge the gap between observed and previously modelled subsidence. The influence of control parameters (rock mechanical material properties, porosity, pore fluid composition, and loading rate) were individually investigated in the laboratory environment at realistic in situ stress conditions on Harlingen core material. The work was carried out in four stages: phase 1 by the Liege University in Belgium and phases 2 to 4 by the NGI in Oslo, Norway.

Using the material property input from the experimental laboratory mechanical tests and correlations available from open chalk literature data sets, a rock mechanical model based on the Rate Type Compaction Model (RTCM, de Waal, 1986 [4]) framework has been derived by NGI. The rock mechanical model gives a description of the distinct elastic and plastic behaviour as well as the pore collapse criterion expected for the Harlingen chalk under the given depletion process, and the time dependent deformation (creep) occurring after shut-in.

The compaction model has been verified against laboratory experiments demonstrating its robustness. It is also in agreement with an independent software package (PLAXIS) based on an alternative theoretical approach (Soft Soil Model by Vermeer et al., 1999 [40]).

The geomechanical work is summarised in Appendix 2 (NGI, 2013 [22]), and described in detail in NGI, 2009a [17], NGI, 2009b [19], NGI, 2011a [20] and NGI, 2011b [21].

4.1 KEY RESULTS

The rock mechanical parameters for the loading period, derived in the rock mechanical studies performed by NGI, are (Table 4-1):

- Compressibility in the elastic state, which is defined by the bulk modulus.
- Compressibility in the plastic state, which is a function of the compressibility coefficient.
- Rate dependency parameter, which describes the translation of lab to field loading conditions.

- Isotropic yield stress, which describes the transition from elastic to plastic state.
- Ratio of effective horizontal to vertical stress for the elastic state, which is related to the Poisson's ratio.
- Ratio of effective horizontal to vertical stress for the plastic state, which is determined by laboratory results.

For these parameters a range of solutions/values fit the experimental chalk data which is shown for three parameters in Figure 4-1.

Table 4-1 Parameters used in volumetric strain modelling stating their definition as a function of porosity (ϕ) or Poisson's ratio (ν)

Definition		Formula	Parameter for sensitivity & tuning	Default value
Compressibility	Elastic compressibility 1/K	$K = BulkMod\_fac \cdot e^{BulkMod\_exp \cdot \phi}$	BulkMod_fac *(60000 – 500000)*	BulkMod_fac: 83596
	Plastic state: function of compressibility coefficient	$\lambda = Lambda\_fac \cdot e^{Lambda\_exp \cdot \phi}$	Lambda_fac *(0.028 – 0.075)* Lambda_exp *(2.5 – 4.5)*	Lambda_fac: 0.032 Lambda_exp: 4.1
Translation of lab to field loading conditions	Rate dependency parameter	$b = b\_fac \cdot e^{b\_exp \cdot \phi}$	b_fac *(0.135 – 0.170)*	b_fac: 0.135
Elastic-plastic transition	Isotropic yield stress	$P_c = Pc\_fac \cdot e^{Pc\_exp * \phi}$	Pc_fac *(250 – 450)*	Pc_fac: 300
Ratio effective horizontal – vertical stress	Elastic state: related to Poisson's ratio	$\Delta K' = \nu / (1-\nu)$	ν *(0.2 – 0.35)*	ν: 0.25
	Plastic state: determined by lab experiments	$\Delta K' = 0.4 - 0.6$	$\Delta K'$ *(0.4 – 0.6)*	$\Delta K'$: 0.6

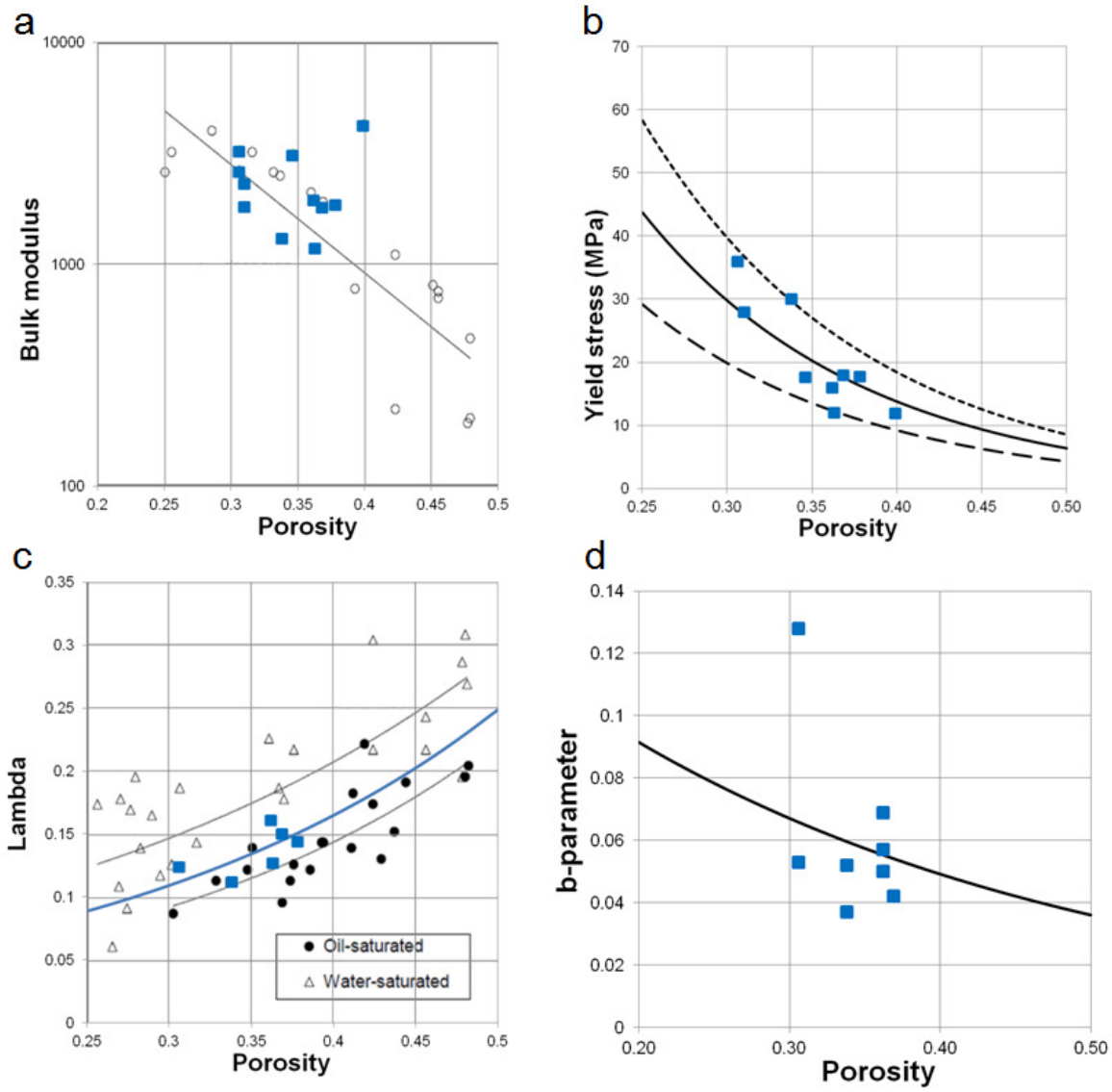

Figure 4-1 **Compressibility parameters vs. porosity, based on [21], for Harlingen Chalk experiments (blue symbols) and data from the JCR database [10]: a) Bulk modulus (trend line from [10]); b) yield stress at pore collapse with lower, average and upper trend lines [21]; c) compressibility coefficient (lambda) with trend lines; d) loading rate dependency parameter (b-parameter).**

The incorporation of these results in the 3D subsurface model is described in Section 5.2.2.3 and Chapter 6 discusses their application in the compaction/subsidence modelling.

5 3D SUBSURFACE MODEL

5.1 DATA AVAILABILITY

5.1.1 WELL DATA

A list of the available well data is given in Table 5-1. Nineteen wells from both inside and outside the field were used. Wells BAS-01, BAS-02, BAS-03 and BAS-04 are salt wells. The "Log data" column in Table 5-1 indicates the depths from which wireline log data were available.

Eight wells were cored (Table 5-1). Porosity and permeability measurements were available for these wells. Formation Factor (FF) measurements were acquired in two wells (FRA-01 and HRL-09), but only the HRL-09 measurements were performed under reservoir conditions and can be used to establish the cementation factor (m). Some cored intervals were sparsely or preferentially sampled. Core samples from HRL-07 were used to perform rock mechanical experiments (described in Chapter 4). An overburden correction was applied to the core porosities by reducing the measured values by 3.5 % This is based on the measurements under stress conducted on core from the wellbore HRL-07.

Other data include:

- Well reports (e.g. EOWR, final drilling reports) and specialist studies (e.g. core structural logging study, sedimentological studies, biostratigraphic studies)
- Composite logs and mud logs available for some wells
- Well log suites and well surveys on 14 wells in the Ommelanden Chalk. Limited section of the overburden and the section below the Ommelanden reservoir
- Capillary pressure data from wells HRL-07 and HRL-09 (Section 5.2.2.2)

Furthermore, gas and water production rates were available for the period 1988-2008 and pressure measurements were available for the period 1988-2013 for all nine wells that produced gas from the field.

Table 5-1 Available well data. Deviated and horizontal wells are indicated with *. Value in "Log data" indicates from which depth the logs are available

	Well	UWI	Drilled in	TD	RT	Log data					Check	Core data			Dynamic data	
						GR	Sonic	Res.	Dens.	Neu.	shots	Phi/K	FF factor	Pc	Production	Pressure
				[mMD]	[m to NAP]	[mMD]	[mMD]	[mMD]	[mMD]	[mMD]	(Y/N)	(Y/N)	(Y/N)	(Y/N)	(Y/N)	(Y/N)
Inside the field	Franeker-01*	FRA-01	1978	1837	5.9	0	330	1029	1029	1029	Y	Y	Y	N	Y	Y
	Harlingen-01	HRL-01	1965	2732	6.8	602	285	1069	-	-	N	Y	N	N	N	N
	Harlingen-02	HRL-02	1965	1870.5	5.2	300	200	200	1015	-	Y	Y	N	N	Y	Y
	Harlingen-03	HRL-03	1965	2003	5.5	310	310	310	1064	-	Y	Y	N	N	N	N
	Harlingen-04	HRL-04	1984	1101	4.5	308	1011	1011	1011	1011	Y	Y	N	N	Y	Y
	Harlingen-05	HRL-05	1984	1112	4.6	410	410	410	410	410	Y	Y	N	N	Y	Y
	Harlingen-06	HRL-06	1985	1117	4.8	830	1028	1028	1028	1028	N	N	N	N	Y	Y
	Harlingen-07*	HRL-07	1992	1635	8.6	0	1228	1228	1228	1228	N	Y	N	Y	Y	Y
	Harlingen-08*	HRL-08	1993	1830	9.0	40	1315	1315	1315	1315	N	N	N	N	Y	Y
	Harlingen-09*	HRL-09	2000	1306	5.8	40	414	1110	1110	1110	Y	N	Y	Y	Y	Y
	Harlingen-10-S3*	HRL-10-S3	2007	1132	9.0	662	662	-	-	-	N	N	N	N	Y	Y
	Harlingen-11-S1*	HRL-11ST1	2007	2054	9.0	1370	-	1370	1370	1370	N	N	N	N	N	N
	Harlingen-11-HTZL*	HRL-11HZTL	2007	2365	9.0	1393	-	1393	1393	1393	N	N	N	N	N	N
	Harlingen-101*	HRL-101	1994	2430	9.0	360	360	360	-	-	N	N	N	N	N	N
Outside the field	Harlingen West 1	HAW-01	1965	3348	8.3	-	220	-	-	-	N	N	N	N	N	N
	Barradeel Salt-01	BAS-01	1994	3055	8.2	-	-	-	-	-	N	N	N	N	Y	N
	Barradeel Salt-02	BAS-02	1995	3134	9	-	-	-	-	-	N	N	N	N	Y	N
	Barradeel Salt-03	BAS-03	2002	4447	9.8	-	-	-	-	-	N	N	N	N	Y	N
	Barradeel Salt-04	BAS-04	2004	2819	9.5	-	-	-	-	-	N	N	N	N	Y	N

5.1.2 SEISMIC DATA

Seventy-four 2D seismic lines over an area of about 250 km^2 were available for the structural interpretation of the Chalk reservoir in the Harlingen – Franeker area. The data originates from different vintages and was re-processed together in order to obtain a homogeneous seismic data-

set. Thirty-five (35) of the seismic profiles were acquired in high resolution mode to allow detailed interpretation of both top and base reservoir. These surveys date from 1983 and 1985. After re-processing the older surveys also allowed interpretation of top and base of the chalk. The full spread of vintages ranges from 1975 to 1989. The 1985 survey had the closet interline spacing of only 150 m giving good structural coverage. With all these datasets it was possible to construct a consistent interpretation of the field. Appendix 4 lists the 2D seismic lines used for this study.

Check shots from wells FRA-01, HRL-02, HRL-03, HRL-04, HRL-05, HRL-06, and HRL-09 were used to calibrate the top- and base of the chalk series in time (Table 5-1).

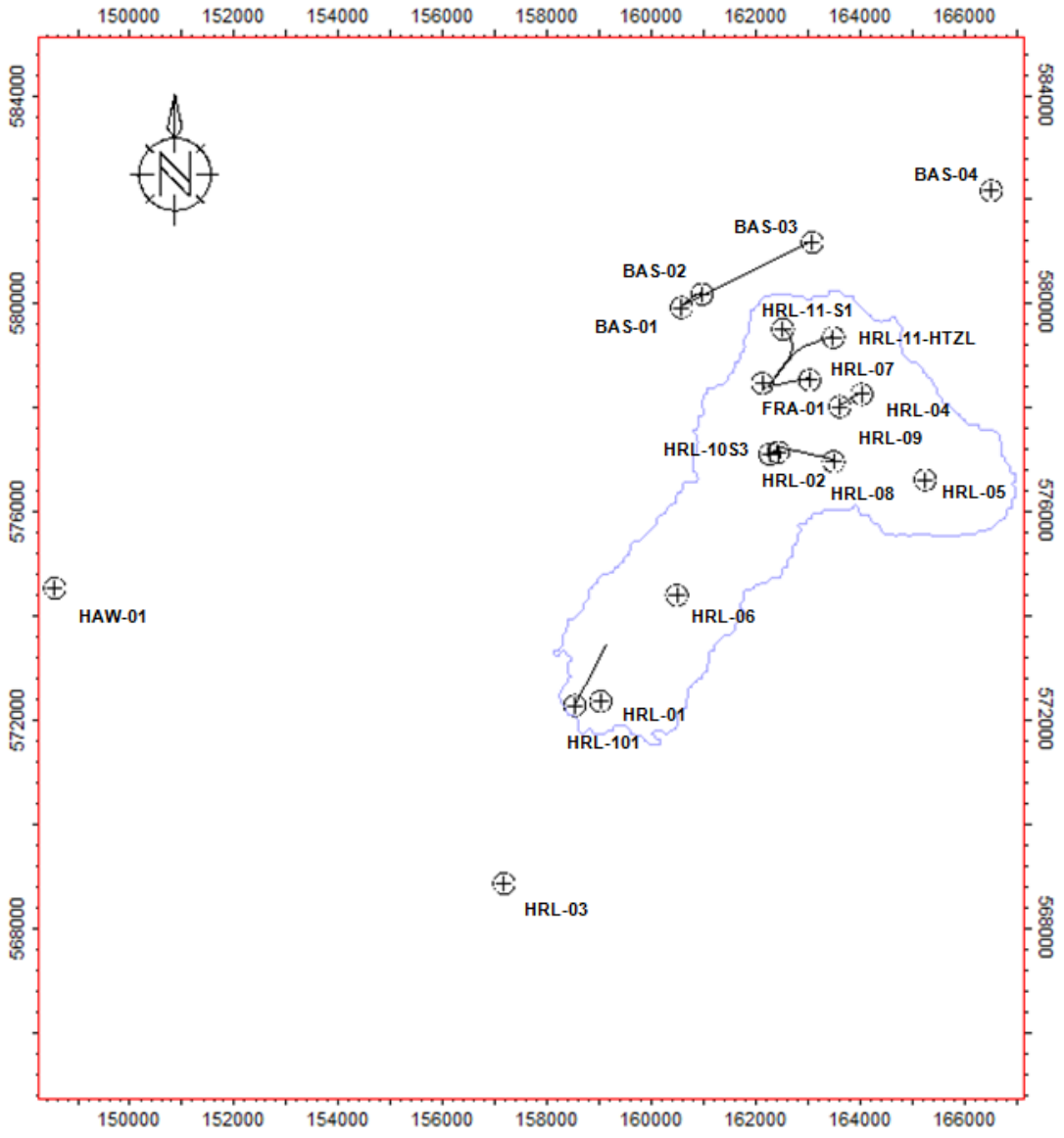

Figure 5-1 Harlingen gas field outline and wells available for this study. Well data availability is shown in Table 5-1.

5.1.3 OTHER DATA

Additional available data (provided by Vermilion) for this study were:

- Vintage core descriptions for all the wells within the field

- Photomicrographs of thin sections of Ommelanden Chalk from a previous study in wells:
  - HRL-02 at 1050.9 mMD and 1065.4 mMD
  - HRL-09 at 1127 mMD and 1131.6 mMD
- Reservoir engineering input for dynamic modelling based on work and interpretations performed by Vermilion prior to this study:
  - Fluid description
  - Interpreted well tests for all gas producing wells
  - Relative permeability characteristics

5.2 PETROPHYSICAL INTERPRETATION

A standard petrophysical model of the Harlingen Chalk gas field was built. This model was then used to define the fluid contacts (Section 5.2.3) and identify porosity and permeability anomalies.

Figure 5-1 and Table 5-1 give an overview of the wells drilled in the Harlingen area in the years 1965 to 2007. Both oil and water based mud were used while drilling the Harlingen wells.

The log data were provided by Vermilion, received as LAS files and loaded to the Terrascience software suite, which was the main software used to conduct the petrophysical evaluation in 2008. Input and output logs are listed in Appendix 3.

The quality control and further investigations were conducted in 2008 and 2009 using the Interactive Petrophysics software package. Appendix 3 shows the final CPIs of the studied wells.

Rock properties were computed based on the available data (Section 5.2.2).

5.2.1 PETROPHYSICAL EVALUATION

5.2.1.1 Data editing, environmental corrections and normalization

The resistivity, density, neutron and sonic curves were depth-shifted to match the GR curve.

Standard corrections were applied to the density and neutron logs. Measured While Drilling (MWD) density and neutron logs in some wells were laterally shifted based on histograms from more reliable wireline logged (WLL) wells.

Gamma Ray curves (GR) were normalized (GRN), so obtaining ~ 8 GAPI for the cleanest chalk, and ~ 70 GAPI for the thick overlying, as shown in Figure 5-2. In case of missing logged interval in the overburden shale section, the shale was stretched to ~ 95 GAPI.

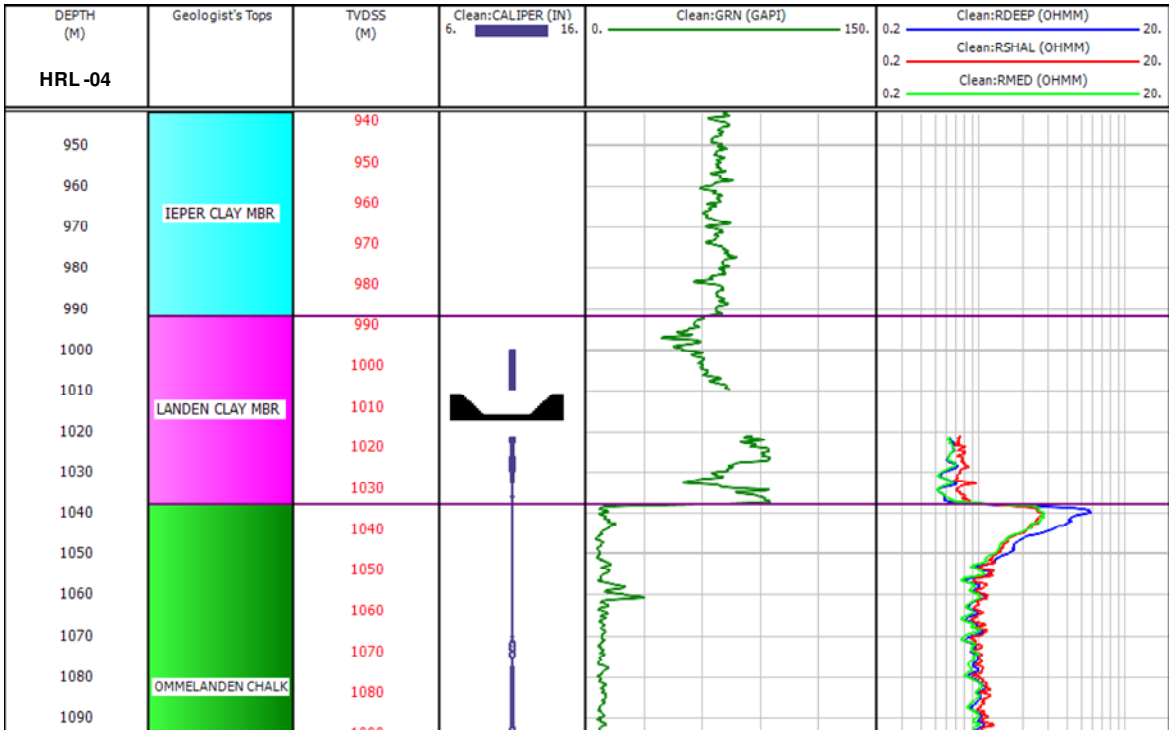

Figure 5-2 Gamma Ray normalization: endpoint values.

5.2.1.2 Volume of shale

The volume of shale (VSH) was calculated from the gamma ray log applying the linear method, as given by the equation:

$$VSH = \frac{GR\_\log - GR\_clean}{GR\_shale - GR\_clean}$$

where:

- GR_clean – 8 GAPI: Gamma Ray value assumed for the cleanest chalk;
- GR_shale – 70 GAPI: Gamma Ray value assumed for the shale;
- GR_log – normalized GR log.

5.2.1.3 Porosity

Different methods were used to calculate porosity from logs, including:

- Neutron-Density porosity;
- Density porosity;
- Sonic (Raymer-Hunt) porosity,
- Gamma ray porosity (only when missing porosity logs).

Reference values for the calcite were assumed as matrix end-points for the porosity calculations.

A gas density of 0.1 g/cm^3 was used for the hydrocarbon. Such a value was based on the gas composition of FRA-01, HRL-09 and HRL-06: the specific gravity at surface conditions was estimated to be around 0.57 (corresponding to ~0.1 when converted to reservoir conditions). A value of 350 µs/ft was instead used to estimate the sonic slowness.

A water density of 1.05 g/cm^3 was assumed according to the formation brine salinity (Section 5.2.1.4). A variable filtrate density was instead used according to the different filtrate types.

All the different porosity methods were computed and compared with core data and with outputs from nearby wells. Comparisons were made in both gas and water zones. Models were run with basic fluid assumptions and with complex fluid substitution of formation water brine saturation (Sw), filtrate invasion (Sxo) and gas saturation (Sg). Hydrocarbon effects were taken in account and proper corrections were made when needed.
By considering the outputs coming from all the methods used, the final total porosities (PHIT_F) were chosen based on calibration to core data (in-situ corrected), comparison to the nearby wells, quality of the input logs, fluid type (gas or water) and borehole conditions. An overview of the methodologies used for PHIT_F is given in Table 5-2 (for all the wells and for both the gas- and water-bearing intervals). The final match of log to core data was very good, as shown in Figure 5-3 and in the CPIs reported in Appendix 3.
The final effective porosity PHIE_F was computed starting from the total porosity PHIT_F and by subtracting to this value less the fraction of the pore space occupied by shale (VSH). It should be noted that, generally, the mineralogy appears to be almost pure chalk, with only few significant clay occurrences.

Table 5-2 Porosity calculation method chosen for each well.

Well	UWI	Drilled [year]	Type	Porosity Method (gas zone)	Porosity Method (wet zone)	Comments
Franeker-01	FRA-01	1978	Deviated	Density	Sonic	Based on Core, used Sonic where Density missing
Harlingen-01	HRL-01	1965	Vertical	Sonic	Gamma Ray	Only Sonic available
Harlingen-02	HRL-02	1965	Vertical	Density	Sonic	Based on Core, used Sonic where Density missing
Harlingen-03	HRL-03	1965	Vertical	Sonic	Sonic	Based on comparison to nearby wells
Harlingen-04	HRL-04	1984	Vertical	Density	Neu/Den	Based on Core, used Sonic where Density missing
Harlingen-05	HRL-05	1984	Vertical	Neu/Den	Neu/Den	Based on Core, used Sonic where Density missing
Harlingen-06	HRL-06	1985	Vertical	Neu/Den	Neu/Den	Based on comparison to HRL-05
Harlingen-07	HRL-07	1992	Horizontal	Neu/Den	Sonic	Used Sonic where Density missing
Harlingen-08	HRL-08	1993	Horizontal	Sonic	-	Based on comparison to nearby wells
Harlingen-09	HRL-09	2000	Deviated	Neu/Den	Sonic	Based on Core and comparison to nearby wells
Harlingen-10-S3	HRL-10-S3	2007	Deviated	Sonic	-	Only Sonic available
Harlingen-11-S1	HRL-11ST1	2007	Horizontal	Neu/Den	-	Based on comparison to nearby wells
Harlingen-11-HTZL	HRL-11HZTL	2007	Horizontal	Neu/Den	Gamma Ray	Based on comparison to nearby wells
Harlingen-101	HRL-101	1994	Horizontal	Sonic	Gamma Ray	Only Sonic available
Harlingen West-01	HAW-01	1965	Vertical	Sonic	-	Only Sonic available

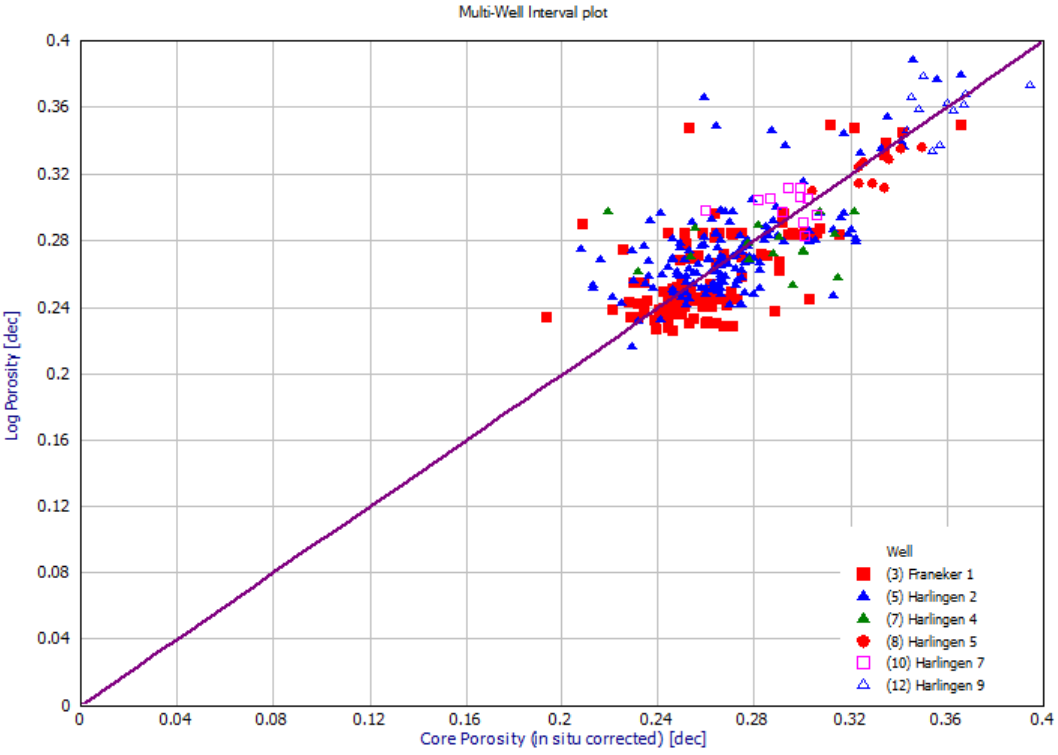

Figure 5-3 Core to log porosity match. 1:1 relationship indicated with purple line.

For quality check purposes, porosities were also calculated probabilistically (by assuming a multi-mineral limestone-clay model) and then compared with the previous determined PHIT_F values. No significant differences were found when comparing the two different interpretation approaches.

5.2.1.4 Formation water salinity

Pickett plots were run for wells HRL-04, HRL-05, HRL-06 and HRL-09 (Figure 5-4). The best fit to the data was found for a salinity of 75000 ppm NaCl equivalent. Nevertheless, in some wells (HRL-06 and HRL-09), a high residual hydrocarbon saturation (~5-10 %) was encountered in the water column. This could be due either to not fully reliable resistivity readings (old induction log data) or to slightly fresher formation water salinity.

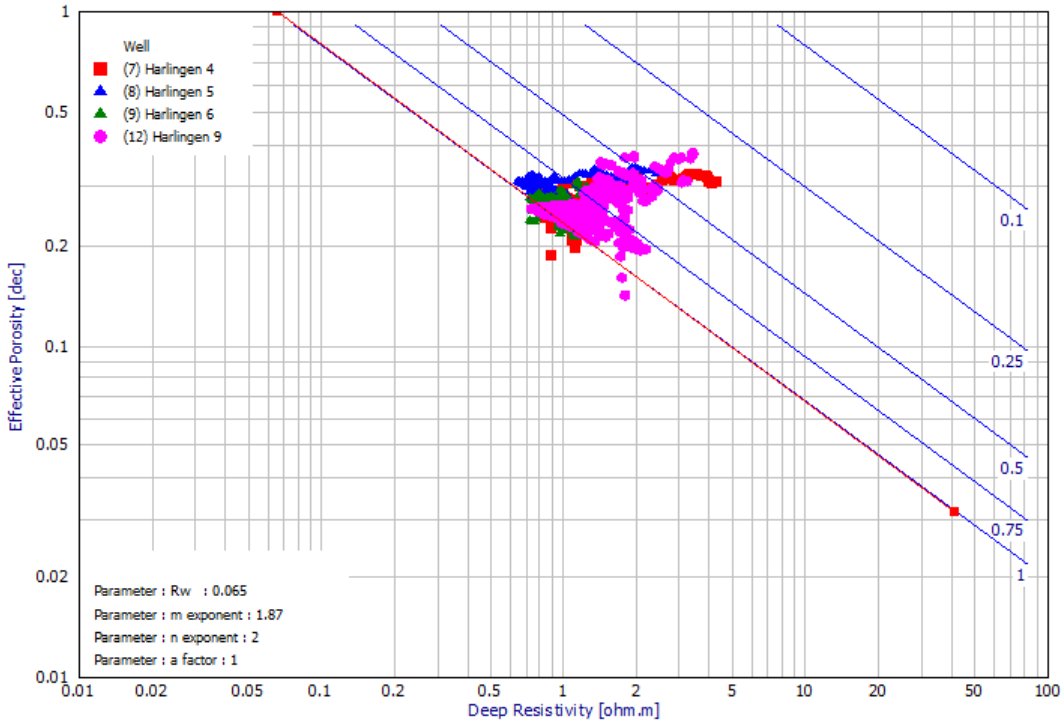

Figure 5-4 HRL-04, HRL-05, HRL-06 and HRL-09 Pickett plot showing a formation water salinity of 75000 ppm NaCl eq.

5.2.1.5 Water saturation

Because of non-significant clay effects, the Archie water saturation model was used in this study.

$$SWE\_F = \sqrt[n]{\left(\frac{a * Rw}{(PHIE\_F)^m * RDEEP}\right)}$$

where:

- SWE_F = water saturation
- RDEEP = deep resistivity (measurements from log)
- a = 1 (Tortuosity factor; assumed, as this is a common a value for Chalk in the North Sea (Spinler et al., 1995 [29])
- m = 1.87 (Cementation exponent; from restored state formation factor tests in HRL-09, Table 5-3)
- n = 2.00 (Saturation exponent; assumed, as this is a common default value where no direct site-specific measurements are available)
- Rw = 0.065 ohmm @ 43 ºC (~75000 ppm NaCl eq., Section 5.2.1.4)

For the water saturation computation, a temperature gradient was used to estimate the downhole temperatures needed to retrieve the correct water resistivities at any depth. On this regard, the formation temperature was derived from the log data and the following equation was used to estimate the gradient:

Temp [ºC] = 7 [ºC] + 0.0339 [ºC/m]*TVDss [m],

corresponding to a reservoir temperature of 43 ºC at 1050 mTVDss.

Table 5-3 Restored state measurements (HRL-09).

Well	Depth [mMD]	Porosity [dec]	Kg [mD]	Kw [mD]	Grain Density [g/cm^3]	FF [-]	m [-]
Harlingen-09	1128.10	0.367	3.2	5.2	2.706	6	1.79
Harlingen-09	1128.38	0.388	2.3	5	2.710	6.37	1.96
Harlingen-09	1132.13	0.369	1.5	4.9	2.704	6.42	1.86
Harlingen-09	1132.62	0.363	1.6	4.5	2.713	6.64	1.87
Harlingen-09	1133.18	0.387	2.5	5.6	2.696	5.94	1.88

5.2.1.6 Permeability

The provided core data for the chalk reservoir showed a permeability range between 0.5 and 20 mD. The permeability model was based on the available core data for the wells HRL-02, HRL-04, HRL-05 and FRA-01 (Figure 5-5), and the following permeability vs. porosity relationship was defined:

$$K\_PHI = 0.0021 * 10^{10.23*(PHIE\_F)},$$

where the permeability is expressed in mD and the effective porosity PHIE_F in decimal.

Core measurements were not conducted under in situ reservoir conditions, therefore a permeability correction was not applied and a slight overestimate is expected when considering core measured values. Nevertheless, the in situ net confining stress was estimated to be 750 psi, corresponding to an expected permeability correction generally lower than 10% (Chen et al., 2002 [2]). The permeability to core match is shown in Figure 5-6.

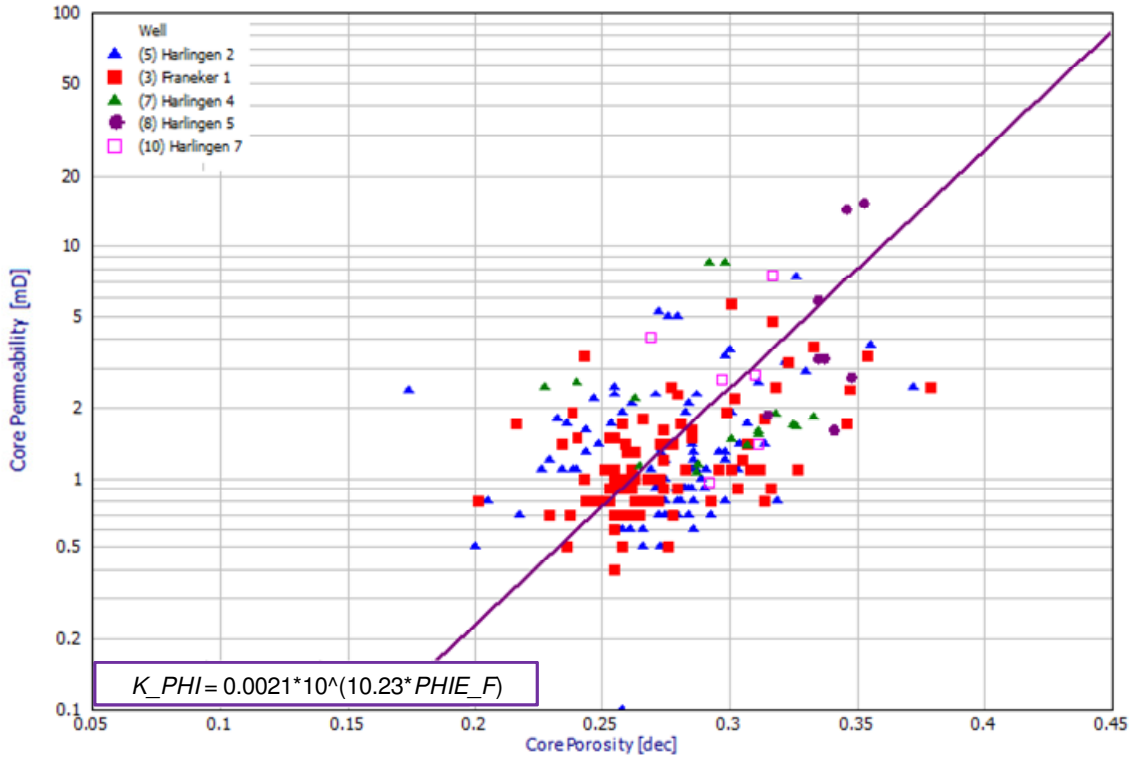

Figure 5-5 Porosity – permeability relationship.

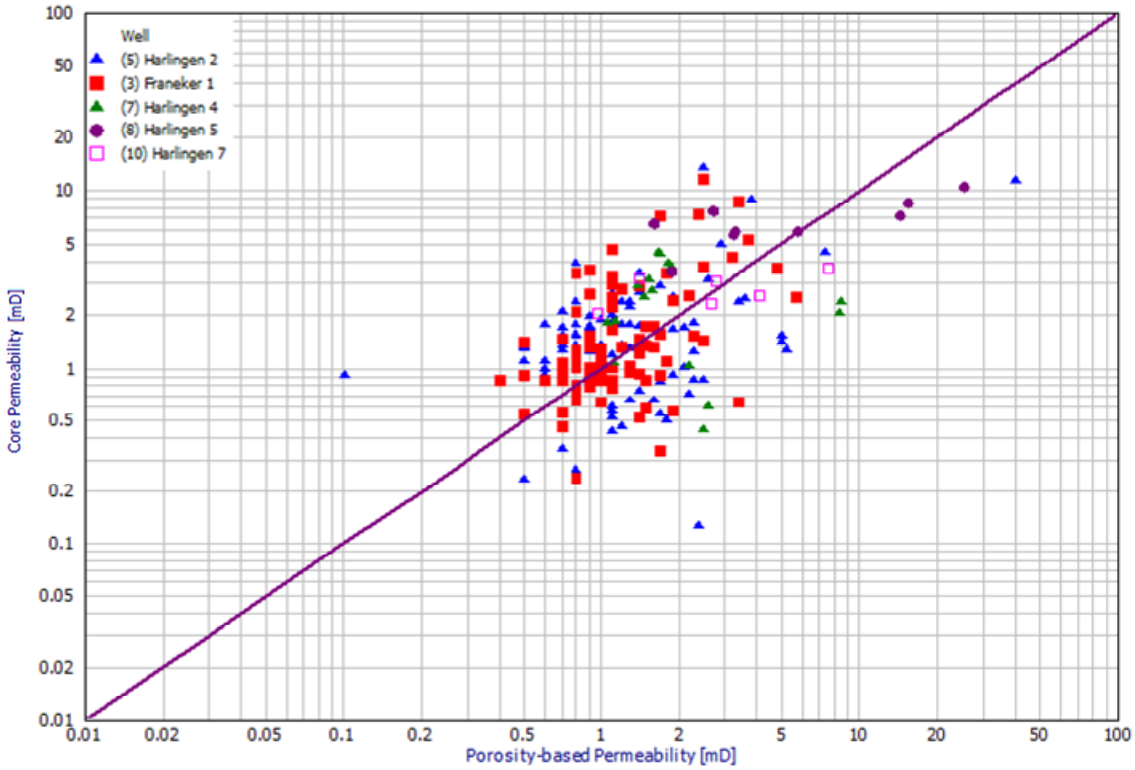

Figure 5-6 **Permeability (from poro-perm) vs. permeability from core. The 1:1 relationship is indicated with a purple line.**

5.2.2 ROCK PROPERTIES

5.2.2.1 Relative permeabilities

Vermilion provided a set of gas-water relative permeability characteristics. Laboratory-measured relative permeability curves were not available. In the course of dynamic simulation it became apparent that a too small amount of gas was mobile in the dynamic model to produce the historical gas rates from the dynamic model. Therefore, the residual gas saturation was changed from 25 to 15 %. Table 5-4 summarizes the relative permeability characteristics and Figure 5-7 shows the relative permeability curves used and compares them to the original set of curves provided by Vermilion.

Table 5-4 **Relative permeability characteristics.**

Swi	[dec]	0.323
Ng	[-]	2
Nw	[-]	2
krg'	[-]	1
krw'	[-]	0.2
Sgr	[dec]	0.25

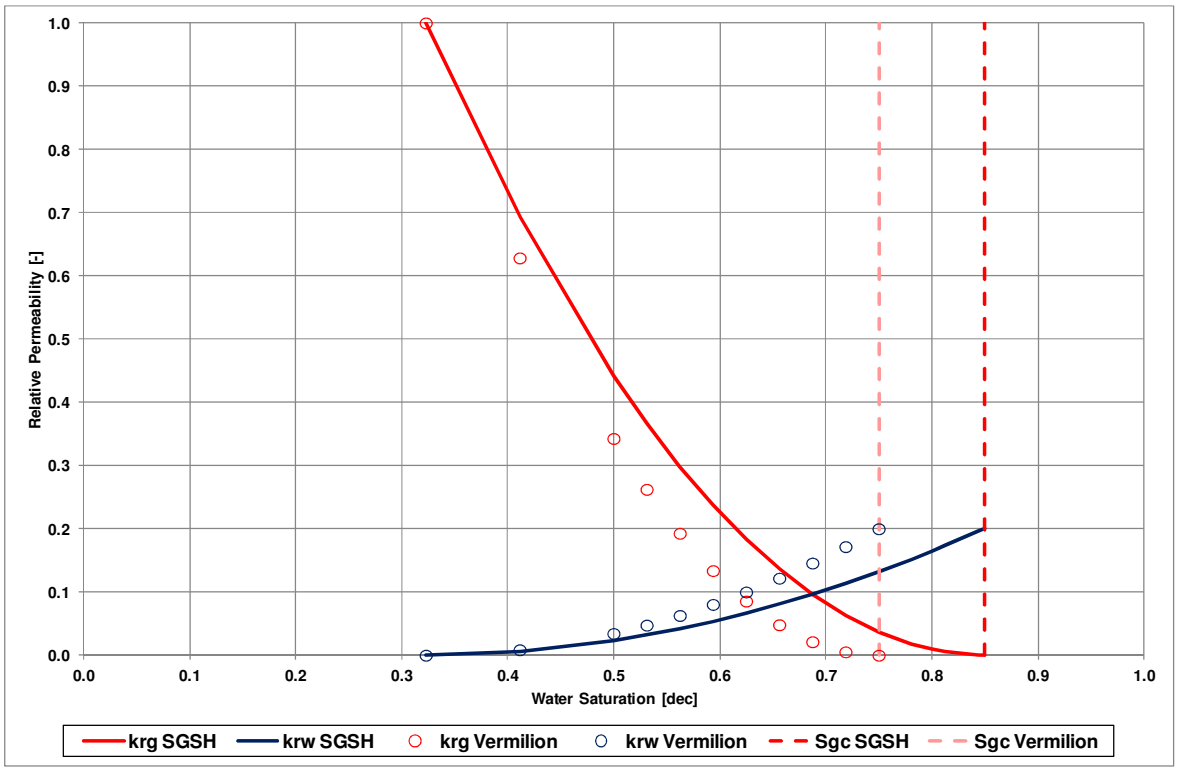

Figure 5-7 Vermilion (dots) and SGSH (line) relative permeability curves.

5.2.2.2 Capillary pressure

Capillary pressure measurements were available for core samples taken in wells HRL-07 and HLR-09. The capillary pressures were measured using mercury injection and centrifuge measurements. The capillary pressure curve used for dynamic work is based on a centrifuge measurement performed on a core sample taken in well HRL-09. The porosity of the respective core sample corresponds to the mode porosity value of 33 %. Figure 5-8 shows the centrifuge capillary pressure curves at laboratory conditions for both, HRL-07 and HRL-09, samples.

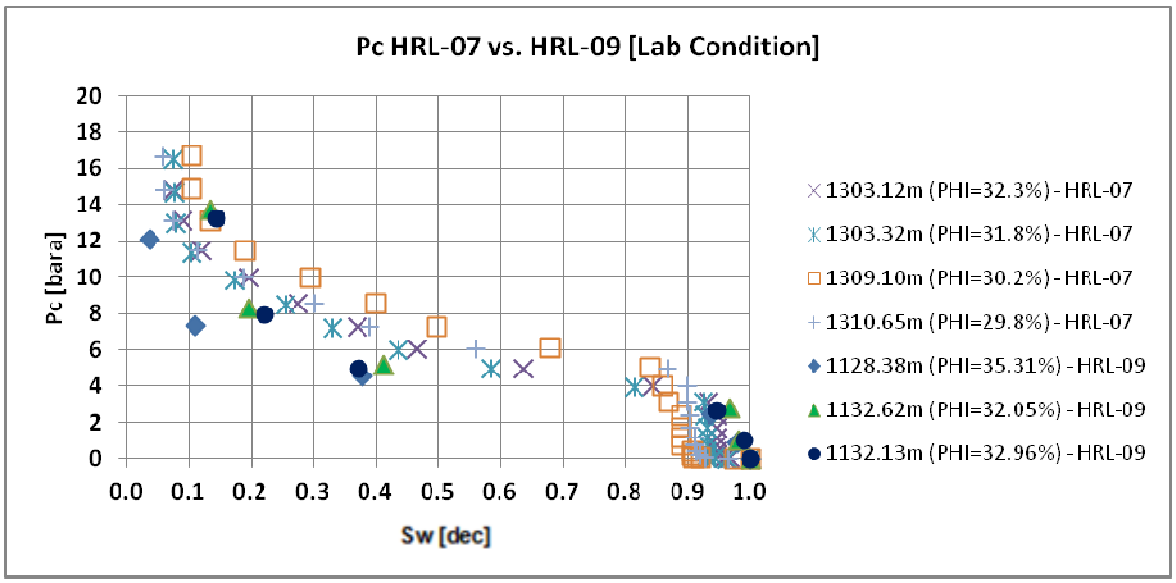

Figure 5-8 Laboratory capillary pressure centrifuge measurements, HRL-09 measurement at 1132.13 m used for model initialization.

Figure 5-9 compares the saturation distribution along an example well based on logs and the applied capillary pressure curve. Furthermore this figure illustrates that the reservoir section is within the transition zone.

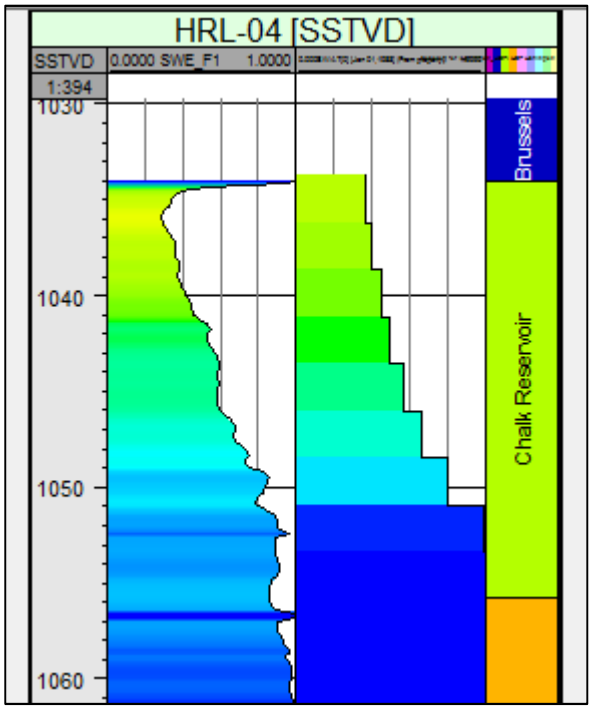

Figure 5-9 Saturation distribution along well HRL-04 from log (left) and dynamic model (right).

5.2.2.3 Rock compressibility

For dynamic modelling rock compaction was modelled as a general function of pressure and was incorporated in the dynamic model (Chapter 5.5) by applying pressure drop dependent porosity multipliers. The NGI laboratory experiment based porosity multipliers (Figure 5-10) quantify the reduction in porosity before and after pore collapse, which is induced by the declining reservoir pressure resulting from gas retrieval.

For the modal porosity of the Harlingen Chalk reservoir of 33 %, pore collapse occurs at a reservoir gas pressure of 101 bar. Initially the reservoir gas pressure was 135 bar at a depth of 1084 mTVDss and it dropped to less than 80 bar in the area of major gas retrieval at the end of the production period in 2008. As a result of the pore collapse the modal porosity of 33 % has been reduced to 32 % in 2008, which is a reduction by up to 3 % of its initial value. Figure 5-10 illustrates the pressure dependent porosity multipliers for the mode and mean porosity in the reservoir. For the mean porosity of the Harlingen Chalk reservoir of 29 % pore collapse occurs at a reservoir gas pressure of 67 bar.

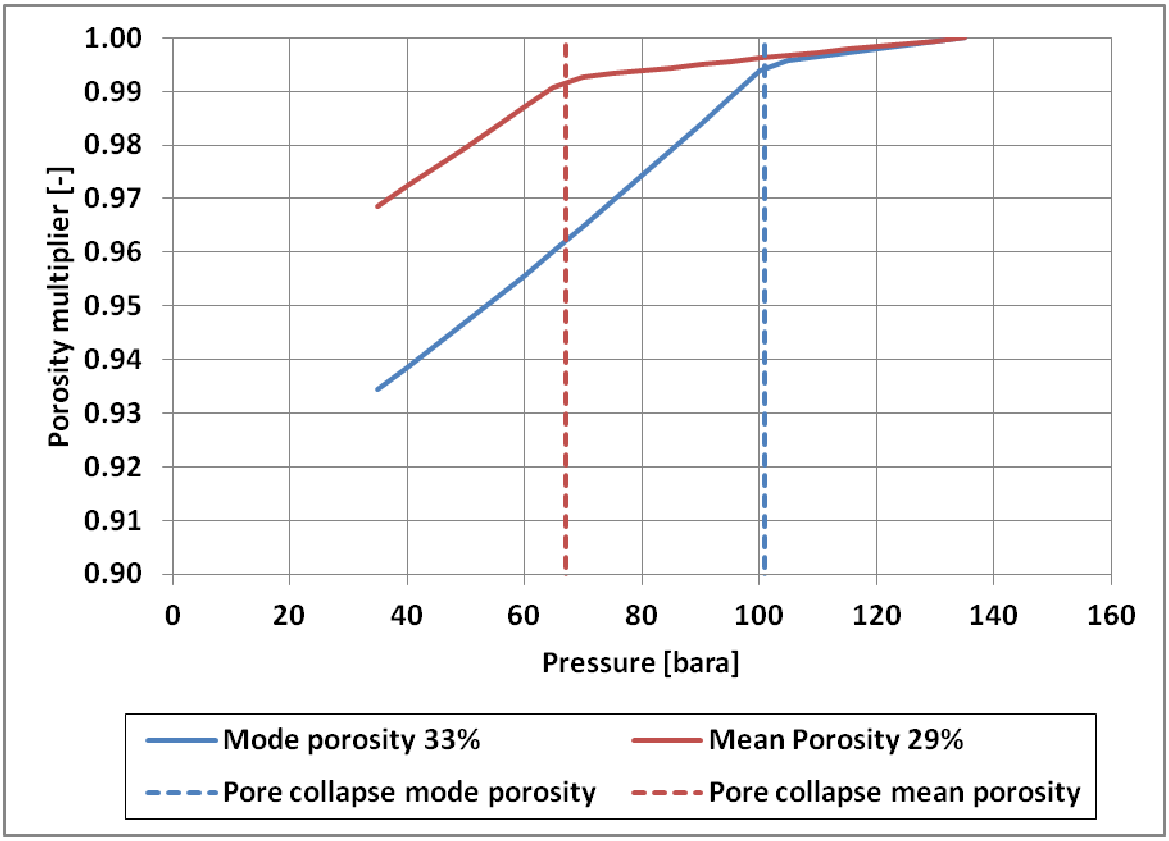

Figure 5-10 Pressure dependent porosity multiplier for mode and mean porosity

The NGI laboratory experiments (Figure 5-11) quantify the pressure drop related permeability reduction, which is incorporated in the dynamic model in the same manner as the porosity reduction.

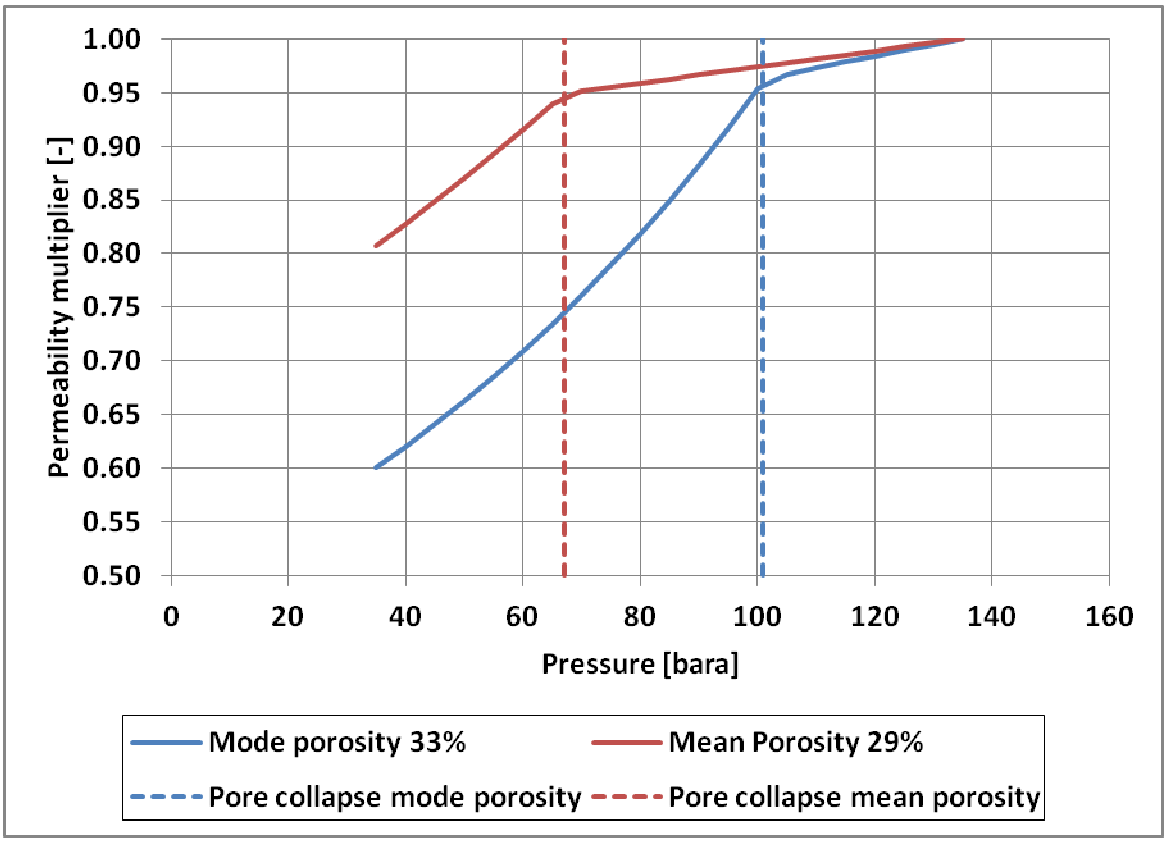

Figure 5-11 Pressure dependent permeability multiplier for mode and mean porosity

Figure 5-11 illustrates the pressure dependent permeability multipliers. Figure 5-12 shows the pressure dependent porosity multipliers for the entire porosity range in the Harlingen Chalk reservoir. The porosity ranges from 4 to 41 %. These porosity multipliers were used in dynamic modelling (Section 5.2.2.3.1 and Section 5.5).

5.2.2.3.1 Application in dynamic modelling

For dynamic modelling the porosity range was subdivided into 38 porosity classes. For each porosity class a pore collapse table was calculated based on the NGI laboratory results and each grid cell in the dynamic model was linked to the pore collapse table representing the respective porosity-pore collapse behaviour of each grid cell. These tables include a pressure drop related porosity and permeability reduction. In the dynamic model the grid block pore volume and the transmissibilities between the grid blocks are recalculated by multiplying the reference value from the initialization with the corresponding multipliers in the tables. Interpolation is performed for non tabulated grid block pressure values.

Figure 5-12 shows that grid cells with porosities lower than 25 % do not encounter pore collapse in the Harlingen Chalk reservoir.

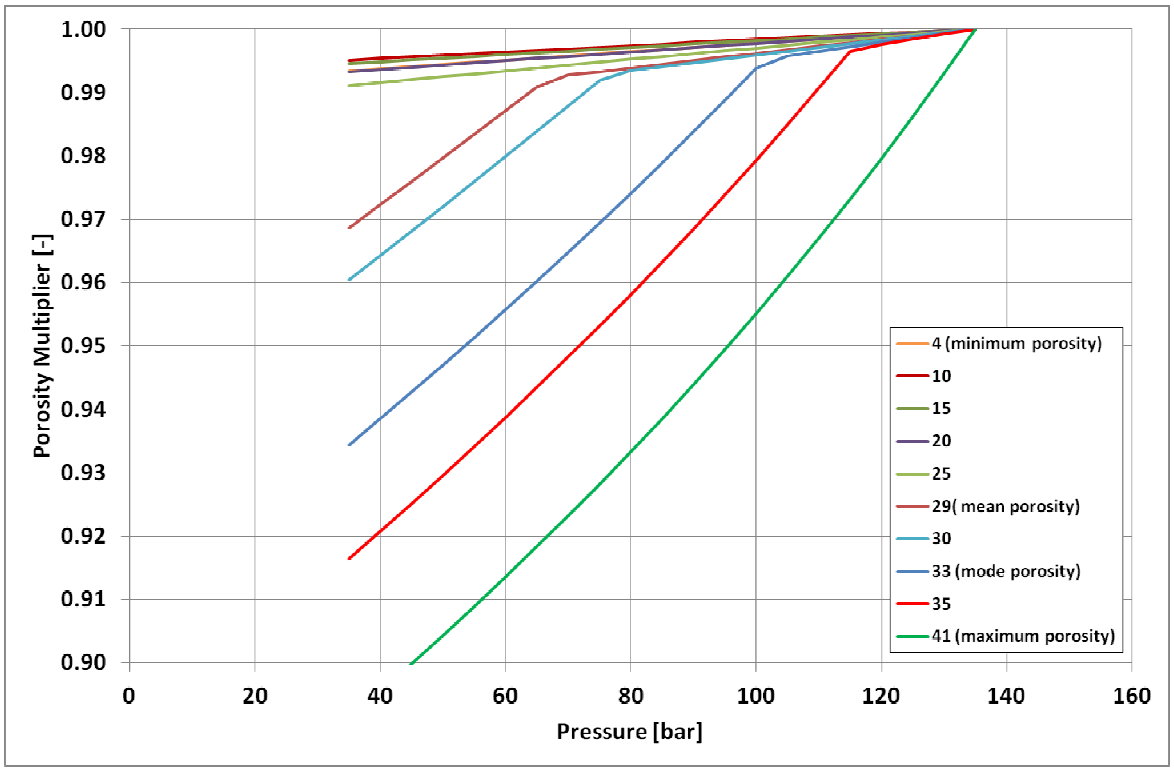

Figure 5-12 Pressure dependent porosity multiplier for entire porosity range

For the purpose of dynamic modelling the rock compaction was considered irreversible. In such a case the pore space does not re-inflate at an increase of pressure.

The overburden pressure was based on the calculated initial equilibrated pressure. The equilibrated pressure at the initial state of the dynamic model is stored and used for referencing the actual pressure dependent pore volume to the initial pore volume at initial reservoir pressure.

5.2.3 FLUID CONTACTS

Pressure versus depth data were not available and therefore it was not possible to rigorously determine the Free Water Level (FWL) of the field.

For this reason, the fluid contacts were mainly estimated by considering the Gas Water Contacts (GWC) observable from the log responses, such as neutron-density cross-over, sonic and resistivity profiles. Information coming from tests, composite logs and end of drilling reports were also integrated and confirmed the contact depths at the well locations. At the well locations the contact depths also correspond with the depth of prominent seismic reflections, as described in Section 5.3.1 (Figure 5-14, Figure 5-16 and Figure 5-17). Contact information from logs is summarized in Figure 5-13, along with Water Up To (WUT) and Gas Down To (GDT) observations.

In the main producing area of the field (FRA-01, HRL-02, HRL-04, HRL-07, HRL-08, HRL-09 and HRL-10-S3) similar contacts were observed, while the southern (HRL-101) and eastern area (HRL-05) showed contacts slightly deeper than the central area. This could either be related to the presence of different compartments in the field or be due to the fact that the field is characterized by a large transition zone without sharp contacts that make the fluid contact pick from logs partially subjective.

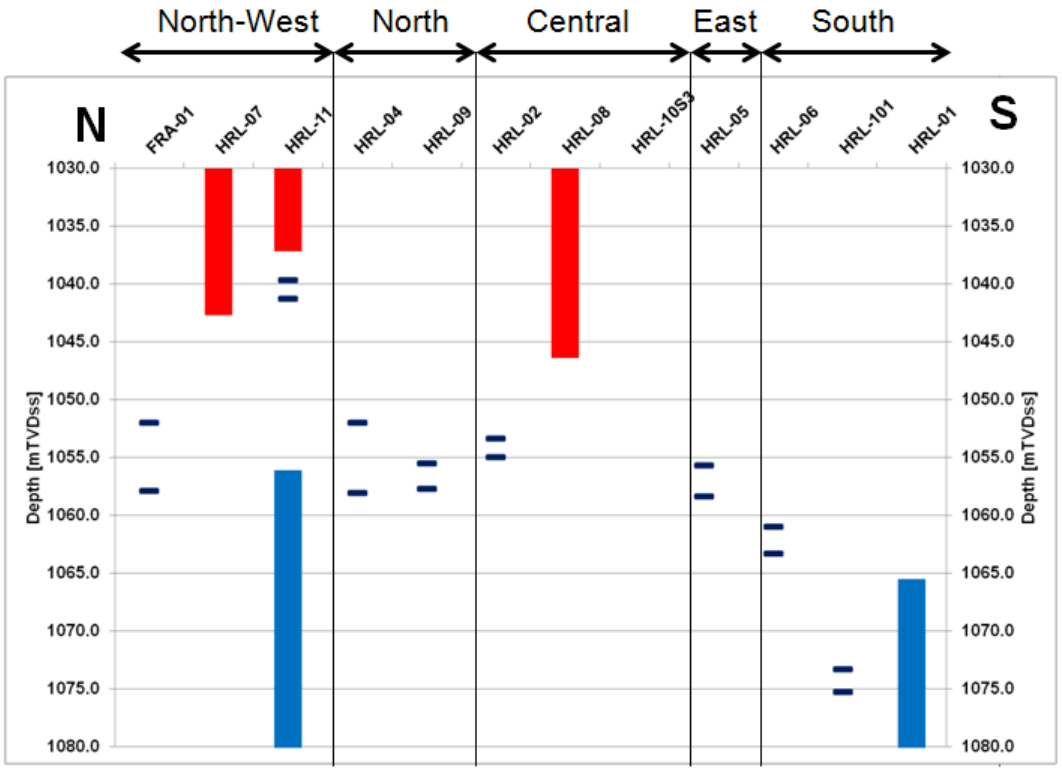

Figure 5-13 **Fluid contacts from petrophysical analysis: red bars refer to GDT, blue bars refer to WUT and minimum and maximum GWCs are represented by horizontal dark blue bars.**

Moreover, available capillary pressure measurements showed different entry heights and thus different heights of GWC above the FWL. The available capillary pressure data showed that the chalk has an entry height in the range of 23 to 35 m, depending on the rock quality. This is shown in laboratory work performed by TotalFinaElf E&P Nederland B.V., 2003 [32]. This means that a gas column above the FWL ranging from 23 to 35 m is required before the hydrocarbon fill becomes visible on the logs.

Based on the information available possible ranges of gas-water contact were established for the central, eastern and southern region of the field.

A shallow contact scenario was defined based on log derived contact depths for each region of the field. A deep contact scenario was defined by the shallow case plus a capillary entry height of 35 m, which is based on the laboratory work performed by TotalFinaElf E&P Nederland B.V [32]. The base scenario was derived in the course of a previous Vermilion study and it was used as the starting point for the dynamic modelling work in agreement with Vermilion. The different scenarios are summarized in Table 5-5.

Table 5-5 **FWL: depth range for the different scenarios.**

	Shallow mTVDSss	Base mTVDSss	Deep mTVDSss
East	1056.0	1068.5	1091.0
Central	1055.0	1063.5	1090.0
South	1061.0	1079.0	1096.0

5.3 SEISMIC INTERPRETATION, DEPTH CONVERSION & ATTRIBUTES

5.3.1 SEISMIC HORIZON INTERPRETATION

Three seismic horizons were interpreted as an input to the structural model (Section 5.4.1): the Top Ommelanden Chalk, the chalk reservoir base and the Top Holland Marl (i.e. the base of the chalk section). Appendix 4 shows the isochron maps of these three main horizons. For the depth conversion additional horizons, the Base of the Upper North Sea Group and the Top Palaeocene, were picked in all seismic lines above the three main horizons (Figure 5-15); the Upper North Sea Group was also used for amplitude normalization (Section 5.3.3). Additionally, for a regional understanding of the Harlingen area, other horizons below the Top Holland Marl were also picked; these are: Base Holland Marl, Base Cretaceous, Kimmerian unconformity and Top Zechstein (Figure 5-15). Due to the nature of 2D seismic it was not possible to pick continuous fault planes.

To determine the correct correlation between the seismic horizons and the geological structure it is necessary to match the seismic to a synthetic seismogram generated from well information. Figure 5-14 shows the calibration of 2D seismic line FR85-18 at the well location FRA-01. The results of the tie show a reasonable correlation after a small time shift of only 10 ms upwards shift in the seismic data. During this correlation phase it is required to confirm the seismic polarity of the data, this was confirmed as negative SEG polarity (Figure 5-17, Zoom of well ties of seismic line FR85-24 to well HRL-02) i.e. a positive reflection coefficient has a negative value or a trough on the displays. Figure 6-2 shows a NE-SW section across the field with the interpreted horizons.

The Top Ommelanden Chalk, i.e. the top of the gas bearing chalk reservoir, corresponds to a change in acoustic impedance which can be seen in Figure 5-16. At the top of the structure and across the field it can be seen that reflection strength is lower than outside of the field (Figure 6-2). This has been interpreted as the reservoir being gas charged, which lowers the bulk density of the chalk. This characteristic of the Top Ommelanden Chalk helps in the delineation of the field.

Below the Top Ommelanden Chalk horizon and within the field, another prominent reflection is present. Based on review of the well synthetic seismograms (Figure 5-14, Figure 5-16 and Figure 5-17) and the fluid contact assessment (Section 5.2.3), this reflection was interpreted as the base of the gas column and subsequently named Chalk reservoir base. Therefore chalk reservoir base was interpreted as the FWL and was used to define the areal extent of the Harlingen field.

The Top Holland Marl horizon (i.e. the base of the chalk section) was fairly difficult to pick due to being generally low frequency and locally noisy. It can be seen in Figure 5-14 that the base of the chalk shales out, leading to reduction of the reflection coefficient and thus of the seismic amplitude.

During the interpretation of the 2D migrated seismic sections there is always a mis-tie of non-flat horizons. As the main area of the field is relatively flat it was mainly at the flanks that there were relatively small mis-ties. A consistent Top Ommelanden Chalk horizon was achieved by smoothing the final picked horizons.

The uncertainty of the seismic horizons in depth is between 2 m and 4 m. The combination of the reservoir being relatively shallow (~ 1050 m) and the simple overburden representation results in this relatively low uncertainty.

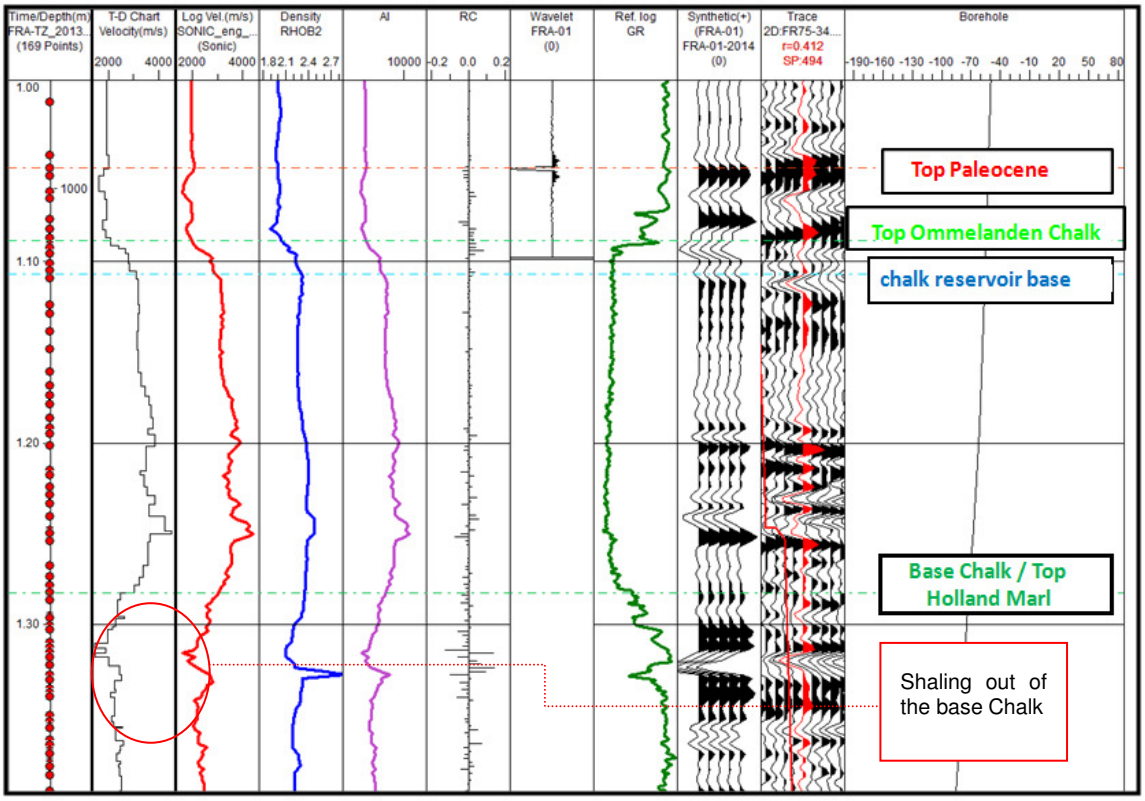

Figure 5-14 **Well tie of seismic line FR85-18 to well FRA-01.**

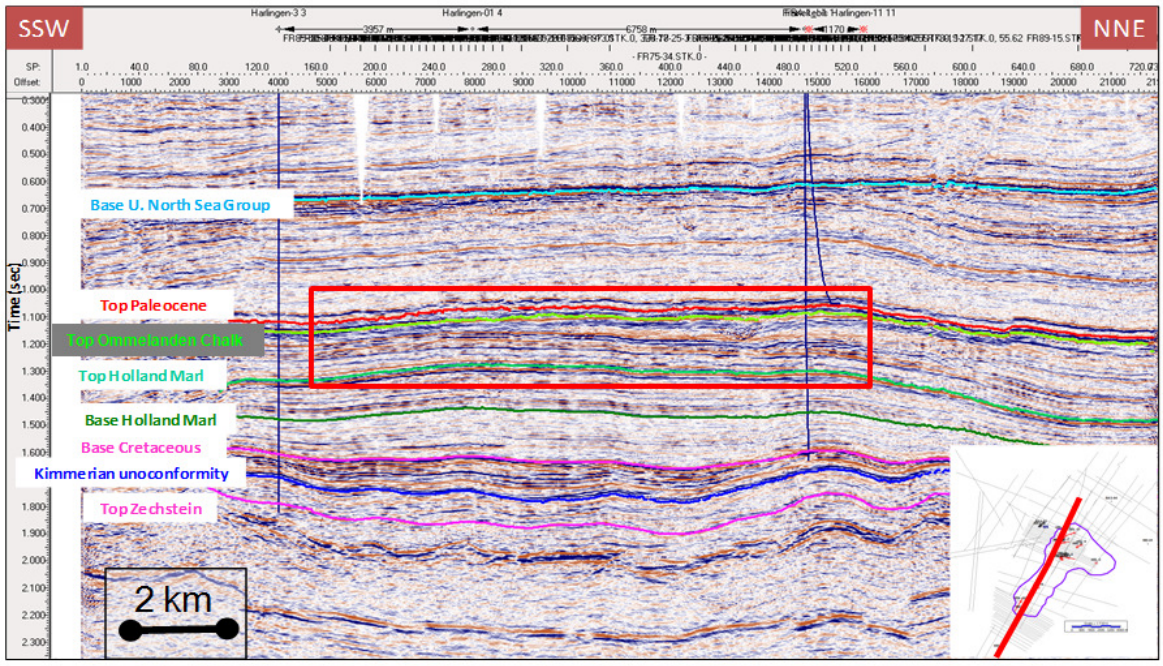

Figure 5-15 **All the interpreted seismic horizons. Red box indicates approximate location of the Harlingen Chalk field. Due to scale of the section, the chalk reservoir base does not appear in this section.**

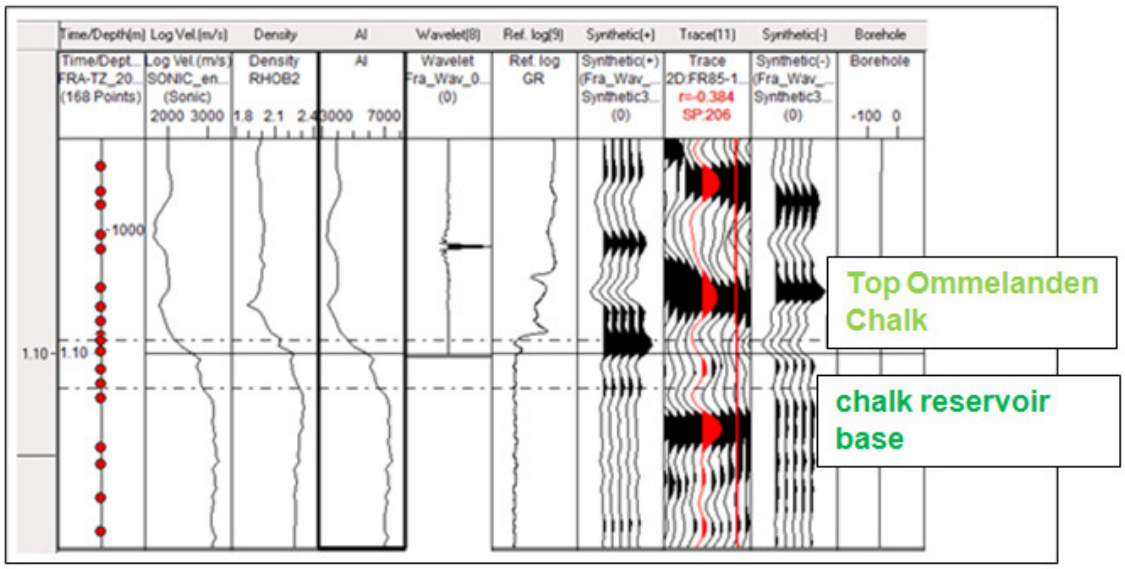

Figure 5-16 Zoom of well tie of seismic line FR85-18 to well FRA-01.

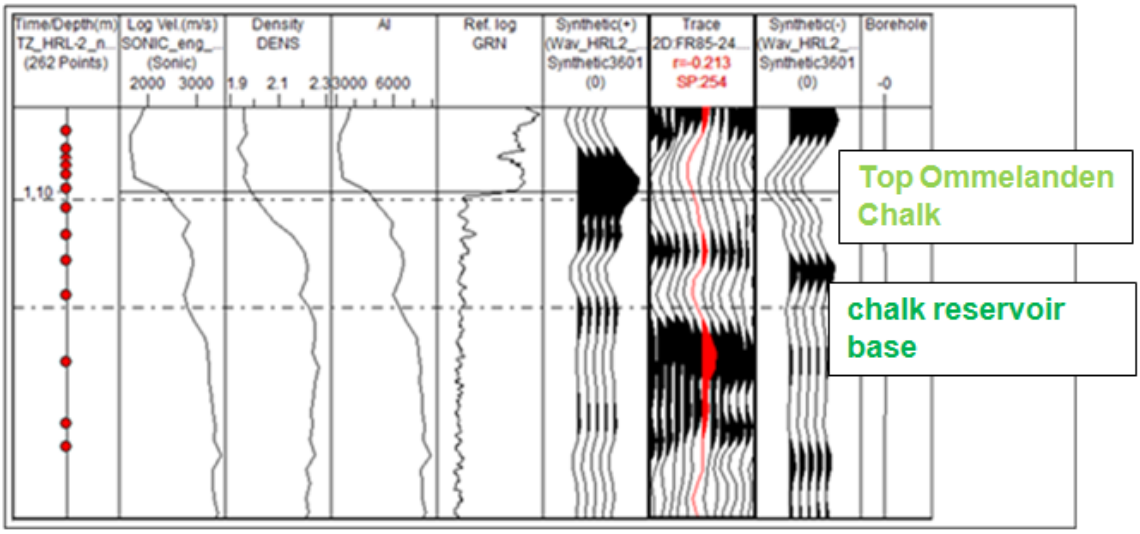

Figure 5-17 Zoom of well tie of seismic line FR85-24 to well HRL-02.

5.3.2 DEPTH CONVERSION

All seismic horizons were picked on the migrated time section, were converted to depth and gridded to generate the final depth maps (Appendix 4). To convert the TWT horizons to depth a velocity model is required. A velocity model was generated based on regional data. The north Netherlands onshore wells in the Velmod-2 database (for details, see Van Dalfsen et al., 2007 [34]) were used and the following model was generated:

- Tertiary (surface to Top Ommelanden Chalk) V = 1778 + 0.331xZ [m/s]
- chalk reservoir (Top Ommelanden Chalk to chalk reservoir base) V = 2500 [m/s]
- chalk below reservoir (chalk reservoir base to Top Holland Marl) V = 2200 + 0.864xZ [m/s]

For the Tertiary a V_0–K velocity function was applied. An average velocity versus midpoint depth was derived to calculate the function. Although the resulting velocity function is not exact (since the average velocity is not exactly at the midpoint), the resulting equation is accurate enough for depth conversion of the Top Ommelanden Chalk. Since logging starts in general halfway the Tertiary interval or just above the Top Ommelanden Chalk, there is not enough information to distinguish between the Upper- and Lower North Sea Groups, so the two series were taken as one group. Velocities of the Upper North Sea Group are only slightly lower than those of the Lower North Sea Group.

The average velocity in the gas bearing part of the chalk reservoir was found to be around 2500 m/s. Although velocities are variable, this constant velocity was applied since the resulting depth errors at the wells were acceptable (Table 5-6).

For the chalk below reservoir (between chalk reservoir base and the Top Holland Marl) the Velmod-2 average V_0–K function was applied, just as for the Lower Cretaceous.

The difference between the Top Ommelanden Chalk well depths and those based on the velocity model described above are on average less than 0.5 %, which is fully acceptable. Table 5-6 lists the residuals at this level.

Analysis of these residuals results in the following:

- Average error: 0.8 m
- Standard deviation: 3.9 m
- Minimum value: -7.1 m
- Maximum value: 8.3 m

Considering that the depth of the target is slightly more than 1000 mTVDss, the largest error value is still less than 1 % of the resulting depth conversion while the standard deviation is less than 0.5 %. Residual values were gridded with a cubic spline algorithm. The converted depth maps were then corrected with these residual maps.

No well-tie was carried out for the chalk reservoir base as it is not a stratigraphic top. The thickness map of the gas-bearing chalk reservoir was created and tied to the wells (Figure 5-18).

Table 5-6 Well residuals at Top Ommelanden Chalk (Top Resv) and chalk reservoir base (Base Resv), Δz in metres.

Well	X-Top Resv	Y-Top Resv	Δz Top Resv	Δz Base Resv
HRL-03	157150	568900	-0.2	-
HRL-101	159000	573150	-0.9	1.7
HRL-01	159000	572400	3.8	-8.7
HRL-06	160500	574450	0	-2.1
BAS-01	160550	579950	7	-
BAS-02	160700	580100	8.3	-
FRA-01	162150	578450	-1.2	0.1
HRL-02	162400	577250	1.4	0.0
HRL-07	162600	578500	3.7	-
HRL-08	162900	577100	-7.1	1.3
HRL-09	163650	578100	-1.5	1.4
HRL-04	164000	578300	-1	0.1
HRL-05	165250	576650	-0.6	0.9
RID-01	169500	578400	0.1	-
		Average	0.8	-0.6
		Stdev	3.9	3.2
		Min	-7.1	-8.7
		Max	8.3	1.7

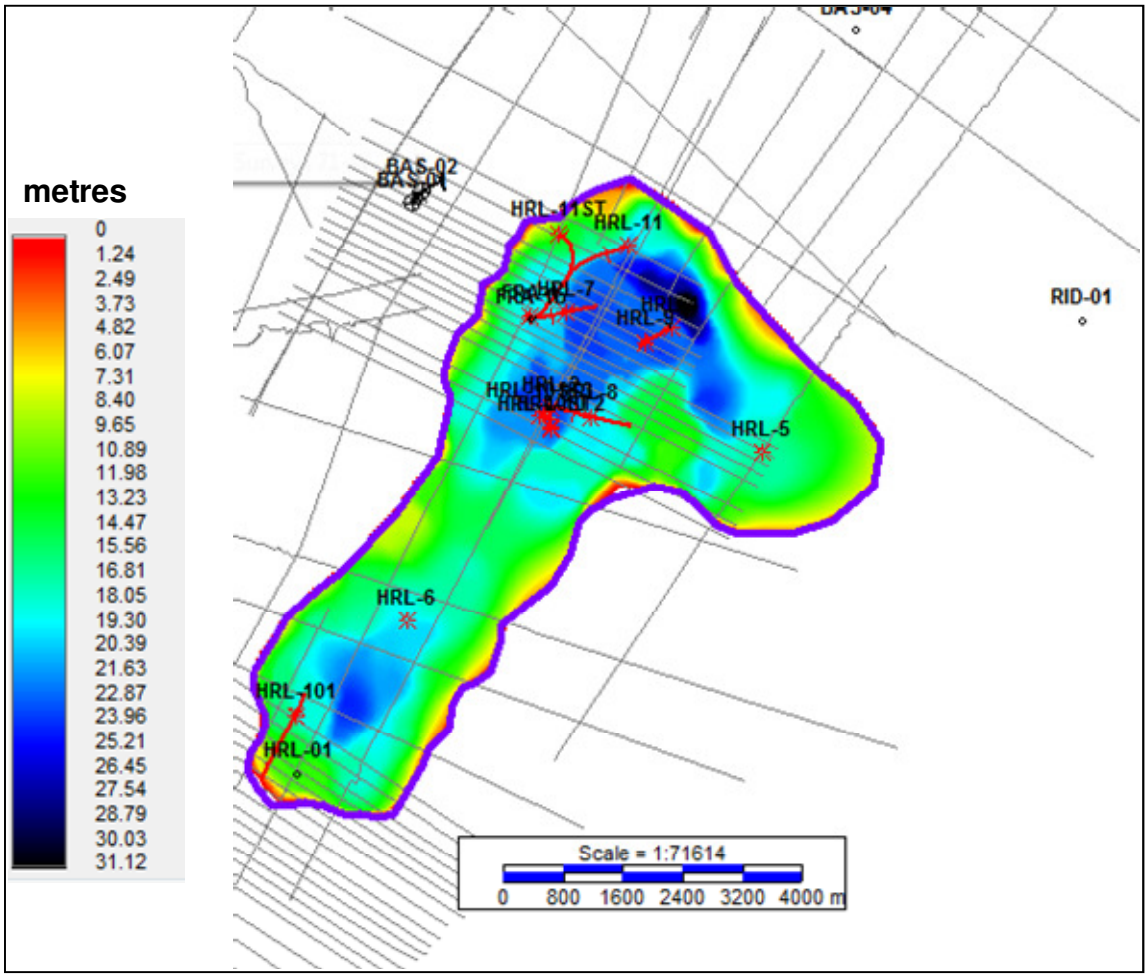

Figure 5-18 Gas-bearing chalk reservoir thickness map.

5.3.3 SEISMIC ATTRIBUTES

An attempt was made to generate seismic attributes (attribute maps) to assess whether these could potentially be used to guide porosity distribution away from the wells. It was not possible to correlate amplitudes with porosity.

Generally, amplitude analysis is done on 3D seismic data, which provides a consistent dataset covering the entire area of interest; however, in Harlingen only legacy 2D seismic data with different acquisition designs was available. Amplitudes at Top Ommelanden Chalk and chalk reservoir base were extracted. These were then normalised with the amplitudes of the interpreted base Upper North Sea Group horizon. This horizon was chosen as it is a continuous seismic reflector across all the seismic lines. Normalized amplitudes were then plotted against the average reservoir porosities at the wells. However, no correlation between normalised seismic amplitudes extracted at the well locations and the average reservoir total porosities at the wells was found (Figure 5-19). Figure 5-20 shows maps of normalized amplitude anomalies after gridding.

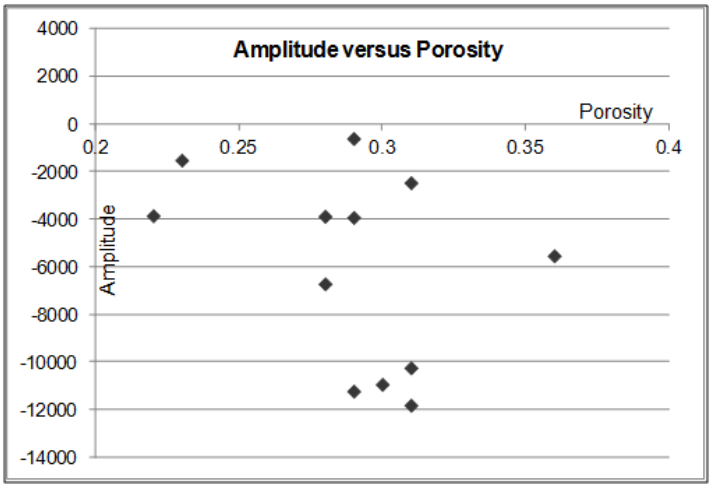

Figure 5-19 **Normalised seismic amplitude versus average total porosity, showing no correlation.**

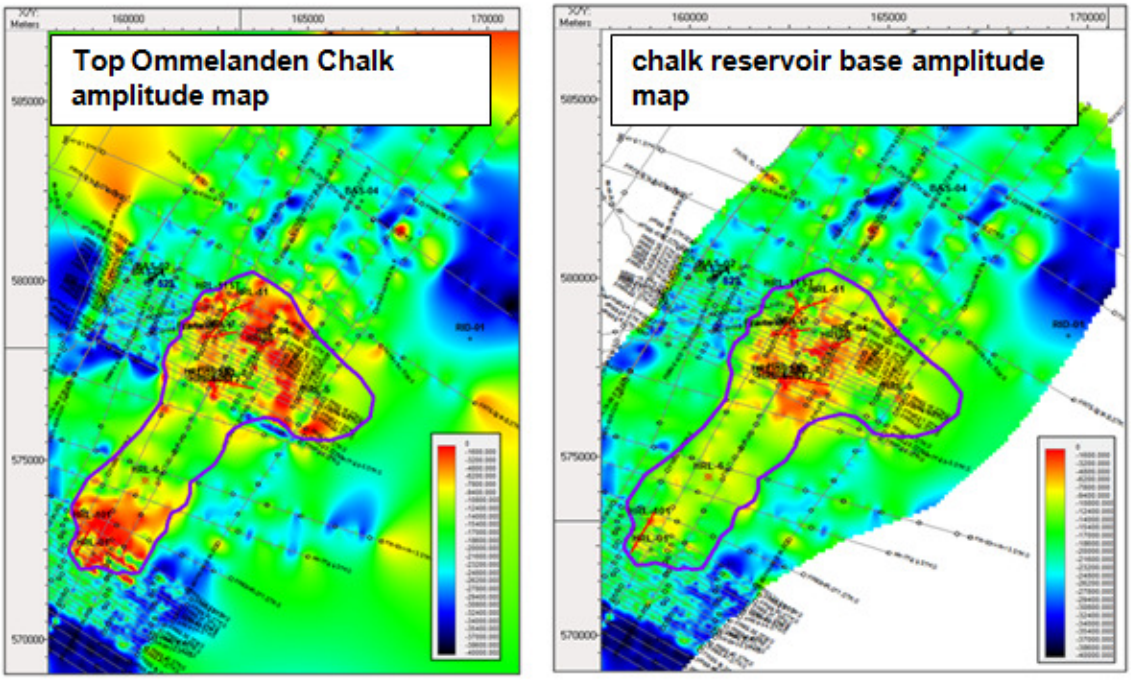

Figure 5-20 **Normalised amplitudes (with Base Upper North Sea) at Top Ommelanden Chalk and chalk reservoir base level.**

5.4 GEOLOGICAL MODELLING

3D Geological modelling of the Harlingen Chalk gas field and the immediately underlying layer of chalk below the reservoir were required in order to prepare the porosity grids that serve as input to the dynamic modelling (history matching) of the field, as well as to the compaction modelling. Furthermore, a permeability grid was required as input for the dynamic modelling.

5.4.1 STRUCTURAL MODEL

A 3D structural model was constructed in Petrel, using the Top Ommelanden Chalk, the chalk reservoir base and the Top Holland Marl surfaces obtained from seismic interpretation and subsequent depth conversion (see Chapter 5.3) as input. No faults could be interpreted from seismic data (Section 5.3.1), and initial dynamic modelling tests showed undesired restrictions of flow across tentative faults modelled in a previous version of the grid. Therefore, no faults were included in the final model and no compartmentalization was implemented to allow maximum flexibility in terms of segmentation in the dynamic model. Top Ommelanden Chalk and Top Holland Marl Formation well tops were used to perform the final tie to well depths. Formation well tops were based on the well reports and well tops.

A relatively high resolution 3D structural grid was built, as the compaction modelling (Chapter 6) is highly sensitive to porosity values. Therefore, averaging of the porosities, which would happen as the grid resolution gets coarser, is undesired. The final model was built with an average horizontal cell spacing of 50 m and subdivision of the chalk zone (i.e. the zone between Top Ommelanden Chalk and chalk reservoir base) into layers with an average cell thickness of 0.3 m. The non-reservoir chalk (i.e. the zone between chalk reservoir base and Top Holland Marl) was subdivided into coarser layers, with an average cell thickness of 12 m (Figure 5-21).

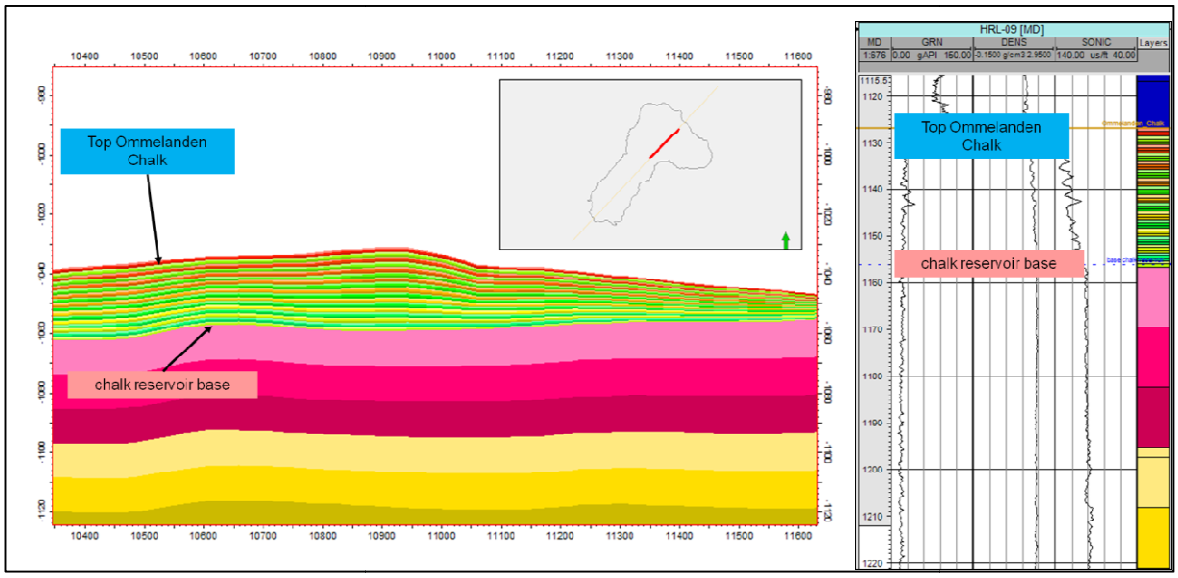

Figure 5-21 Static model cross-section through the reservoir and part of the non-reservoir chalk section.

5.4.2 POROSITY MODEL

In order to create the 3D porosity property, the porosity values were distributed away from the well locations. As one of the purposes of the porosity grid was to use it for compaction modelling, which is very sensitive to the absolute porosity values, a requirement of the porosity grid was that the spread in the porosities as observed from the wells should be retained as much as possible. This

meant that methods whereby the porosities away from the direct well influence range are based on averaging of the well porosities were deemed inappropriate. In order to minimise the averaging, a statistical distribution algorithm was chosen. Based on the extent to which the Petrel software allows detailed control of settings, the Gaussian Random Function (GRF) modelling algorithm was selected for the porosity distribution.

5.4.2.1 Well log upscaling and data analysis

The porosity, as described in Section 5.2.1.3, was upscaled arithmetically into the 3D grid at the well locations.

A series of statistical analyses was performed on the upscaled porosity dataset for the ”chalk reservoir zone” in the model in order to derive the most appropriate modelling settings. No other zones were considered for data analysis, as only for the “chalk reservoir zone” a porosity grid was required for dynamic and subsidence modelling. Evaluation concerned assessment of the need for any transformations prior to 3D modelling and analysis for the presence of any horizontal or vertical trends in the dataset.

First-pass analysis of the data also included assessment of the applicability of a seismic attribute surface as a horizontal trend for porosity modelling. This was investigated by checking the correlation between the well porosity values and the amplitude values of the seismic surface. As a very low correlation coefficient was observed between the porosity at wells and the seismic amplitudes, it was decided not to use seismic amplitudes to guidance the porosity distribution (see Section 5.3.3 for more details).

Initial statistical analysis of the porosity logs showed that the well HRL-01 was an outlier in the dataset, with average porosity values in the “chalk reservoir zone” significantly lower than in all other wells. Mode porosity for this well is approximately 17-18 %, while the mode for the other 13 wells combined is ~32-33 %. It was decided to exclude this well from the final upscaling and data analysis process, as it is located in the southernmost part of the gas field (Figure 5-1), while the focus of the study was on the northern part of the field where most production and subsidence have taken place. Inclusion of the well would lead to overall lowering of the porosities in the field outside the well influence range, also in the northern part of the area, which was deemed undesirable since this would likely lead to an underestimate of the porosities and hence inaccurate modelling of the subsidence behaviour in this focal area.

Data analysis of the remaining 13 wells showed the presence of a porosity-depth trend. Following removal of this depth trend, horizontal and vertical variogram analyses were carried out to establish the appropriate spatial correlation distances. Vertical variogram analysis for the “chalk reservoir zone” was deemed reasonably reliable, and the correlation range was established at 2 m. Horizontal variogram analysis was deemed highly uncertain due to the small number of wells available. Nevertheless, horizontal variogram ranges were interpreted in an attempt to capture the heterogeneities of the chalk across the field. For the “chalk reservoir zone”, a spherical variogram with an isotropic 300 m correlation range was deemed most appropriate.

5.4.2.2 Porosity distribution

The porosity values were distributed away from the well locations with a Gaussian Random Function (GRF) modelling algorithm with modelling settings as derived from the data analysis described in the previous section. In order to accurately model the observed depth trend in the porosity, a transformation was carried out which enabled a more refined implementation of co-dependence between porosity and depth in the model.

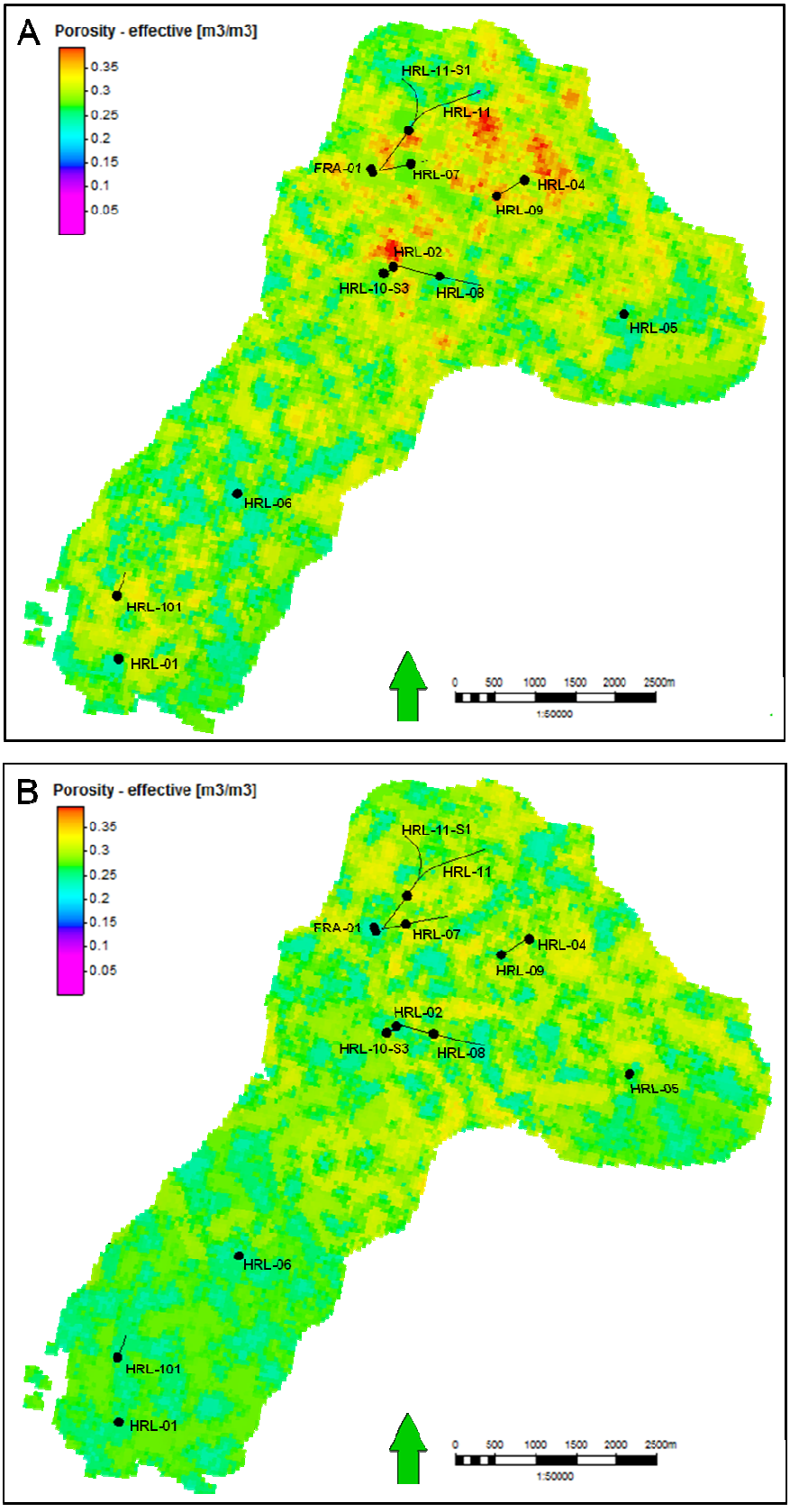

Figure 5-22 **Example porosity maps for GRF distribution realisation number 76, for a) the uppermost and b) the lowermost chalk reservoir layer. Well locations indicated at Top Ommelanden Chalk level with black dots, well paths indicated by black lines.**

Since the GRF algorithm is probabilistic in nature, it results in a different but equiprobable outcome in each run. To capture this effect, a loop of 100 Monte-Carlo runs was executed, to generate 100 porosity realisations for further screening in the dynamic modelling phase (Section 5.5.3.1).

Examples of resultant porosity maps for one of the realisation are given in Figure 5-22.

5.4.2.3 Grid upscaling

In order to create a workable grid for first-pass dynamic simulation and screening (Section 5.5.3), the resolution of the fine scale structural model was reduced through grid upscaling. The horizontal spacing of cells was increased from 50 m in the original grid to 150 m in the coarse grid. The number of vertical layers in the model was also significantly reduced, leading to an increase in average vertical cell size in the “chalk reservoir zone” from 0.3 m to 1.6 m.

All 100 porosity realizations that were created in the fine grid were upscaled arithmetically into the coarse grid.

For the final subsidence modelling the fine grid porosity version of the models was used in both the dynamic simulation and geomechanical modelling.

5.4.3 PERMEABILITY

A permeability property was created in the model by calculating for each of the cells in the “chalk reservoir zone” the appropriate permeability value by applying the porosity-permeability relationship as shown and discussed in Section 5.2.1.6. The permeability grid was used as input for the dynamic model.

5.5 DYNAMIC MODELLING

The objective of dynamic modelling was to provide the pressure development through time for the subsequent calculation of the pressure dependent compaction and subsidence behaviour of the chalk.

5.5.1 WORKFLOW

The workflow applied in dynamic modelling is illustrated in Figure 5-23. After preparation of the simulation input a workable coarse grid was used for screening the porosity realizations for applicability in history matching (Section 5.4.2.3). A history match was performed on the coarse grid model and then transferred to the fine grid model. This bespoken workflow ensured that a workable coarse grid model with a reasonable simulation run time was available for dynamic modelling.

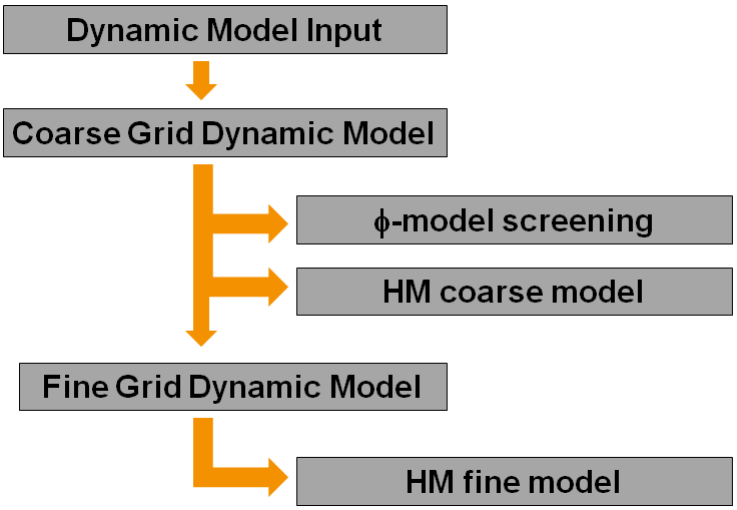

Figure 5-23 Dynamic modelling workflow.

5.5.2 DYNAMIC MODEL INPUT

5.5.2.1 Well tests

A well test was performed in all nine gas producing wells at least once in the time period between 1984 and 2008:

- FRA-01 (1991)
- HRL-02 (1996, 2006, 2008)
- HRL-04 (1984, 1996, 2005, 2008)
- HRL-05 (1984, 1996, 2005, 2008)
- HRL-06 (1987, 2005, 2008)
- HRL-07 (2006, 2008)
- HRL-08 (1996, 2006, 2008)
- HRL-09 (2006, 2008)
- HRL-10-S3 (2008)

The well test interpretation was performed by Vermilion. In this available interpretation the permeability ranges from 0.17 to 2.2 mD and the wells were considered being connected to fractures. The results are summarized in Appendix 6. Evidence from other sources, such as cores and image logs also indicate that the reservoir is naturally fractured. However, the type of fractures and their properties remain mostly unknown or uncertain due to limited data and low quality of core material. Therefore, fractures were not modelled explicitly, however in the course of the history match permeability was multiplied and thereby a preferred flow direction and permeability enhancement was introduced. A general observation was that the well test derived permeability was not impaired by reservoir compaction (Figure 5-24).

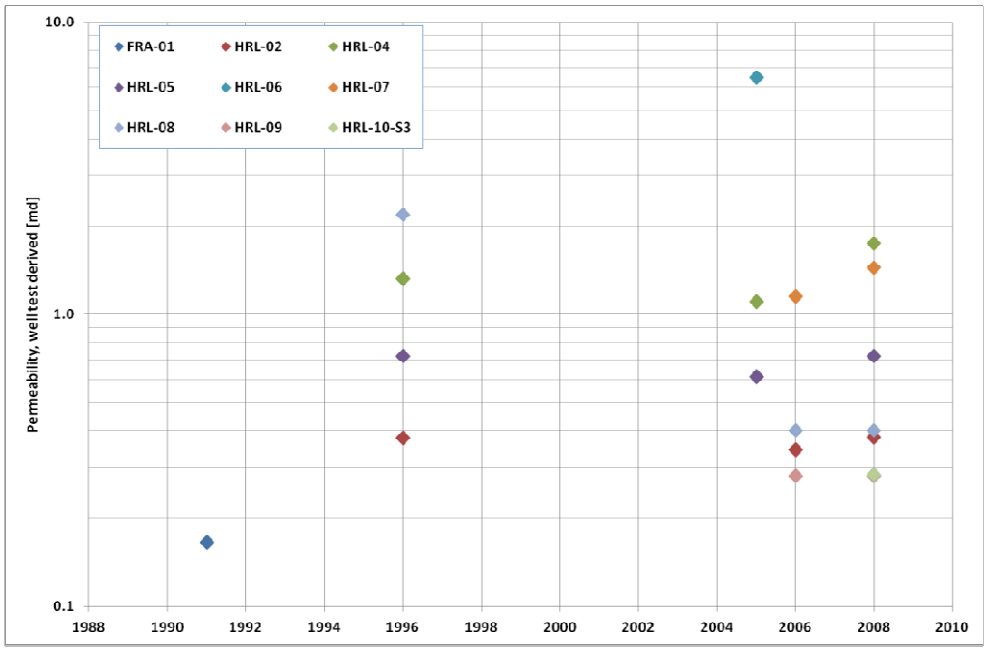

Figure 5-24 Well test derived permeability through time.

5.5.2.2 Production history

The gas production started in November 1988 from well HRL-04. Later in 1988 two additional wells, HRL-02 and HRL-05, were put on stream. In the period 1989 to 1993 four more wells, FRA-01, HRL-07, HRL-08 and HRL-06, started gas production. In May 1997 FRA-01 stopped gas production. In January 2001 HRL-09 started production and in November 2007 the last well HRL-10-S3 started gas production. Since July 2008 the field has been shut-in.

To date, the reported cumulative gas produced from the nine producing wells is 1.77×10^9 Sm^3 and the recovery factor is approximately 35 %. 1.47×10^9 Sm^3 of gas were produced from the seven wells located in the central area of the Harlingen field. 2.16×10^8 Sm^3 were produced from well HRL-05, which is located to the east of the central area and 7.67×10^7 Sm^3 were produced from well HRL-06, which is located to the south of the central area of the field. The water production of all wells is minor, with rates less than 0.02 Sm^3/day. Figure 5-25 gives an overview of the gas production history of the field.

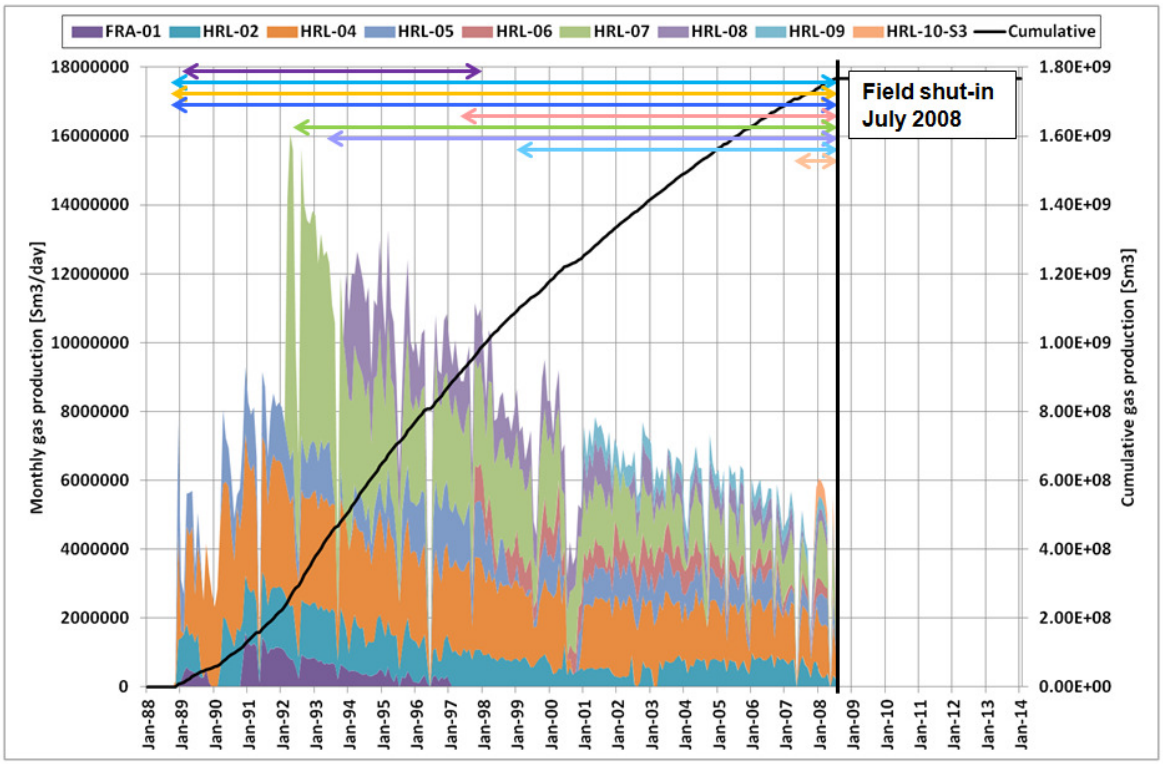

Figure 5-25 Gas production history.

After a critical review of the production data performed by Vermilion, 2014 [42], the gas production from well HRL-07 was adjusted for the time period 2000-2008. This adjustment increases the total production to 1.54×10^9 Sm^3 from the central pool and the overall total production to 1.83×10^9 Sm^3. The adjustment represents an increment of 4 % to the cumulative field gas production.

5.5.2.3 Pressure history

Pressure data were available for all gas production wells. For the production period of the field a summary spreadsheet was available, for the post shut-in period original pressure surveys were available. In order to account for the degree of reliability of the pressure data they were classified according to the duration of the shut-in/build-up period. This classification of pressures was performed jointly by Vermilion and SGS Horizon.

- Reliable
  - Extrapolated shut-in pressures (p*)
  - Last measured pressures (LMP) from shut-in periods longer than two weeks and post shut-in
- Not reliable
  - Last measured pressures (LMP) from shut-in periods shorter than two weeks

LMP obtained from long shut-in periods might not be as reliable as p* due to the tightness of the reservoir. For the history match the pressures considered reliable were taken into consideration. The difference between p* and LMP is considered as an error bar on the measurement itself. In general, p* is larger than LMP in the production phase.

5.5.2.4 Fluid properties

5.5.2.4.1 Gas

In this study a fluid model provided by Vermilion was used. The provided fluid model was validated by SGSH using published correlations and Prosper. The gas characteristics at initial reservoir pressure of 135 bara are:

- Gas density; 108 kg/m^3
- Gas viscosity: 0.0163 cP
- Gas formation volume factor: 0.0066 rm^3/Sm^3

The fluid properties and their validation are shown in Appendix 6.

5.5.2.4.2 Water

One water sample from the Upper Cretaceous taken in well HRL-02 was available. Vermilion provided the corresponding simulation input which was validated using published correlations. Table 5-7summarizes the water properties.

The expected condensed water production at initial reservoir pressure of 135 bar is $7.8x10^{-7}$ m^3/m^3 and $9.0x10^{-7}$ m^3/m^3 at a reservoir pressure of 100 bar.

Table 5-7 Water and gas properties.

Densities			
Gas gravity	**γgas**	0.587	-
Gas density	**ρgas**	0.720	kg/m^3
Water density Upper Cretaceous	**ρwat - UC**	1035	kg/m^3
Water properties			
Water formation volume factor	**Bw**	1.006	rm^3/Sm^3
Water compressibility	**cw**	4.63E-07	1/kPa
Water viscosity	**μw**	0.833	cP
Pressure dependence of water viscosity		0	cP/kPa

5.5.2.5 Material balance

A material balance analysis was performed to obtain insight into the dynamic communication between the gas producing wells in the Harlingen Chalk gas field, the initial gas volume in place and possible pressure support for the reservoir.
The major findings from this analysis were:

- The FRA-01 and HRL-07 area is likely to be isolated or less connected to the central area, while the other parts of the central area including wells HRL-02, HRL-04, HRL-08, HRL-09 and HRL-10-S3, remain highly connected. This is supported by the observed historical well pressures of wells FRA-01 and HRL-07, which are lower than the well pressures of the other central pool wells, and the petrophysical contact analysis.
- The southern pool, where well HRL-06 is located, is not fully connected to the central pool.
- The eastern pool, where well HRL-05 is located, is not fully connected to the central pool.
- The results on possible external pressure support were inconclusive.

For further work it was assumed that source for external pressure support is not an aquifer, based on the production and pressure history of the field (Section 5.5.2.2 and 5.5.2.3). This assumption implies that a potential compaction in the water leg is not considered.

5.5.2.6 Rock Properties

The rock properties used in the simulation model are discussed in the petrophysics section of this report (Section 5.2.2).

- Relative permeability curves
- Capillary pressure curves
- Fluid contacts
- Rock compressibility

5.5.3 COARSE GRID MODEL

The fine grid model was upscaled (Section 5.4.2.3) to obtain a workable coarse grid model with a reasonable simulation run time. The key figures of the coarse grid model are summarized below:

- Model dimensions: 90x85x26 cells
- Active cells: 72316
- Areal cell dimension: 150x150 m
- Average cell thickness:
  - Chalk reservoir: 1.6 m
  - Chalk below the reservoir (water): 33 m
- Layering:
  - Chalk reservoir: layers 3 to 11
  - Chalk below the reservoir (water): layers 12 to 21
- Average porosity:
  - Chalk reservoir: 29 %
  - Chalk below the reservoir (water): 22 %
- Average permeability:
  - Chalk reservoir: 2 mD
  - Chalk below the reservoir (water): 0.51 mD
- Run time ~ 1.5 min

Preliminary dynamic modelling showed that the communication between the gas bearing chalk interval and the underlying water leg in the chalk below the main reservoir has to be considered negligible. This finding is supported by the porosity log readings and by the fact that the water production from the gas producing wells is negligible. If communication between the gas bearing chalk interval and the underlying water leg in the chalk below would be allowed in the model, considerable amounts of water would be produced along with the gas, which is not in line with observations from the wells.

No faults are implemented in the dynamically simulated model because no obvious, major faults or barriers could be mapped (Chapter 5.3). In addition, initial dynamic modelling showed undesired restrictions to flow across tentative faults modelled in a previous version of the grid. Therefore, no faults are included in the reservoir section in the final model (Section 5.4.1).

Nevertheless, based on observed pressure behaviour (Section 5.5.2.3), material balance analysis (Section 5.5.2.5) and derived free water levels (Section 5.2.3), the dynamic reservoir model was notionally subdivided into five regions. The regions and the wells located within each of these regions are shown in Figure 5-26. As the placement of the baffles could not be based on mapped barriers alternative region sizes for region 4 were evaluated in order to identify a fit for purpose region size.

- Region 1 and 2 (southern pool):
  - In general the wells to the south of the main producing area showed deeper FWL compared to the central pool wells.
  - The subdivision into two regions was based on the finding that well HRL-101 showed a deeper FWL than wells HRL-01 and HRL-06.
- Region 3 and 4 (central pool):
  - The material balance analysis indicated that the north-western wells FRA-01 and HRL-07 are likely to be isolated or very poorly connected to the other wells in the central pool.

- Region 5 (eastern pool):
  - The eastern well HRL-05 showed a deeper FWL than the central pool wells.

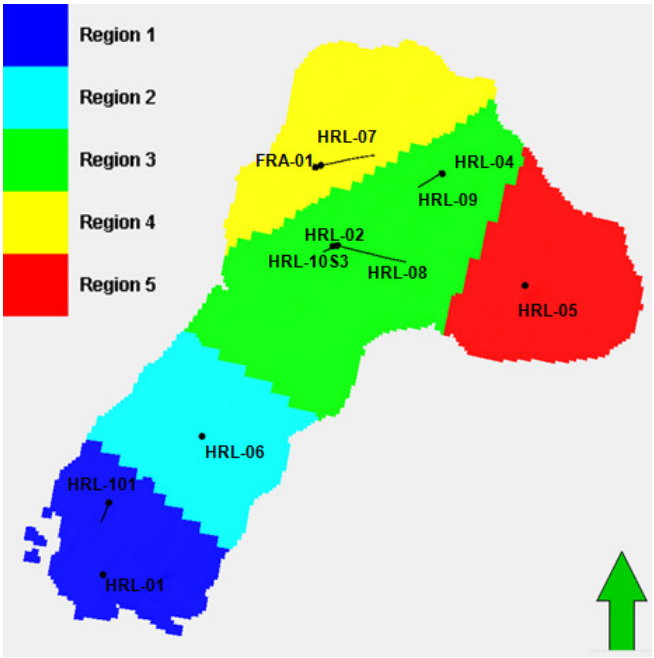

Figure 5-26 Regions in the dynamic model.

5.5.3.1 Porosity model screening

A screening process using dynamic qualifiers was applied to identify the most suitable porosity realisation for history matching among the 100 available porosity models (Section 5.4). The dynamic qualifiers were historical pressure data and well gas production. The historical pressure data were weighted according to the pressure classification described in Section 5.5.2.3. Reliable LMP pressures were assigned less weight than p* and non-reliable LMP pressures were excluded.

In porosity screening a simplified rock compaction representation was chosen to accelerate this step in the workflow. In this simplification it was assumed that the rock compaction derived for the mode porosity of 33 % applies to the entire model (Figure 5-27). This simplification is supported by the fact that in gas reservoirs the pressure is dominated by the gas compressibility, which is more than two orders of magnitude greater than rock compressibility. A sensitivity analysis comparing the simplified and detailed rock compaction description in terms of resulting pressures showed that the applied simplification is valid for the porosity screening. In the dynamic modelling steps following the porosity model screening the detailed rock compaction description is applied.

The FWL set applied in the porosity model screening process was based on the base scenario FWL set (Table 5-5). The FWL defined for the southern pool was applied to regions 1 and 2, the contact defined for the central pool as applied to regions 3 and 4.

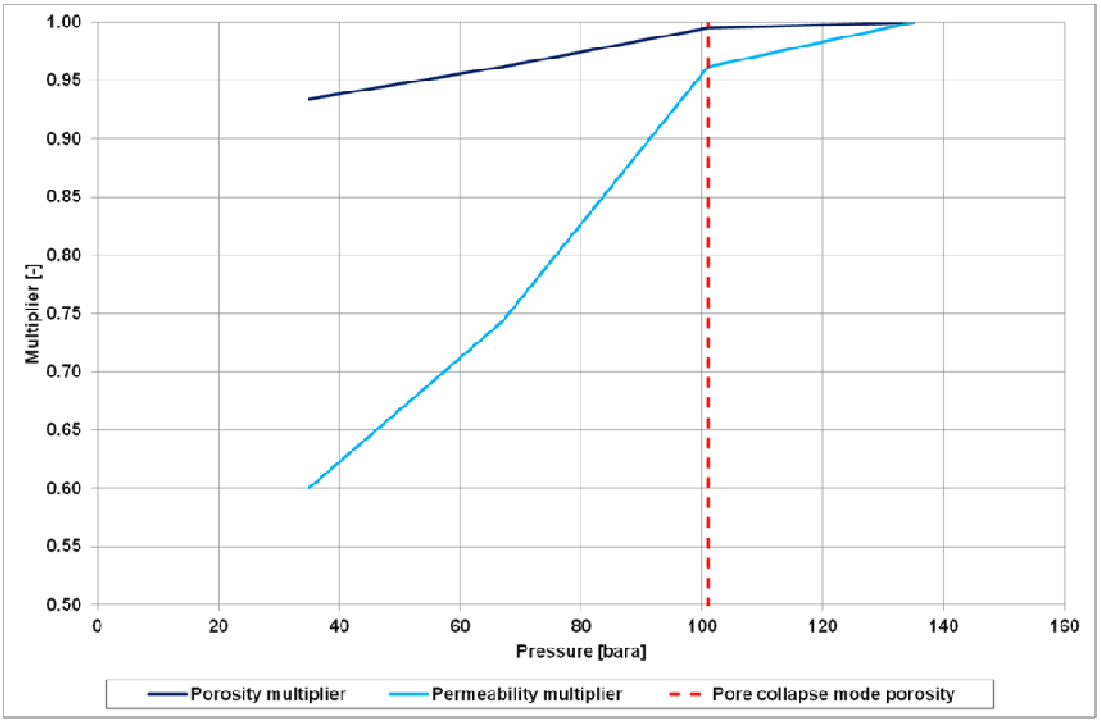

Figure 5-27 Rock compaction simplification for porosity screening.

After the 100 porosity models were ran with the historical data, the porosity models were ranked according to their overall performance in terms of how well they could reflect the historical pressure and production data.

A subset of porosity realizations was taken forward to the coarse grid history matching exercise for further evaluation; the final history match was performed on the porosity realization requiring least amendments.

5.5.3.2 History match

The coarse grid dynamic reservoir model was history-matched to the static well pressure and production measurements taken from the onset of gas production in 1988 up to the time gas production stopped in mid 2008, as well as to the static pressure measurements of the post production build-up period up to 2012. The history-matched dynamic model represents a good fit to the measured production and pressure data and is regarded as applicable for predicting future dynamic reservoir behaviour. An exception to this is the history match of well HRL-07.

To obtain a history matched dynamic model in each region the gas-water contact, pore volume and permeability were modified within a realistic range. Furthermore the vertical communication and the communication between the wells in the major producing pool, i.e. between regions 3 and 4, were adjusted to the observed dynamic behaviour. The history match parameters and the corresponding ranges considered are summarized in Table 5-8.

Table 5-8 History match parameter ranges.

Property	Type	Starting Point	Minimum	Maximum	Applied to
permeability in x-direction [mD]	Multiplier	1.0	0.5	1.5	regions
permeability in y-direction [mD]	Multiplier	1.0	0.5	1.5	regions
kv/kh [-]	value	0.5	0.1	0.9	field
pore volume [rm^3]	Multiplier	1.0	0.8	1.2	regions
transmissibility [cP rm^3/day/bar]	Multiplier	1.0	0.001	1.5	between regions 3 and 4
FWL, Region 1, South-South [mTVDss]	value	1079.0	1061.0	1096.0	region 1
FWL, Region 2, South [mTVDss]	value	1079.0	1061.0	1096.0	region 2
FWL, Region 3, Central [mTVDss]	value	1063.5	1055.0	1090.0	region 3
FWL, Region 4, North-West [mTVDss]	value	1063.5	1055.0	1090.0	region 4
FWL, Region 5, East [mTVDss]	value	1068.5	1056.0	1091.0	region 5
permeability in x-direction around HRL-06 [mD]	Multiplier	1.0	0.5	5.0	box around HRL-06
permeability in y-direction around HRL-06 [mD]	Multiplier	1.0	0.5	5.0	box around HRL-06

The parameter values with which the history match was obtained are summarized in Table 5-9. The GIIP of the history matched dynamic model is $5x10^9$ Sm^3. The parameter $\tau 34$ is a dimensionless multiplier for the transmissibility between regions 3 and 4 in the dynamic model.

Table 5-9 History match parameters, coarse grid.

Coarse Grid: History match parameters					
Parameter	Regions				
	1	2	3	4	5
FWL [mTVDss]	1071.69	1076.03	1069.02	1061.45	1076.04
PERMX multiplier [-]	1.45	0.87	1.42	0.75	1.12
PERMY multiplier [-]	1.10	0.62	0.76	1.50	1.29
PORV multiplier [-]	0.83	1.17	0.80	0.80	0.91
kvkh [-]			0.11		
τ 34 multiplier [-]			0.05		
PERMX HRL-06 multiplier [-]		4.78			
PERMY-HRL-06 multiplier [-]		4.84			

5.5.4 FINE GRID MODEL

The fine grid model was the underlying model for the subsidence calculations (Chapter 6). The coarse and fine grid characteristics are compared in Table 5-10.

Table 5-10 Comparison: coarse and fine grid characteristics.

		Coarse Grid	Fine Grid
Number of grid cells	x	90	414
	y	85	408
	z	26	87
Total Number of Cells		~ 200000	~ 15000000
Active Cells		71000	663000
Average Areal Dimension [m]		150	50
Average Cell Thickness [m]	Chalk	1.6	0.3
	Chalk below Reservoir	33	12
Layering	Chalk	3 to 11	3 to 52
	Chalk below Reservoir	12 to 21	53 to 82
Run time [min]		1.5	35

In order to decrease the simulation run time of the fine grid model the chalk below the reservoir was set inactive in the dynamic model and by this any compaction in the water leg was excluded. This was possible because the communication between the reservoir and the underburden is considered negligible (Section 5.5.3).

5.5.4.1 History match

The starting point for the fine grid history match was the coarse grid history match parameters (Table 5-9). The coarse grid history match parameters were applied to the fine grid model and following that they were manually fine tuned where necessary. Table 5-11 summarizes the fine grid history match parameters. The only parameter that required adjustment was the permeability around well HRL-06.

Table 5-11 History match parameters, fine grid.

Fine Grid: History match parameters					
Parameter	Regions				
	1	2	3	4	5
FWL [mTVDss]	1071.69	1076.03	1069.02	1061.45	1076.04
PERMX multiplier [-]	1.45	0.87	1.42	0.75	1.12
PERMY multiplier [-]	1.10	0.62	0.76	1.50	1.29
PORV multiplier [-]	0.83	1.17	0.80	0.80	0.91
kvkh [-]			0.11		
τ 34 multiplier [-]			0.05		
PERMX HRL-06 multiplier [-]		15.00			
PERMY-HRL-06 multiplier [-]		15.00			

On average, the quality of the history match was considered suitable for carrying the model forward to dynamic modelling forecasts and subsidence evaluations. The historical gas production rates were matched and the difference between calculated and measured pressures was reasonably good. An example of a reasonably good pressure match is shown in Figure 5-28.

An exception was the pressure match for well HRL-07, where the calculated pressures for the time period after the year 2000 were up to 20 bar higher than the measured LMP pressures and around 10 bar higher than the extrapolated pressures p*. An attempt was made to overcome that discrepancy by alternative history matches using different parameter modifications and varying sizes of the region, where well HRL-07 is located. However, the quality of the history match could not be improved by these means (Figure 5-29). As the model pressures up to about 2000 do match the measurements, this suggests that there is nothing fundamentally wrong with the modelled reservoir and well characteristics and the reason for the later mismatch may lie elsewhere, i.e. possibly with the reported HRL-07 gas rates in the period from 2000 to shut-in 2008 (see Section 5.5.4.1.1).

These observations triggered a critical review of production measurements and metering in Harlingen performed by Vermilion. This review provided evidence of possible underlying causes for the observed pressure mismatch in well HRL-07 (Vermilion, 2014 [42], and Appendix 5):

- In the period 1999–2003, a production allocation issue had occurred between the fields being processed at the Harlingen Treatment Center.
- The metering on a well basis has a theoretical accuracy of ± 20 % (applies to all wells).
- The meter requires a minimum gas rate of 30000 Nm^3/day to perform within specification.
- Suspicious metering behaviour was detected in HRL-07 during meter calibration in 2008.
- The interpretation of the analog meter output creates an additional error at low flow rates on a well by well basis.

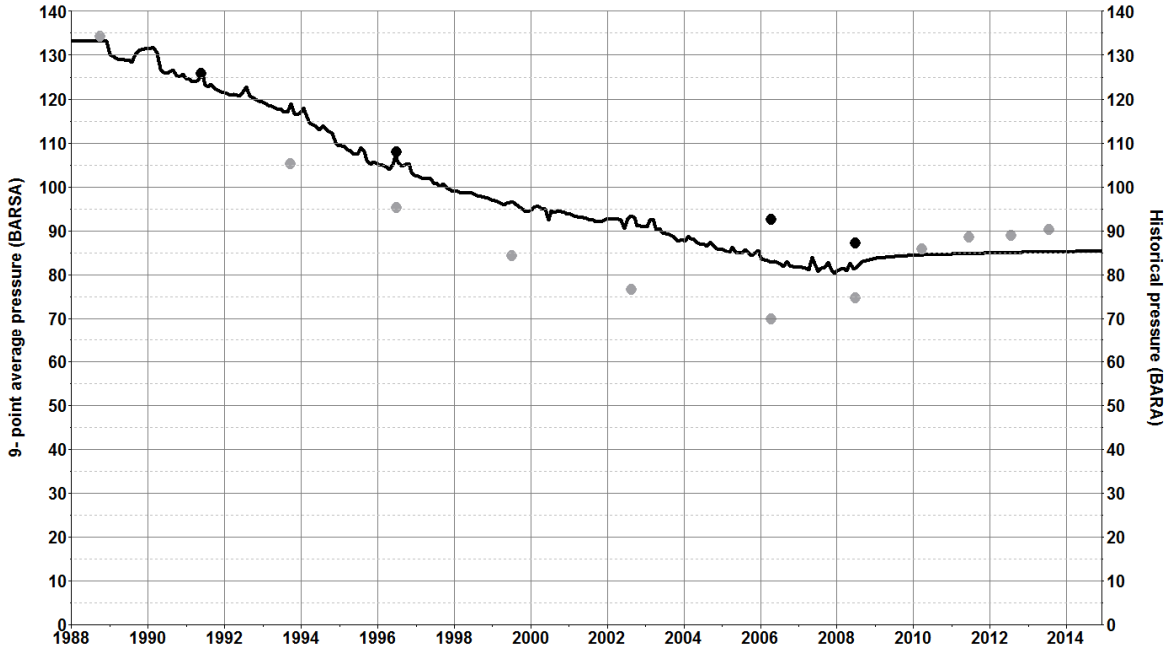

Figure 5-28 **Well HRL-02: comparison of measured and modelled pressures. Pressure points classification: p* (black), LMP (grey).**

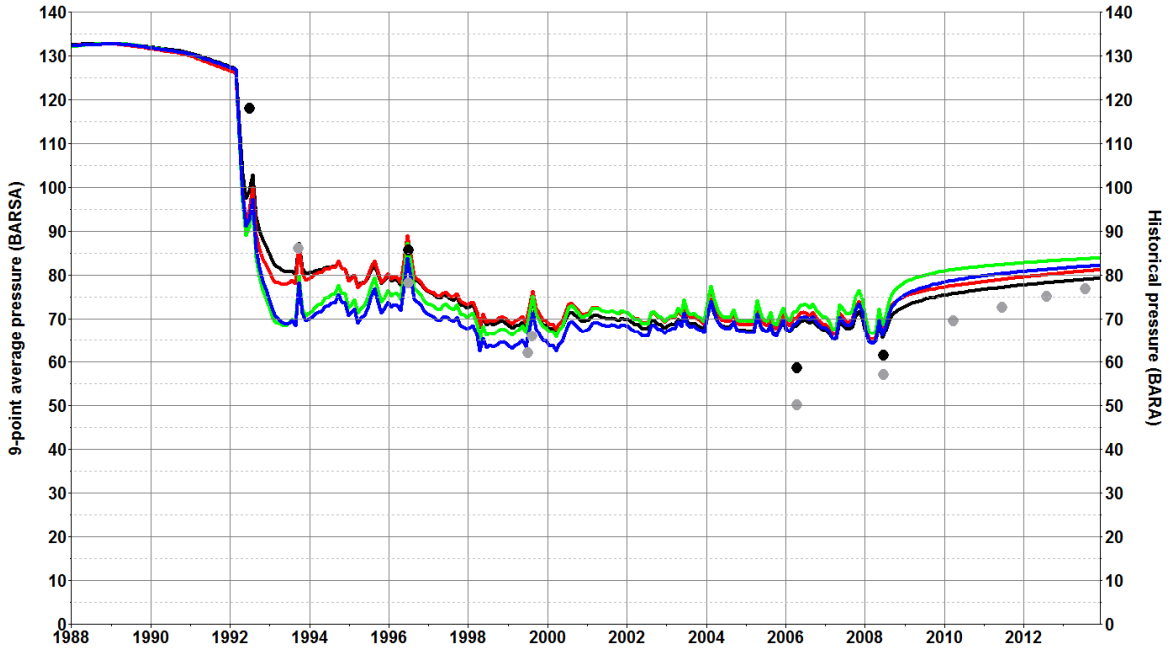

Figure 5-29 **Well HRL-07: comparison of measured and modelled pressures for various sensitivity runs (black line represents reference case). Different line colours represent different HM parameters and region setup applied to the same underlying porosity model. Pressure points classification: p* (black), LMP (grey).**

5.5.4.1.1 Adjusted offtake HRL-07

The history matched model, as presented in Section 5.5.4.1, was re-run applying an adjusted offtake to well HRL-07. Based on the Vermilion review (Vermilion, 2014 [42], and Appendix 5), a 50 % higher gas production rate from HRL-07 from 2000 onwards was used (Figure 5-30). The additional cumulative field gas production for this adjusted offtake scenario represents an increment of 4 %.

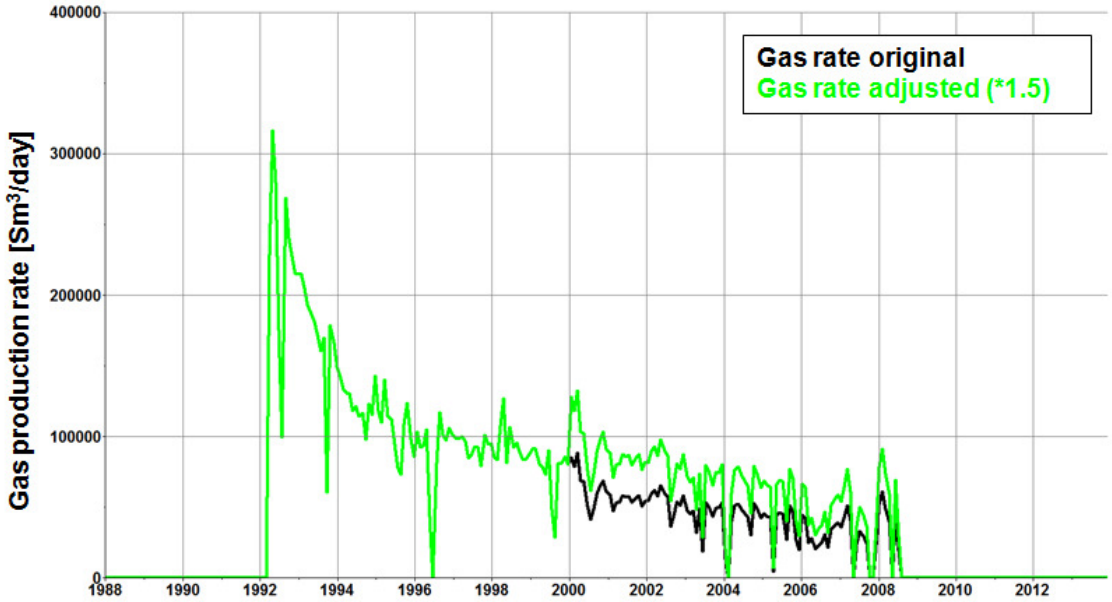

Figure 5-30 Gas production rate at well HRL-07 before (black) and after (green) adjustment.

Model pressures at HRL-07 are now much more in line with measured pressures (Figure 5-31). The quality of the history match for the other wells remains good.

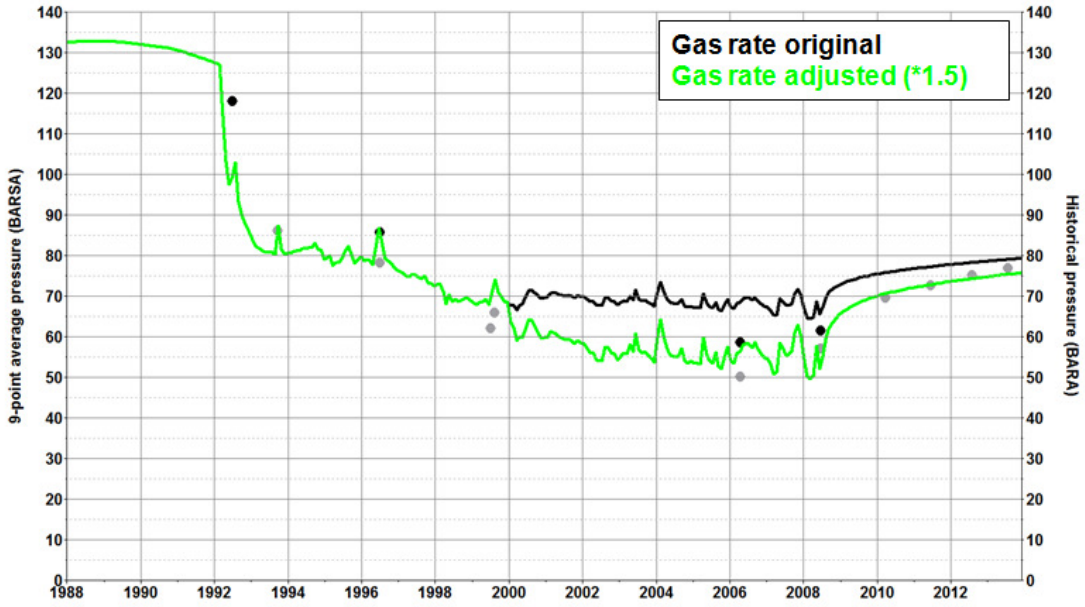

Figure 5-31 **Well HRL-07: Comparison of modelled and measured pressures before (black) and after (green) modification of the offtake rate. Pressure points classification: p* (black), LMP (grey).**

As a consequence, the HRL-07 adjusted offtake scenario is now used as reference history match case. The reservoir pressure maps for this case now show a deeper and wider pressure sink in the north-west of the field in 2008 (Figure 5-32), compared with the previous history match case (Figure 15-13).

The line plots for each well are shown in Appendix 6.

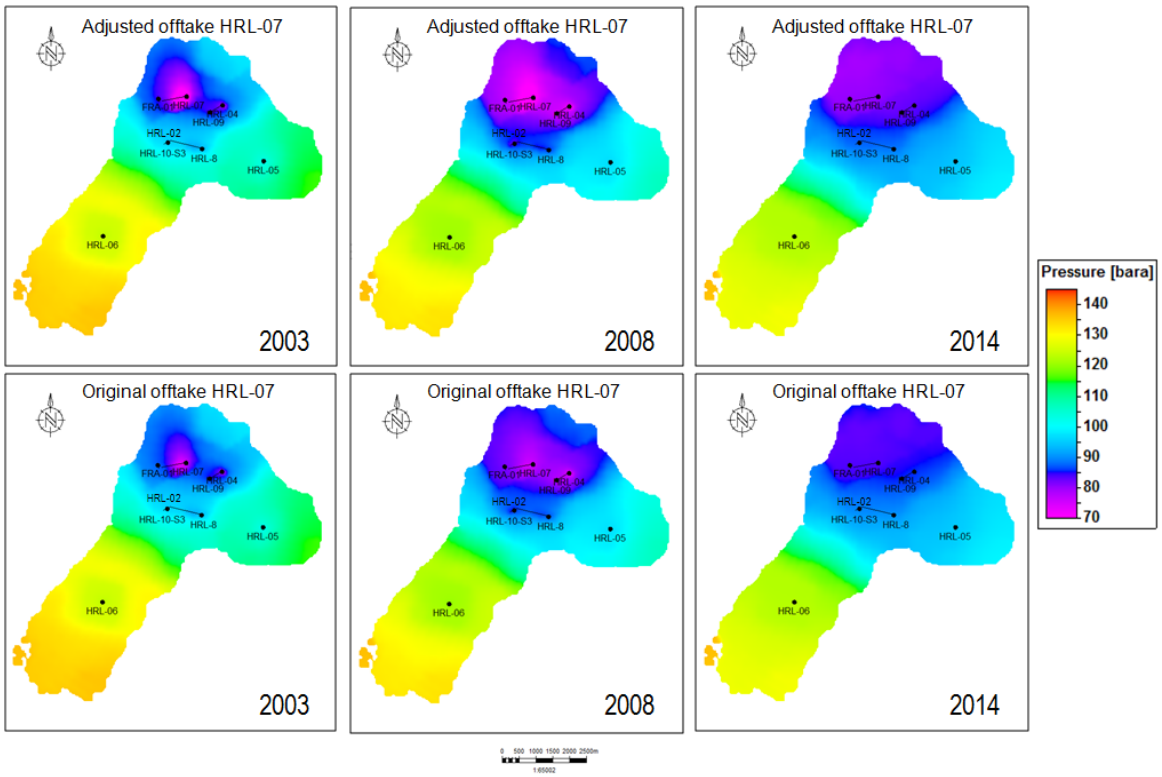

Figure 5-32 Pressure development for the originally reported (lower row) and HRL-07 adjusted offtake scenario (upper row).

5.5.5 FORECAST

Forecast calculations were performed for two end member scenarios: (1) field remains shut-in and (2) gas production continuation from 2008 onwards at average late well gas production rates. The scenarios give a mid-term outlook up to 2030 and a long-term outlook up to 2050.

The NFA (No Further Action) mid-term outlook forecast is used for predicting subsidence in the next 15 years and the NFA long-term outlook is used to evaluate when subsidence rates will reach autonomous rates (Chapter 7).

The basis for the forecasts was the history match described in Section 5.5.4.1. In the forecast calculations no constraints in terms of pressures and rates were applied. The line plots for each well are shown in Appendix 6.

5.5.5.1 Field remains shut-in

In the first scenario, the field remains shut-in and no further activities are assumed in terms of production or drilling new wells. This scenario is also referred to as the 'No Further Action' (NFA) case. In this scenario the dynamic model predicts that the average reservoir pressure in the central and the eastern pool of the Harlingen Chalk field stabilizes at around 85 bar after about 30 years of shut-in. After 2040 the average reservoir pressure in this northern part of the field remains stable in this scenario.

Figure 5-33 shows the pressure development up to 2050 and the location of the former gas producing wells and Figure 5-34 the average pressure development for each individual region in the dynamic model.

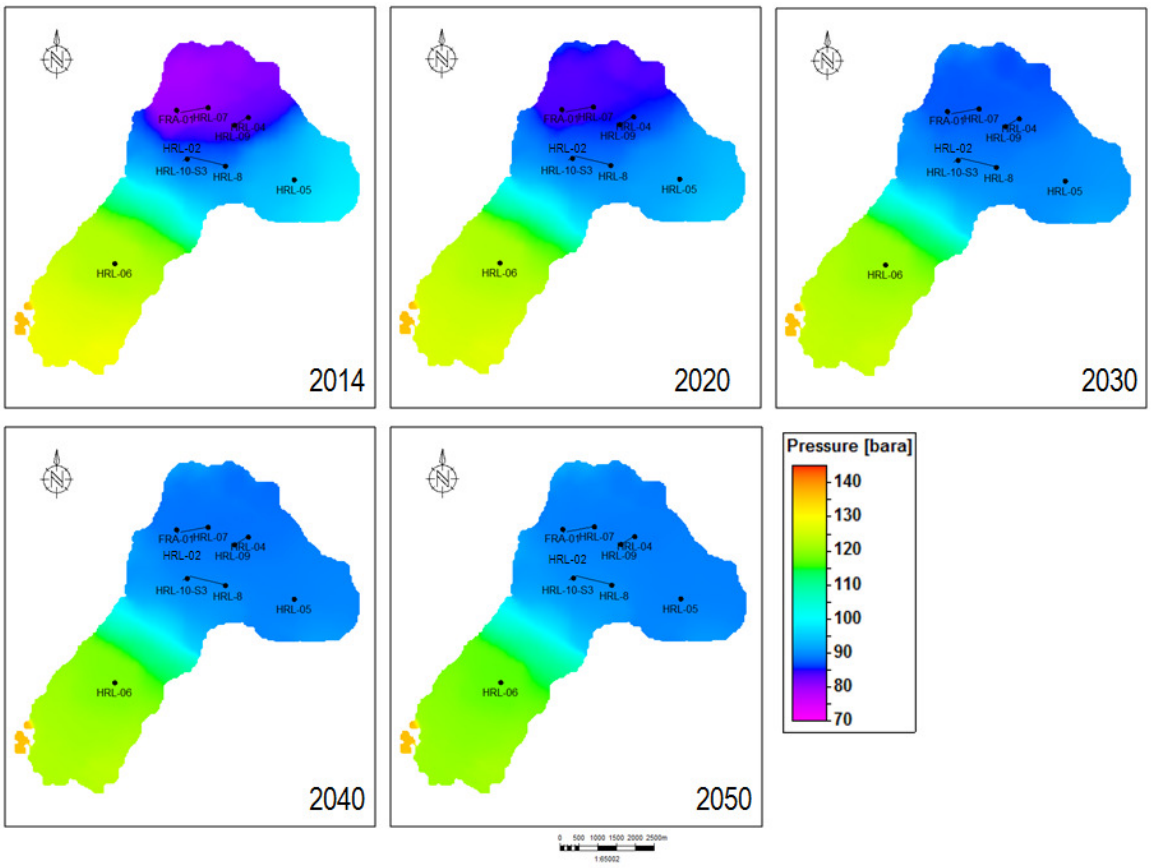

Figure 5-33 **Reservoir pressure development in the Harlingen Chalk gas field for the NFA case after 2014.**

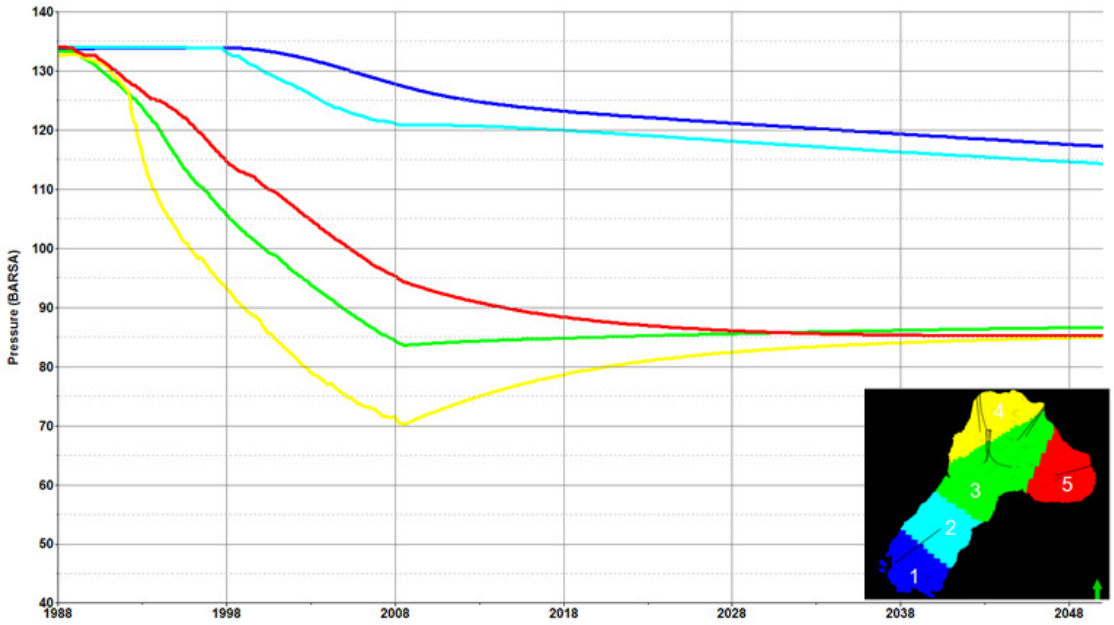

Figure 5-34 **Average region pressure development in the Harlingen Chalk gas field for the NFA case.**

5.5.5.2 Continued production

In the second scenario the hypothetical assumption was made that the field would not have been shut-in but would have continued production. The objective of this what-if scenario was to evaluate what might have happened if the field had not been shut-in in 2008.

In this second scenario, all wells except FRA-01, which was stopped long before the field shut-in, were produced at late average historical rates from August 2008 onwards. These rates were calculated based on the average well rates during the last year of production.

In this scenario, the average reservoir pressure in the central pool drops below 50 bar after about 25 years of additional gas production after 2008 and below 40 bar in the area of well HRL-07 in the same time period.

Figure 5-35 shows the pressure development for this case until 2050 and Figure 5-36 shows the average region pressure in the model. Comparison of these results to those of the NFA case shows an additional significant pressure drop in the entire field. In comparison to the NFA case the additional pressure drop due to continued production would have been 10 bar in 2014. At the end of the forecast period in 2050 the calculated pressure in the central pool would have halved compared to the NFA case.

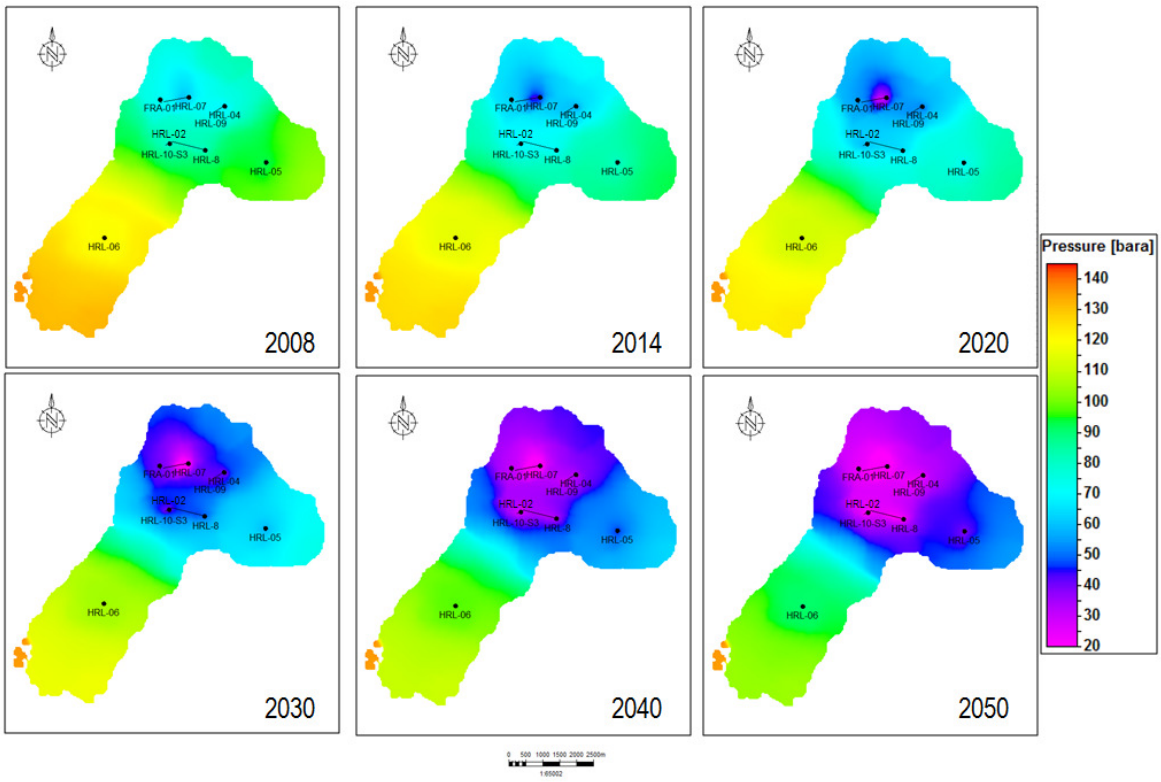

Figure 5-35 Reservoir pressure development in the Harlingen Chalk gas field for the continued production case.

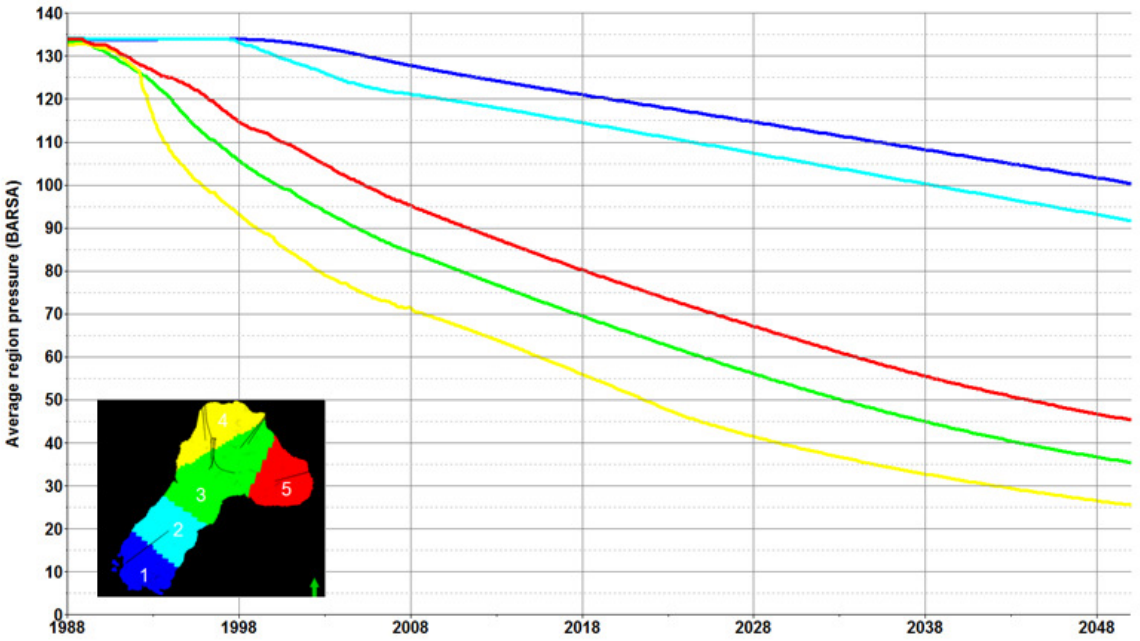

Figure 5-36 Average region pressure development in the Harlingen Chalk gas field for the continued production case.

5.5.6 FRANEKER AREA SENSITIVITY

In this scenario it was evaluated, if the ultimate subsidence calculated would change to the worse for the area in which the city of Franeker is located in case another porosity model would have been selected for modelling.
In general high porosity areas are more prone to pore collapse during pressure depletion and subsequent subsidence. In this sensitivity it was especially evaluated if high porosity areas in the eastern pool would result in ultimately more subsidence in the area of Franeker. In order to evaluate such a scenario the 100 available porosity realizations were screened to select the one with the highest number of cells with a porosity of more than 35 % in the eastern part of the field (Figure 5-37). The history matched model was then re-run with the adjusted off-take scenario. For the selected porosity model a history match was performed applying the workflow outlined in Section 5.5.1. In Table 5-12 the history match parameters are summarized.

Figure 5-38 shows the pressure development throughout history and Figure 5-39 shows the pressure development for the NFA case until 2050.

The line plots for each well are shown in Appendix 6.

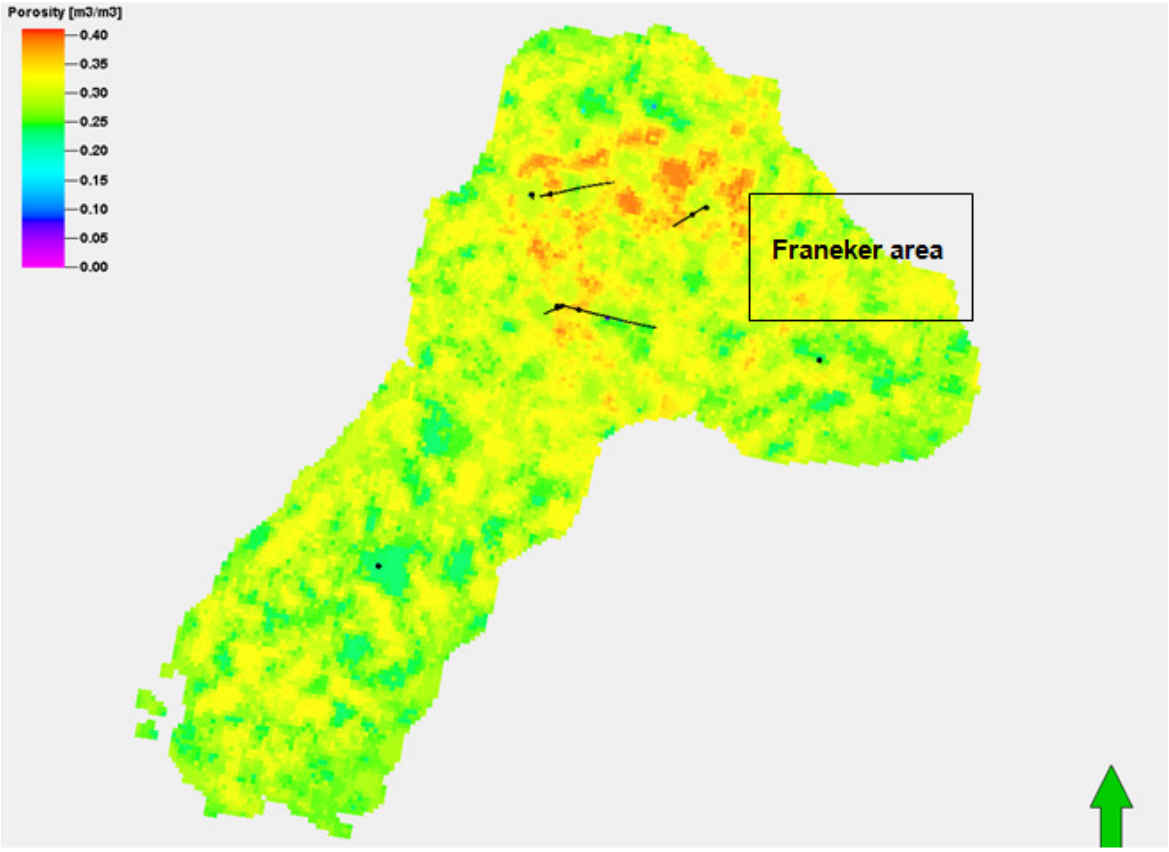

Figure 5-37 **Top layer view of the selected porosity model for the Franeker sensitivity, the box indicates the location of the town of Franeker.**

Table 5-12 **History match parameters, Franeker area sensitivity.**

Franeker Area Sensitivity: History match parameters					
	Regions				
Parameter	1	2	3	4	5
FWL [mTVDss]	1062	1081	1068	1061.7	1074
PERMX multiplier [-]	1	0.77	0.62	0.77	1.4
PERMY multiplier [-]	0.75	1.5	1.5	1.25	0.9
PORV multiplier [-]	1	1.05	0.8	1.06	0.8
kvkh [-]			0.70		
τ 34 multiplier [-]			0.00015		
PERMX HRL-06 multiplier [-]		1.00			
PERMY-HRL-06 multiplier [-]		1.00			

The transmissibility between the HRL-07 area (region 4) and the remainder of the central pool (region 3) is significantly lower compared to the reference history match (Table 5-12). This is reflected in the pressure behaviour during depletion and build-up period (Figure 5-40). This supports the finding that the region around well HRL-07 is poorly connected to the remaining field.

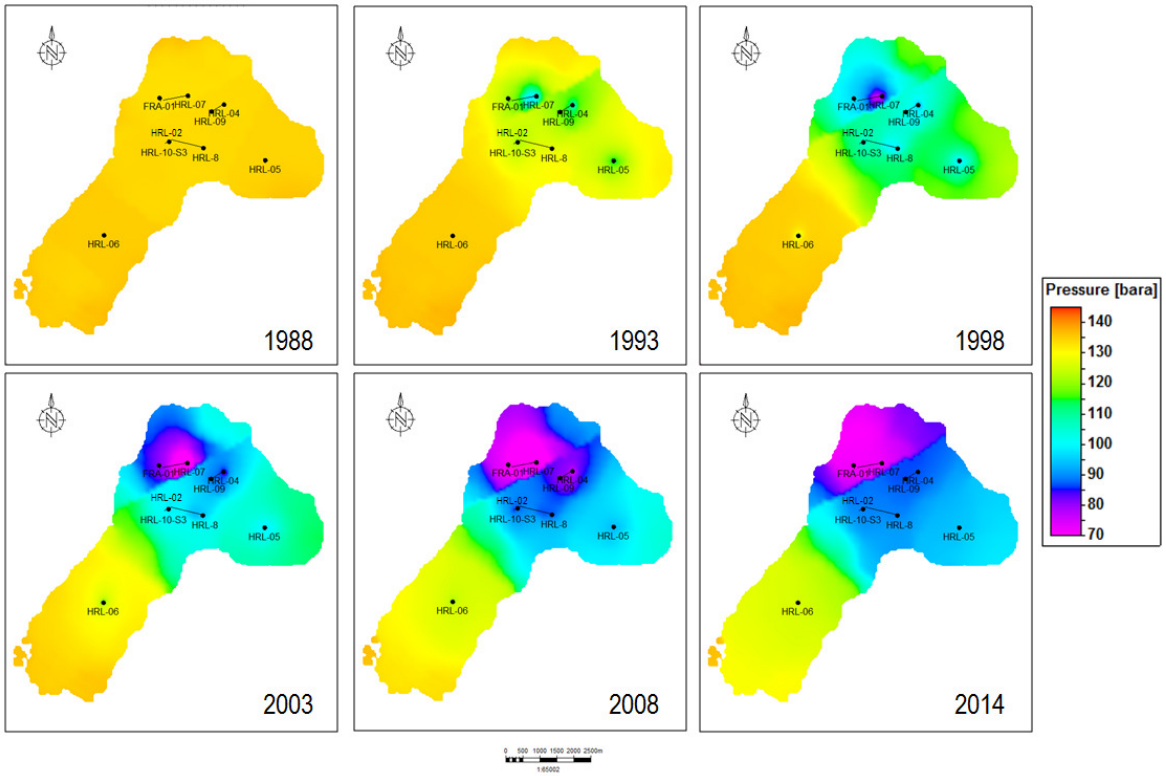

Figure 5-38 Franeker sensitivity history match.

The results of the dynamic modelling work described were taken forward to the compaction and subsidence modelling discussed in Chapter 6 and subsidence forecasting discussed in Chapter 7.

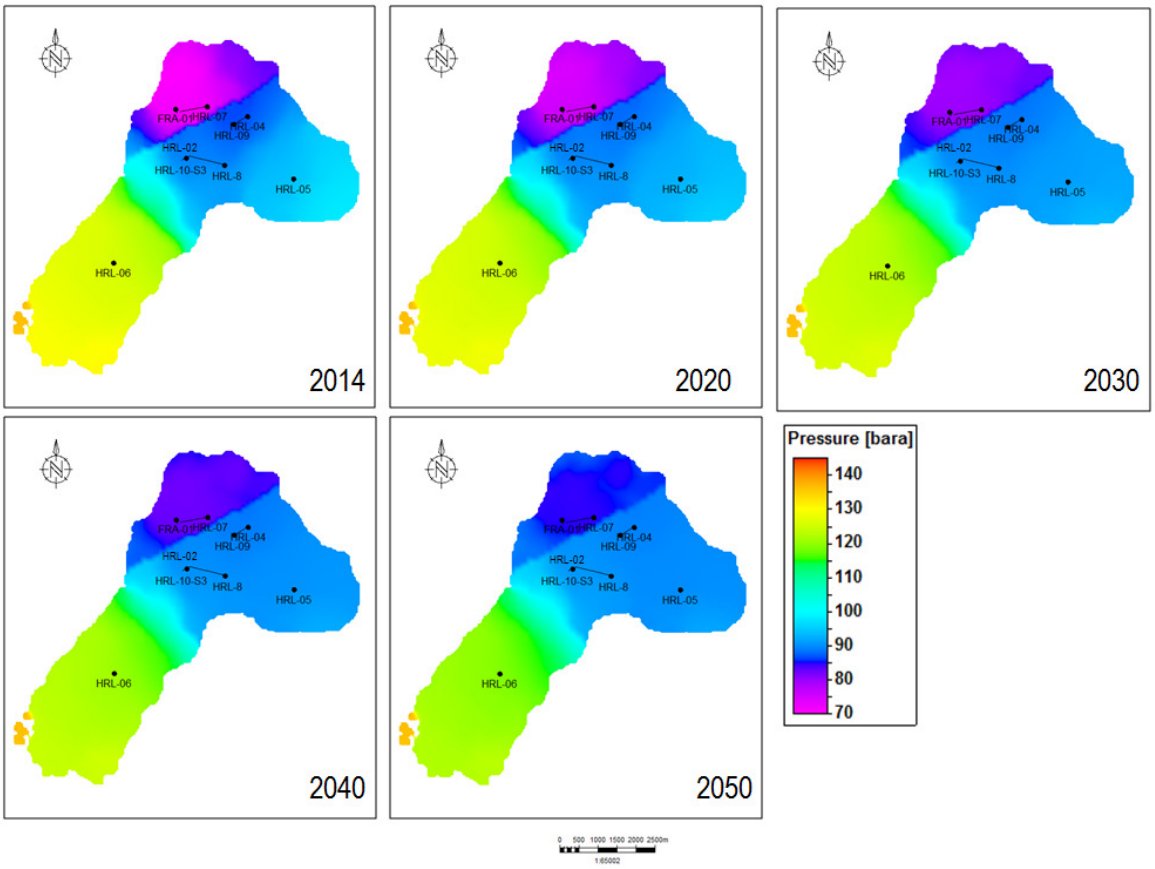

Figure 5-39 **Reservoir pressure development in the Harlingen Chalk gas field for the NFA case after 2014 for the Franeker sensitivity.**

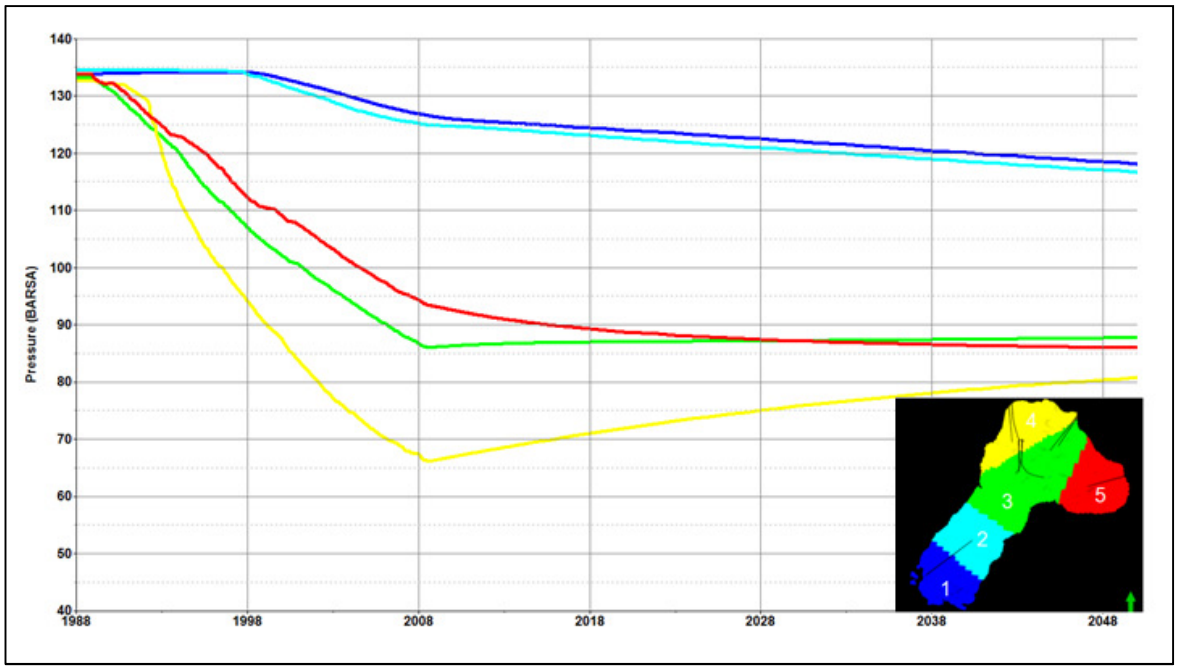

Figure 5-40 **Average region pressure development in the Harlingen Chalk gas field for the NFA case for the Franeker area sensitivity.**

6 SUBSIDENCE MODELLING

Subsidence modelling was performed in two steps: first, the volumetric strain as a result of pressure depletion was computed, resulting in a model for reservoir compaction. The second step was to translate this compaction at reservoir depth to subsidence at the surface. Initial modelling for the production period 1988 - 2008 was followed by modelling continued subsidence for the period post shut-in, including future subsidence still to be expected in the area.

All subsidence modelling steps were performed using Matlab programming language. A script for the RTCM based compaction model was provided by NGI. For the subsidence modelling the method of Van Opstal, 1974 [39], was utilised which was adapted for Matlab by TNO-AGE. For compaction modelling, input described in previous chapters was used: the 3D grid (dimension and coordinates of cells) and initial porosity from the static model (Chapter 5.4) and the reservoir pressures from the dynamic modelling (Chapter 5.5). All steps related to compaction and subsidence modelling are described in this chapter.

6.1 VOLUMETRIC STRAIN

Compaction is calculated by multiplication of bulk rock volume with volumetric strain, which in turn is calculated using the NGI-derived Rate Type Compaction Model based rock mechanical model. This model describes three modes of compactional behaviour: elastic deformation, plastic deformation and creep. Initially, the rock response to stress can be described using elastic parameters. Continued stress build-up can lead to permanent deformation (pore collapse) which is described by plastic parameters. On top of that, compaction can continue after stress relief which is described by creep. A summary of the rock mechanical model, which is briefly described in Chapter 4, is provided by NGI [22] and presented in Appendix 2.

6.1.1 COMPACTION DURING LOADING

The way the rock responds to stress build-up (loading) can be described by defining compressibility, stress rate dependency and the yield stress. The yield stress describes the shear failure criterion and determines the transition from elastic to plastic behaviour. In case of the latter, as soon as the effective stress on the rock exceeds the yield stress, pore collapse occurs causing permanent deformation of the rock, i.e. going from elastic to plastic mechanical response. The stress rate dependency parameter (*b*) is used to translate rock deformation under laboratory loading conditions to field conditions. Experimental data indicate that all of these parameters are dependent on porosity (ϕ) and the relationship can independently be described by a power law function (Appendix 2).

Rock deformation (strain) is calculated as a result of effective stress build-up in the rock due to pore pressure reduction. The rock response to this stress build-up is characterised by the effective stress ratio ($\Delta K'$) between effective horizontal and vertical stress. This ratio is defined and distinct for both the elastic state (via Poisson's ratio) and for the plastic state.

All volumetric strain parameters and their formulas are listed and described in Table 6-1. For these parameters a range of solutions/values fit the experimental chalk data which is shown for three parameters in Figure 6-1. First, the sensitivity of the model to each of these parameters is investigated. The factors used in evaluating these parameters, including their value ranges, are based on the results from the rock mechanical experiments (Appendix 2) and are listed in the table below. The last column of the table contains the default value, typically associated with the best fit to the Harlingen Chalk lab results (Appendix 2).

Table 6-1 Parameters used in volumetric strain modelling stating their definition as a function of porosity (ϕ) or Poisson's ratio (ν).

Definition		Formula	Parameter for sensitivity & tuning	Default value
Compressibility	Elastic compressibility 1/K	$K = BulkMod\_fac \cdot e^{BulkMod\_exp \cdot \phi}$	BulkMod_fac *(60000 – 500000)*	BulkMod_fac: 83596
	Plastic state: function of compressibility coefficient	$\lambda = Lambda\_fac \cdot e^{Lambda\_exp \cdot \phi}$	Lambda_fac *(0.028 – 0.075)* Lambda_exp *(2.5 – 4.5)*	Lambda_fac: 0.032 Lambda_exp: 4.1
Translation of lab to field loading conditions	Rate dependency parameter	$b = b\_fac \cdot e^{b\_exp \cdot \phi}$	b_fac *(0.135 – 0.170)*	b_fac: 0.135
Elastic-plastic transition	Isotropic yield stress	$P_c = Pc\_fac \cdot e^{Pc\_exp * \phi}$	Pc_fac *(250 – 450)*	Pc_fac: 300
Ratio effective horizontal – vertical stress	Elastic state: related to Poisson's ratio	$\Delta K' = \nu / (1-\nu)$	ν *(0.2 – 0.35)*	ν: 0.25
	Plastic state: determined by lab experiments	$\Delta K' = 0.4 - 0.6$	$\Delta K'$ *(0.4 – 0.6)*	$\Delta K'$: 0.6

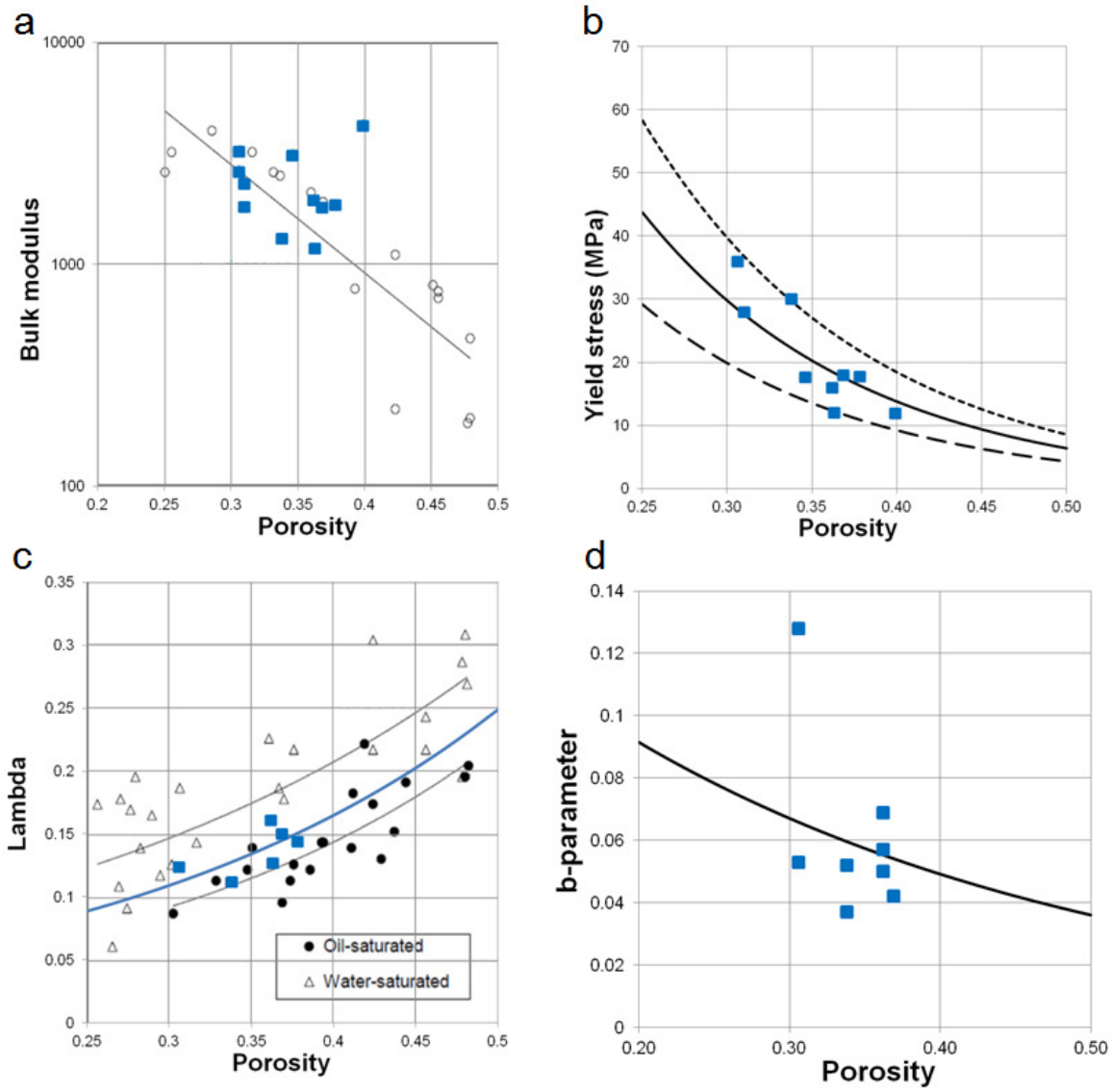

Figure 6-1 **Compressibility parameters vs. porosity, based on [21], for Harlingen Chalk experiments (blue symbols) and data from the JCR database [10]: a) Bulk modulus (trend line from [10]); b) yield stress at pore collapse with lower, average and upper trend lines [21]; c) compressibility coefficient (lambda) with trend lines; d) loading rate dependency parameter (b-parameter).**

6.1.2 TIME DEPENDENT COMPACTION: CREEP

Continued subsidence above the gas field after shut-in (Figure 6-2) is attributed to creep, which is modelled using RTCM formulation (de Waal, 1986 [4]) and explained in more detail in Appendix 2. Creep deformation is considered to be present from the onset of production and during the loading phase. The RTCM accounts for creep by the application of the rate dependency parameter. After loading however, when pressures stabilise or start redistributing, creep deformation needs to be accounted for by a separate part of the compaction model. The model assures continuity of the compaction rate when passing from a loading to a pure creep phase.

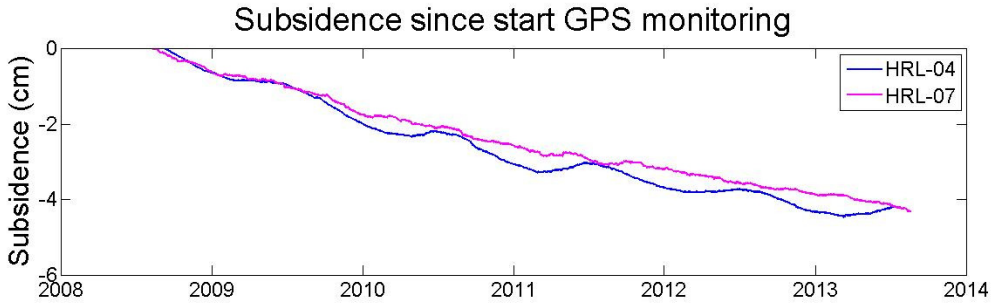

Figure 6-2 **Continued subsidence at GPS stations above two wells at the Harlingen Chalk gas field (8 week moving average, data available on www.nlog.nl [43]). A seasonal effect can be observed at HRL-04 and to a lesser extend in HRL-07.**

The process of creep (no stress change) adds volumetric strain to the rock based on the strain rate the rock experienced during loading. Over time the strain rate decreases logarithmically, ultimately converging towards zero. Creep will mainly affect rock volumes that have experienced pore collapse (plastic deformation). Elastic deformation is in principle non-permanent, and rocks that have only experienced this type of deformation therefore will be little affected by creep.

In the compaction calculation workflow, creep is implemented as a discretization of an integral, which is sensitive to the time steps used. Ideally, the smallest time steps are closest to the best solution, but increasing the number of increments increases the computing time. For the Harlingen Chalk field model a monthly evaluation gives a reasonable balance between convergence and runtime: smaller time steps did not result in a significantly different subsidence calculation.

Pressure build-up occurs in large areas of the Harlingen Chalk field after shut-in of the field. Build-up effectively reduces the stress on the rock, thereby also affecting the volumetric strain rate. A stable result with a reasonable computing time was found when updating the stress state and corresponding strain rate every time the pressure increases by 1 bar.

6.1.3 STRAIN PARAMETER SENSITIVITY TESTING

Sensitivity testing of the compaction parameters on the subsidence model was carried out on an early history matched pressure model. Testing was performed using the default parameter values as a base case and subsequently varying a single parameter value each time. The default parameters are those that were initially used to fit the Harlingen Chalk laboratory tests and were provided by NGI. Based on the work by NGI (Appendix 2 and NGI, 2011b [21]), values were selected that would cover the range of lab results. The sensitivity of each parameter is evaluated at the time of field shut-in (2008) after ~20 years of production.

Figure 6-3 shows the result of sensitivity testing for two parameters: one for which the modelling sensitivity is medium (bulk modulus) and one for which sensitivity is extremely high (isotropic yield stress). Sensitivity is considered low if the maximum variability in subsidence in 2008 between the most extreme parameters is < 5 cm, medium if 5 – 10 cm and high if > 10 cm. The sensitivities to the compaction parameters in this modelling workflow are:

- Compressibility before collapse (Bulk modulus): medium
- Compressibility after collapse (Lambda): medium
- Rate dependency (*b*): medium
- Isotropic yield stress (P_c): high
- Effective stress ratio before collapse (Poisson's ratio): medium
- Effective stress ratio after collapse: low

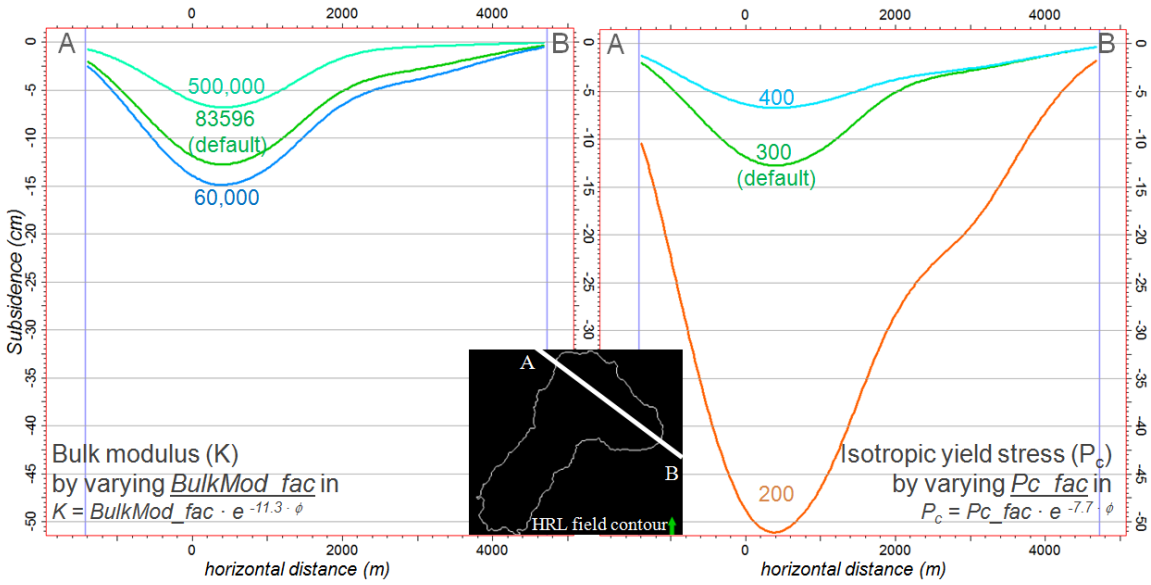

Figure 6-3 **Sensitivity of two compaction parameters on the model for gas induced subsidence: Bulk modulus ('BulkMod_fac') and isotropic yield stress ('Pc_fac'). Cross-section through the deepest part of the subsidence bowl after 20 yrs of production. Blue lines in cross sections indicate field outline (white in inset figure).**

6.1.4 MODELLING COMPACTION

The calculation for volumetric strain as described above is implemented in a single script. The input for the script are the initial porosity, coordinates and bulk volume of each grid cell, along with the pressures resulting from dynamic modelling. These pressures are exported for each time step on the 3D grid and are the result of dynamic simulation of the Harlingen Chalk field (Chapter 5.5). A schematic representation of the compaction modelling workflow, which is based on the work by NGI (Appendix 1), is illustrated with a flow chart in Figure 6-4.

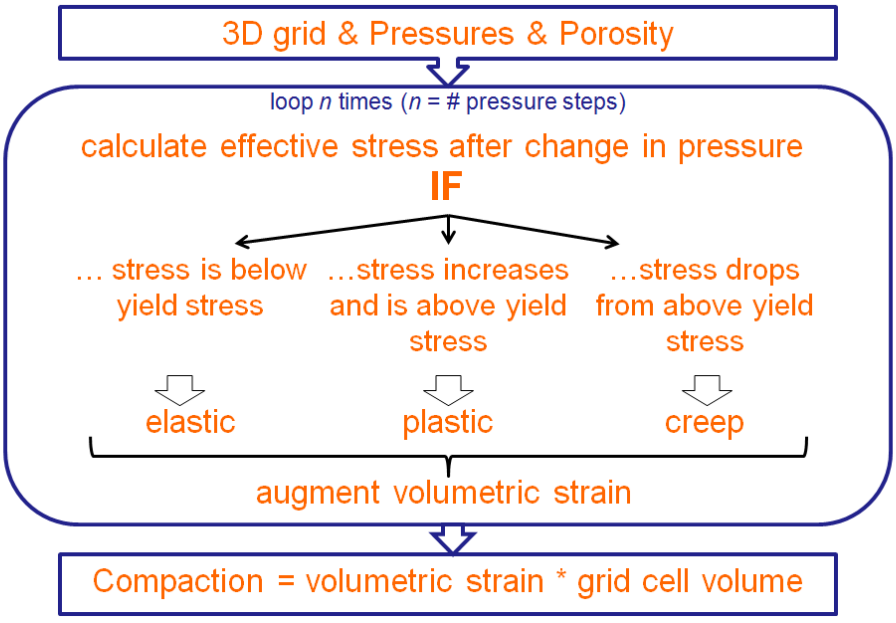

Figure 6-4 **Compaction modelling flow chart.**

Figure 6-4 shows the steps applied to calculate volumetric compaction for each cell in the 3D grid. For every pressure step the change in effective stress is updated and compared to the yield stress. If the stress increases strain is calculated using either elastic or plastic compressibility parameters. If the stress state does not change or decreases and the rock has experienced plastic deformation before an increase in volumetric strain is calculated using the latest strain rate. The script gives a volumetric strain value for each pressure step applied which is multiplied with the cell volume to obtain compaction.

6.2 MODELLED SUBSIDENCE

Translating compaction at reservoir depth to subsidence at surface requires a realistic representation of the geology in the area. Ideally, the model should be able to account for 3D heterogeneities of the reservoir itself and of the under- and overburden. However, the application of such a refined model asks for a lot of understanding of the elastic parameters for all lithologies involved. Attempts to incorporate these effects through 3D finite element modelling by Golder Associates in Turin (Italy) were abandoned during the course of this study. Subsequently a simplified modelling tool (AEsubs) has been employed where the surrounding geometry can be simulated through elasticity profiles of the overburden and underburden (Fokker, 2008 [7]). Because these profiles consist of horizontal layers with single properties (i.e. laterally homogeneous) the model can be considered as pseudo 3D. Unfortunately, testing of the AESubs software by SGSH revealed that, for the particular configuration of the Harlingen Chalk field, the AESubs code shows unstable behaviour, and therefore does not return reliable modelled subsidence results. Modelling with this software tool was therefore abandoned, and it was decided to proceed with the 'Geertsma - van Opstal' method which assumes a completely homogeneous half space in which the reservoir is embedded (i.e. no layering of the surrounding geometry).

The implication of these assumptions is that any effect of asymmetric overburden geometry will not be taken into account. It should be kept in mind that the analytical solution presented here is a highly simplified representation of the real subsurface. These simplifications contribute to the model uncertainty.

6.2.1 GEERTSMA-VAN OPSTAL

Translation of compaction at depth to subsidence at surface was performed with the method developed by van Opstal, 1974 [39]. As Van Opstal bases his methodology to a large extent on the method formulated by Geertsma, 1966 [8], this method to calculate subsidence is generally referred to as the 'Geertsma–van Opstal' model. This analytical model assumes linear and uniform elastic behaviour of the formations surrounding the reservoir. The model further assumes a rigid basement below the reservoir, at or below which displacement is zero for all rock, and a constant thickness and Poisson's ratio for the overburden. The depth of the rigid basement determines the shape of the subsidence bowl and as such mimics the elastic behaviour of the overlying layers. The model's default constant Poisson's ratio is 0.25. Subsidence can be calculated at any specified point at surface or on a dense grid of surface locations.

For the Harlingen Chalk field, the basement and reservoir depths were both set to 1000 m for reasons explained below, while the model's default Poisson's ratio of 0.25 was considered to give a reasonable representation of the Tertiary overburden and was therefore left unchanged (van Opstal, 1974 [39]).

The functions to compute the subsidence which are given in the publication by Van Opstal, 1974 [39], were programmed in Matlab by TNO-AGE, who supplied the Matlab code to SGSH for the purpose of this study.

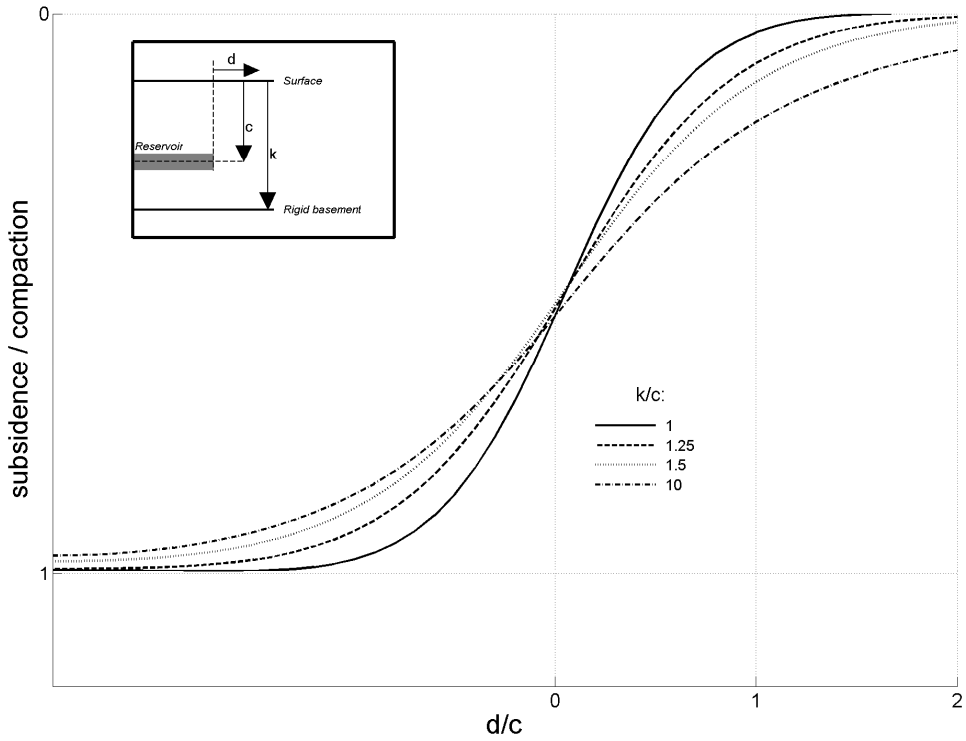

Figure 6-5 **Rigid basement effect on shape of subsidence bowl for a simple disc-shaped reservoir using the Geertsma-van Opstal subsidence model (geometry illustrated in inset). The horizontal axis displays distance from the reservoir edge as a ratio of the reservoir depth, the vertical axis shows the amount of subsidence as a ratio of the amount of compaction at reservoir depth.**

The depth of the rigid basement influences the shape of the subsidence bowl, which is illustrated in Figure 6-5. Subsidence is shown along a line across a rectangular reservoir with uniform compaction. The vertical axis shows the amount of subsidence relative to the amount of compaction in the reservoir. The horizontal axis highlights the extent of the bowl beyond the edge of the reservoir (d) as a factor of the reservoir depth (c). The deepest and steepest bowl is obtained with a rigid basement depth (k) equal to the reservoir depth (k/c = 1).

For the Harlingen Chalk field a rigid basement directly underneath the chalk is assumed, simulating the stiffness profile of the relatively soft Tertiary sediments on top of the strong Cretaceous Chalk formation in the over- and underburden respectively. Therefore k/c =1 and the solid line in Figure 6-5 represents modelled subsidence above the Harlingen Chalk field. A depth of 1000 m is assumed to be a reasonable approximation of the average reservoir depth and the core area of the field (from the highest amount of measured subsidence to the field edge) has a radius of ca 2 km. According to the figure the amount of subsidence should be almost equal to the amount of reservoir compaction near the center of the subsidence bowl while subsidence rapidly reduces when moving away from the reservoir edge. Figure 6-5 indicates that, with a k/c of 1, gas-production induced subsidence extends beyond the reservoir with a distance approximately equal to the depth of the reservoir, in this case 1 km.

6.3 MODELLING RESULTS FOR PRODUCTION PERIOD 1988-2008

The model for gas induced subsidence was evaluated by considering the difference between the modelled and measured subsidence at the benchmark locations. As explained in Chapter 3, subsidence at the benchmark locations is a combined effect of gas production, salt mining in the nearby Barradeel salt caverns and autonomous subsidence. To be able to evaluate the model for gas-production induced subsidence only, the benchmark data has been corrected for salt induced and autonomous subsidence.

The correction for the salt induced subsidence is taken as the midpoint between the Frisia Gaussian subsidence bowl and TNO-AGE subsidence model. The differences between the two salt models are considered to give an indication of the uncertainty of the subsidence contribution due to salt mining. It should be noted however that this uncertainty does not take into account modelling uncertainties on either of the two models. The uncertainty used could therefore be considered a conservative estimate of the true uncertainty on the subsidence attributed to salt mining activities above the Harlingen Chalk field.

It was decided to treat the autonomous subsidence rate as a variable during the tuning runs on the subsidence model. This evaluation, which is described below, led to an average rate of 0.09 cm per year above the gas reservoir, which is considered to be in reasonable agreement with the average autonomous subsidence rate estimated by Oranjewoud, 2007 [23], especially those found above the Harlingen Chalk field (Figure 3-4). Because of the large variability of the autonomous subsidence rates the uncertainty on the average rate applied in this study is large. It is difficult to quantify this uncertainty and to obtain a statistically satisfying number with only 6 samples. The maximum difference between the observed subsidence rates above the Harlingen Chalk field and the average rate is +0.05 and -0.07 cm/yr at benchmark locations ‘000A2756’ and ‘000A2750’ respectively.

This model evaluation is carried out using all available benchmark locations within 1 km from the Harlingen Chalk field outline. The 1 km radius is chosen based on the influence radius of reservoir compaction using the Geerstma-van Opstal subsidence model (Section 6.2.1).

6.3.1 TUNING RESULTS

The volumetric strain parameters for the rock compaction model leading to the smallest misfit between modelled and measured subsidence were determined by a tuning exercise. Parameters varied were the bulk modulus, the isotropic yield stress, the lambda exponent and the lambda factor (describing the plastic compressibility), the beta factor (rate dependency parameter), the Poisson’s ratio, the plastic effective stress ratio, and the autonomous subsidence rate. This involved generating a minimum of 10000 subsidence models using different, randomly chosen parameter values (from a pre-set, relevant bandwidth of values) every model run. Relevant bandwidths for each parameter were based on results from the NGI study (Appendix 2 and NGI, 2011b [21]). At the end of each run, the model was evaluated against the measured benchmark subsidence. Besides the seven compaction parameters, the autonomous subsidence rate was included as a tuning parameter. The final parameters used are average values of the best five results for a more stable solution.

For the model evaluation the misfit was computed for each period of time between two consecutive height measurements. The different compaction mechanisms (elastic and plastic) have different compaction rates and are expected to be dominant mechanisms at different periods of time (plastic following elastic deformation). Taking consecutive height measurement for the evaluation, rather than total subsidence over long periods of time, avoids time averaging of model performances and ensures the subsidence (rate) is captured at best for each period of time.

This resulted in a total of 523 subsidence intervals over which the model can be evaluated. Each misfit is compared to the uncertainty (two times standard deviation, 2σ) on the benchmark measurement, which is a combination of the uncertainties discussed in Section 3.1 and the salt modelling uncertainty which is half the difference ($\pm$) of the two available salt models (Section 3.2). The squared ratio of misfit over uncertainty is summed to obtain an overall model performance indicator:

$$\sum_{i=1}^{523} \frac{(Measured\ subsidence_i - Modelled\ subsidence_i)^2}{Measurement\ uncertainty_i{}^2}$$

The lower the total performance indicator value, the better the average fit to the benchmark data.

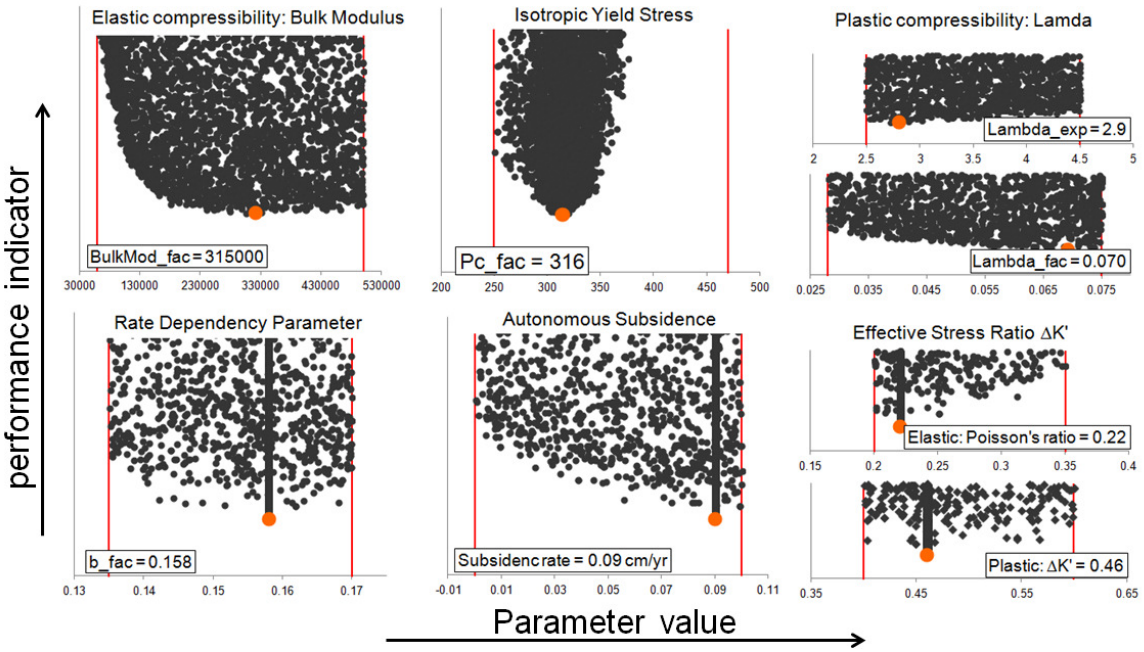

Figure 6-6 **Tuning results of compaction parameters and autonomous subsidence, plotted against the model quality indicator value. Each black dot represents a model run. Red lines indicate the extent of the tuning ranges, the value resulting in the lowest total model quality indicator value is shown in orange.**

Plots of each parameter against the performance indicator of the resulting subsidence model shows convergence toward a minimum value (Figure 6-6). This convergence is most pronounced for the more sensitive parameters (Section 6.1.2), which is to be expected.

The resulting parameters from the lowest performance indicator are compared to the lab experiments of the Harlingen Chalk data. The elastic compressibility, defined by the Bulk modulus, of the final model fits the Harlingen experimental data, although it is on the low side (high Bulk modulus means low compressibility) as can be seen in Figure 6-7. The optimum yield stress fits nicely to the lab results, being almost equal to the average (default) value. The resulting model has a high plastic compressibility (Lambda) which is higher than all Harlingen lab data, but fits the water saturated chalk results from the Joint Chalk Research (JCR) database (open symbols in Figure 6-7, Hickman, 2004 [10]). The final model has a Poisson's ratio of 0.21, which is typical value for chalk (NGI, 2011b [21]).

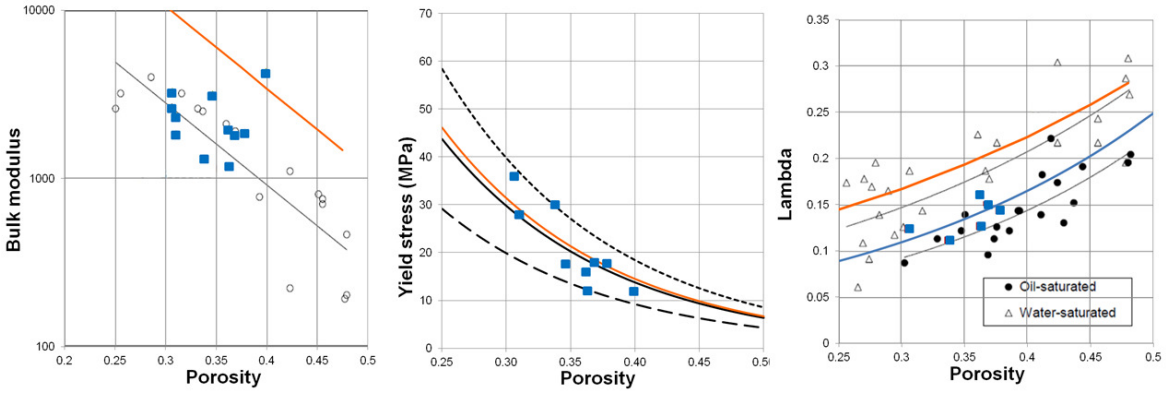

Figure 6-7 Compressibility parameters vs. porosity of the final fit (orange) on top of experimental data: data from Harlingen Chalk (blue symbols) and JCR database (from Hickman, 2004 [10]).

6.3.2 SUBSIDENCE MODELLING RESULTS

The modelling results show that a good average fit to the measured subsidence data for the production period 1988-2008 can be obtained using the history matched pressure model. The average ratio misfit/uncertainty is less than one, which means that the average subsidence rate is captured well in the model. Besides matching the subsidence rates the objective of the model is to explain observed total subsidence since the onset of production. This could be expressed through the chi-square goodness of fit test which is defined as:

$$x^2 = \sum_{i=1}^{n}\sum_{t=1}^{m} \frac{(Measured\ subsidece_{it} - Modelled\ subsidence_{it})^2}{(Measurement\ uncertainty_{it})^2}$$

The summations are for 'm' number of subsidence measurements at each benchmark location and for 'n' number benchmark locations. The evaluation is done on subsidence since the initiation (t_0) of the individual benchmark point which is different at each location. Also the number (m) of measurements differs for individual locations. The reduced chi-square value of the model (chi-square divided by the number of degrees of freedom) is 0.7 meaning that the average misfit is smaller than the uncertainty on the measurements.

Despite the good average model performance, problems remain at some benchmark locations where the misfit between modelled and measured subsidence is large (shown in Appendix 7).

The largest misfits are found near the centre of the subsidence bowl, around well HRL-07. Subsidence measurements at the benchmark location closest to that ('0003004') started in 1997 and Figure 16-1 shows that modelled subsidence falls behind ~5.5 cm by 2008 (Appendix Section 16.1). This location and the two nearby locations to the south have been subject of several previous assessments and have at various times been in- or excluded of the database. In the last critical review, with the help of satellite data, they have been classified as reliable measurements (Muntendam-Bos et al., 2009 [15]).

It was decided by the TCM that the match of the subsidence model around the deepest point of the bowl is critical to the overall performance of the model. Subsequent sensitivity analysis highlighted the subsidence model's sensitivity to changes in the dynamic pressure development. The mismatch in the centre could be substantially reduced in a scenario with an adjusted offtake rate at the HRL-07 well (Section 5.5.4.1) resulting in added pressure depletion around this area. Figure 6-8 shows the result of this adjusted offtake scenario on the subsidence model: at the majority of intervals with a large misfit modelled subsidence exceeds measured data. However, at benchmark locations on the southern flank, especially those nearest to the deepest point, the adjusted

dynamic pressure model results in a good fit of cumulative subsidence at the time of shut-in (2008).

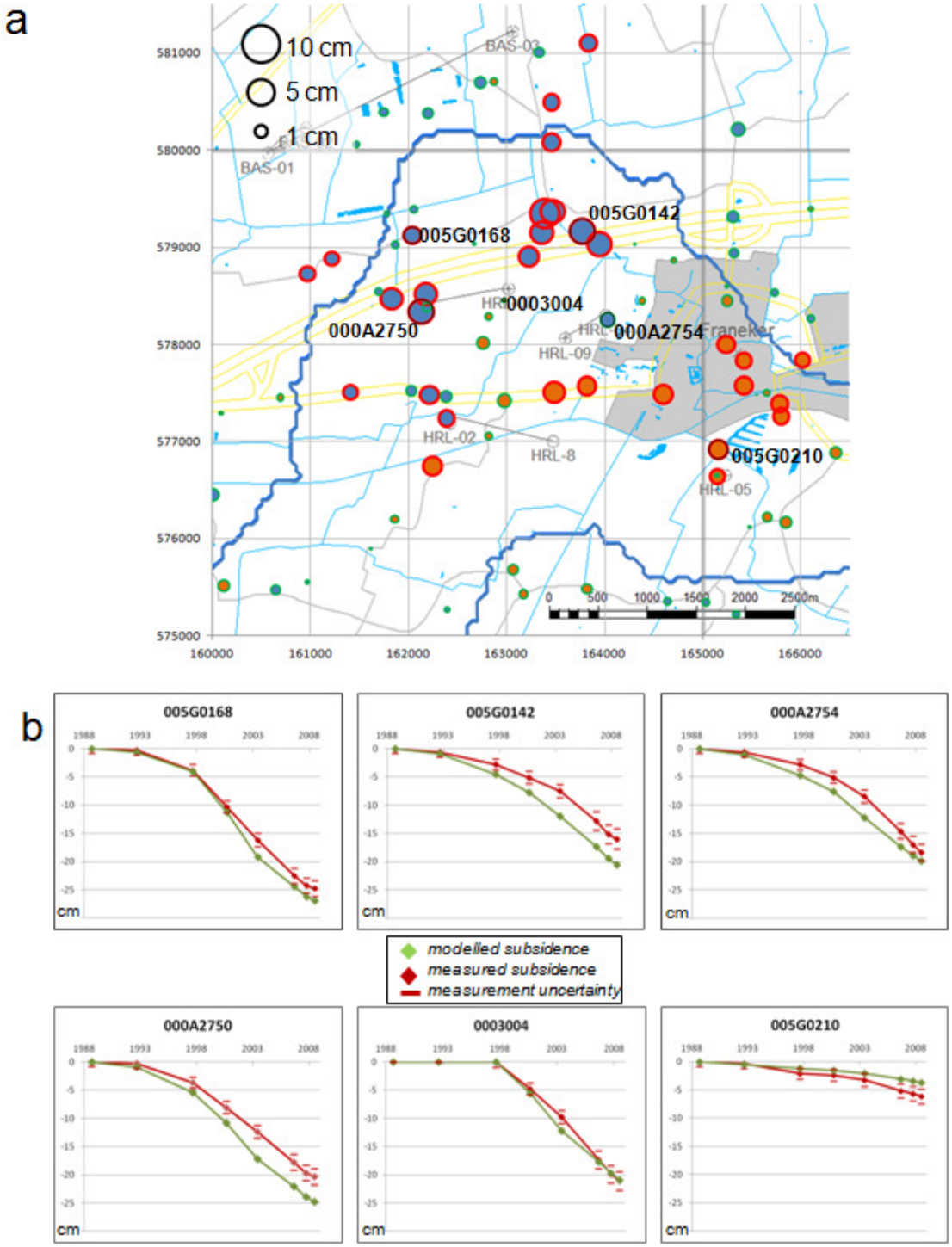

Figure 6-8 **a) difference between modelled and measured subsidence in 2008 indicating if the model exceeds measured subsidence (blue), falls behind (orange), size is proportional to the amount; b) modelled versus measured subsidence at selected benchmark locations since the start of measuring.**

The HRL-07 adjusted offtake model results in an improved match of the well pressures in HRL-07 (Section 5.5.4.1) and a better fit of the subsidence model in 2008 to the measured subsidence near the deepest point of the bowl (Figure 6-8). The figures below show resulting subsidence maps for gas induced (Figure 6-9) and total subsidence (Figure 6-10) at field shut-in (July 2008), indicating a maximum of 23 cm gas induced subsidence and a maximum total subsidence (including salt induced and autonomous subsidence) of 30 cm. The locations of this deepest point differs slightly due to the interaction of the individual subsidence bowls.

Based on an analysis of benchmark levelling data alone, Houtenbos [11] reported a maximum total subsidence above the Harlingen Chalk field of 26 cm in 2009. Combining benchmark and satellite data led Muntendam-Bos et al. [15] to report a maximum of at least 26.5 cm above the field in 2009. Even though the maximum total subsidence of 30 cm presented here is more than what has been reported in these previous studies, this model is in general agreement with these studies in terms of shape and position of the subsidence bowl.

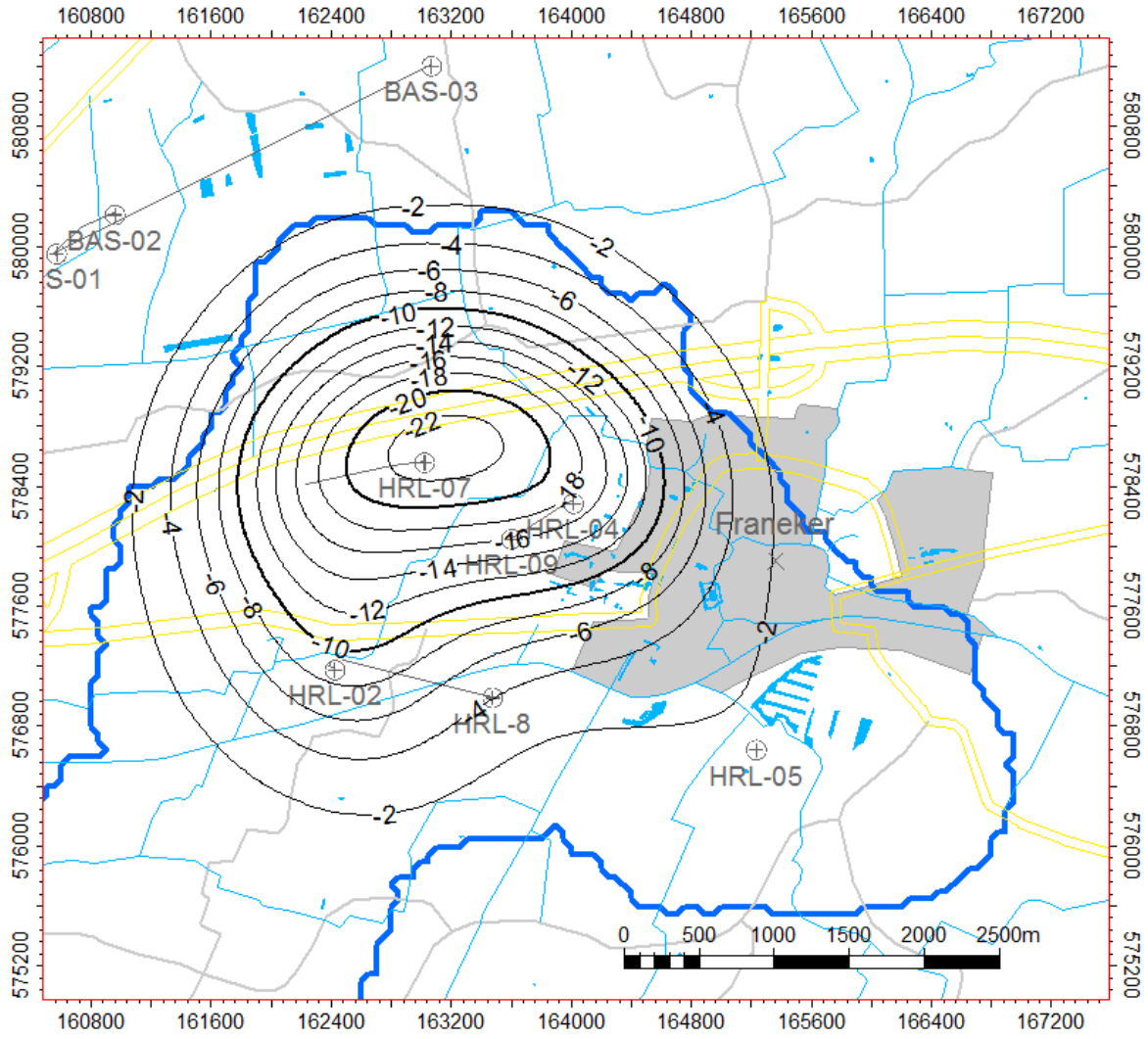

Figure 6-9 **Modelled gas induced subsidence between September 1988 and July 2008 in cm. Field outline in blue, well names and symbols for deviated wells are shown at the base of the well trajectory.**

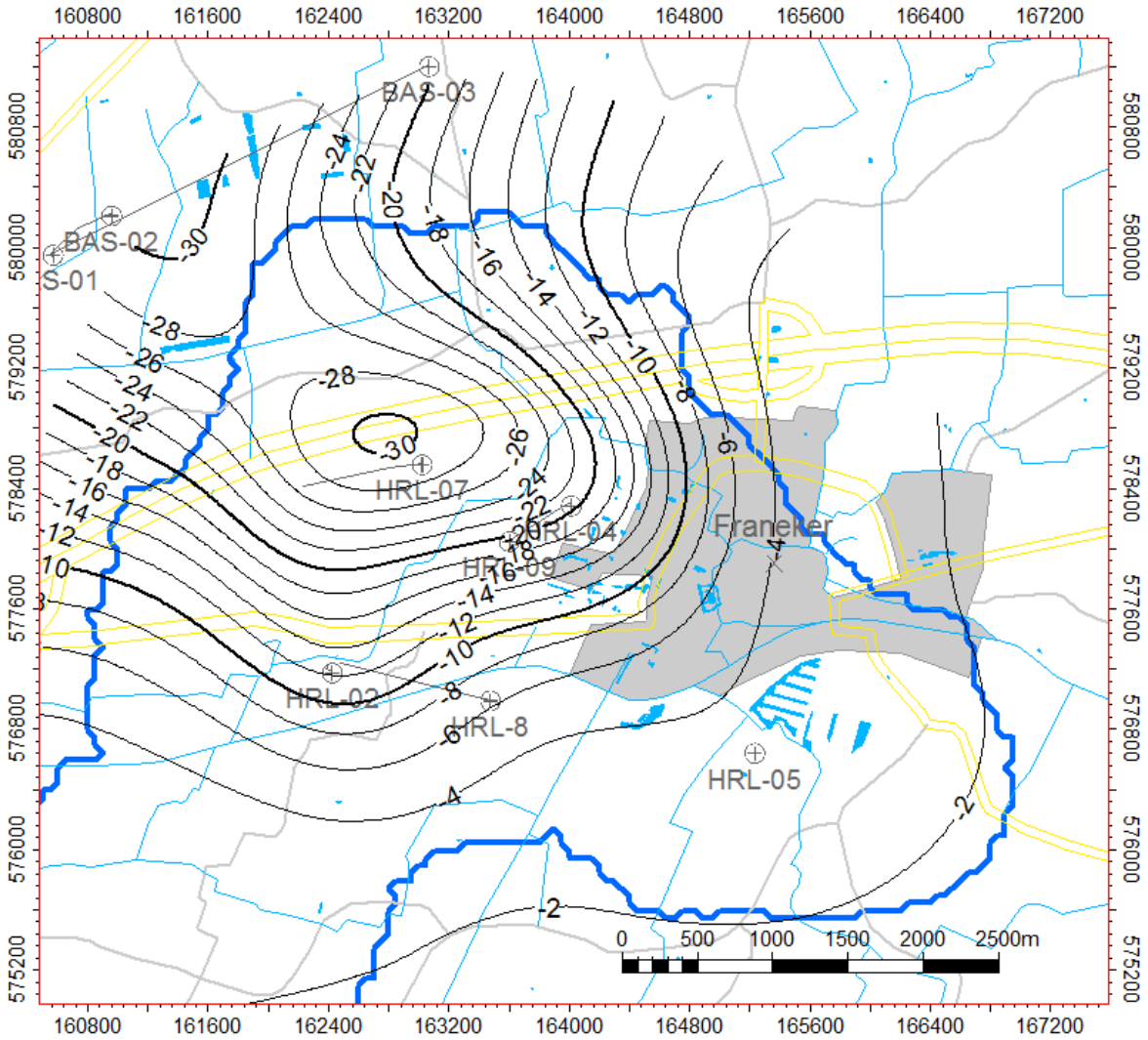

Figure 6-10 **Modelled total subsidence (including salt induced and autonomous) between September 1988 and July 2008 in cm. Field outline in blue, well names and symbols for deviated wells are shown at the base of the well trajectory.**

6.3.3 MODELLING UNCERTAINTIES

The modelled subsidence presented in Figure 6-9 is based on a series of modelling steps, all of which carry uncertainties. Uncertainties are related to measured data, interpretations and to modelling assumptions and simplifications. All modelling steps, however, carry an inherent dependency, ultimately leading to a model which satisfies well pressure measurements (Chapter 5.5) and observed subsidence at the benchmark locations above the reservoir (this chapter). To illustrate the effect some of the modelling steps have on the final result an alternative scenario was considered starting with a different porosity distribution. A distribution was selected with relatively high porosities in the east near the city of Franeker, it was therefore called the 'Franeker area sensitivity' case, see Section 5.5.6 for details. The porosity and associated history matched pressures were used to obtain a set of compaction parameters, the same way as described in Section 6.3.1. Note that this is not a complete uncertainty analysis but is intended to give an illustration of the uncertainties that can be expected. A full uncertainty analysis would include all modelling steps (static, dynamic and subsidence) and has not been part of this study. Such an analysis would give insight into the associated uncertainties but would not affect the modelled subsidence for the production period, which is calibrated to the measured data.

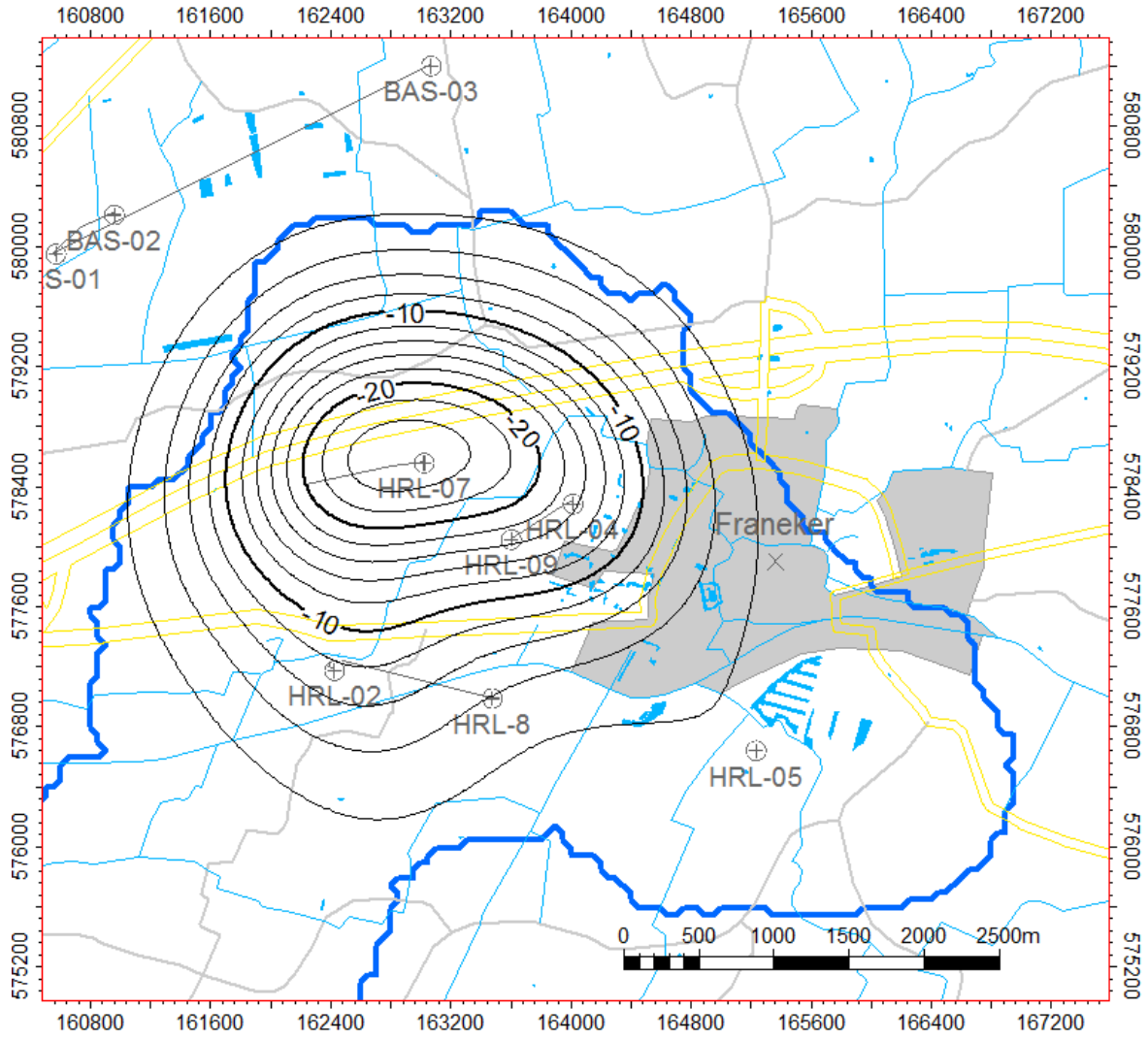

Figure 6-11 Modelled gas induced subsidence between September 1988 and July 2008 using the Franeker area sensitivity case in cm (2 cm contour interval).

The compaction parameters resulting from the Franeker area sensitivity case are different from the ones for the reference case but differences are small, typically less than 5 %. The resulting maps for gas induced and total subsidence at the time of shut-in (2008, Figure 6-11) are very comparable to the map derived from the reference case (Figure 6-9), although the Franeker area sensitivity case produces a slightly deeper and steeper gas induced subsidence bowl. Contrary to expectation, this case produces less subsidence in the eastern part near the city of Franeker, although the porosities are higher. This can possibly be explained by less pressure depletion in this area (Section 5.5.6). The maximum difference between the subsidence models based on two porosity distributions is ~3.5 cm.

6.4 SUBSIDENCE POST PRODUCTION: 2008-2013

After shut-in of the field in July 2008 the pressure development in the field changed substantially (Section 5.5.2.3). While in some parts of the field pressure continued to decline, build-up occurred in other areas, especially near the wells (Figure 6-12). As described in Section 6.1, volumetric strain will be modelled using rock compressibility parameters in case of pressure depletion, but creep will be modelled for cells that experience pressure build-up. The creep model adds

volumetric strain based on the late strain rate from the late depletion phase. After shut-in, the central area of the Harlingen Chalk field is dominated by pressure build-up (Figure 6-12) therefore post production subsidence in this region is modelled following creep induced compaction.

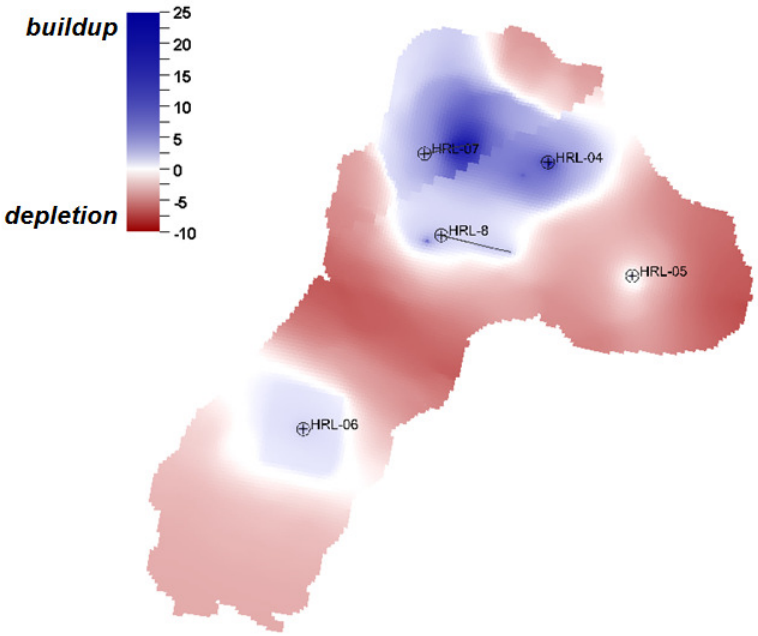

Figure 6-12 Modelled pressure development (bar) in the Harlingen Chalk field between July 2008 (shut-in) and January 2014. Also shown is the surface location of some of the wells.

Continued subsidence has been observed above the central area of the Harlingen gas field by the GPS stations at the HRL-04 and HRL-07 well sites (Figure 6-2). Subsidence continues but rates decline as can be inferred from the shape of the curves.

At both GPS locations the modelled subsidence (2008-2013) is substantially less than the subsidence observed (Appendix 7, Section 16.2). The shape of the subsidence curves, however, compares well with the average shape of the GPS subsidence curves, showing declining subsidence rates over time. This suggests there is probably no fundamental error in the model, but that the rate of subsidence at the onset of creep in 2008 may be underestimated by the current model.

The two GPS locations are above a part of the reservoir experiencing post 2008 pressure build-up (Figure 6-12) and hence compaction for this period is modelled using creep. As described in Section 6.1.2 and Appendix 2, compaction due to creep is modelled using the compaction rate inherited from the preceding depletion period. Once this rate is set at the onset of a creep phase the compaction curve is defined for the remainder of that period and therefore getting a correct initial compaction rate is essential to a good fit of the subsidence model during a period of creep. The results shown in Figure 16-2 (Appendix 7) demonstrate that this inherited compaction rate is not adequate and higher initial compaction rates are needed to make the creep model correctly match the data.

One reason that could explain part of this mismatch is that the model evaluates the reservoir pressures between periods of approximately one year, the dates of which are chosen to match the dates of the benchmark subsidence surveys (see Section 3.1). Short term fluctuations in reservoir pressure will not be accounted for in the model, but could have an impact on compaction rates in the field. Thus the compaction rate shortly before shut-in, which is a critical parameter to the estimation of creep induced compaction, may not be captured well. In an attempt to mitigate the mismatch, the compaction rate at the onset of creep was doubled resulting in an acceptable match

of the modelled subsidence to the observed subsidence at the GPS stations (Figure 6-13). The doubling of the compaction rate at the initiation of creep modelling is a pragmatic solution to the observed discrepancies but at the same time serves as an illustration of the uncertainties related to this part of the model. Modelling uncertainties are discussed in Chapter 7.

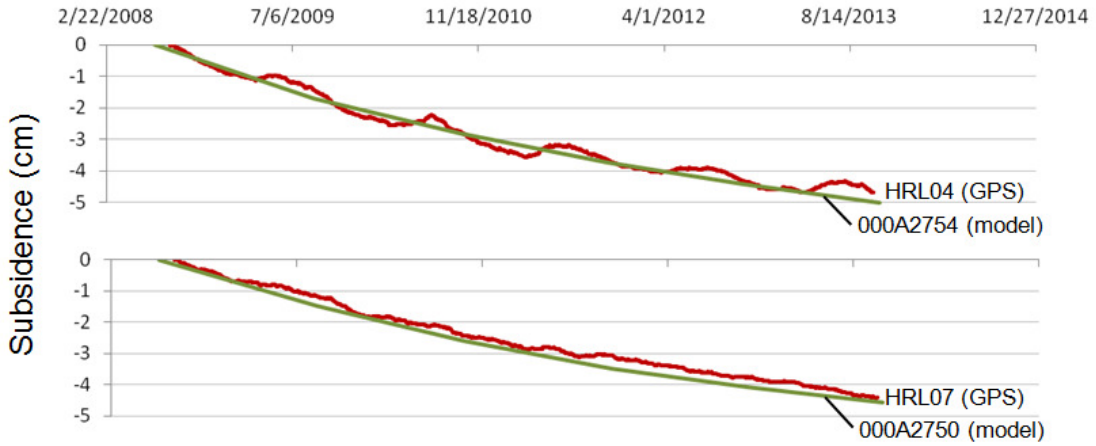

Figure 6-13 Subsidence post 2008 as measured at two GPS station above the Harlingen gas field (red) and as modelled at two nearby benchmark locations (green), with double initial compaction rates when going from depletion to creep based compaction modelling.

Figure 6-14 shows the result of the subsidence model in 2013, when the last subsidence measurement is available: at benchmark locations on the eastern and southern flank, especially those nearest to the deepest point, the model results in a good fit of cumulative subsidence at the time of the last measurement (2013). The contours in this figure show the gas induced subsidence bowl.

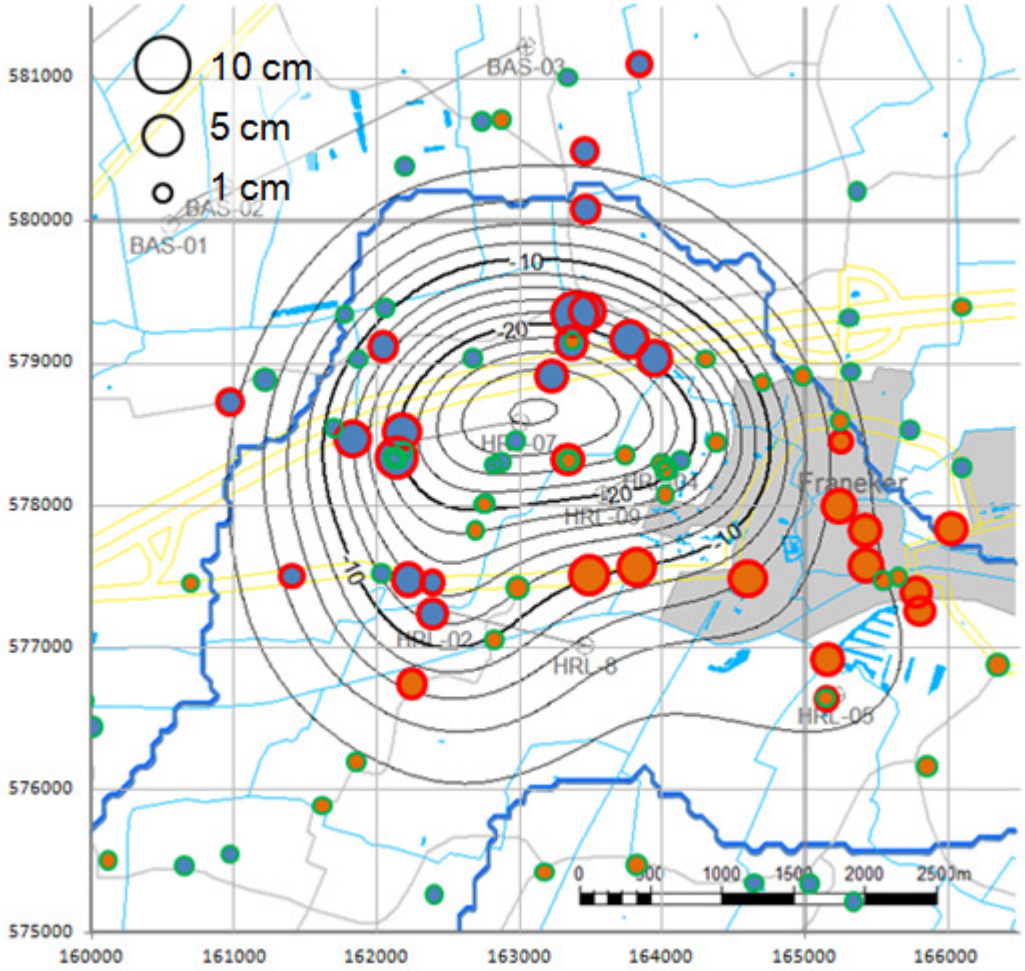

Figure 6-14 **Difference between modelled and measured subsidence for the latest levelling survey in 2013 indicating if the model exceeds measured subsidence (blue), falls behind (orange), size is proportional to the amount. Red (green) outline means the misfit is larger (smaller) than the uncertainty on the measurement. Contour lines in the background are for the gas-induced subsidence bowl in 2014 in cm (Figure 6-15a).**

The subsidence model shows that currently the gas induced subsidence amounts to a maximum of ~28 cm and this point is located above the reservoir section of well HRL-07 (Figure 6-15a). This demonstrates that, even after shutting the field in, subsidence has continued and added another 5 cm to the maximum subsidence at the time of shut-in. Also shown in this figure is a modelled gas induced subsidence bowl (Figure 6-15b) for a scenario where production would have continued at late production rates before shut-in (see Section 5.5.5.2 for details). According to the model this would have resulted in 3–4 cm more gas induced subsidence by 2014 compared to the situation as of 2014.

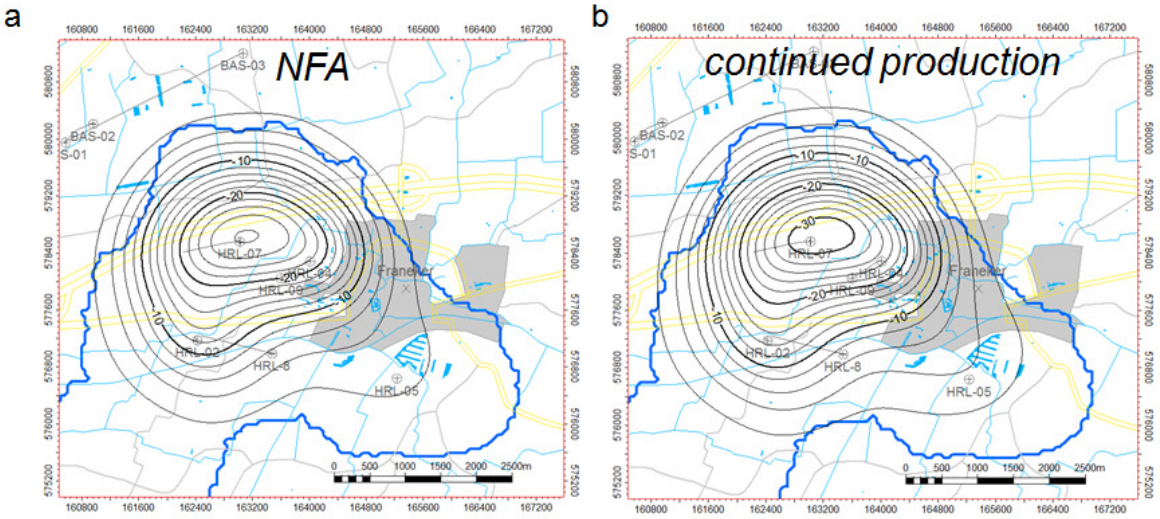

Figure 6-15 **Modelled gas induced subsidence in cm between 1988 and 2014 for a NFA (a) and a continued production (b) case in cm (2 cm contour interval).**

7 SUBSIDENCE FORECAST

The subsidence model, as described in Chapter 6, has been used to generate subsidence forecasts.

Whilst the subsidence model has been calibrated to match observed subsidence during the gas production period up to 2008 and the subsequent post production period, the model contains a simplified description of the physics of the subsidence process, (e.g. assumptions about the behaviour of the overburden and underburden, use of the analytical formulation of Geertsma-van Opstal model, approximation when representing time dependent compaction (Section 6.1.2)) and these limitations should be expressed in terms of forecasting uncertainties. Furthermore uncertainties in the values of reservoir and model parameters (e.g. porosity distribution, initial compaction rate for the creep model) should also lead to uncertainties in the subsidence forecasts.

As the current subsidence model approach is not well suited to generate forecast uncertainty bands an alternative forecasting method has been developed whereby observed subsidence post production has been fitted with an appropriate analytical function (decline curve type approach) to generate forecasts and estimate uncertainties.

The subsidence forecast assumes that the field is will remain shut-in, which is referred to as NFA (No Further Activity) case. Furthermore it is assumed that salt induced subsidence has ceased.

7.1 FORECAST PERIOD

In this study a mid-term subsidence forecast until 2030 was performed. This time frame is based on the fact that the fitting procedure, applied in the alternative approach, is valid for forecasting subsidence for a time period of about 15 years.

Furthermore a long-term forecast up to 2050 was generated to estimate when the subsidence rate becomes smaller than the autonomous subsidence, i.e. 0.09 cm/yr.

7.2 MODEL BASED FORECAST

The subsidence model described in Chapter 6 can be used to forecast the results of continued subsidence in the area above and near the Harlingen gas field. Figure 7-1 shows the gas induced subsidence since the onset of production (1988) for the years 2030 and 2050. The forecast assumes that the field will remain shut-in (NFA case, also see Section 5.5.5.1) and is based on doubling compaction rates for grid cells going into creep based compaction (as described in Section 6.4). What can be observed is that the shape of the subsidence bowl remains largely the same throughout the period 2008-2050 and that the position of the deepest point does not change notably. In the east an additional 2 cm of gas induced subsidence can be expected around the HRL-05 well between 2014 (Figure 6-15) and 2050, but the largest amount of additional subsidence can be observed in the central area: forecasting from 2014 a maximum additional subsidence of 5 and 7 cm can be expected in 2030 and 2050, respectively.

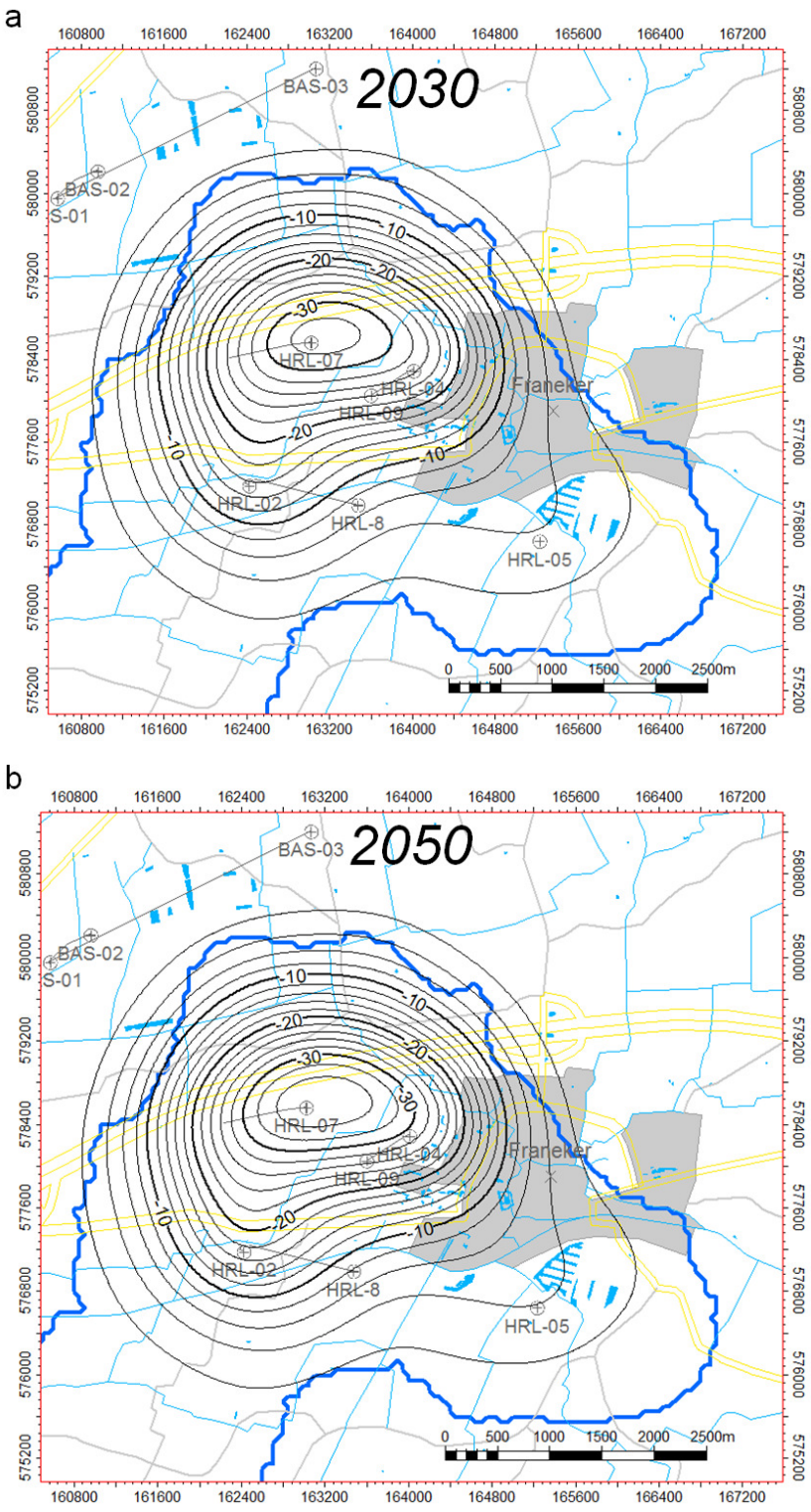

Figure 7-1 **Modelled gas induced subsidence in cm between 1988 and 2030 (a) and 2050 (b) based on a NFA case (2 cm contour interval).**

7.3 FITTING PROCEDURE BASED FORECAST

To combine the lessons on the subsidence mechanism, captured in the subsidence model, with the locally observed subsidence in the period 2008–2013, an alternative approach was

implemented to generate additional estimates of the subsidence over a short/mid-term time period and to create high- and low-case scenarios that take into account the measurement errors of the benchmark data. Such an approach consists essentially of a fitting exercise performed on the subsidence values measured in the post production period at the benchmark locations. The idea behind this approach is to assume a subsidence decline curve with a mathematical structure compatible with the physics underlying the creep/compaction behaviour and to use the measured data to calibrate the decline curve via a least-squares method. As a result, time-dependent decline curves were determined for all the benchmark locations. From a probabilistic point of view, the main limitations of such an approach are the statistical representativeness of the data (i.e. the temporal coverage of the measurements) and the degrees of freedom of the system (i.e. the number of experimental data used for the fit). The reliability of the fitting procedure is therefore expected to increase as soon as new measured data will become available.

7.3.1 FIT FORECAST

A simplified subsidence decline curve, compatible with the creep/compaction behaviour assumed in the forward model of Chapter 6, was used to fit the measured data while describing the time-dependent decline behaviour of the subsidence. Details of the fitting procedure used are given in Appendix 8, where it is fully reported how a physically-based/time-dependent decline curve was developed by implementing a non-linear regression. The latter allowed to forecast the future subsidence through the evaluation of the subsidence values measured (post shut-in) between 2008 and 2013 at the different benchmark locations of the field.

For the fit forecast, it was decided to create mid-term subsidence predictions until 2030 (as stated in Section 5.5.5), assuming neither further activity nor gas production from the field will take place. An example of the results obtained is given in Figure 7-2, which depicts, according to the definitions reported in Appendix 8:

- The measured subsidence values (y^{meas}), with the related error bars ($2\sigma_{meas}$)
- The forecasted subsidence values (y^{ls}) obtained by fitting the measured data, with the associated high- and low-case scenarios ($y^{ls_{MAX}}$ and $y^{ls_{\min}}$).

A full overview of the forecasts obtained by applying the fitting procedure is given in the histograms of Figure 7-3, where the additional subsidence that occurred after the field shut-in is shown. In particular, the values of the subsidence predicted for the year 2030 are reported along with the associated high- and low-case scenarios. Subsidence forecasts are reported for all benchmark locations (indicated in the second column of the table in Appendix 1 and ordered according to the distance from the deepest point (as shown in Figure 17-4) of the modelled gas induced subsidence bowl in 2008) where consistent measurements made it possible to reach convergent fit solutions.

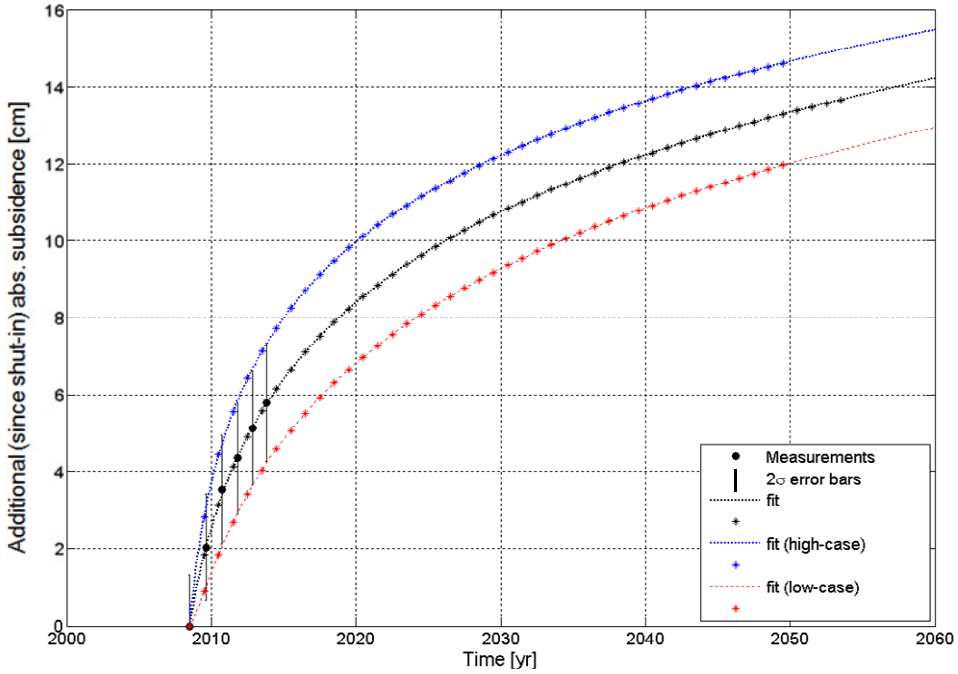

Figure 7-2 **Additional (since 2008) measured subsidence values (black dots with related error bars) and subsidence forecasts. Forecasted subsidence in black, high- and low-case scenarios in blue and red, respectively. Asterisks indicate values until the subsidence rate becomes smaller than autonomous subsidence (0.09 cm/yr). Measured data refer to the benchmark location 0003004 (i.e. the one closest to the deepest point of the 2008 gas induced modelled subsidence bowl, as defined in Figure 17-4).**

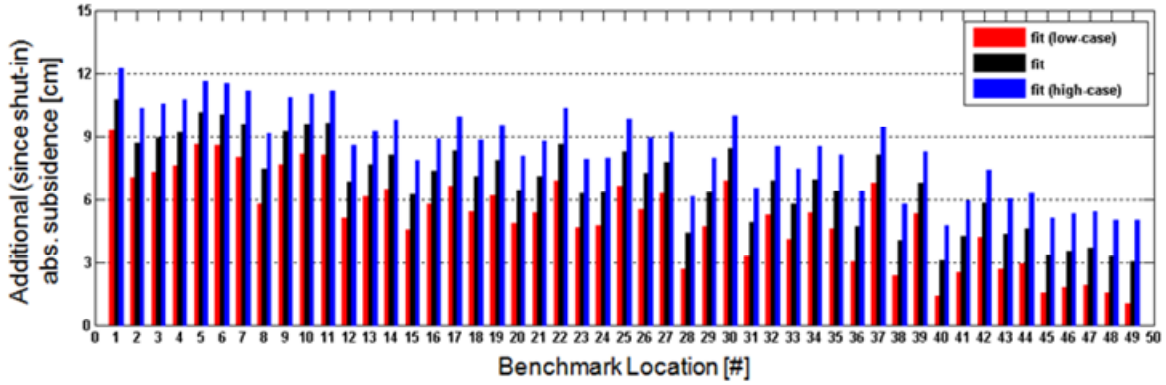

Figure 7-3 **Forecasted additional subsidence (since 2008) per benchmark location in 2030. Subsidence values are reported (in black) with the related high- and low-case scenarios (in red and blue, respectively).**

The forecasts of subsidence at each benchmark location since field shut-in (2008) based on the fitting procedure have been used to obtain gas induced subsidence maps for 2030. Figure 7-6 shows the total subsidence maps for the low, mid and high case by 2030. The maps have been generated using a convergent interpolation algorithm to grid up the forecasted subsidence at the benchmark locations (2008 – 2030) and adding to that the gas induced subsidence map for the period 1988 - 2008 (Figure 6-9). To be able to look at the effect of gas only, the fitting results have been corrected for autonomous subsidence using an average autonomous subsidence rate of 0.09 cm/yr. Note that the maps in Figure 7-6 to Figure 7-6 are only based on actual fit forecasts at the benchmark locations, indicated by the black symbols. In between these locations the forecast

value is determined by interpolation for the 2008 – 2030 subsidence forecast, and is therefore dependent on the algorithm of choice.

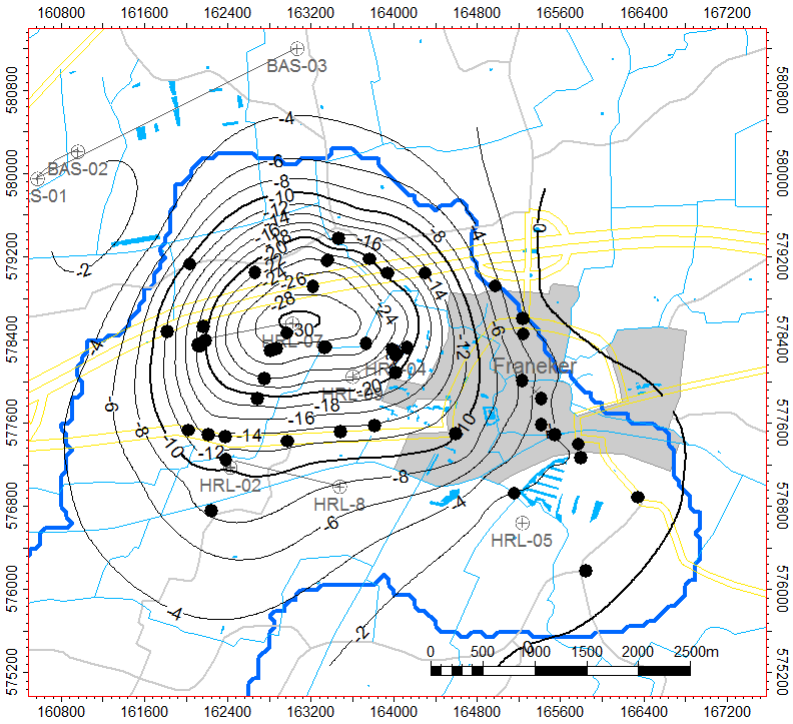

Figure 7-4 **Modelled plus forecasted gas induced subsidence in cm between 1988 and 2030 based on the fitting procedure for a low case fit. Black symbols indicate benchmark locations where the fit forecasts are available.**

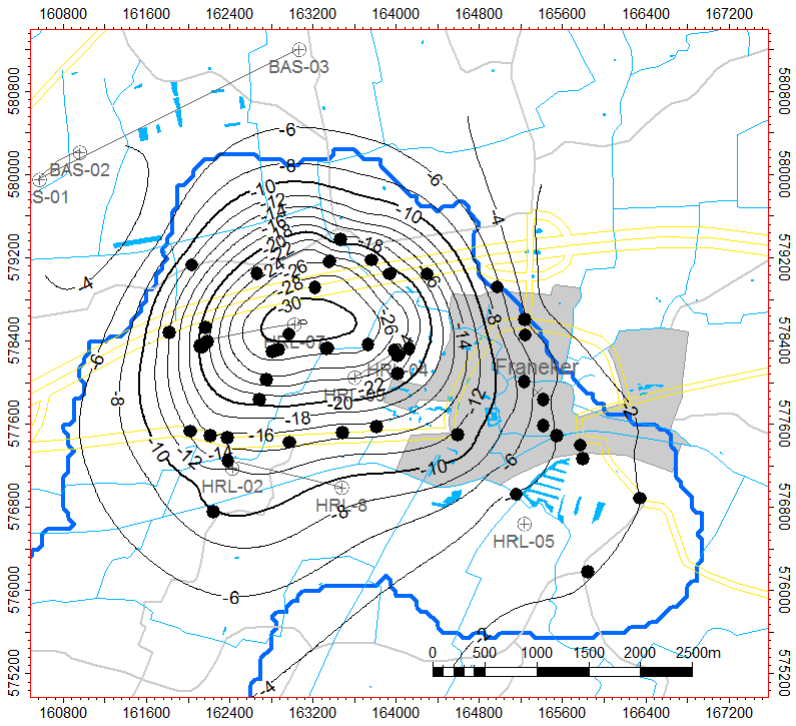

Figure 7-5 **Modelled plus forecasted gas induced subsidence in cm between 1988 and 2030 based on the fitting procedure for a mid case fit. Black symbols indicate benchmark locations where the fit forecasts are available.**

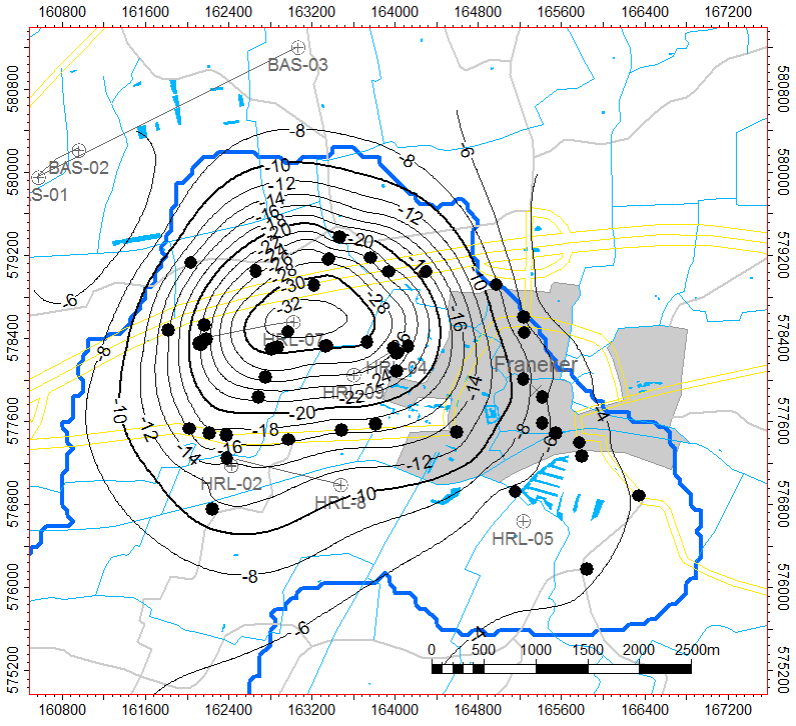

Figure 7-6 **Modelled plus forecasted gas induced subsidence in cm between 1988 and 2030 based on the fitting procedure for a high case fit. Black symbols indicate benchmark locations where the fit forecasts are available.**

7.4 SUBSIDENCE FORECAST UNCERTAINTIES

The subsidence model (presented in Chapter 6) and the fitting procedure (summarized in this chapter and explained in more detail in Appendix 8) are two alternative approaches to perform forecasting and their differences can be used as an illustration of the modelling uncertainties related to the subsidence predictions computed for 2030 (and reported in the map of Figure 7-1, subset a). Furthermore, the difference between the high and low case scenarios of the fit gives an indication of the measurement uncertainties that should also be taken in account when predicting the subsidence.

The main outputs of the two forecasting approaches are summarized in Figure 7-7 where, for four representative benchmark locations, are shown:

- The measured subsidence values with error bars indicating the related 2 standard deviations (Section 3.1).
- The subsidence values coming for the subsidence model chosen for forecasting the post production period (Section 7.2).
- The forecasted subsidence values (y^{fit}) obtained by fitting the measured data, with the associated high- and low-case scenarios (y^{fit_high} and y^{fit_low}).

The fitted values (y^{fit})reported here differ from the ones of Section 7.3.1 for the fact that the average contribution of 0.09 cm/yr related to the autonomous subsidence (Section 3.3) has been added to the y^{ls} values to make them consistent with the model outputs.

It can be seen from the Figure 7-7 that in some locations the subsidence model forecasts more subsidence than the fitted curve (e.g. at benchmark locations labelled '005G0179' and '000A2754'), sometimes less ('005G0110') and sometimes both predictions are nearly overlapping ('0003004').

In order to take account of this spread in the forecasts, the ultimate uncertainty on the subsidence forecast was obtained by combining the standard deviation related to the difference between the two forecasting approaches (i.e. the model and the fit) and the standard deviation related to the difference between the fit based high-case and low-case scenarios. This resulted in a standard deviation (σ) that statistically propagates the model, the measures and the fit uncertainties. For each analyzed benchmark location, a model prediction within two times the value of such a standard deviation (2σ) was considered acceptable.

The procedure described above results in different uncertainty ranges at the benchmark locations. For example, as illustrated in Figure 7-8, at benchmark '0003004' the difference between the fit and the model outputs is relatively small, therefore the total forecast uncertainty is dominated by the difference between the fit based high- and low-case scenarios. This implies that, for this location, the measurement uncertainties resulted to be the main contribution to the 2σ estimate. On the other hand, at the '000A2754' station, the fit and the model outputs diverge substantially and therefore the ultimate forecast uncertainty is mainly controlled by this divergence.

A full overview of all the uncertainties estimated is given in the histogram of Figure 7-9, where the 2σ values are reported for all the analyzed benchmark stations (here ordered, as indicated in the second column of the tables in Appendix 1, according to the distance from the deepest point of the gas induced subsidence bowl modelled in 2008, which is shown in Figure 17-4).

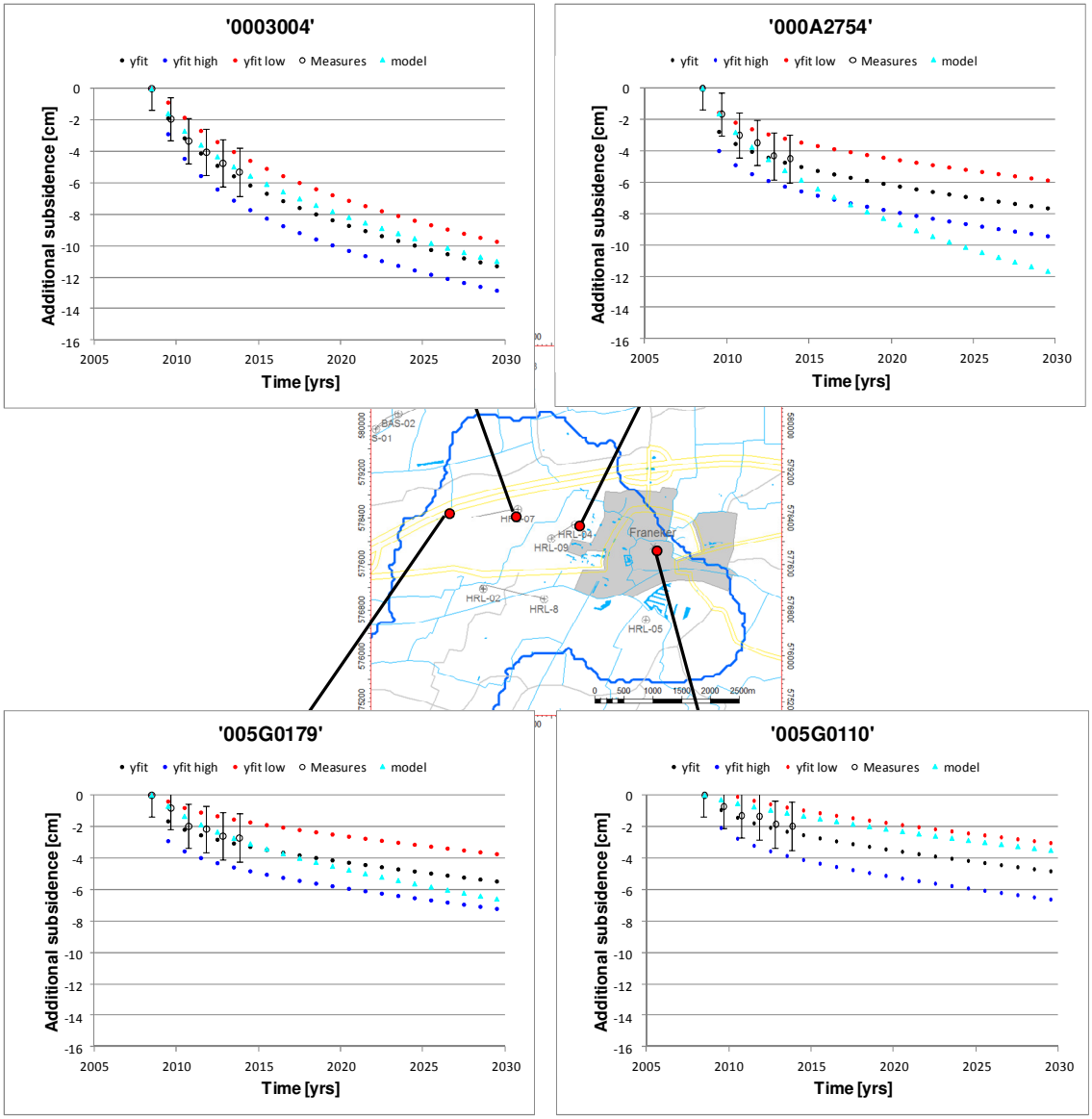

Figure 7-7 **Additional (since 2008) forecasted subsidence at selected benchmark locations according to the model and the fitting procedure. Subsidence shown is in cm since the time of shut-in (2008). Colours are for subsidence model (cyan), fit (black), fit-high case (blue) and fit low case (red).**

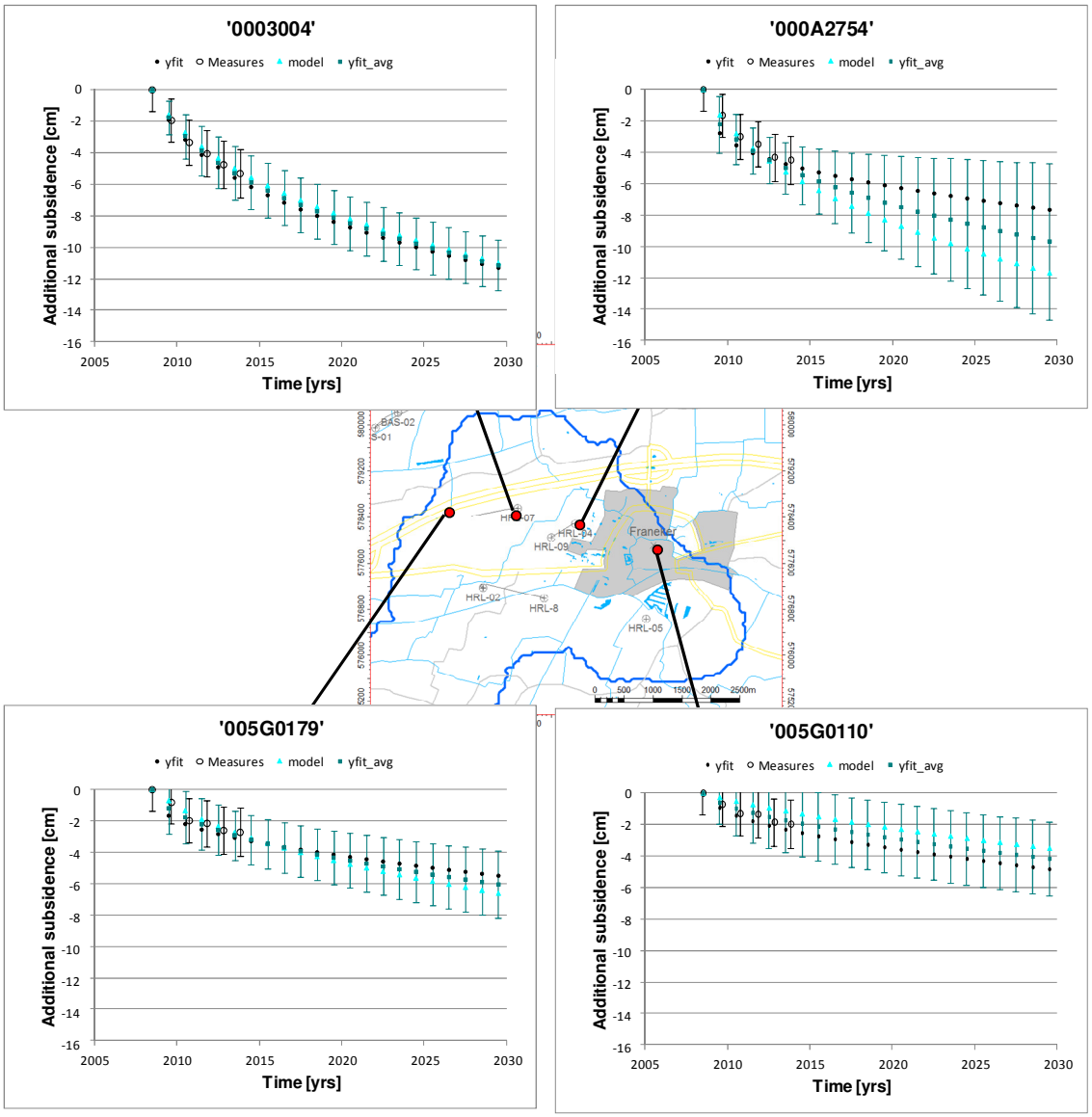

Figure 7-8 **Additional (since 2008) forecasted subsidence according to the model (cyan) and fitting procedure (black) with uncertainties (2σ error bars). Subsidence shown is in cm since the time of shut-in (2008). Error bars are displayed centred around the subsidence values obtained by averaging the outputs from the model and the fitting procedure.**

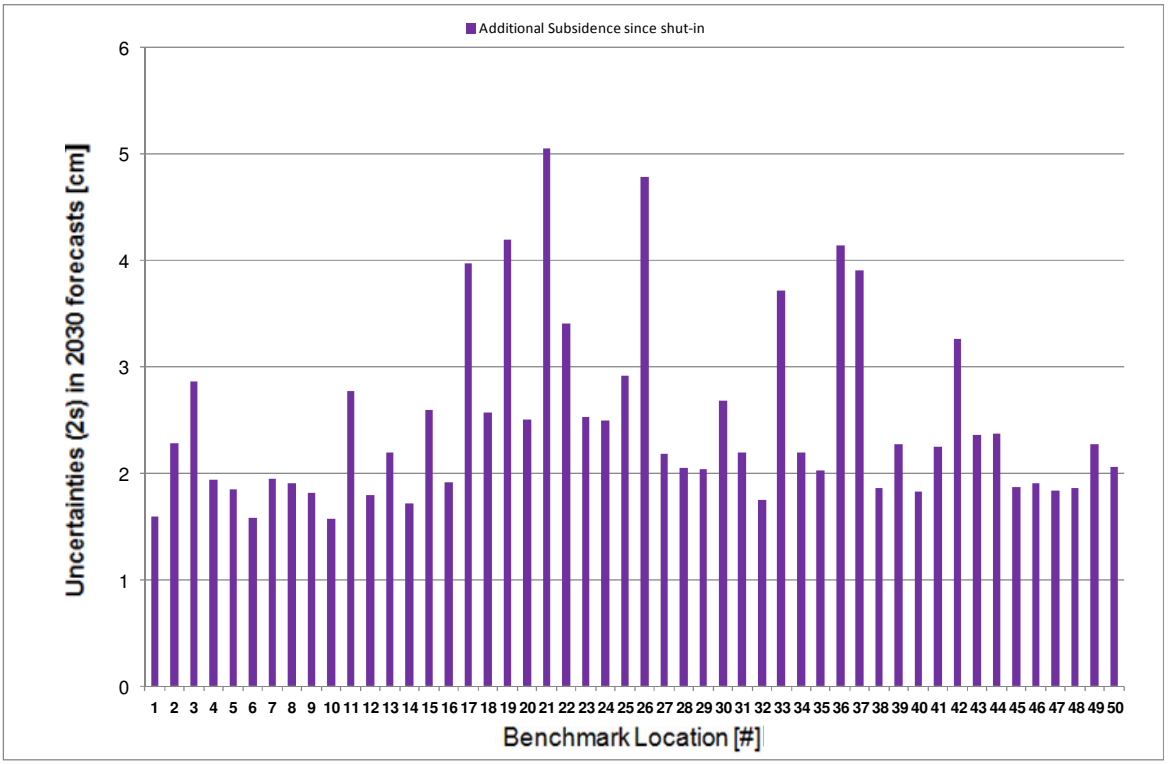

Figure 7-9 **Uncertainty on the additional (since 2008) forecasted subsidence at 2030 for the different benchmark locations. Locations are sorted according to increasing distance from the deepest point of the modelled gas induced subsidence bowl in 2008.**

As can be seen from the uncertainties reported in Figure 7-9, 2σ values range from less than 1.5 cm up to 5.0 cm, showing a quite uniform distribution with an average value of about 2.5 cm.

The 2σ uncertainties distribution across the field is shown in the map of Figure 7-10. It can be observed that almost all uncertainties surrounding the deepest point of the 2008 modelled gas induced subsidence bowl show values of less than 3 cm. A 2σ of about ± 3 cm can therefore be considered a reasonable uncertainty value when considering the maximum additional subsidence value obtained via the model forecast for 2030.

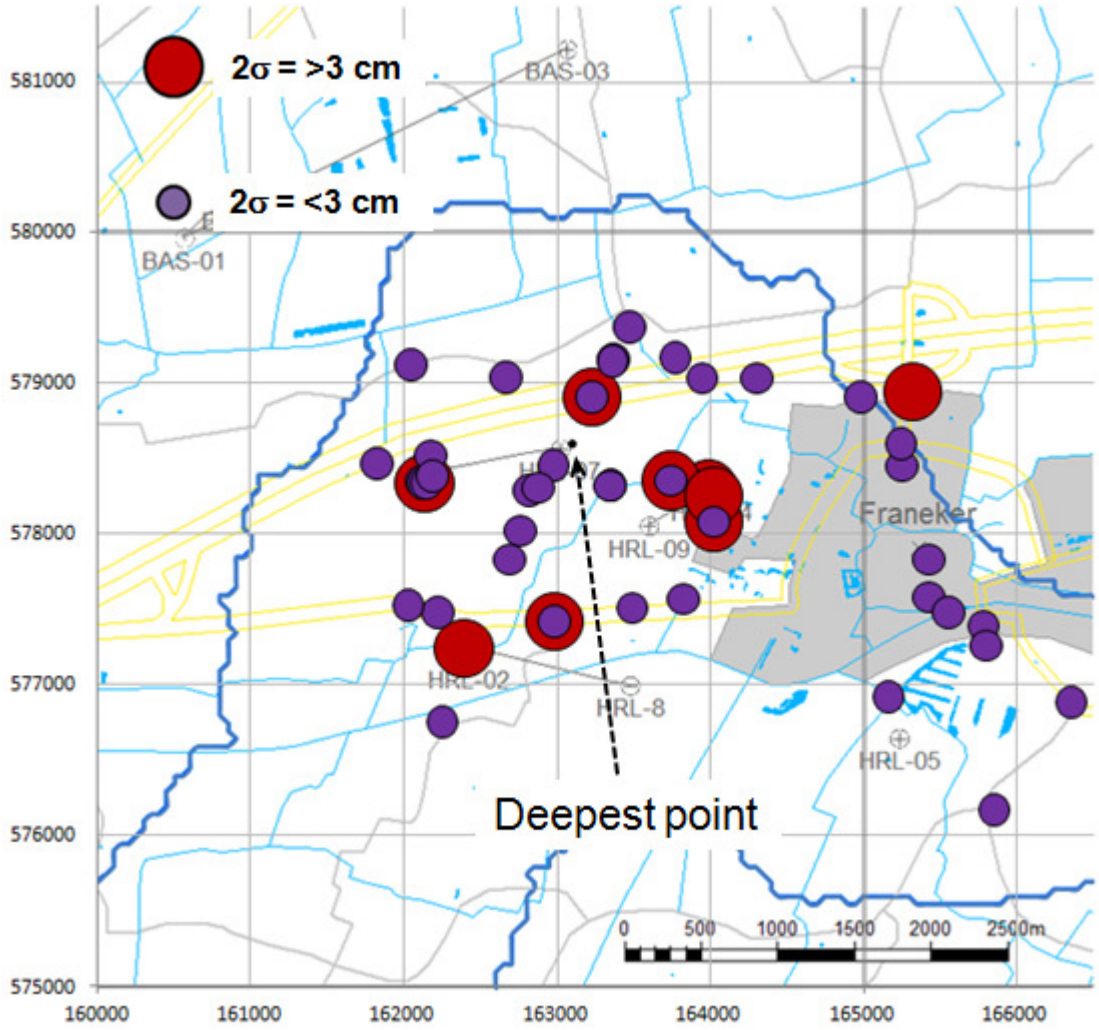

Figure 7-10 **Uncertainty on the additional (since 2008) forecasted subsidence at 2030. Uncertainty values for the benchmark locations greater and lower than 3 cm are indicated in red and purple, respectively. The deepest point of the modelled subsidence bowl in 2008 is also shown.**

Key outputs for significant locations are reported in Table 7-1, where the 2030 model and fit outputs are shown along with the 2σ uncertainties.

Table 7-1 **Uncertainties associated to the 2030 forecast of the additional subsidence that occurred since 2008. Subsidence values, from the model of Section 7.2, are indicated in the first column while in the second column the values obtained via the fitting procedure are shown.**

	Additional Subs. (model forecast) [cm]	Additional Subs. (fit forecast) [cm]	Additional Subs. 2σ Uncertainty [cm]
2030			
	Benchmark Location with Max Uncertainty (2σ)		
	11.8	7.7	5.1
	Benchmark Location with Min Uncertainty (2σ)		
	9.9	10.2	1.6
	Benchmark Location with Max Total Subsidence		
	11.1	11.4	1.6
	Benchmark Location with Max Add. Subsidence		
	12.2	10.3	2.8
	Benchmark Location with Min Total Subsidence		
	2.7	3.5	2.3
	Benchmark Location with Min Add. Subsidence		
	2.7	3.5	2.3
	Benchmark Location 0003004: Closest to the Deepest Point of the 2008 gas induced subsidence bowl		
	11.1	11.4	1.6

Based on the mean 2σ uncertainty characterizing the 2030 forecast of the additional subsidence occurring after the field shut-in (2008) for the entire field area, a similar exercise was performed to obtain an estimate of the uncertainty characterizing the forecast of total subsidence since the start of production in 1988. In order to achieve that, the above uncertainties (Figure 7-9) were combined with the ones characterizing the 2008 subsidence values. The 2008 uncertainties were, coherently with what was performed for the additional subsidence, obtained by combining the standard deviation related to the difference between the model and the measurements at that time and the measurement standard deviations (Appendix 8).

Results for significant locations are shown in Table 7-2.

Table 7-2 **Uncertainties associated to the 2030 forecast of the total subsidence that occurred since 1988. Subsidence values, from the model, are indicated in the first column while in the second are shown the values obtained via the fitting procedure.**

	Total Subs. (model forecast) [cm]	Total Subs. (fit forcast) [cm]	Total Subs. 2σ Uncertainty [cm]
2030			
	Benchmark Location with Max Uncertainty (2σ)		
	31.7	27.6	5.5
	Benchmark Location with Min Uncertainty (2σ)		
	31.8	32.1	2.3
	Benchmark Location with Max Total Subsidence		
	39.2	39.5	2.1
	Benchmark Location with Max Add. Subsidence		
	35.5	33.5	3.1
	Benchmark Location with Min Total Subsidence		
	5.0	5.8	2.9
	Benchmark Location with Min Add. Subsidence		
	5.0	5.8	2.9
	Benchmark Location 0003004: Closest to the Deepest Point of the 2008 gas induced subsidence bowl		
	39.2	39.5	2.1

The same procedures were applied to the 2050 forecast in order to evaluate when the autonomous subsidence rate will be achieved. By 2050 the subsidence rate has dropped to or below autonomous subsidence rate of 0.09 cm/year for most of the benchmark locations.

8 SUMMARY AND MAIN CONCLUSIONS

1) The measured subsidence above the Harlingen Chalk gas field is a combination of subsidence due to gas extraction from the Harlingen Chalk gas field, subsidence due to salt mining by Frisia in the Barradeel area to the north-west of the gas field and autonomous subsidence. Focus of the current work was to understand and model gas production induced subsidence.
2) The transition from chalk elastic to plastic behaviour via pore collapse, which was not anticipated in pre-2008 forecasts, is the most important cause of the higher than expected and sudden increase in compaction and surface subsidence.*
3) Extensive laboratory testing and measurements carried out by NGI on Harlingen Chalk samples, combined with literature data on similar rock types, have provided better understanding of the physical mechanism controlling the compaction behaviour of the reservoir rocks. They have led to identification of reasonable ranges for Harlingen Chalk rock mechanical properties, and have resulted in a model for compaction calculation as a function of reservoir porosity and pressure development.
4) Subsidence modelling in the area above the Harlingen Chalk gas field for the production period 1988-2008 shows a reasonable fit with benchmark-measured subsidence in the area. On average the sum of gas induced, salt-mining induced and autonomous subsidence falls within the uncertainty band (2 sigma) of the benchmark measurements.
5) A critical indicator for the performance of the entire model is the match of the subsidence model around the deepest point of the bowl at the time of field shut-in. The deepest point of the bowl is located near the reservoir section of well HRL-07. A good match of the subsidence in the deepest part of the bowl was achieved after including a modification to the originally reported gas offtake in well HRL-07 based on Vermilion's recommendation after a thorough data investigation.
6) Based on the subsidence model, gas induced subsidence contributed a maximum of 23 cm to the total depth of the subsidence bowl at the time of shut-in in 2008 and the total maximum subsidence, including salt induced and autonomous subsidence, amounted to 30 cm.
7) A comparison of this study's results to the analysis of benchmark levelling data performed by Houtenbos in 2010 [11] and subsidence maps prepared by Muntendam-Bos et al. in 2009 [15] based on a combination of interpolated benchmark and satellite measurement data shows consistency of the resulting subsidence maps in terms the shape and position of the bowl. According to Houtenbos [11] the total maximum subsidence was 26 cm over the deepest point of the Harlingen subsidence bowl in 2009, and at least 26.5 cm in 2008 according to Muntendam-Bos et al. [15].
8) Post shut-in, time dependent creep is dominating the compaction of the chalk reservoir, leading to continued surface subsidence.**
9) The additional gas induced subsidence modelled for the period between field shut-in and 2014 amounts to a maximum of 5 cm. Therefore, by 2014 the modelled gas induced subsidence amounted to a maximum gas induced subsidence of 28 cm.
10) If the field would not have been shut-in and gas production would have continued at late average gas production rates this would have resulted in a maximum gas induced subsidence of ~32 cm by 2014. This is approximately 4 cm more subsidence in the deepest point compared to the situation as of 2014.
11) Forecast models to predict future subsidence show that, if there would be no further production from the Harlingen Chalk gas field, a maximum additional (post-2008) total subsidence of 12 cm ± 3 cm is expected in the year 2030. The maximum total subsidence includes the salt contribution and autonomous subsidence.
12) By 2030 the maximum total subsidence (gas and salt production induced subsidence + autonomous subsidence) since the start of the production in 1988 amounts to ~42 cm ± 3 cm in the location of the deepest point of the subsidence bowl. In some areas of the field the uncertainty is higher, up to ± 6 cm.
13) After 2030, the gas production induced subsidence is expected to continue with a rate higher than the autonomous subsidence rate. By 2050 the autonomous subsidence rate is expected to become the dominant effect in most areas of the field.

* A sudden significant increase in rock compressibility after a given amount of pressure depletion

** Continued compaction at constant stress

9 REFERENCES

1. BECi, 2007. Analysis of leveling survey, v3, September 2006.
2. Chen, Q., Kinzelbach, W., Ye, C., and Yue Y., 2002. Variations of Permeability and Pore Size Distribution of Porous Media with Pressure. J. Environ. Qual., Vol. 31, p. 500-505.
3. Collin, F., Cui, Y. J., Schroeder, C. and Charlier, R., 2002. Mechanical behaviour of Lixhe chalk partly saturated by oil and water: experiment and modeling, International Journal for Numerical and Analytical Methods in Geomechanics; 26:897–924 (DOI: 10.1002/nag.229).
4. De Waal, J.A., 1986. On the Rate Type Compaction Behaviour of Sandstone Reservoir Rock. PhD Thesis, 166 pages.
5. Duin, E.J.T., Doornebal, J.C., Rijkers, R.H.B., Verbeek, J.W. and Wong, T. E., 2006. Subsurface structure of the Netherlands – results of recent onshore and offshore mapping. Geologie en Mijnbouw, 85, p. 245-276.
6. Fabricius, I. L., G. T. Bachle, and G. P. Eberli, 2010. Elastic moduli of dry and water-saturated carbonates: Effect of depositional texture, porosity, and permeability: Geophysics, 75, no. 3, N65–N78 (DOI: 10.1190/1.3374690).
7. Fokker, P., 2008. AEsubs – General Description and Quick User Guide.
8. Geertsma, J., 1966. Problems of Rock Mechanics in Petroleum Production Engineering. Proceedings 1st Congress of the International Society of Rock Mechanics, Lisbon, I, 585.
9. Heggheim, T., Madland, M.V., Risnes, R., and Austad, T., 2005. A chemical induced enhanced weakening of chalk by seawater. Journal of Petroleum Science and Engineering 46, pp. 171-184.
10. Hickman, R. J., 2004. Formulation and Implementation of a Constitutive Model for Soft Rock. PhD Thesis.
11. Houtenbos, A.P.E.M., 2010. Bodemdaling NW-Friesland 1976-2009, 38 pages.
12. Korsnes, R.I., Madland, M.V., and Austad, T., 2006. Impact of brine composition on the mechanical strength of chalk at high temperature. EUROCK 2006 Van Cotthem, Charlier, Thimus & Tshibangu (eds), pp. 133-140.
13. Leroueil, S., 2006. The isotache approach. Where are we 50 years after its development by Professor Šuklje? 2006 Prof. Šuklje's Memorial Lecture.
14. Madland M.V. 2005. Water weakening of chalk: A mechanistic study. Dr. Ing. Thesis, University of Stavanger, ISBN: 82-7644-257-9, JCR.
15. Muntendam-Bos, A.G., Hanssen, R.F., van Thienen-Visser, K., Samieie-Esfahany, S., 2009. PS-InSAR-analyse van de bodemdaling in Noordwest-Friesland. TNO report TNO-034-UT-2009-02318/A, 116 pages.
16. Muntendam-Bos, A.G., Breunese, J., van Thienen-Visser, K., Peters, L., Juez-Larre, J., 2012. Toestsing van de belasting op de gebruiksruimte in de kombergingsgebieden Pinkegat en Zoutkamperlaag door bodemdaling ten gevolge van gaswinning onder de Waddenzee. TNO report TNO-060-UT-2011-02035/c, 106 pages.

17. NGI, 2007. Uniaxial Compression Coefficient of Chalk – Compressibility of Harlingen Chalk 20071135-1-R.
18. NGI, 2009a. Harlingen chalk triaxial compaction experiments: Uniaxial strain tests and isotropic tests on brine saturated chalk, 20091179-00-1-R.
19. NGI, 2009b. Time dependent deformation of Harlingen chalk, 20092206-00-3-TN.
20. NGI, 2011a. Rate and fluid effects on chalk mechanical behavior, 20100236-00-1-R.
21. NGI, 2011b. Harlingen Upper Cretacious Investigation - Technical Committee. Development of conceptual model for compaction analysis, 20100377-00-2-R.
22. NGI, 2013. Revised Chalk Model - Harlingen revised compaction model, 20120191-01-R.
23. Oranjewoud, 2007. Peilmerkdaling nabij Franeker in de periode 1988-2006.
24. Orlic, B., Fokker, P., 2006. Subsidence Study Harlingen Field. TNO report 2006-U-R0102/C, 39 pages.
25. Pasachalk, 2004. Mechanical Behavior of Partially and Multiphase Saturated Chalks Fluid-Skeleton Interaction: Main Factor of Chalk Oil Reservoirs Compaction and Related Subsidence –Part 2, Final Report, EC Contract no. ENK6-2000-00089.
26. Priol G., 2005. Comportement mécanique différé et mouillabilité d'une craie pétrolifère. Thèse de l'Ecole nationale des ponts et chaussées.
27. Samieie-Esfahany, S., Hanssen, R.F., van Thienen-Visser, K., Muntendam-Bos, A., 2009. On the effect of horizontal deformation on InSAR subsidence estimates. Proceedings Fringe 2009 Workshop, Frascati, Italy, ESA SP-677.
28. Schroeder, C., Fourmaintraux, D., and Bois, A.P, 2009. Waterflooding experiments on Harlingen gas saturated chalk, Power Point presentation from Meeting Den Haag 6th January.
29. Smits, R.M.M., de Waal, J.A., van Kooten, J.F.C., 1988. Prediction of Abrupt Reservoir Compaction and Surface Subsidence Caused by Pore Collapse in Carbonates, SPE Formation Evaluation, June.
30. Spinler, E.A., and Hedges, J.H., 1995. Variation in the electrical behavior of the ekofisk field in the North Sea, 1995. SCA Conference Paper number 9516.
31. Taylor, J. R., 1982. An introduction to uncertainty analysis: the study of uncertainties in physical measurements. Mill Valley: University Science Books.
32. TotalFinaElf E&P Nederland B.V., 2003: HAR-9 well Basic Petrophysical measurements and Capillary Pressure measurements by Mercury injection, G/W Restored States and G/W Centrifugation. DGEP/GSR/TG/COP/LABO 03-037, 117 pages.
33. Total E&P Nederland B.V., 2004. Aanvraag instemming winningsplan ingevolge Mijnbouwwet artikel 34. Voorkomen: Harlingen Upper Cretaceous., 26 pages.
34. Van Dalfsen, W., Van Gessel, S.F., Doornenbal, J.C., 2007. Velmod-2, Joint Industry Project. TNO report 2007-U-R1272C, 97 pages.
35. Van den Bosch, W.J., 1983: The Harlingen Field, the only gas field in the Upper Cretaceous Chalk of the Netherlands. Geologie en Mijnbouw, 62, p. 145-156.
36. Van der Molen, A., 2004. Sedimentary development, seismic stratigraphy and burial

compaction of the Chalk Group in the Netherland North Sea area. PhD thesis, University Utrecht, 175 pages.

37. Van der Molen, A.S., Wong, Th. E., 2007. Towards an improved lithostratigraphic subdivision of the Chalk Group in the Netherlands North Sea area – A seismic stratigraphic approach. Geologie en Mijnbouw, 86, 131-143.
38. Van Ditzhuijzen, P.J.D., de Waal, J.A., 1984. Reservoir compaction and surface subsidence in the Central Luconia gas bearing carbonates, offshore Sarawak. Proc. 5th Offshore South East Asia Conference, Singapore.
39. Van Opstal, G.H.C., 1974. The effect of base-rock rigidity on subsidence due to reservoir compaction. Proc. 3rd Congr. of the Int. Soc. of Rock Mech., Denver, II, Part B, 1102-1111.
40. Vermeer, P.A., Naher, H.P., 1999. A soft soil model that accounts for creep. Beyond 2000 in Computational Geotechnics – 10 Years of Plaxis International.
41. Vermilion Oil & Gas Netherlands B.V., 2007. Subsidence Study – Harlingen Upper Cretaceous (Chalk) Reservoir. 127 pages.
42. Vermilion Oil & Gas Netherlands B.V, 2014. Harlingen-7 Modified Offtake Rate, 1 page.
43. www.nlog.nl

10 APPENDIX 1

10.1 BECNHMARK LOCATIONS AND MEASUREMENTS

The following tables in this chapter show the 340 available benchmarks:

- Serial number
- Benchmark number
- Fitted benchmark location (see Chapter 7)
- X-location
- Y-location
- Benchmark measurements for the time period 1988 to 2013

#	Benchmark Number	Fitted Benchmark Location #	X	Y	Measurements in m												
					1988	1992	1997	2000	2003	2003	2006	2007	2008	2009	2010	2011	2012	2013
1	0000001		160514	580010			0.8138	0.6804	0.5836		0.5210	0.5110	0.5136	0.5117	0.5053	0.5071	0.5049	0.5080
2	0000002		160542	579965			0.9516	0.8201	0.7212		0.6575	0.6468	0.6480	0.6460	0.6395	0.6409	0.6387	0.6410
3	0000006		161550	580114			0.8404	0.7311										
4	0000007		161800	580300			0.5341	0.4455	0.3695									
5	0000008		162196.77	580386.03			1.1873	1.1292	1.0770		1.0066	0.9884	0.9818	0.9689	0.9591	0.9586	0.9539	0.9546
6	0000009		162266.01	580914.76			0.9390	0.8996	0.8605		0.7906	0.7684	0.7599	0.7463	0.7346	0.7334	0.7295	0.7305
7	0000010		158500.42	580307.53			1.0507	1.0334	1.0103		1.0023	0.9931	0.9960	0.9949	0.9899	0.9909	0.9886	0.9928
8	0000011		158810.43	580870.53			1.3982	1.3737	1.3452		1.3313	1.3210	1.3231	1.3210	1.3154	1.3158	1.3147	1.3173
9	0000012		159313.91	581609.55			1.4216	1.3993	1.3737		1.3596	1.3509	1.3541	1.3508	1.3464	1.3470	1.3457	1.3479
10	0000013		160060.99	582142.24			1.3388	1.3199	1.2956		1.2810	1.2747	1.2767	1.2729	1.2694	1.2699	1.2683	1.2705
11	0000014		158861.88	580019.57			2.2071	2.1725	2.1405		2.1175	2.1077	2.1101	2.1072	2.1015	2.1022	2.0995	2.1018
12	0000015		159203.23	579347.3			2.0835	2.0402	2.0028		1.9768	1.9677	1.9700	1.9667	1.9623	1.9630	1.9609	1.9647
13	0000016		161006.23	581257.09			0.6527	0.5810	0.5168		0.4699	0.4574	0.4571	0.4510	0.4439	0.4432	0.4405	0.4438
14	0000017		160702.51	581826.16			1.3251		1.2511		1.2230	1.2135	1.2136	1.2086	1.2035	1.2043	1.2026	1.2040
15	0000018		161910	579340			-0.5785	-0.6603										
16	0000019		160250	578730			1.0136	0.9556	0.9044									
17	0000020		159582.18	577893.65			-0.9513	-0.9651	-0.9831		-0.9901	-0.9959	-0.9944	-0.9937	-0.9997	-0.9984	-1.0000	-0.9977
18	0000021		160107.22	578341.56			0.8381	0.8043	0.7689		0.7447	0.7379	0.7395	0.7380	0.7324	0.7323	0.7302	0.7314
19	0000022		159605.85	577485.99			0.1180	0.1099	0.0998		0.0962	0.0909	0.0921	0.0937	0.0884	0.0899	0.0882	0.0909
20	0000023		160113.36	578534.29			0.0845	0.0386	-0.0042		-0.0383	-0.0465	-0.0455	-0.0478	-0.0531	-0.0523	-0.0544	-0.0541
21	0000024		160366.39	579281.68			-0.5461	-0.6435	-0.7224		-0.7713	-0.7802	-0.7809	-0.7795	-0.7867	-0.7848	-0.7875	-0.7849
22	0000027		161193.65	580181.16			0.4623	0.3386	0.2419		0.1740	0.1629	0.1615	0.1577	0.1510	0.1527	0.1495	0.1515
23	0000028		160961.45	580024.87			0.6290	0.4982	0.3966		0.3329	0.3237	0.3224	0.3188	0.3141	0.3159	0.3134	0.3158
24	0000029		158160.04	579092.2			0.8350	0.8257	0.8115		0.8048	0.7982	0.8007	0.7988	0.7951	0.7956	0.7938	0.7981
25	0000030		158612.14	579819.98			1.4688	1.4442	1.4224		1.4079	1.3978	1.4007	1.3981	1.3940	1.3945	1.3921	1.3961
26	0000032		160661.71	582822.34			-0.0271	-0.0344	-0.0488		-0.0521	-0.0588	-0.0556	-0.0596	-0.0619	-0.0613	-0.0633	-0.0608
27	0000033		160400.08	579735.41			-0.3957	-0.5156	-0.6097		-0.6653	-0.6746	-0.6748	-0.6749	-0.6805	-0.6789	-0.6811	-0.6778
28	0000034		160770	579950			-0.2648	-0.3958	-0.4978									
29	0000035		160334.66	579476.22			-0.2080	-0.3150	-0.4007		-0.4527	-0.4620	-0.4619	-0.4617	-0.4684	-0.4666	-0.4691	-0.4665
30	0000036		160516.92	580297.93			0.2161	0.0898	-0.0060		-0.0658	-0.0765	-0.0731	-0.0753	-0.0814	-0.0805	-0.0823	-0.0792
31	0000039		160540	579880			1.2464	1.1147	1.0144		0.9503	0.9403	0.9410	0.9390				
32	0000040		158264.89	576408.17				0.7789	0.7765		0.7816	0.7760	0.7768	0.7752	0.7749	0.7760	0.7755	0.7773
33	0000041		157771.31	576407.31				0.8633	0.8610		0.8647	0.8608	0.8619	0.8641	0.8594	0.8623	0.8614	0.8633
34	0000042		161434.38	583687.12				1.4386	1.4306		1.4311	1.4244	1.4256	1.4231	1.4208	1.4200	1.4190	1.4214
35	0000043		161170	583350				1.6113	1.5986		1.5999							
36	0000045		157682.14	578237.03				5.6120	5.6042		5.5888	5.5881	5.5884	5.5810	5.5790	5.5814	5.5778	5.5802
37	0000046		157517.26	577812.18				6.1460	6.1440		6.1392	6.1383	6.1428	6.1368	6.1350	6.1396	6.1369	6.1402
38	0000047		157157.46	577450.13				2.9451	2.9427		2.9408	2.9370	2.9416	2.9360	2.9337	2.9378	2.9352	2.9366
39	0000048		157210	577284				4.1646	4.1632		4.1623	4.1594	4.1623	4.1584				
40	0000049		164160	582270				-0.7551	-0.7577		-0.7641	-0.7774		-0.7907				

#	Benchmark Number	Fitted Benchmark Location #	X	Y	Measurements in m												
					1988	1992	1997	2000	2003	2003	2006	2007	2008	2009	2010	2011	2012	2013
41	0000050		164198.78	581303.32				0.7703	0.7669		0.7475	0.7292	0.7226	0.7099	0.6969	0.6929	0.6869	0.6855
42	0000051		163835.2	581110.85				-0.7147	-0.7197		-0.7547	-0.7762	-0.7834	-0.7983	-0.8114	-0.8150	-0.8182	-0.8180
43	0000052		163458.63	580499.93				0.9979	0.9852		0.9431	0.9199	0.9121	0.8977	0.8858	0.8838	0.8794	0.8804
44	0000053		163261.14	581315.34				-0.0821	-0.0948		-0.1522	-0.1799	-0.1899	-0.2079	-0.2217	-0.2243	-0.2280	-0.2288
45	0000054		163044.52	582096.23				0.7727	0.7479		0.7144	0.6938	0.6889	0.6764	0.6656			
46	0000055		162747.25	582691.15				-0.5591	-0.5668		-0.5819	-0.5943	-0.5982	-0.6041	-0.6112	-0.6125	-0.6157	-0.6143
47	0000056		160787.47	581624.82				1.1602	1.1138		1.0818	1.0712	1.0718	1.0677	1.0611	1.0611	1.0590	1.0619
48	0000058		158540	577080				0.5090	0.5051									
49	0000059		157020	576730				1.7929	1.7917		1.7945							
50	0000060		162310	583300				1.8077	1.8014									
51	0000062		159446.35	579718.67				1.6003	1.5447		1.5098	1.5020	1.4988	1.4969	1.4964	1.4979	1.4956	1.5006
52	0000063		160588.68	579874				1.1760	1.0767		1.0155	1.0062	1.0071	1.0056	1.0008	1.0018	1.0003	1.0037
53	0000065		158406.19	576894.42					0.7709		0.7754	0.7698	0.7707	0.7692	0.7685	0.7704	0.7694	0.7710
54	0000066		164529.8	581341.99					0.6013		0.5887	0.5743	0.5667	0.5549	0.5413	0.5351	0.5268	0.5215
55	0000067		163771.71	581917.59					0.8774		0.8507	0.8328	0.8269	0.8133	0.8026	0.7993	0.7953	0.7951
56	0000068		163777.02	581935.22					0.6138		0.5848	0.5657	0.5613	0.5473	0.5366			
57	0000069		161470	580065					0.8198		0.7545	0.7407	0.7391					
58	0000070		162054.7	579394.04					-0.5166		-0.5776	-0.5945	-0.5989	-0.6062	-0.6193	-0.6225	-0.6282	-0.6285
59	0000071		162871.69	580714.84					0.6193		0.5510	0.5243	0.5134	0.4952	0.4826	0.4819	0.4776	0.4775
60	0000072		163332.81	581011.64					-0.0578		-0.1136	-0.1408	-0.1499	-0.1681	-0.1820	-0.1845	-0.1885	-0.1879
61	0000073		163092.05	581833.48					0.5760		0.5313	0.5079	0.5011	0.4833	0.4714	0.4692	0.4667	0.4677
62	0000074		163690.26	581595.99					-0.1593		-0.1958	-0.2176	-0.2256	-0.2408	-0.2535	-0.2571	-0.2601	-0.2602
63	0000075		161774.32	579349.12					-0.2647		-0.3265	-0.3403	-0.3431	-0.3491	-0.3601	-0.3619	-0.3672	-0.3664
64	0000076		166530	582419					-0.2160		-0.2124	-0.2277		-0.2754				
65	0000077		165731.52	578534.45					0.4647		0.4617	0.4574	0.4575	0.4539	0.4504	0.4513	0.4470	0.4470
66	0000078		161867.77	579032.08							-0.5623	-0.5774	-0.5805	-0.5881	-0.6004	-0.6036	-0.6085	-0.6087
67	0000079		169780	583170							-0.0485	-0.0528		-0.0525				
68	0000081		167870	582875							0.0250	0.0183		0.0076				
69	0000082		167480	583398							-0.0096	-0.0175		-0.0280				
70	0000084		169780	583210							-0.0005	-0.0045		-0.0033				
71	0000086		160660	579990							-0.7205	-0.7314	-0.7338	-0.7368	-0.7441	-0.7434	-0.7467	-0.7457
72	0000101		166235	582193							0.2688	0.2528		0.2008				
73	0000102		166412	582066							0.4069	0.3907		0.3390				
74	0000103		166422	582041							0.3736	0.3564		0.3054				
75	0000104		163246	581360								0.1120	0.1032	0.0851	0.0718	0.0694	0.0603	0.0611
76	0000105		163244	581370								0.1836	0.1740	0.1561	0.1425	0.1400	0.1368	0.1379
77	0000106		163242	581380								0.0021	-0.0071	-0.0245	-0.0378	-0.0401	-0.0433	-0.0422
78	0000107		157028.68	576736.05								1.6661	1.6667	1.6674	1.6649	1.6681	1.6660	1.6684
79	0003001	2	163225	578909			1.4684	1.4302		1.3868	1.3191	1.2923	1.2807	1.2603	1.2434	1.2355	1.2269	1.2231
80	0003003	33	162386	577465			1.0699	1.0458		1.0217	0.9854	0.9707	0.9637	0.9515	0.9401	0.9356	0.9281	0.9257

#	Benchmark Number	Fitted Benchmark Location #	X	Y	Measurements in m													
					1988	1992	1997	2000	2003	2003	2006	2007	2008	2009	2010	2011	2012	2013
81	0003004	1	162976	578457			0.6871	0.6389		0.5894	0.5133	0.4880	0.4761	0.4557	0.4407	0.4326	0.4247	0.4182
82	0003005	6	162817	578290			0.5418	0.4966		0.4481	0.3775	0.3530	0.3414	0.3226	0.3085	0.3006	0.2917	0.2862
83	0003006	10	162760	578020			0.3855	0.3460		0.3052	0.2431	0.2219	0.2094	0.1927	0.1797	0.1718	0.1630	0.1578
84	0003009		167950	576850			1.0384	1.0365		1.0378	1.0335							
85	0003010		163175	575427			0.9387	0.9375		0.9343	0.9237	0.9239	0.9217	0.9170	0.9155	0.9172	0.9149	0.9120
86	0003011		165476	576120			1.6602	1.6600		1.6569	1.6472	1.6469	1.6449	1.6417				
87	0003013		159990	574700			2.1446	2.1423										
88	0003014		164149	578571			0.8818	0.8610		0.8328	0.7744							
89	0003017	9	163370	579160									0.5171	0.4973	0.4826	0.4757	0.4676	0.4627
90	0003018		162750	578010									0.2533	0.2321	0.2213	0.2136	0.2046	0.1944
91	0003019	13	162690	577830									0.5342	0.5199	0.5063	0.4997	0.4913	0.4877
92	0003020	25	164020	578080									0.6929	0.6759	0.6623	0.6561	0.6473	0.6433
93	0003021	17	163987.64	578302.94									0.6447	0.6258	0.6126	0.6059	0.5971	0.5932
94	0003022	26	164130	578320									0.7718	0.7541	0.7403	0.7348	0.7261	0.7231
95	0003023	38	164980	578910									1.0186	1.0106	1.0044	1.0018	0.9970	0.9950
96	0003024	23	162120	578350									0.8343	0.8216	0.8086	0.8027	0.7952	0.7926
97	0003025		167867.9	576816.06									0.8823	0.8827	0.8789	0.8797	0.8795	0.8791
98	0003026	24	162123.16	578336.32									0.1986	0.1867	0.1731	0.1676	0.1602	0.1575
99	0003027	20	162146.65	578333.54									0.2485	0.2364	0.2219	0.2162	0.2080	0.2054
100	0003028	4	162873.45	578308.23									-0.1628	-0.1814	-0.1969	-0.2045	-0.2136	-0.2181
101	0003029		163333.59	578325.82									-0.6342	-0.6533	-0.6696	-0.6774	-0.7148	-0.7201
102	0003030	5	163349.5	578322.32									0.5141	0.4946	0.4787	0.4709	0.4618	0.4564
103	0003031	11	163738.98	578355.51									-0.2948	-0.3135	-0.3283	-0.3354	-0.3444	-0.3495
104	0003032	19	164021.12	578252.43									-0.0943	-0.1125	-0.1266	-0.1325	-0.1415	-0.1450
105	0003033	22	164036.74	578254.82									0.0460	0.0227	0.0092	0.0031	-0.0058	-0.0097
106	0004011		161873.6	583912.35				9.4939	9.4839		9.4804	9.4716	9.4745	9.4640	9.4660	9.4671		
107	0004012		161890.65	583890.67				1.3851	1.3765		1.3785	1.3741	1.3746	1.3731	1.3685	1.3699		
108	0004013		161939.35	583836.21				1.3216	1.2855		1.2842	1.2768	1.2777	1.2742	1.2693	1.2726		
109	0004021		159119.45	581459.32				9.5812	9.5517		9.5344	9.5256	9.5298	9.5212	9.5193	9.5199		
110	0004022		159139.38	581449.32				1.2988	1.2719		1.2590	1.2502	1.2529	1.2511	1.2461	1.2463		
111	0004023		159169.13	581418.74				0.0935	0.0641		0.0428	0.0344	0.0357	0.0309	0.0266	0.0285		
112	0004031		158004.53	579298.36				9.6297	9.6115		9.6024	9.5976	9.5995	9.5929	9.5891	9.5930		
113	0004032		158029.15	579286.87				1.2716	1.2568		1.2500	1.2469	1.2474	1.2443	1.2414	1.2429		
114	0004033		158031.78	579189.31				0.0552	0.0420		0.0383	0.0321	0.0342	0.0311	0.0288	0.0295		
115	0004041		163807	585272					9.1985			9.1915						
116	0004042		163813	585246					1.2528			1.2498						
117	0004043		163829	585206					0.2820			0.2782						
118	010E0072		161710	573620			0.6964	0.6933			0.6799							
119	010E0078		162700	574630			0.9008	0.8988			0.8914							
120	010E0115		161490	574900			0.7201	0.7192			0.7076							

#	Benchmark Number	Fitted Benchmark Location #	X	Y	Measurements in m												
					1988	1992	1997	2000	2003	2003	2006	2007	2008	2009	2010	2011	2012	2013
121	010E0132		161250	573680			1.0999	1.0992			1.0841							
122	010E0173		160300	574380			0.5046	0.5004			0.4756							
123	010E0183		160980	574180			0.6505	0.6480			0.6390							
124	000A2748		159820	577420	0.2058	0.2074	0.2039	0.1965	0.1857	0.1876	0.1827	0.1764	0.1775	0.1796	0.1722	0.1749	0.1733	0.1762
125	000A2750		162134.9	578338.21	0.2183	0.2155	0.1812	0.1372	0.0907	0.0945	0.0401	0.0215	0.0147	0.0032	-0.0113	-0.0158	-0.0239	-0.0255
126	000A2752	36	162390	577240	-0.0382	-0.0410	-0.0599	-0.0799		-0.0988	-0.1268	-0.1406	-0.1459	-0.1557	-0.1665	-0.1695	-0.1758	-0.1777
127	000A2754	21	164031.89	578256.33	0.0282	0.0216	-0.0004	-0.0231		-0.0567	-0.1181	-0.1416	-0.1558	-0.1733	-0.1878	-0.1936	-0.2028	-0.2055
128	000A2756		165150	576640	-0.1237	-0.1261	-0.1414	-0.1445		-0.1513	-0.1671	-0.1703	-0.1740	-0.1788	-0.1835	-0.1838	-0.1906	-0.1899
129	000A2758		168340	577120	-0.3983	-0.4005	-0.4064	-0.4066		-0.4078	-0.4092		-0.4110	-0.4090	-0.4129	-0.4124	-0.4125	-0.4124
130	000A2760		169320	578650	0.2840	0.2840	0.2840	0.2840		0.2840	0.2840	0.2840	0.2840	0.2840	0.2840	0.2840	0.2840	0.2840
131	000A2761	3	163340.18	578320.36									-0.3653	-0.3838	-0.4006	-0.4079	-0.4180	-0.4220
132	000A4020		156613.04	576552.19				6.9920	6.9920		6.9923	6.9866	6.9898	6.9881	6.9866	6.9868	6.9872	6.9884
133	005D0003		156837.89	576063.35				3.4054	3.4037		3.4041	3.4010	3.4015	3.3991	3.3979	3.4005	3.3988	3.4010
134	005D0004		157119.98	576281.4				1.7229	1.7208		1.7238	1.7212	1.7216	1.7223	1.7192	1.7215	1.7206	1.7226
135	005D0005		157186.54	576478.23				2.0142	2.0121		2.0145	2.0118	2.0134	2.0128	2.0103	2.0124	2.0112	2.0141
136	005D0007		157302.53	576983.16				2.1151	2.1127		2.1168	2.1129	2.1149	2.1140	2.1113	2.1140	2.1127	2.1158
137	005D0012		159006.84	577253.41			2.6677	2.6641	2.6606		2.6589	2.6538	2.6557	2.6526	2.6509	2.6537	2.6531	2.6543
138	005D0015		158756.53	578750.97			0.8797	0.8618	0.8438		0.8293	0.8218	0.8235	0.8203	0.8176	0.8169	0.8164	0.8193
139	005D0017		158794.91	579657.27			1.0988	1.0686	1.0433		1.0231	1.0157	1.0183	1.0150	1.0115	1.0126	1.0112	1.0131
140	005D0034		159309.04	579595.75			2.1257	2.0723	2.0230		1.9930	1.9839	1.9857	1.9825	1.9773	1.9778	1.9705	1.9765
141	005D0037		157116.93	576123.56				2.6978	2.6956		2.6997	2.6965	2.6976	2.6968	2.6945	2.6969	2.6955	2.6985
142	005D0038		157200	576560				2.3575	2.3545									
143	005D0039		159550	579140			1.2802	1.2273	1.1787									
144	005D0040		159818.12	578577.57			0.5180	0.4775	0.4384		0.4132	0.4027	0.4044	0.4013	0.3968	0.3970	0.3945	0.3948
145	005D0041		159560	577190	0.8937	0.8940												
146	005D0052		159780	577360	1.6254	1.6252												
147	005D0053		159612.38	580902.76			1.8260	1.7680	1.7168		1.6861	1.6765	1.6787	1.6751	1.6701	1.6704	1.6676	1.6716
148	005D0056		159061.68	580263.83			1.4728	1.4319	1.3926		1.3696	1.3602	1.3625	1.3611	1.3559	1.3574	1.3544	1.3582
149	005D0057		158017.96	579193.76				0.8397	0.8266		0.8225	0.8160	0.8181	0.8126	0.8142	0.8152	0.8137	0.8178
150	005D0059		159710.74	577441.39			1.8165	1.8082	1.7979		1.7949	1.7884	1.7905	1.7909	1.7860	1.7871	1.7860	1.7886
151	005D0064		159950	576630	0.5252	0.5229	0.5132	0.5075		0.5052	0.4970	0.4945	0.4950	0.4934	0.4891	0.4917	0.4902	0.4889
152	005D0066		157760.4	577159.98				2.2593	2.2563		2.2595	2.2548	2.2566	2.2547	2.2530	2.2548	2.2537	2.2571
153	005D0067		158484.5	577539.95			0.9837	0.9807	0.9751		0.9657	0.9609	0.9618	0.9583	0.9560	0.9568	0.9567	0.9584
154	005D0069		156720	576060							3.9708	3.9655	3.9670	3.9662	3.9629	3.9642	3.9633	3.9641
155	005D0070		158210	577760				5.4870	5.4815		5.4802	5.4747	5.4777	5.4732	5.4711	5.4731	5.4713	5.4746
156	005D0072		156634.43	576572.42				6.1419	6.1409		6.1402	6.1341	6.1365	6.1353	6.1330	6.1332	6.1334	6.1340
157	005D0073		156600	576550				6.0769	6.0720									
158	005D0074		158614.01	578078.86			1.0832	1.0740	1.0627		1.0577	1.0516	1.0533	1.0513	1.0482	1.0491	1.0484	1.0518
159	005D0078		159720	577110			0.6929	0.6873		0.6827	0.6794	0.6755	0.6748	0.6738	0.6688			
160	005D0081		156617.16	576559.61							6.4673	6.4617	6.4644	6.4628	6.4611	6.4620	6.4615	6.4627

#	Benchmark Number	Fitted Benchmark Location #	X	Y	Measurements in m													
					1988	1992	1997	2000	2003	2003	2006	2007	2008	2009	2010	2011	2012	2013
161	005D0082		158477.87	577002.97							0.6570	0.6502	0.6523	0.6500	0.6483	0.6505	0.6498	0.6518
162	005D0083		158030	578820							4.8100	4.8069	4.8082	4.7993	4.7967	4.7989	4.7960	4.7976
163	005D0084		159610	579060							2.0775	2.0677	2.0693	2.0667	2.0626	2.0629	2.0610	2.0639
164	005D0087		158550	578050							5.0000	4.9881	4.9878	4.9804	4.9738	4.9730	4.9698	4.9699
165	005D0088		159600	579110							2.0605	2.0508	2.0527	2.0502	2.0456	2.0465	2.0440	2.0473
166	005D0089		159550	577010								0.4710	0.4711	0.4702	0.4642	0.4689	0.4665	0.4682
167	005G0001		165340	575220							0.5268	0.5296	0.5281	0.5252	0.5250	0.5275	0.5247	0.5229
168	005G0004	39	162250	576750	0.7898	0.7798	0.7590	0.7429		0.7334	0.7032	0.6993	0.6913	0.6829	0.6741	0.6753	0.6698	0.6655
169	005G0007		161408.35	577505.86	-0.1537	-0.1544	-0.1655	-0.1836	-0.2038	-0.2006	-0.2211	-0.2284	-0.2310	-0.2345	-0.2438	-0.2448	-0.2492	-0.2487
170	005G0008	34	162220	577480	1.7316	1.7275	1.7083				1.6290	1.6165	1.6098	1.5968	1.5872	1.5842	1.5781	1.5739
171	005G0010	27	163490	577510	1.0720	1.0674	1.0440	1.0216		0.9966	0.9550	0.9396	0.9304	0.9173	0.9044	0.8985	0.8905	0.8866
172	005G0017		164980	578900	0.2363	0.2314												
173	005G0018		165319.37	578945.14	0.7408	0.7381	0.7331	0.7281	0.7211	0.7250	0.7154	0.7096	0.7079	0.7037	0.6990	0.6979	0.6940	0.6931
174	005G0019	42	165240	578000	1.7948	1.7893	1.7780	1.7682		1.7608	1.7413	1.7313	1.7273	1.7170	1.7104	1.7081	1.7022	1.6988
175	005G0020		167680	578280	1.5844	1.5787	1.5741	1.5717		1.5708	1.5663	1.5670	1.5659	1.5595	1.5621	1.5617	1.5606	1.5587
176	005G0021		169110	578510	1.0021	0.9981	0.9944	0.9923		0.9911	0.9862	0.9869	0.9860	0.9852	0.9860	0.9855	0.9859	0.9829
177	005G0026		167250	579130					3.8216		3.8208							
178	005G0028		160020.36	580120.99			1.3641	1.2602	1.1757		1.1252	1.1149	1.1178	1.1171	1.1105	1.1117	1.1099	1.1130
179	005G0032		165362.75	580215.79					1.0204		1.0220	1.0124	1.0089	1.0039	0.9955	0.9907	0.9827	0.9783
180	005G0033		165530.57	580158.47					2.6214		2.6238	2.6157	2.6131	2.6074	2.5996	2.5946	2.5864	2.5823
181	005G0034		166436.28	580513.88					1.2980		1.3017	1.2920	1.2850	1.2759	1.2626	1.2513	1.2371	1.2272
182	005G0035		166930	580970					3.1178		3.1191	3.1111		3.0857				
183	005G0036		160790	581620			1.2413							1.0999	1.0939	1.0936	1.0918	1.0940
184	005G0038		160909.69	581003.42			4.0794	3.9886	3.9148		3.8621	3.8504	3.8500	3.8458	3.8386	3.8392	3.8367	3.8400
185	005G0039		161419.57	581534.74			1.1630	1.1163	1.0716		1.0291	1.0135	1.0120	1.0045	0.9962	0.9951	0.9913	0.9937
186	005G0040		161500.16	581375.7			2.9859	2.9333	2.8845		2.8375	2.8198	2.8171	2.8087	2.8000	2.7988	2.7945	2.7972
187	005G0045		168530	581850							2.7598	2.7563		2.7514				
188	005G0049		162989.81	582334.86				0.8819	0.8754		0.8493	0.8319	0.8287	0.8184	0.8087	0.8065	0.8042	0.8055
189	005G0052		163260	583040				2.2322	2.2270		2.2234	2.2128		2.2063				
190	005G0053		164500	583250					2.0595		2.0585	2.0489		2.0391				
191	005G0054		165440	583400					3.7820		3.7834	3.7762		3.7608				
192	005G0057		165230	583960					1.8910		1.8932	1.8846		1.8792				
193	005G0063		163340	584070					1.8010		1.8046	1.7966		1.7945				
194	005G0065		164800	584960					0.8159		0.8145	0.8051		0.8022				
195	005G0071		167220	585970					2.2535			2.2530		2.2528				
196	005G0072		169230	585260							1.3246	1.3184		1.3168				
197	005G0085		163820	575480	3.5336	3.5316	3.5218											
198	005G0088		165660	576220	0.7532	0.7512	0.7396	0.7389		0.7324	0.7240	0.7239	0.7216					
199	005G0090		165030	575340	0.7970	0.7952	0.7875	0.7876		0.7867	0.7844	0.7851	0.7822	0.7823	0.7806	0.7826	0.7794	0.7804
200	005G0091	50	166350	576880	0.6362	0.6344	0.6222	0.6206		0.6164	0.6104	0.6051	0.6046	0.5998	0.5970	0.5974	0.5926	0.5910

#	Benchmark Number	Fitted Benchmark Location #	X	Y	Measurements in m													
					1988	1992	1997	2000	2003	2003	2006	2007	2008	2009	2010	2011	2012	2013
201	005G0092		165310	581640					1.5041		1.5041	1.4931		1.4607				
202	005G0093		165860	582320					1.1939		1.1955	1.1831		1.1374				
203	005G0097		168150	585350					1.9237			1.9257		1.9252				
204	005G0101		160970	575550			1.0188	1.0197		1.0185	1.0077	1.0090	1.0074	1.0044	1.0021	1.0030	1.0020	1.0036
205	005G0102		162400	575270	0.7213	0.7174	0.7138	0.7115		0.7102	0.7000	0.7021	0.7024	0.6978	0.6959	0.6960	0.6941	0.6946
206	005G0104		163070	575680	1.3349	1.3329	1.3253	1.3220		1.3189	1.3076	1.3055	1.3036	1.2970	1.2965			
207	005G0105		160120	576280	0.9990	0.9918												
208	005G0108	49	165850	576170	1.0835	1.0811	1.0706	1.0695		1.0669	1.0534	1.0531	1.0505	1.0450	1.0423	1.0455	1.0403	1.0385
209	005G0109	47	165780	577390	1.5996	1.5948	1.5809	1.5787		1.5734	1.5614	1.5540	1.5518	1.5444	1.5394	1.5387	1.5331	1.5312
210	005G0110	43	165420	577830	1.8886	1.8854	1.8749	1.8676		1.8627	1.8460	1.8383	1.8348	1.8266	1.8198	1.8184	1.8125	1.8103
211	005G0111		166020	577840	1.3559	1.3526	1.3445	1.3388		1.3350	1.3255	1.3182	1.3176	1.3119	1.3090	1.3008	1.2952	1.2924
212	005G0112		166740	578020	0.8411	0.8352	0.8297	0.8275		0.8270	0.8154	0.8179	0.8199	0.8107			0.8140	0.8087
213	005G0113		165072.22	581067.1					0.6038		0.6023	0.5916	0.5833	0.5738	0.5591	0.5495	0.5374	0.5304
214	005G0115		165360	583330					1.3802		1.3839	1.3752		1.3601				
215	005G0116		166450	583780					1.7644		1.7705	1.7625		1.7485				
216	005G0117		168380	584770					1.5217		1.5300	1.5241		1.5225				
217	005G0118		163770	585170					1.9649			1.9625		1.9629				
218	005G0122		162860	584580					0.1814			0.1811		0.1815				
219	005G0125	29	162980	577420	1.4223	1.4193	1.3945	1.3697		1.3453	1.3073	1.2914	1.2835	1.2710	1.2588	1.2536	1.2461	1.2433
220	005G0126	37	164600	577490	1.3427	1.3359	1.3213	1.3105		1.2981	1.2704	1.2585	1.2510	1.2389	1.2295	1.2251	1.2181	1.2132
221	005G0127	41	165250	578450	0.9971	0.9928	0.9833	0.9754		0.9689	0.9526	0.9450	0.9422	0.9335	0.9278	0.9260	0.9214	0.9191
222	005G0129		160391.01	580569.7			0.7379	0.6237	0.5360		0.4797	0.4697	0.4718	0.4692	0.4637	0.4654	0.4636	0.4659
223	005G0132		161898.25	583866.2				0.9194	0.9141		0.9171	0.9108	0.9115	0.9092	0.9063	0.9080	0.9054	0.9094
224	005G0135		165580	582770					1.6459		1.6495	1.6386		1.6084				
225	005G0138		169160	579220							1.0104	1.0089	1.0071	1.0039	1.0048	1.0048	1.0054	1.0036
226	005G0140		166120	579600							0.4699	0.4625	0.4637	0.4606	0.4553	0.4521	0.4470	0.4453
227	005G0142	14	163770.6	579171.88	0.9965	0.9902	0.9683	0.9451	0.9166	0.9209	0.8683	0.8443	0.8360	0.8171	0.8029	0.7964	0.7883	0.7845
228	005G0143	7	163360	579150			0.6947	0.6638		0.6303	0.5662	0.5439	0.5339	0.5138	0.4995	0.4924	0.4844	0.4791
229	005G0145	15	162174.5	578522.08	0.4169	0.4120	0.3742	0.3223	0.2709	0.2747	0.2114	0.1939	0.1844	0.1709	0.1574	0.1527	0.1455	0.1429
230	005G0153		166000	585540					1.0547			1.0534		1.0538				
231	005G0154		164010	584460					2.0367		2.0414	2.0318		2.0296				
232	005G0155		162920	583720					1.2118		1.2114	1.2042		1.2004				
233	005G0158		168270	579570							1.5783	1.5762	1.5744	1.5728	1.5703	1.5718	1.5697	1.5682
234	005G0160		164400	581490				1.0350	1.0340		1.0129	0.9977		0.9743				
235	005G0161		164240	582570				1.1768	1.1748		1.1704	1.1592		1.1482				
236	005G0164		160223.74	581415.32			1.4792	1.4233	1.3741		1.3397	1.3310	1.3315	1.3284	1.3223	1.3241	1.3215	1.3242
237	005G0165		160120	575510	0.2752	0.2686	0.2564	0.2533		0.2530	0.2444	0.2452	0.2452	0.2383	0.2381	0.2402	0.2384	0.2405
238	005G0166		161860	576200	0.3573	0.3539												
239	005G0167		160973.3	578730.41	0.8075	0.8081	0.7924	0.7264	0.6672	0.6712	0.6217	0.6130	0.6131	0.6108	0.6026	0.6028	0.6006	0.6018
240	005G0168	28	162042.84	579124.89	0.6330	0.6303	0.5946	0.5299	0.4670	0.4710	0.4076	0.3906	0.3853	0.3764	0.3638	0.3598	0.3544	0.3529

#	Benchmark Number	Fitted Benchmark Location #	X	Y	Measurements in m													
					1988	1992	1997	2000	2003	2003	2006	2007	2008	2009	2010	2011	2012	2013
241	005G0169		162720	579070	1.0216	1.0184	0.9777	0.9229	0.8683	0.8723								
242	005G0170		167000	576140	1.1003	1.0987	1.0900	1.0902		1.0896	1.0839		1.0838	1.0802	1.0790	1.0814	1.0790	1.0782
243	005G0177		167840	576580	1.5252	1.5115	1.5013	1.4993		1.5018	1.4934		1.4886	1.4788	1.4797	1.4846	1.4845	1.4762
244	005G0179	31	161827.8	578471.87	0.5098	0.5054	0.4763	0.4281	0.3797	0.3836	0.3324	0.3182	0.3131	0.3039	0.2913	0.2886	0.2832	0.2811
245	005G0180	18	163944.05	579035.5	0.8358	0.8300	0.8077	0.7870	0.7582	0.7625	0.7095	0.6858	0.6749	0.6577	0.6425	0.6367	0.6283	0.6255
246	005G0182		166100	579400							3.0017	2.9943	2.9937	2.9916	2.9878	2.9856	2.9842	2.9811
247	005G0183		167723.98	579313.33					0.9171		0.9222	0.9178	0.9192	0.9178	0.9143	0.9142	0.9127	0.9126
248	005G0184		169150	578970							1.4973	1.4955	1.4945	1.4938	1.4934	1.4935	1.4937	1.4935
249	005G0187		162734.76	580702.56			0.4941	0.4676	0.4399		0.3729	0.3463	0.3367	0.3217	0.3083	0.3067	0.3018	0.3030
250	005G0189		161767.71	581747.04			1.0447	1.0156	0.9847		0.9440	0.9262	0.9236	0.9147	0.9051	0.9044	0.8998	0.9021
251	005G0192		161540	575890	0.7096	0.7088												
252	005G0193		163020	575170			0.0175	0.0148										
253	005G0194		168630	578490	1.0705	1.0663	1.0658	1.0649		1.0634	1.0610	1.0634	1.0614	1.0606	1.0614	1.0604	1.0614	1.0597
254	005G0195	44	165420	577580	1.5364	1.5320	1.5204	1.5129		1.5066	1.4897	1.4818	1.4787	1.4700	1.4635	1.4613	1.4553	1.4530
255	005G0196		166100	578270	1.2414	1.2399	1.2359	1.2325		1.2317	1.2274	1.2229	1.2238	1.2199	1.2180	1.2184	1.2151	1.2145
256	005G0197	40	165242.02	578600.53	0.8765	0.8732	0.8656	0.8582	0.8503	0.8541	0.8398	0.8317	0.8289	0.8233	0.8167	0.8153	0.8105	0.8092
257	005G0198		162820	577060	5.2475	5.2403	5.2141	5.1899		5.1703								
258	005G0199	48	165800	577260	0.8739	0.8706	0.8566	0.8541		0.8484	0.8360	0.8306	0.8270	0.8210	0.8164	0.8152	0.8093	0.8078
259	005G0200		161219.72	578883.93	1.5269	1.5272	1.5069	1.4330	1.3676	1.3716	1.3155	1.3060	1.3067	1.3016	1.2934	1.2919	1.2890	1.2888
260	005G0201		163390	579350	0.5869	0.5846	0.5627	0.5369		0.5094	0.4601	0.4391	0.4312	0.4151	0.4001	0.3943	0.3864	0.3850
261	005G0203		164160	578600	0.8566	0.8254												
262	005G0204	30	163820	577570	0.9642	0.9578	0.9394	0.9212		0.8973	0.8576	0.8422	0.8334	0.8176	0.8071	0.8017	0.7933	0.7887
263	005G0205	35	162029.48	577523.61	1.4170	1.4106	1.3899	1.3661	1.3409	1.3446	1.3057	1.2907	1.2859	1.2658	1.2541	1.2510	1.2452	1.2424
264	005G0206		160695.56	577453.77	1.0668	1.0617	1.0512	1.0346	1.0185	1.0212	1.0045	0.9993	0.9981	0.9950	0.9897	0.9911	0.9883	0.9891
265	005G0207		160010	576450	2.4517	2.4523	2.4479	2.4445		2.4405	2.4393	2.4365	2.4372	2.4350	2.4313	2.4336	2.4315	2.4336
266	005G0208		160650	575470	0.9174	0.9158	0.9143	0.9121		0.9119	0.9034	0.9036	0.9037	0.9005	0.8983	0.8996	0.8984	0.9007
267	005G0209		164640	575350	-0.2817	-0.2826	-0.2893	-0.2892		-0.2904	-0.2953	-0.2936	-0.2965	-0.2970	-0.2994	-0.2973	-0.3006	-0.3002
268	005G0210	45	165160	576920	1.9325	1.9293	1.9114	1.9084		1.9001	1.8811	1.8757	1.8713	1.8642	1.8586	1.8558	1.8493	1.8481
269	005G0211		169390	578610	1.0887	1.0864	1.0839	1.0818		1.0825	1.0802	1.0796	1.0777	1.0749				
270	005G0212		169290	577800	0.8781	0.8745	0.8677	0.8687		0.8691	0.8669		0.8642	0.8655	0.8661	0.8654	0.8656	0.8650
271	005G0213		168900	577580	0.4498	0.4464	0.4391	0.4378		0.4377	0.4341		0.4323	0.4313	0.4326	0.4311	0.4324	0.4309
272	005G0214		168120	577250	1.0035	0.9991	0.9921	0.9908		0.9903	0.9852		0.9839	0.9846	0.9815	0.9817	0.9811	0.9810
273	005G0215		167360	576170	0.5463	0.5445												
274	005G0216		169680	578140	1.1591	1.1580	1.1549	1.1564		1.1575	1.1576		1.1547	1.1553	1.1563	1.1559	1.1567	1.1562
275	005G0217		165020	578930		1.9181	1.9084	1.8997	1.8874	1.8914	1.8709							
276	005G0218		164700	578870		0.8350	0.8218	0.8092			0.7634	0.7476	0.7403	0.7277	0.7182	0.7146	0.7078	0.7064
277	005G0219	16	162188.96	578388.74		1.2033	1.1514	1.0998	1.0491	1.0529	0.9902	0.9712	0.9620	0.9483	0.9340	0.9282	0.9202	0.9168
278	005G0220		161620	575890		0.9702	0.9668	0.9625		0.9584	0.9482	0.9500	0.9484	0.9452	0.9414	0.9409	0.9377	0.9402
279	005G0221		162440.23	582446.38				-0.0385	-0.0534		-0.0799	-0.0943	-0.0981	-0.1066	-0.1157	-0.1175	-0.1216	-0.1205
280	005G0223		168950	584260							0.6907	0.6849		0.6843				

#	Benchmark Number	Fitted Benchmark Location #	X	Y	Measurements in m													
					1988	1992	1997	2000	2003	2003	2006	2007	2008	2009	2010	2011	2012	2013
281	005G0224		168310	582420							-0.0475	-0.0519		-0.0589				
282	005G0227	12	163472.31	579371.11			0.9866	0.9615	0.9320	0.9362	0.8873	0.8660	0.8582	0.8410	0.8271	0.8214	0.8140	0.8112
283	005G0228		161880.45	580910.85			0.5855	0.5262	0.4711		0.4077	0.3883	0.3834	0.3727	0.3624	0.3609	0.3568	0.3594
284	005G0230		165680	583440					1.6459		1.6518	1.6423		1.6250				
285	005G0231		164050	583150				1.3016	1.2988		1.2995	1.2900		1.2829				
286	005G0232		164400	584800					1.1371		1.1470	1.1366		1.1359				
287	005G0233		165310	585260					1.6832			1.6789		1.6806				
288	005G0234		163820	575480				2.8175		2.8137	2.8065	2.8046	2.8021	2.7970	2.7938	2.7944	2.7913	2.7901
289	005G0235		161860	576200			0.1428	0.1337		0.1295	0.1165	0.1177	0.1151	0.1106	0.1038	0.1026	0.1018	0.1023
290	005G0236		166760	585840					1.0827			1.0817		1.0809				
291	005G0239		161900	583870							1.6903	1.6840	1.6859	1.6836	1.6806	1.6823	1.6799	1.6836
292	005G0242		166930	584170					2.0317		2.0400	2.0329		2.0262				
293	005G0243		165980	583620					1.5376		1.5423	1.5331		1.5175				
294	005G0244		166070	583440					0.9438		0.9495	0.9399		0.9198				
295	005G0245		166710	582630					0.7921		0.7984	0.7836		0.7424				
296	005G0246		166700	582060					0.6867		0.6925	0.6768		0.6271				
297	005G0247		166570	581490					1.1098		1.1176	1.1052		1.0614				
298	005G0248		166880.53	580752.19					0.6504		0.6541	0.6446	0.6369	0.6255	0.6098	0.5959	0.5797	0.5680
299	005G0249		166882.34	580426.67					1.0103		1.0128	1.0055	0.9997	0.9916	0.9807	0.9714	0.9596	0.9513
300	005G0250		167510	579650					-0.6921		-0.6867	-0.6905	-0.6914	-0.6913				
301	005G0251		166639.51	578481.85					-0.0048		-0.0003	-0.0063	-0.0044	-0.0073	-0.0092	-0.0081	-0.0107	-0.0109
302	005G0252		166066.16	580272.44					2.6666		2.6712	2.6631	2.6606	2.6534	2.6426	2.6347	2.6237	2.6182
303	005G0253		165670	581990					1.2204		1.2245	1.2107		1.1687				
304	005G0254	32	164303.82	579034.51			0.7204	0.7008	0.6780	0.6822	0.6365	0.6171	0.6070	0.5922	0.5795	0.5746	0.5670	0.5638
305	005G0255		167370	584200					0.9151		0.9218	0.9164		0.9116				
306	005G0256		168600	584920					1.1509		1.1567	1.1515		1.1504				
307	005G0257		167980	585770					-0.3261			-0.3226		-0.3201				
308	005G0258		165306.65	579320.9					0.8688		0.8676	0.8602	0.8591	0.8553	0.8507	0.8491	0.8447	0.8435
309	005G0260		168710	580950							-0.0419	-0.0442		-0.0452				
310	005G0261		168300	583150							0.5676	0.5603		0.5557				
311	005G0263		165850	582260							0.7866	0.7731		0.7275				
312	005G0264		168000	581300							1.3202	1.3136		1.3030				
313	005G0265		168700	581930							1.6734	1.6703		1.6662				
314	005G0266		160323.85	578678.82							0.8670	0.8592	0.8592	0.8565	0.8519	0.8531	0.8505	0.8514
315	005G0267		162930	583750							1.2402	1.2330		1.2298				
316	005G0270		160094.85	577293.02							0.4315	0.4258	0.4262	0.4260	0.4199			
317	005G0271		169210	583650							-0.2479	-0.2537		-0.2525				
318	005G0273		167850	581450							0.0770	0.0690						
319	005G0274		162380	583300							1.6009	1.5921	1.5918	1.5885	1.5828	1.5842	1.5821	1.5836
320	005G0275		163460	580090				1.0294	1.0115		0.9737	0.9530	0.9460	0.9330	0.9211	0.9185	0.9135	0.9129

#	Benchmark Number	Fitted Benchmark Location #	X	Y	Measurements in m													
					1988	1992	1997	2000	2003	2003	2006	2007	2008	2009	2010	2011	2012	2013
321	005G0277		169450	585050							2.9616	2.9556		2.9533				
322	005G0278		169380	582350							0.5711	0.5667		0.5667				
323	005G0279		167530	581180							0.6944	0.6875		0.6700				
324	005G0280		168890	580350							0.8069	0.8061		0.8048				
325	005G0281	8	162670	579040							1.0339	1.0104	1.0013	0.9843	0.9685	0.9612	0.9530	0.9500
326	005G0282		161750	580400							0.4365	0.4201	0.4173	0.4099	0.3997			
327	005G0285		165650	577500			0.7885	0.7884		0.7848	0.7743	0.7672	0.7663	0.7598	0.7547	0.7539	0.7479	0.7474
328	005G0286		162820	577060							4.9941	4.9844	4.9748	4.9619	4.9531	4.9491	4.9414	4.9386
329	005G0287		161700	578550							-0.4186	-0.4315	-0.4351	-0.4426	-0.4538	-0.4558	-0.4615	-0.4617
330	005G0288		167150	582150							0.8864	0.8746		0.8366				
331	005G0289		168850	583500								0.6775		0.6777				
332	005G0290		168880	579920								2.3193	2.3172	2.3169	2.3149	2.3164	2.3152	2.3148
333	005G0291		167850	579490								0.4571	0.4557	0.4547	0.4516	0.4520	0.4505	0.4473
334	005G0292		169100	584700								0.0678		0.0672				
335	005G0293		167250	579130								3.2231	3.2234	3.2199	3.2181	3.2179	3.2159	3.2139
336	005G0294	46	165550	577480								0.8804	0.8779	0.8703	0.8643	0.8629	0.8565	0.8550
337	005G0295		164380	578450								0.5028	0.4906	0.4740	0.4604	0.4555	0.4466	0.4448
338	005G0296		165140	576650								0.6485	0.6445	0.6382	0.6346	0.6338	0.6278	0.6281
339	005H0044		170140	582700							0.9089	0.9054		0.9074				
340	005H0270		170540	582800								1.3910		1.3947				

11 APPENDIX 2

11.1 NGI SUMMARY REPORT

Technical note

NGI

To: Harlingen Technical Committee
Attn.: Barbara Schatz, SGS Horizon
From: NGI
Date: 20131108
Project: 20120191
Prepared by: Øistein Johnsen

Main office:
PO Box 3930 Ullevål Stadion
NO-0806 Oslo
Norway

Trondheim office:
PO Box 1230 Pirsenteret
NO-7462 Trondheim
Norway

T (+47) 22 02 30 00
F (+47) 22 23 04 48

BIC No. DNBANOKK
IBAN NO26 5096 0501 281
Company No.
958 254 318 MVA

ngi@ngi.no
www.ngi.no

1 Rock mechanical behaviour

Gas production without sustained pressure support supplied by an external source will lead to field pressure reduction. The change in reservoir pressure increases the effective stress in the reservoir and the nearby rock formation. As a response to the increased stresses the rock formation the rock may deform by compaction.

Chalk displays a particular susceptibility to deformation, more complex than many other rock materials. The behaviour is strongly dependent on several factors; such as the chalk porosity, pore fluid composition and degree of saturation, as well as loading rate (i.e. depletion/production rate). From a mechanical point of view the implications of these parameters become particularly apparent when applying load or stress beyond the virgin consolidation.

Compaction due to increased loading is described as elastic up to a certain stress limit which is determined by porosity, pore fluid and production rate. Beyond this limit the stress-strain behaviour is characterized by pore collapse, a plastic behaviour inducing significantly larger strain than in the elastic domain. Thus, the pore collapse threshold is a crucial parameter to quantify.

Post production, when depletion is terminated, the reservoir and surrounding formation typically exhibit continued compaction adding to the cumulative deformation and subsidence. This is an intrinsic time dependent behaviour (creep) related to the visco-plastic attributes of the chalk, and depends on its material properties and the loading history (from deposition to production and shut-in).

All three distinct compaction behaviours – elastic, plastic, and creep – needs to be addressed and described by their own set of mechanical parameters and mathematical relations in order to achieve an adequate model description of the compaction and subsidence in the lifetime of the field and sustained subsidence after shut in.

Summary (cont.)

1.1 Laboratory test program

A laboratory testing program was launched to improve the rock mechanical understanding and bridge the gap between observed and modelled subsidence. The influence of control parameters (rock mechanical material properties, porosity, pore fluid composition, and load rate) were individually investigated in laboratory environment at realistic in situ stress conditions. The work was carried out in four stages: phase 1 by the Liege University in Belgium and phases 2, 3, and 4 by the NGI.

Phase 2 - Uniaxial Compaction Coefficient of Chalk (NGI 2007a):

Uniaxial strain compaction experiments (K_0) have been carried out on Harlingen-7 chalk (dry and brine saturated chalk with an initial porosity around 31%) with the aim of studying compressibility. Main findings were (see also Table A1):

1. The compressibility depends on the fluid in place. Higher compressibility values are obtained in brine saturated chalk, especially beyond pore collapse.
2. The onset of pore collapse starts at circa 40 MPa effective axial stress for dry chalk, and circa 23 MPa for brine saturated chalk. Given the initial stress conditions at Harlingen (effective vertical stress of 90 bars or 9 MPa, initial reservoir pressure of 135 bars or 13.5 MPa) and expected final reservoir pressure at abandonment (30 bars or 3 MPa, corresponding to 19.5 MPa effective vertical stress), pore collapse is not expected for the porosity intervals of 31% and below. Pore collapse may occur in the higher porosity chalk intervals if existing in the reservoir.

Phase 3 - Uniaxial strain tests and isotropic tests on brine saturated chalk (NGI 2009a):

Triaxial tests were conducted on Harlingen chalk: pore pressure depletion under uniaxial strain conditions (K0), and hydrostatic conditions at constant pore pressure. The pore collapse threshold was investigated under the respective conditions for consistency with the pore collapse threshold boundaries interpreted from other known studies on Harlingen and neighboring Lixhe chalks (ULG, phase 1) and defining a failure envelope as displayed in Figure 1.

Time dependent deformation (under zero load rate) proves to be an important contributor to the accumulated strain recorded in all conducted tests. The amount of creep deformation particularly becomes substantial beyond pore collapse stresses.

Summary (cont.)

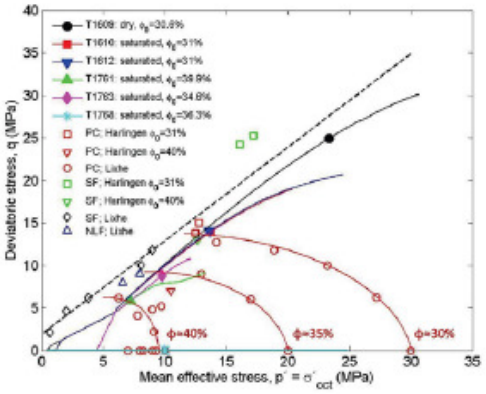

Figure 1: Synthetic display of pore collapse stress levels and the indicative failure threshold for different porosities. Included here are stress levels and stress paths obtained by the two NGI studies (solid marks), and failure points from ULG's studies on Harlingen and Lixhe chalk (Schroeder, 2009). ULG data appear with empty markers. PC is short for pore collapse, SF denotes shear failure, and NLF mean non-localized failure. The dashed black annotation line marks the shear failure boundary, and is adapted to the Lixhe shear failure data by a linear fit.

Phase 4 - Rate and fluid effects on chalk mechanical behavior (NGI 2010a):

Chalk samples from Harlingen well HRL-7 and HRL-9 were tested for geo-mechanical characterization with a varied rate test protocol (ref.Figure 2) to investigating the effects of porosity, applied load rate, and pore fluid type and degree of saturation on the mechanical behavior under isotropic loading conditions. Onset of yield (pore collapse), elastic and plastic parameters and time dependent behavior proved significantly affected by these three governing parameters (Table A2 - A5). Data from the open literature was used to supplement and verify the tests.

The rate dependency can be estimated from a creep phase – 0.00 MPa/h loading conditions (Table A6). Two phases of constant isotropic load was thus included in test T1840 for the benefit of analyzing the material time dependency according to the RTCM model (de Waal, 1986). See more details on formalism in Section 1.3.4.

Summary (cont.)

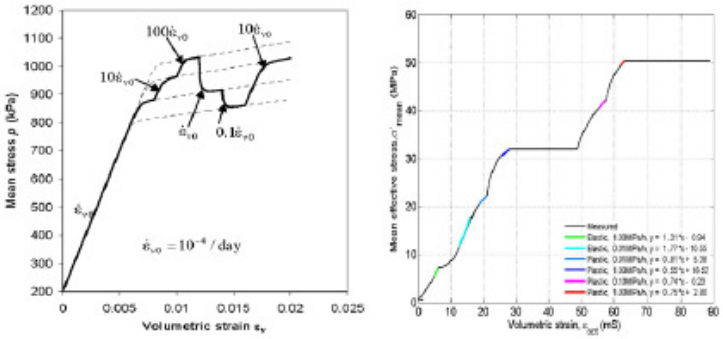

Figure 2: a) Principle of varied rate test (strain-rate controlled 1-dimensional hydrostatic compression)(Hickmann, 2004): When the applied strain rate is changed, the stress-strain curve quickly approaches the backbone stress-strain curve for the new applied strain rate. b) A typical varied load rate testing protocol used in NGI study, including two creep phases.

1.2 Rock mechanical model

With field data (Table A7), material property input from experimental laboratory mechanical tests and correlation with open chalk literature data sets, a rock mechanical model based on the Rate Type Compaction Model (RTCM) (de Waal, 1986) framework has been implemented (NGI 2009b, NGI 2011b, NGI 2012). The work flow of the depletion is given in Figure 5, and additionally a routine to handle creep after shut in is provided. The mechanical model gives a description of the distinct elastic and plastic behaviour as well as the pore collapse criterion expected for the Harlingen chalk.

In the following sub sections the physical mechanisms and input parameters are elaborate.

Summary (cont.)

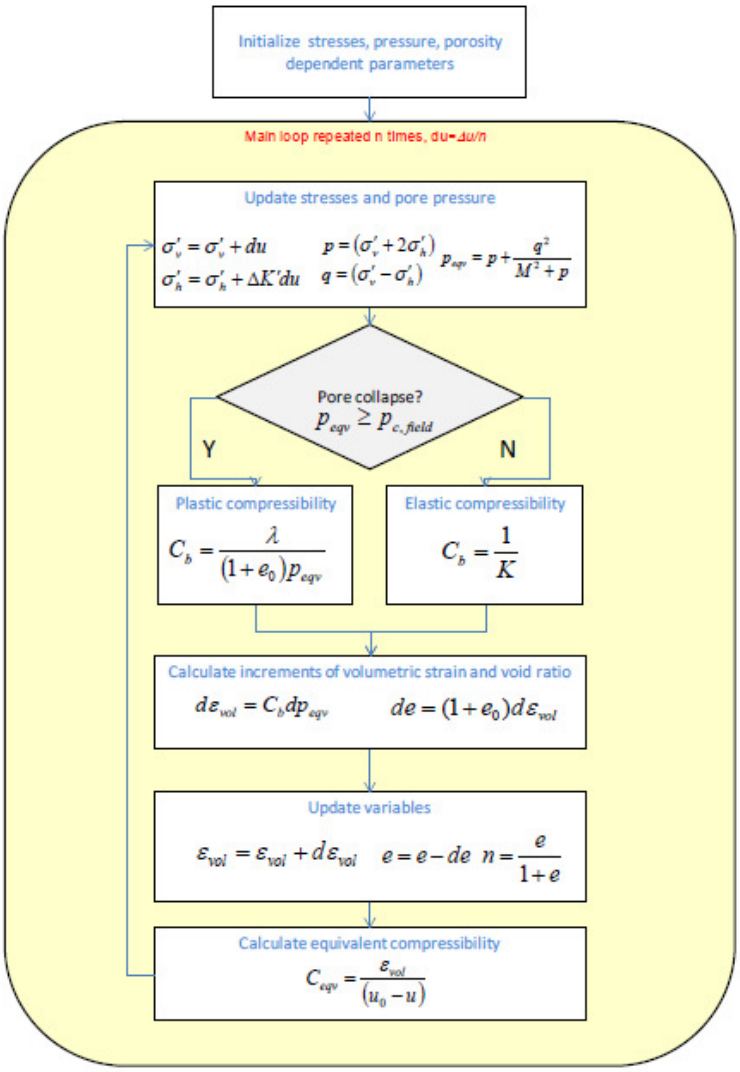

*Figure 3: Work flow of Matlab mechanical model script of uniform chalk depletion (*stress relations as given does not including Biot formalism).*

Summary (cont.)

1.2.1 Compressibility

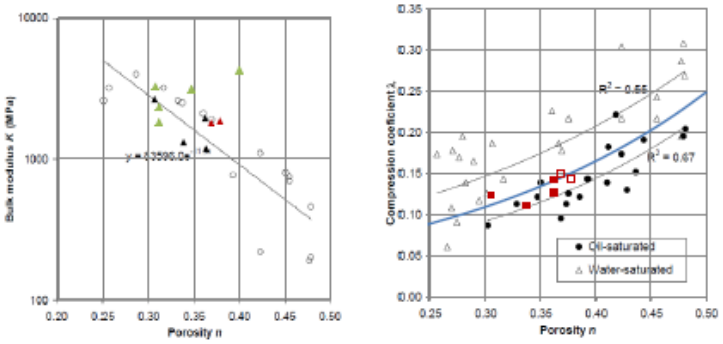

Figure 4: a) Bulk modulus for Harlingen chalk (filled symbols) plotted together with water-saturated experiments (open symbols) from JCR database (data from Hickman, 2004). The thin black line represents the trend line defined by Hickman. Green triangle: UST, brine saturated; black triangle: isotropic, brine saturated: Red triangle: isotropic, 30% brine saturated samples. b) Compression coefficient from isotropic compression tests on Harlingen chalk compared with JCR data. Red square symbols: 100% brine saturated: Empty square symbols: 30% brine saturated. JCR data with filled black symbols (oil-saturated) and empty triangles (water-saturated). Trend line through Harlingen data is shown with a blue solid line.

Chalk elasticity appears to be rather linear than stress-dependent (Hickman, 2004). Before pore collapse, the bulk compressibility is therefore computed as $C_{be} = 1/K$ where K is the tangent elastic bulk modulus. Likewise the pore compressibility reads $C_{pe} = 1/(K\, n_o)$. The bulk modulus for Harlingen chalk is plotted in Figure 3. against the Joint Chalk Research (JCR) database for water and brine saturated chalk (Hickman, 2004), with a trend line:

$$K = 83596e^{-11.3n} \qquad (1)$$

where n is the porosity in fraction and K the bulk modulus in MPa.

If one disregards the uniaxial strain experiments (subjected to uncertainty related to Poisson's ratio), a similar trend and scatter in the bulk modulus data is observed for Harlingen chalk as for the Joint Chalk data. The experiments with 30% water saturation are above the trend line, but within the general scatter observed.

Summary (cont.)

The compressibility of chalk after pore collapse is stress dependent. Along the virgin consolidation line it is expressed as:

$$C_{bp} = \frac{d\varepsilon_{vol}}{dp} = \frac{\lambda}{(1+e_0)p} \quad (2)$$

where λ is the compression coefficient, e_0 is the initial void ratio. Based on the available data, compression coefficient trend line is defined as

$$\lambda = 0.032\, e^{4.1n} \quad (3)$$

For Harlingen Chalk, where n is the porosity in fraction.

1.2.2 Load rate parameter

$$\frac{p_2}{p_1} = \left(\frac{\dot{\varepsilon}_{v2}}{\dot{\varepsilon}_{v1}}\right)^b \quad (4)$$

The load rate parameter b is used in order to extrapolate pore collapse P_c at lab rates to a P_c at field rate, and as an input parameter to the creep model. Time dependent deformation under continued loading is implicitly handled through the b-parameter.

The compaction and subsidence modeling proves highly sensitive to the b-parameter, in terms of onset of pore collapse and accumulated strain.

Where a fixed value was proposed initially and expected to be in the range b = 0.05-0.65 for fully brine saturated samples, literature also suggests a porosity dependence $b = 0.17\, e^{-3.1n}$ (Kristiansen *et al.*, 2010) which matches rather well with data from tests conducted on fully saturated chalk.

Together with trends from Priol's work on different saturating fluids (Priol 2005) and trusting absolute values from NGI studies, de Waal, we may well justify that the b-parameter for 30% brine is somewhat lower than the brine saturated, effectively shifting the 0.05-0.06 range a bit down for partial fluid saturation, introducing instead a modified trend line

$$b = 0.135\, e^{-3.1n} \quad (5)$$

The porosity trend is captured but at a lower value suiting partial saturation load rate values better. This reproduces b = 0.043 as NGI tests suggest for 37% porosity saturated samples, while at 31% porosity it becomes 0.052 which falls into

Summary (cont.)

the appropriate range (0.05-0.055) as concluded in SGS subsidence modeling and parameter sensitivity analysis.

The effect of tweaking the *b*-parameter introduces a more nuanced value, slightly shifting the onset of pore collapse to higher reservoir pressures for 31% (earlier onset), but at higher porosities the effect will be the opposite.

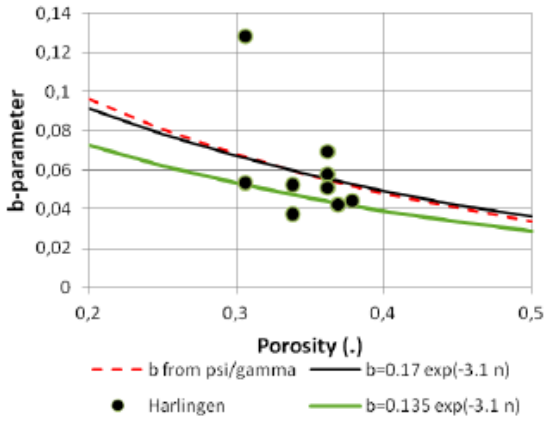

Figure 5: Comparing Harlingen data and trendlines: from JCR (psi/gamma measurement), $b = 0.17\ e^{-3.1n}$ (Kristiansen et al., 2010), and a modified version for partially saturated chalk inspired by the former, $b = 0.135\ e^{-3.1n}$.

1.2.3 Poroelasticity

According to the principle of effective stresses (Terzaghi, 1923), soils deform in response to changes in effective stresses as:

$$\sigma' = \sigma - u \tag{6}$$

in which σ' is the effective stress, σ the total stress, and u is the pore pressure.

The volumetric strain due to combined changes of pore pressure u and total stress σ may be written as (Skomedal *et al.*, 2002):

$$\sigma' = \sigma - \alpha u \tag{7}$$

where α is Biot's coefficient defined by:

Summary (cont.)

$$\alpha=1-K/K_s. \quad (8)$$

K is the bulk modulus of the skeleton due to a change in effective stresses (as defined in Eq.1) or drained bulk modulus, and K_s the mineral bulk modulus of the skeleton constituents due to a change in pore pressure under constant effective stresses. Basically it describes how the fluid becomes less responsible for counteracting outer stresses as cementation increases, while the matrix itself becomes more load bearing. Effective stress is increased in the rock as α decreases (Nur & Byerlee, 1971).

Consulting literature K_s = 75 GPa was used, obtaining a Biot's coefficient of 0.97-0.99 using bulk modulus porosity trend line in Figure 3 and Eq. 1.
Model investigation indicated the strain contribution from grain compressibility to be small; hence the compaction being governed almost exclusively by porosity reduction.

1.2.4 Time dependent deformation - Creep

During its lifetime of production a chalk reservoir can experience elastic, plastic and time dependent "creep" deformation depending on the production and load parameters, i.e. load rates and degrees of pressure remediation, with respect to the in situ conditions. The total induced volumetric strain $\Delta\varepsilon_{tot}$ can thus be separated into occurred elastic $\Delta\varepsilon_{el}$, plastic $\Delta\varepsilon_{pl}$ (after pore collapse) and time dependent $\Delta\varepsilon_{creep}$ contribution:

$$\Delta\varepsilon_{tot} = \Delta\varepsilon_{el} + \Delta\varepsilon_{pl} + \Delta\varepsilon_{creep} \quad (9)$$

Several models describing the time dependent deformation with a shared origin in soil mechanics has been proposed (NGI, 1969, Kolymbas, 1978, Borja and Kavanzanjian, 1985 and de Waal, 1986).

The time dependent deformation is sensitive to ageing and mechanical loading history.

Following the outlines of de Waal's formalism (de Waal, 1986), creep deformation occurring at zero load rate ($d\sigma/dt = 0$) is given as

$$\varepsilon_t = C_c \ln\left[1+\frac{t}{\tau}\right] \quad (10)$$

in which $1/C_c$ and τ/C_c relates to the inverse strain rate

Summary (cont.)

$$\dot{\varepsilon}_t = \frac{C_c}{t+\tau} \tag{11}$$

as the slope ($1/C_c$) and the offset (τ/C_c) respectively. $C_c = bc_{b,\sigma}p$ and $\tau = bc_{b,\sigma}p/\dot{\varepsilon}_o$, where b is the rate sensitivity parameter, and the parameters representative of the instant of creep onset t= 0 is the volumetric strain rate $\dot{\varepsilon}_o$, the bulk compressibility $c_{b,\sigma}$, and the mean effective stress level p.

Three scenarios is to consider and dynamically select in modeling depending on load rate in terms pore pressure change over time:

1) Creep after shut in – no pressure changes

Creep deformation is considered present from the end of production and can be calculated by integration of Eq. () over a time t which leads to a time dependent strain contribution

$$\Delta\varepsilon_t = \int_0^t \frac{C_c}{t+\tau} dt \tag{12}$$

The integration is carried out by discretization of t into N number of elements (number of iterations) for which Eq. (10) is solved. The onset of creep is defined at t = 0 with a set of parameters p, $b(n)$, $c_{b,0}$, and $\dot{\varepsilon}_o$ inherited from the very end of the depletion phase (given $C_c = bc_{b,\sigma}p$ and $\tau = bc_{b,\sigma}p/\dot{\varepsilon}_o$). Integration of Eq. (10) over a given N iterations (time steps $\Delta t = t/N$) leads to a volumetric strain contribution

$$\Delta\varepsilon_{creep} = C_c \ln\left[1+\frac{\Delta t}{\tau}\right] \quad , \tag{13}$$

which accumulates over the creep period and adds to the previously occurred elastic and plastic.

Given the logarithmic function of $\Delta\varepsilon_{creep}$ the resulting strain is affected by number of integration steps (i.e. step size). The necessary number of time steps N must be considered since finer subdivision of t leads to the integration converging towards a stable solution. Increasing the number of time steps will necessarily increase computation time.

Summary (cont.)

2) Creep during loading – pressure redistribution

For a creep situation with changing reservoir pressure one might have to consider creep for incremental loading (i.e. pressure change) opposed to the "ideal" situation of zero load rate.

For each pressure step Δp in an iterative loading sequence a time step Δt can be assigned granted that the load rate is known at all times. The time step Δt is sub divided into a number time increments N for discrete numerical integration of Eq. (10):

$$\Delta\varepsilon_{creep}^{\Delta P} = \int_{t}^{t+\Delta t} \frac{C_c}{t+\tau} dt \quad . \tag{14}$$

For each pressure step the reservoir effective pressure state is updated: a new onset of creep is defined with a set of parameters p, $b(n)$, $c_{b,0}$, and $\dot{\varepsilon}_o$. At creep onset t is set to zero and a creep period of duration $\Delta t'$ is applied for the pressure step. These bounding conditions and parameter input give a minute time dependent volumetric strain contribution

$$\Delta\varepsilon_{creep}^{\Delta P} = C_c \ln\left[1+\frac{\Delta t'}{\tau}\right] \tag{15}$$

which adds to the elastic and plastic incurred strain during pressure changes, i.e. due to redistribution in the reservoir.

For pressure build–up the strain creep contribution will decrease over time as indicated in Figure 6 (conversely it will be increased by higher stresses in the case of continued pressure decrease). It is important to ensure that strain contribution is not accounted for more than once, so for each creep curve (black) only the strain for the given interval (red) should be added to the total strain.

One challenge in handling the integration of time dependent strain during applied pressure change is the computing time. Obtaining a stable solution for the creep strain $\Delta\varepsilon_{creep}^{\Delta P}$ requires a fine segmentation of the time interval Δt, and solving it by discrete numerical integration inside a pressure/loading loop rapidly increases computing time.

Summary (cont.)

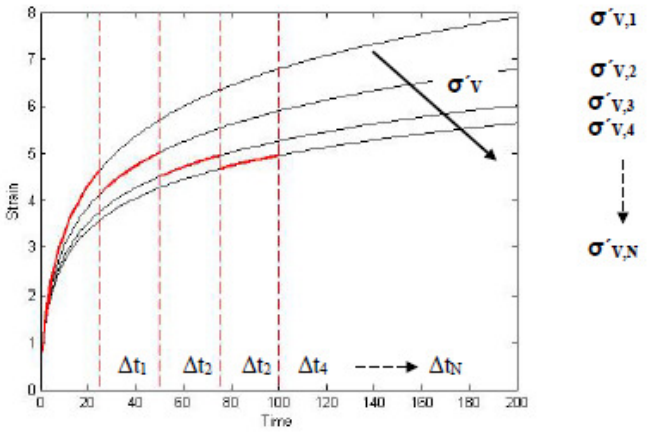

Figure 6: Creep curves for different stress levels. Occurring creep strain becomes less for lower stresses, i.e. as pressure builds up in reservoir due to redistribution. Red line segments shows the principle of strain contribution during a sequential decrease.

3) Pressure redistribution – load phase consideration

A simpler and more efficient solution to cope with pressure reduction due to redistribution than iteratively handling creep for updated pressures is to consider the pressure time variations after shut in as continued loading/unloading phase, with the appropriate set of field pressure parameters and mechanical properties inherited from the preceding depletion phase.

With a known pressure profile the in situ "load rate" is known, thus with a reasonable *b*-parameter the link is made towards the constitutive model for compaction and subsidence calculation. For grid elements of continued pressure depletion compaction will occur, either elastically if the reservoir pressure is above the pore collapse threshold (effective stress $< P_c$) and plastically if the reservoir pressure is below (effective stress $\geq P_c$).

In the case of pressure build-up an elastic strain rebound can be accepted only if the element is still within the elastic domain. In the plastic phase deformation is permanent and cannot be remediated with increased reservoir pressure. None the less, sufficient pore pressure increase can have a counteracting effect and reduce strain rate.

Summary (cont.)

By applying a pressure cutoff for when the pressure changes are considered insignificantly small, a regular creep by approximation to zero load rate may account for the added creep strain.

After shut in determination of creep or pressure depletion should be performed dynamically by iteratively checking the grid elements for their current state; if belonging to elastic or plastic regime, and if the reservoir pressure is nearly constant (within cut off limits), decreasing or building up, and thereof choose the continued mode of loading.

1.2.5 Parameter tuning and model verification

The mechanical behavior is verified versus PLAXIS soft soil model (Vermeer and Naher, 1999) and two laboratory model experiments with similar stress path conditions. Being of a different theoretical framework input parameters was selected to fit with the model data. In the laboratory case, adjustment of the mechanical parameter correlations (pore collapse pressure, elastic bulk modulus, and plastic compressibility) originally determined from experimental data was necessary to achieve a good fit.

Literature correlation and direct calibration with laboratory experiments indicate a rather broad band of plausible values for most mechanical parameters. Thus, the optimal absolute values rely on tuning exercise (as performed by SGS) in order to achieve the best possible subsidence history match.

REFERENCES

Borja, R. and Kavanzanjian, E. (1985). A Constitutive Model for the Stress-Strain-Time Behaviour of 'Wet' Clays. Geotechnique, Vol. 35, No. 3, 283-298.

de Waal J.A. (1986). PhD Thesis On the rate Type compaction behaviour of sandstone reservoir rock.

Havmøller O. and Foged N. (1996). Review of rock mechanical data for chalk. Proceedings of the 5th North Sea Chalk Symposium, Reims, France

Hickman, R. J. (2004). Formulation and Implementation of a Constitutive Model for Soft Rock. PhD Thesis, Virginia Polytechnic Institute, September 2004.

Summary (cont.)

Kolymbas, D., (1978). Ein Nichtlineares Viscoplastisches SToffgestetz für Boden, Thesis, Institues für Bodenmechanik der Universitat Fridericiana in Karlsruhe.

Kristiansen, T. Golder and B. Plischke (2010). History Matched Full Field Geomechanics Model of the Valhall Field Including Water Weakening and Re-Pressurisation, EUROPEC/EAGE Annual Conference and Exhibition held in Barcelona, Spain, 14–17 June 2010.

NGI (1969). One year oedometer tests on plastic Drammen clay. Internal Report No 30826.

NGI (2007). Uniaxial Compaction Coefficient of Chalk – Compressibility of Harlingen Chalk, 20071135-1.

NGI (2009a). Harlingen chalk triaxial compaction experiments: Uniaxial strain tests and isotropic tests on brine saturated chalk, 20091179-00-1-R.

NGI (2009b). Time dependent deformation of Harlingen chalk, 20092206-00-3-TN.

NGI (2011a). Rate and fluid effects on chalk mechanical behavior, 20100236-00-1-R.

NGI (2011b). Harlingen Upper Cratacious investigation - technical committee, 20100377-00-0-R

NGI (2012). Harlingen revised compaction model, 20120191-01-R.

Nur, A. & Byerlee, J.D. (1971). An exact effective stress law for elastic deformation of rocks with fluids. Journal of Geophysical Research 76, 6414-6419.

PASACHALK (2004), Mechanical Behavior of Partially and Multiphase Saturated Chalks Fluid-Skeleton Interaction: Main Factor of Chalk Oil Reservoirs Compaction and Related Subsidence –Part 2, Final Report, EC Contract no. ENK6-2000-00089.

Priol G. (2005). Comportement mécanique différé et mouillabilité d'une craie pétrolifère. Thèse de l'Ecole nationale des ponts et chaussées.

Schroeder C., Illing P., Fourmaintraux D., and A.P. Bois (2009). Waterflooding experiments on Harlingen gas saturated chalk. Presentation at Meeting Den HAAG, 06 January 2009.

Summary (cont.)

Skomedal E., Jostad H.P., and Hettema M. (2002). Effective of pore pressue and strsss path on rock mechanical properties for HPHT Application, SPE/ISRM 78152, Rock Mechanics Conference, Irving, Texas, Oct. 20-23, p 10.

Terzaghi, K. (1923). Die Berechnung der Durcglässigkeitsziffer des Tones aus dem Verlauf der hydrodynamischen Spannungserscheinungen. Sitzungsber. Akad. Wiss. Wien. Math. Naturwiss. K., Abt. 2A 132 125-132 138.

Vermeer, P.A., Stolle D.F.E., and Bonnier, P.G. (1997), From classical theory of secondary compression to modern creep. Computer Methods and Advances in Geomechanics, Vol. 4, Wuhan 1997, pp. 2469-2478.

Vermeer, P.A. and Naher, H.P. (1999). A soft soil model that accounts for creep. Beyond 2000 in Computational Geotechnics – 10 Years of Plaxis International.

APPENDIX

Table A1:

Fluid Type	Effective axial stress σ'_v (MPa)	Bulk compressibility C_{bm} (/MPa)	Pore compressibility C_{pp} (/MPa)
dry	6-40 MPa	1.70E-04	5.49E-04
dry	>40 MPa	2.67E-04	8.61E-04
brine*	6-23 MPa	2.58E-04	8.38E-04
brine*	23-30 MPa	3.92E-04	1.27E-03
brine*	>30 MPa	7.02E-04	2.28E-03

*average value of two identical tests

Summary (cont.)

Table A2: Overview of elastic/plastic regimes in conducted tests.

Sample ID	Test ID	Fluid type	Porosity (%)	Load Rate (MPa/h)	Plastic/ Elastic	Tangent modulus *Et* (GPa)	Pore collapse @ exp. load rate σ'_{oct} (MPa)	Pore collapse equivalent of 1.0 MPa/h load rate σ'_{oct} (MPa)
E_A	T1838	brine	36.2	1.00	E	1.94		16.0
				0.01	E	1.30		
				0.01	P	0.50	8.1	
				0.10	P	0.28		
				1.00	P	0.26		
				0.01	P	0.50		
				0.10	P	0.58		
4	T1839	brine	30.6	1.00	E	2.64		36.0
				0.01	P	0.97	14.0*	
				0.10	P	0.60		
				1.00	P	0.59		
E_B	T1840	brine	33.8	1.00	E	1.31		30.0
				0.01	E	1.77		
				0.01	P	0.81	18.0	
				1.00	P	0.55		
				0.10	P	0.74		
				1.00	P	0.75		
H10	T1841	30% brine	36.9	1.00	E	1.80		18.0
				1.00	P	0.24	18.0	
				10.0	P	0.19		
				1.0	P	0.50		
H27	T1855	30% brine	37.4	1.00	E	1.93		17.8
				1.00	P	0.21	17.8	
				10.0	P	0.17		
				1.00	P	0.50		

* extrapolated as intersection between elastic (1.00 MPa/h) and plastic (0.00 MPa/h) linear trend lines.

Summary (cont.)

Table A3: Compressibility of Harlingen chalk at standard laboratory rates

Sample ID	Test ID	Fluid type	Porosity (%)	Bulk Modulus, K (GPa)	Bulk Compressibility, C_{bm} (1E-4 /MPa)
H33*	T1768	brine	36.3	1.18	8.47
EA	T1838	brine	36.2	1.94	5.15
4	T1839	brine	30.6	2.64	3.79
EB	T1840	brine	33.8	1.31	7.63
H10	T1841	30% brine	36.9	1.80	5.56
H27	T1855	30% brine	37.4	1.85	5.41

* Isotropic test T1768 on sample H33 from well HRL-9 (NGI, 2009a) included for more data points

Table A4: Compression coefficient from isotropic compression experiments on Harlingen chalk.

Sample ID	Test ID	Fluid type	Porosity (%)	Compression coefficient, λ
H33*	T1768	brine	36.3	0.127
EA	T1838	brine	36.2	0.161
4	T1839	brine	30.6	0.124
EB	T1840	brine	33.8	0.112
H10	T1841	30% Brine	36.9	0.150
H27	T1855	30% brine	37.4	0.144

* Isotropic test T1768 on sample H33 from well HRL-9 (NGI, 2009a) included for more data points

Summary (cont.)

Table A5: Rate sensitivity of Harlingen chalk from change in loading rate

Sample ID	Test ID	Fluid type	Porosity (%)	Mean stress (MPa)		Mean stress rate (MPa/h)		
				p_1	p_2	p_1	p_2	b
E_A	T1838	brine	36.2	14.10	16.10	0.01	0.10	0.057
				20.61	24.18	0.10	1.00	0.069
				34.60	43.70	0.01	1.00	0.050
4	T1839	brine	30.6	31.10	41.77	0.01	0.10	0.120
				50.64	57.27	0.10	1.00	0.053
E_B	T1840	brine	33.8	22.00	28.00	0.01	1.00	0.052
				42.00	45.77	0.10	1.00	0.037
H10	T1841	30% brine	36.9	23.50	25.90	1.00	10.0	0.042
H27	T1855	30% brine	37.4	21.37	23.66	1.00	10.0	0.044

Table A6: Rate sensitivity estimated from creep phase (T1840).

Mean Stress p (MPa)	Slope inverse strain rate versus time, $1/C_c$	Offset τ/C_c	ε_{vo} (mS)	$c_{b,0}$ (10^{-3}/MPa)	b
31.86	0.199	1.37	0.73	2.40	0.0651
50.22	0.148	0.77	1.30	4.90	0.0271

Table A7: *Initial stress conditions for Harlingen (from Elf, 1993).*

Stress / Pore pressure	Value (MPa)
Total vertical stress σ_V	22.5
Initial total horizontal stress σ_H	18.0
Initial octahedral stress $\sigma_{oct} = (\sigma_V+2\sigma_H)/3$	19.5
Initial total stress ratio $K = \sigma_V/\sigma_H$	0.8
Initial reservoir pressure u_o	13.5
Initial effective vertical stress σ'_V	9.0
Initial effective horizontal stress σ'_H	4.5
Initial effective octahedral stress σ'_{oct}	6.0
Initial effective stress ratio $K' = \sigma'_V/\sigma'_H$	0.5

Kontroll- og referanseside/ Review and reference page

NGI

Dokumentinformasjon/*Document information*		
Dokumenttittel/*Document title* XX		**Dokument nr**/*Document No.* XX
Dokumenttype/*Type of document* ☒ **Rapport**/*Report* ☐ **Teknisk notat**/*Technical Note*	**Distribusjon**/*Distribution* ☐ **Fri**/*Unlimited* ☒ **Begrenset**/*Limited* ☐ **Ingen**/*None*	**Dato**/*Date* XX **Rev.nr.**/*Rev.No.*
Oppdragsgiver/*Client* XX.		
Emneord/*Keywords*		

Stedfesting/*Geographical information*	
Land, fylke/*Country, County*	**Havområde**/*Offshore area*
Kommune/*Municipality*	**Feltnavn**/*Field name*
Sted/*Location*	**Sted**/*Location*
Kartblad/*Map*	**Felt, blokknr.**/*Field, Block No.*
UTM-koordinater/*UTM-coordinates*	

Dokumentkontroll/*Document control*

Kvalitetssikring i henhold til/*Quality assurance according to* **NS-EN ISO9001**

Rev./ *Rev.*	Revisjonsgrunnlag/*Reason for revision*	Egen-kontroll/ *Self review* av/*by:*		Sidemanns-kontroll/ *Colleague review* av/*by:*		Uavhengig kontroll/ *Independent review* av/*by:*		Tverrfaglig kontroll/ *Inter-disciplinary review* av/*by:*	
0	Original document								

Dokument godkjent for utsendelse/ *Document approved for release*	Dato/*Date*	Sign. Prosjektleder/*Project Manager*
		XX

Skj.nr. 043

NGI er et internasjonalt ledende senter for forskning og rådgivning innen geofagene. Vi utvikler optimale løsninger for samfunnet, og tilbyr ekspertise om jord, berg og snø og deres påvirkning på miljøet, konstruksjoner og anlegg.

NGI arbeider i følgende markeder: olje og gass, bygg og anlegg, samferdsel, naturskade og miljøteknologi.

NGI er en privat stiftelse med kontor og laboratorier i Oslo, avdelingskontor i Trondheim og datterselskap i Houston, Texas, USA.

NGI ble utnevnt til "Senter for fremragende forskning" (SFF) i 2002, og leder "International Centre for Geohazards" (ICG).

www.ngi.no

NGI is a leading international centre for research and consulting in the geosciences.

NGI develops optimum solutions for society, and offers expertise on the behaviour of soil, rock and snow and their interaction with the environment, installations and structures.

NGI works within the oil and gas, building and construction, transportation, natural hazards and environment sectors.

NGI is a private foundation with office and laboratory in Oslo, branch office in Trondheim and daughter company in Houston, Texas, USA. NGI was awarded Centre of Excellence status in 2002, and leads the International Centre for Geohazards (ICG).

www.ngi.no


NGI
Hovedkontor/Main office:
PO Box 3930 Ullevål Stadion
NO-0806 Oslo
Norway
Besøksadresse/Street address:
Sognsveien 72, NO-0855 Oslo
Avd Trondheim/Trondheim office:
PO Box 1230 Pirsenteret
NO-7462 Trondheim
Norway
Besøksadresse/Street address:
Pirsenteret, Havnegata 9, NO-7010 Trondheim
T: (+47) 22 02 30 00
F: (+47) 22 23 04 48
ngi@ngi.no
www.ngi.no
Kontonr 5096 05 01281/IBAN NO26 5096 0501 281
Org. nr/Company No.: 958 254 318 MVA
BSI EN ISO 9001
Sertifisert av/Certified by BSI, Reg. No. FS 32989

12 APPENDIX 3

12.1 PETROPHYSICAL MNEMONICS

12.1.1 INPUT LOGS

RDEEP = Final Deep Resistivity

GRN = Normalized gamma ray

NPHILS = Final Neutron Porosity in limestone units (edited, normalized, environmentally. corrected)

DENS = Final Density (edited, normalized, environmentally. corrected)

SONIC = Final sonic curve

SPN = Self potential

12.1.2 OUTPUT LOGS

VSHGRL1 = Volume of shale from linear gamma ray relationship

PHIT_F1 = Final total porosity

PHIE_F1 = Final effective porosity

PRM_F1 = 0.0021*(exp(23.548*PHIE_F1)) – Final

SWE_F1 = Archie water saturation using PHIE_F1, RDEEP

a=1.00, m=1.97 (HRL-09), n=2.00 (assumed)

Rw = 0.065ohmm @ 110F (75kppm NaCl - Pickett Plots from HRL-04, HRL-05, HRL-06 & HRL-09)

BVW_F1 = Bulk Volume water (PHIE_F1*SWE_F1)

12.2 CPIs

12.2.1 FRA-01

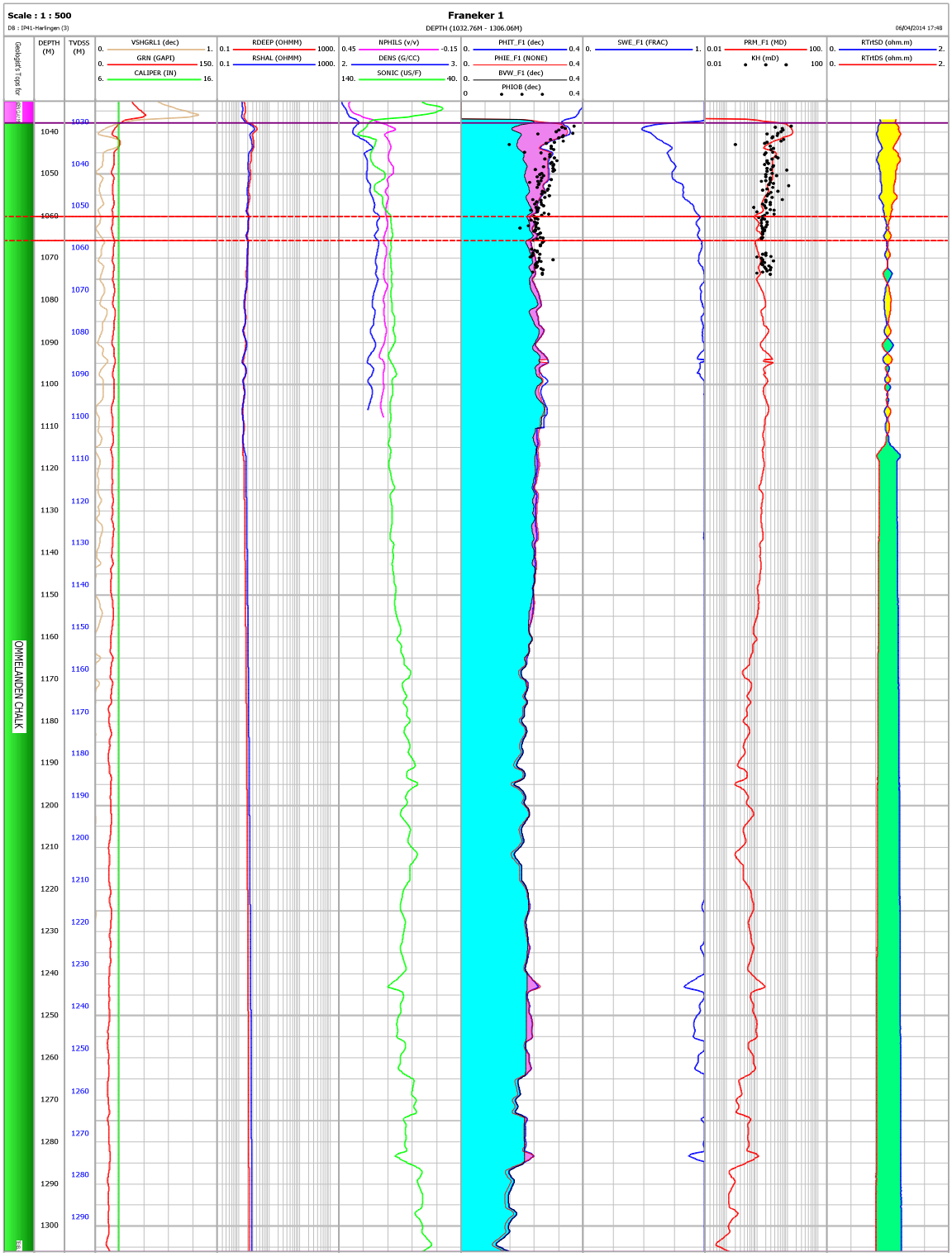

12.2.2 HRL-01

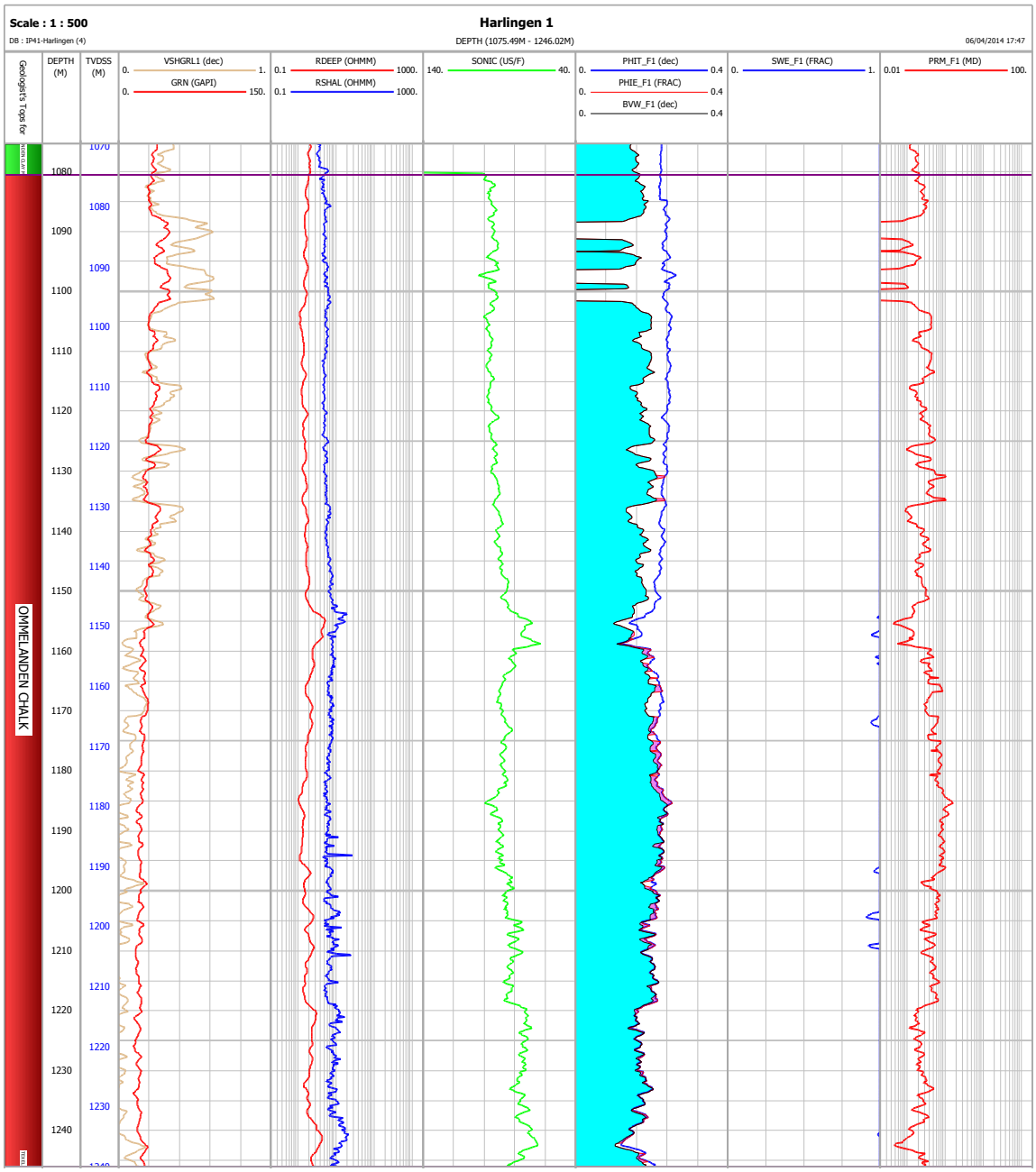
Scale : 1 : 500
Harlingen 1
DB : IP41-Harlingen (4)
DEPTH (1075.49M - 1246.02M)
06/04/2014 17:47
Geologist's Tops for
DEPTH (M)
TVDSS (M)
VSHGRL1 (dec)
GRN (GAPI)
RDEEP (OHMM)
RSHAL (OHMM)
SONIC (US/F)
PHIT_F1 (dec)
PHIE_F1 (FRAC)
BVW_F1 (dec)
SWE_F1 (FRAC)
PRM_F1 (MD)
OMMELANDEN CHALK

12.2.3 HRL-02

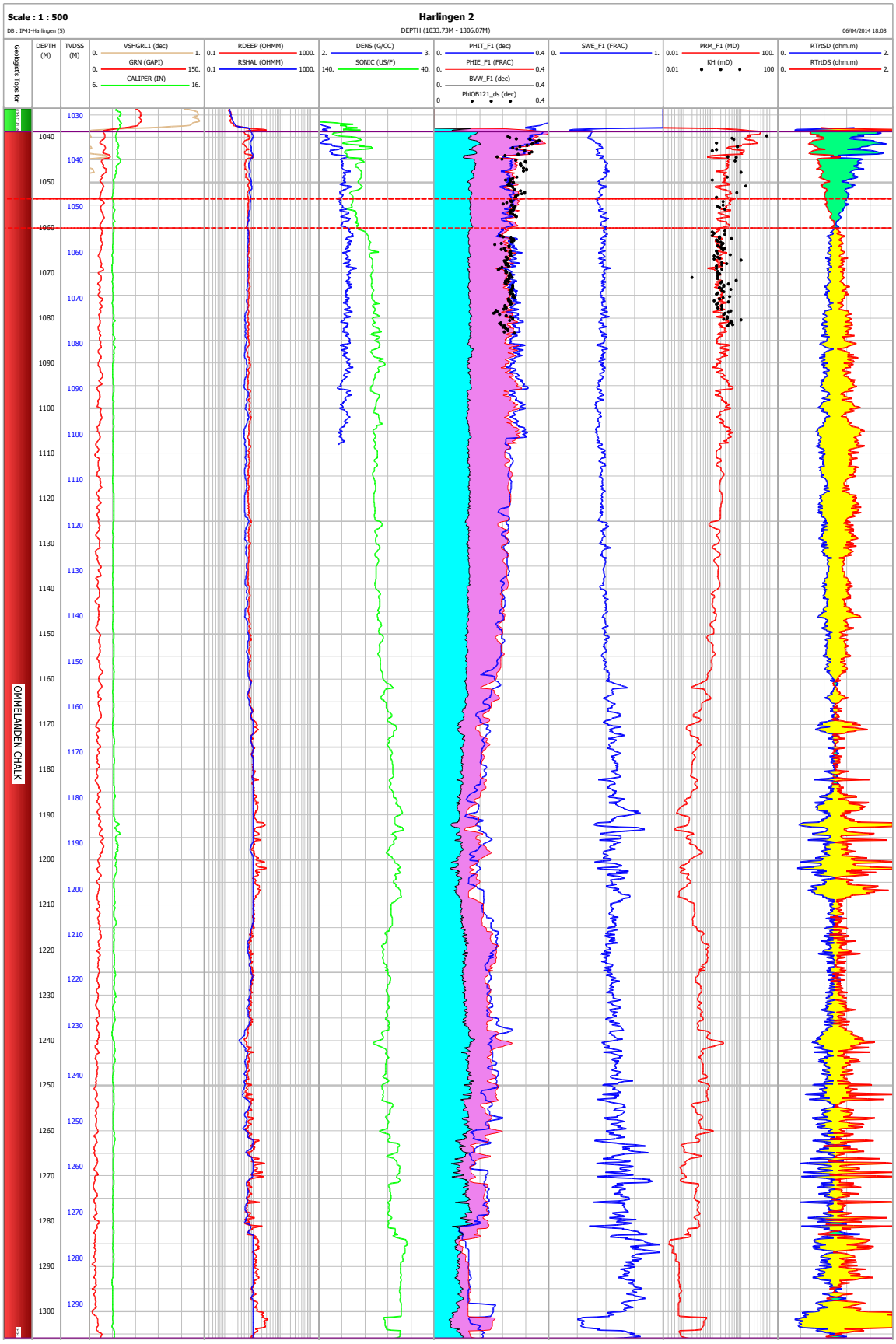
Scale : 1 : 500
Harlingen 2
DEPTH (1033.73M - 1306.07M)
06/04/2014 18:08
DEPTH (M)
TVDSS (M)
VSHGRL1 (dec)
GRN (GAPI)
CALIPER (IN)
RDEEP (OHMM)
RSHAL (OHMM)
DENS (G/CC)
SONIC (US/F)
PHIT_F1 (dec)
PHIE_F1 (FRAC)
BVW_F1 (dec)
PhiOB121_ds (dec)
SWE_F1 (FRAC)
PRM_F1 (MD)
KH (mD)
RTrtSD (ohm.m)
RTrtDS (ohm.m)
OMMELANDEN CHALK

12.2.4 HRL-03

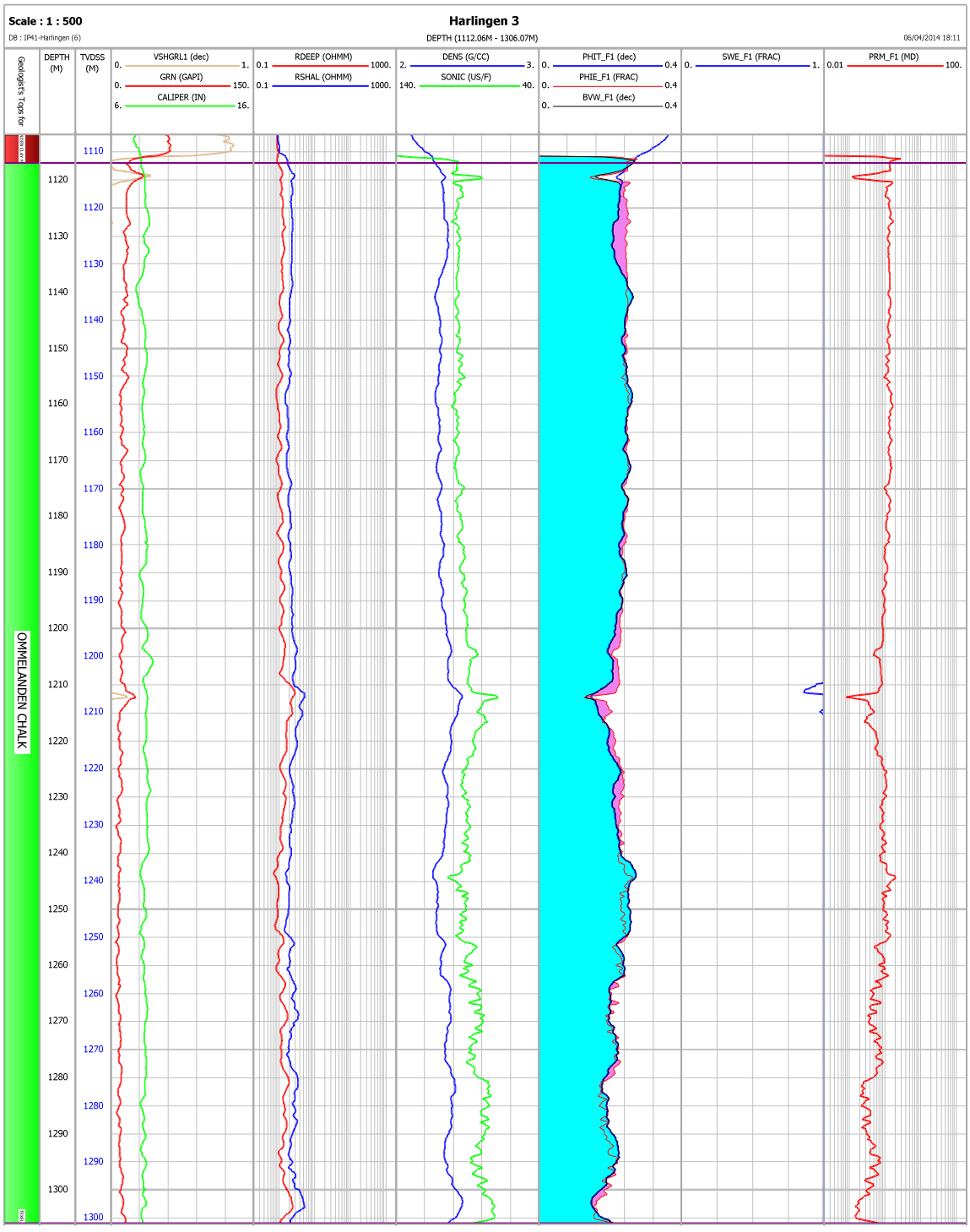
Scale : 1 : 500
Harlingen 3
DB : IP41-Harlingen (6)
DEPTH (1112.06M - 1306.07M)
06/04/2014 18:11
Geologist's Tops for
DEPTH (M)
TVDSS (M)
VSHGRL1 (dec)
GRN (GAPI)
CALIPER (IN)
RDEEP (OHMM)
RSHAL (OHMM)
DENS (G/CC)
SONIC (US/F)
PHIT_F1 (dec)
PHIE_F1 (FRAC)
BVW_F1 (dec)
SWE_F1 (FRAC)
PRM_F1 (MD)
OMMELANDEN CHALK

12.2.5 HRL-04

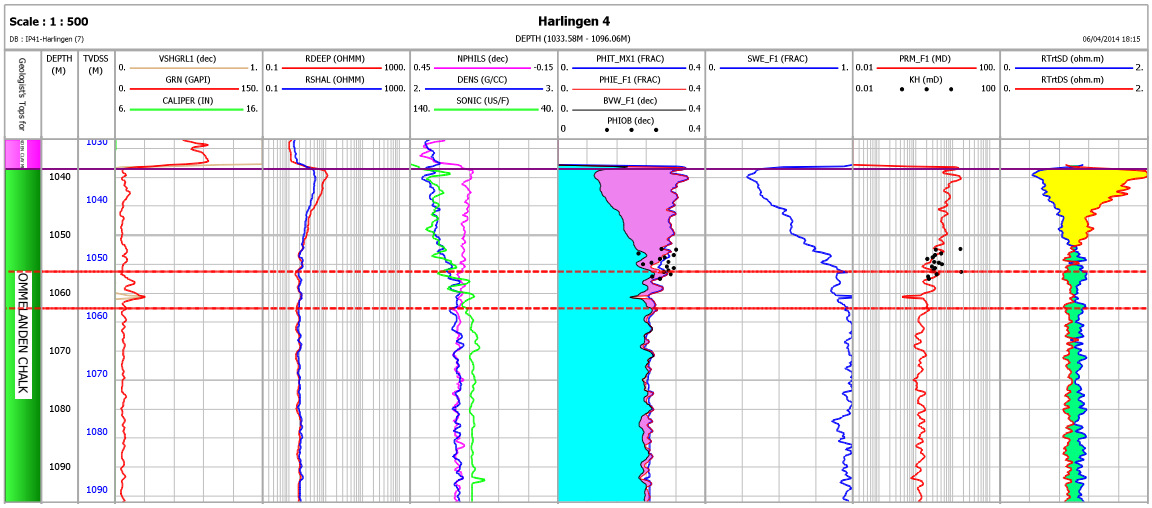

12.2.6 HRL-05

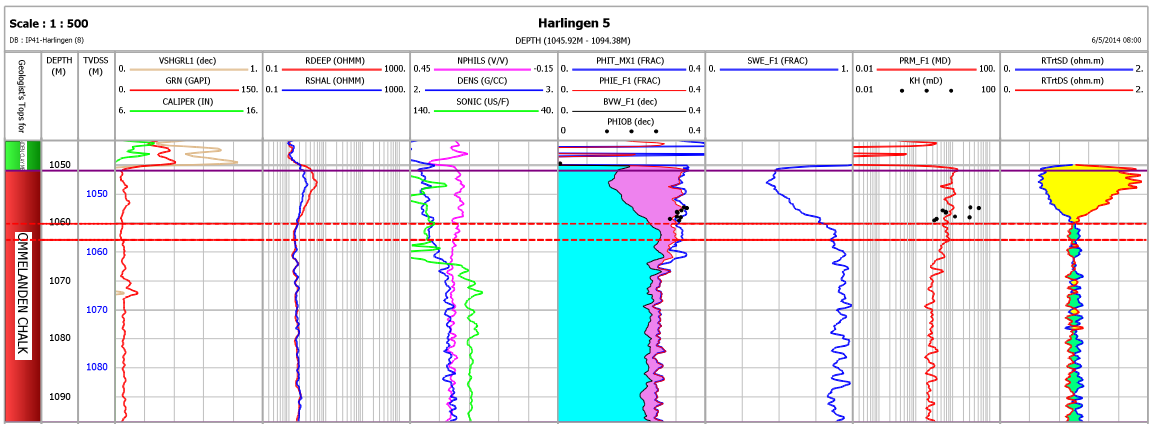

12.2.7 HRL-06

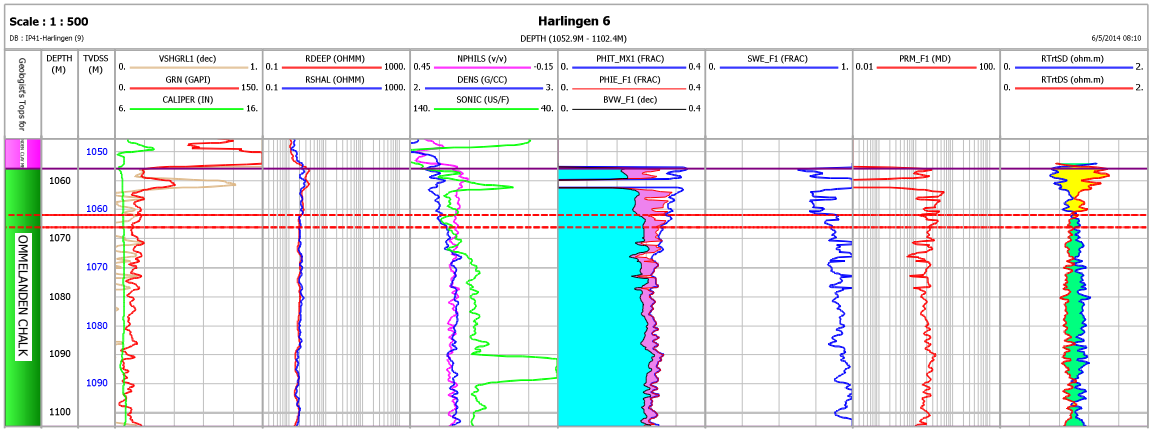

12.2.8 HRL-07

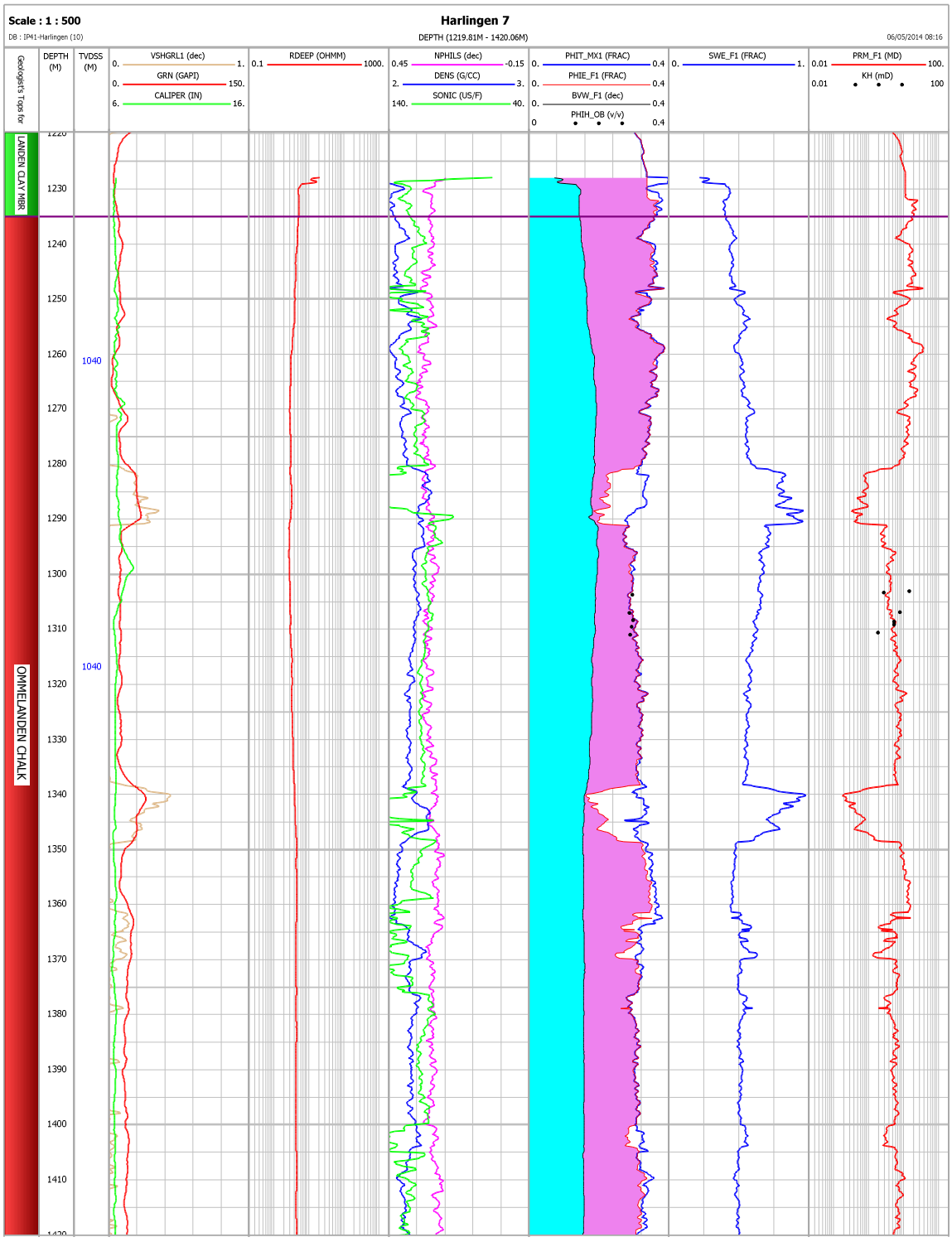
Scale : 1 : 500
Harlingen 7
DEPTH (1219.81M - 1420.06M)
06/05/2014 08:16
DEPTH (M)
TVDSS (M)
VSHGRL1 (dec)
GRN (GAPI)
CALIPER (IN)
RDEEP (OHMM)
NPHILS (dec)
DENS (G/CC)
SONIC (US/F)
PHIT_MX1 (FRAC)
PHIE_F1 (FRAC)
BVW_F1 (dec)
PHIH_OB (v/v)
SWE_F1 (FRAC)
PRM_F1 (MD)
KH (mD)
LANDEN CLAY MBR
OMMELANDEN CHALK
1040
1040

12.2.9 HRL-08

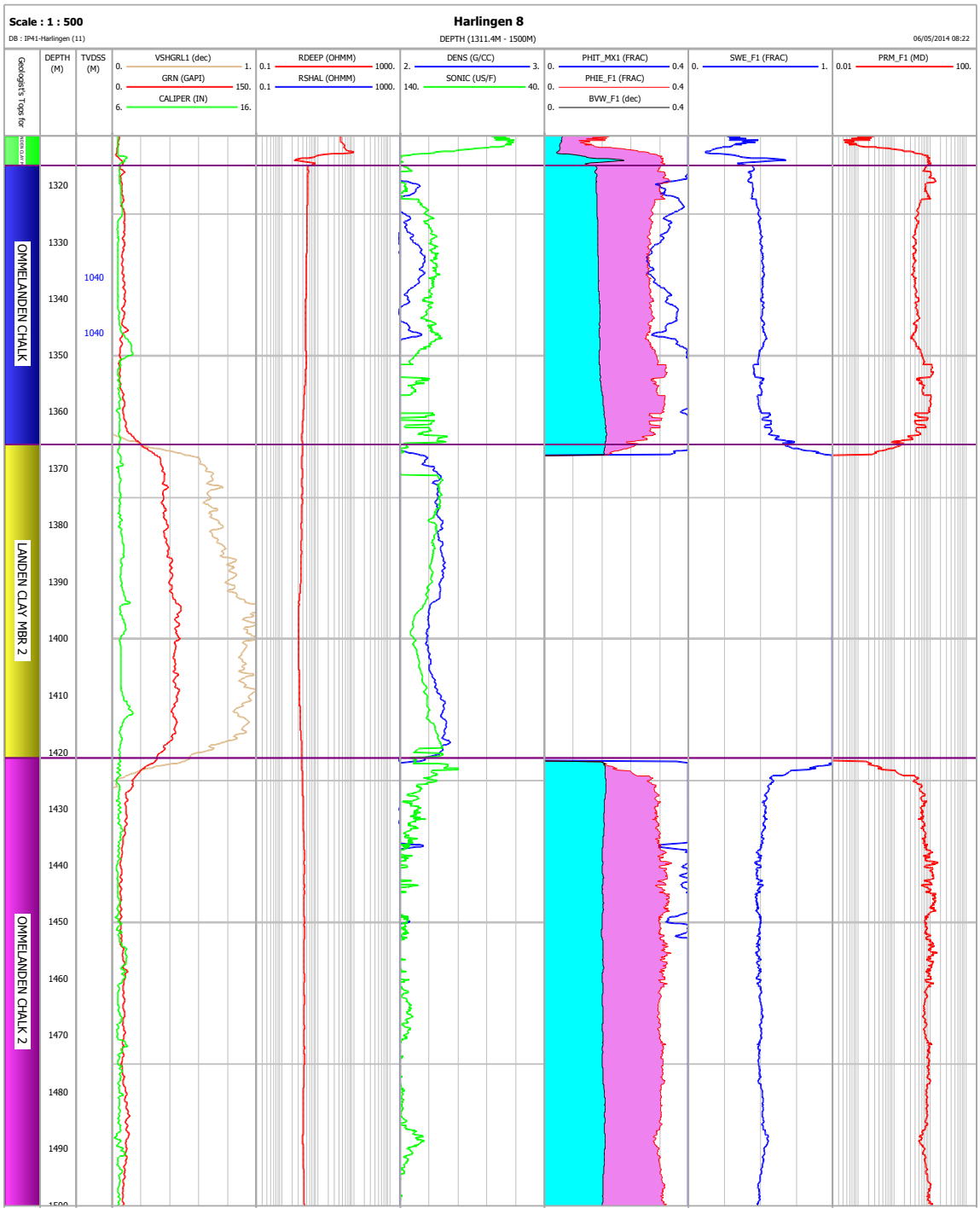
Scale : 1 : 500
Harlingen 8
DB : IP41-Harlingen (11)
DEPTH (1311.4M - 1500M)
06/05/2014 08:22
Geologist's Tops for
DEPTH (M)
TVDSS (M)
VSHGRL1 (dec)
GRN (GAPI)
CALIPER (IN)
RDEEP (OHMM)
RSHAL (OHMM)
DENS (G/CC)
SONIC (US/F)
PHIT_MX1 (FRAC)
PHIE_F1 (FRAC)
BVW_F1 (dec)
SWE_F1 (FRAC)
PRM_F1 (MD)
OMMELANDEN CHALK
LANDEN CLAY MBR 2
OMMELANDEN CHALK 2
1040
1040

12.2.10 HRL-09

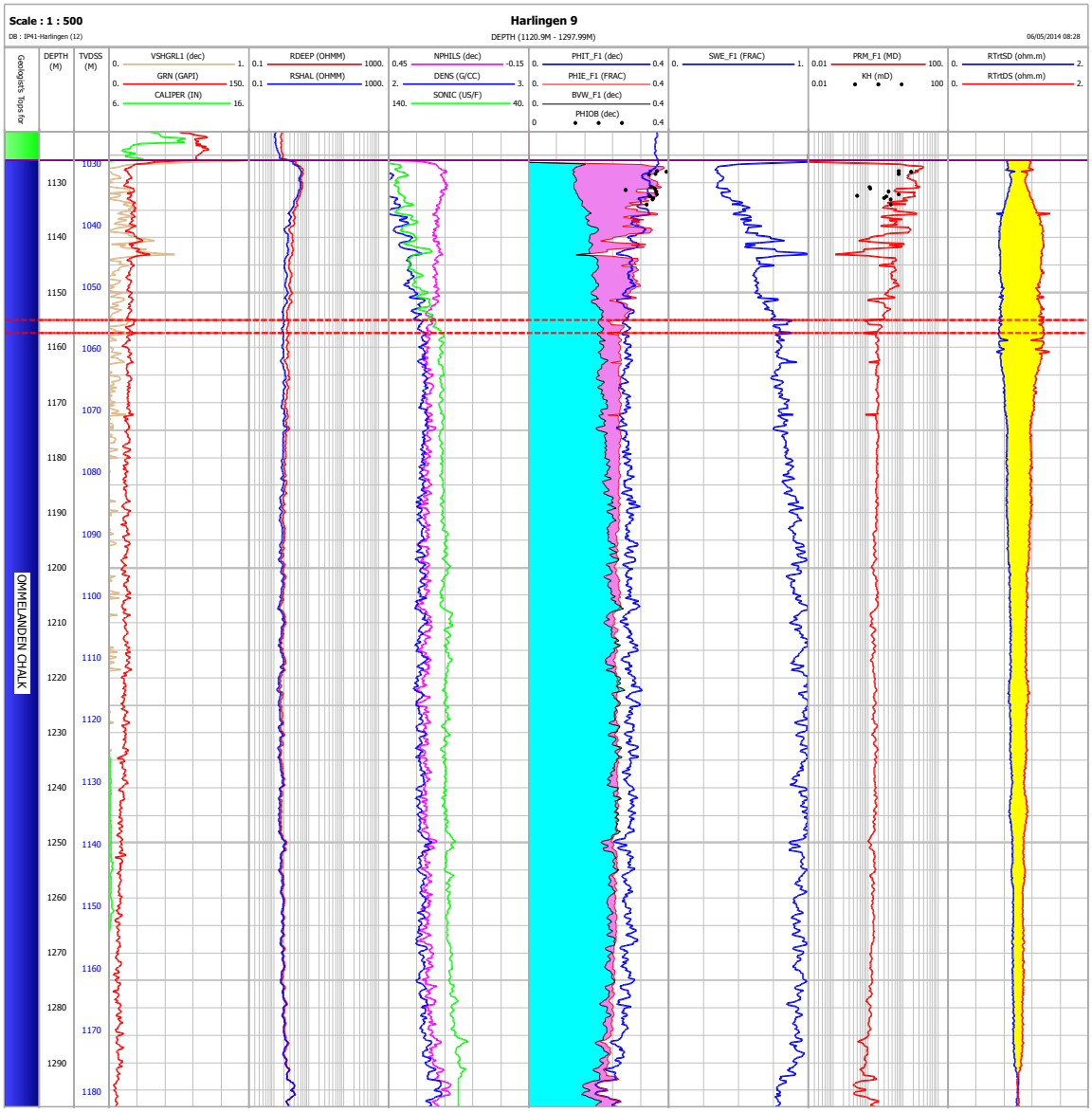
Scale : 1 : 500
Harlingen 9
DEPTH (1120.9M - 1297.99M)
06/05/2014 08:28
DEPTH (M)
TVDSS (M)
VSHGRL1 (dec)
GRN (GAPI)
CALIPER (IN)
RDEEP (OHMM)
RSHAL (OHMM)
NPHILS (dec)
DENS (G/CC)
SONIC (US/F)
PHIT_F1 (dec)
PHIE_F1 (FRAC)
BVW_F1 (dec)
PHIOB (dec)
SWE_F1 (FRAC)
PRM_F1 (MD)
KH (mD)
RTrtSD (ohm.m)
RTrtDS (ohm.m)
OMMELANDEN CHALK

12.2.11 HRL-10-S3

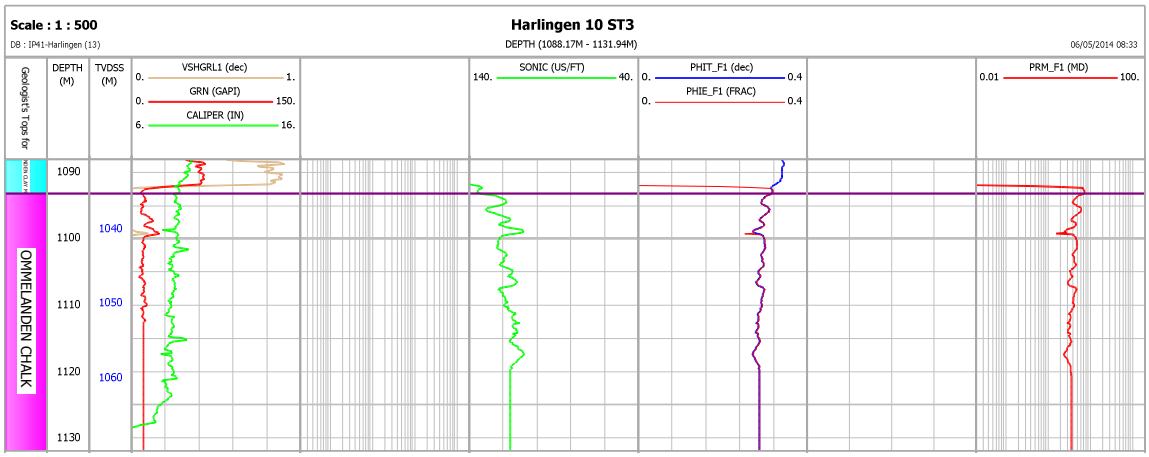

12.2.12 HRL-11-HTZL

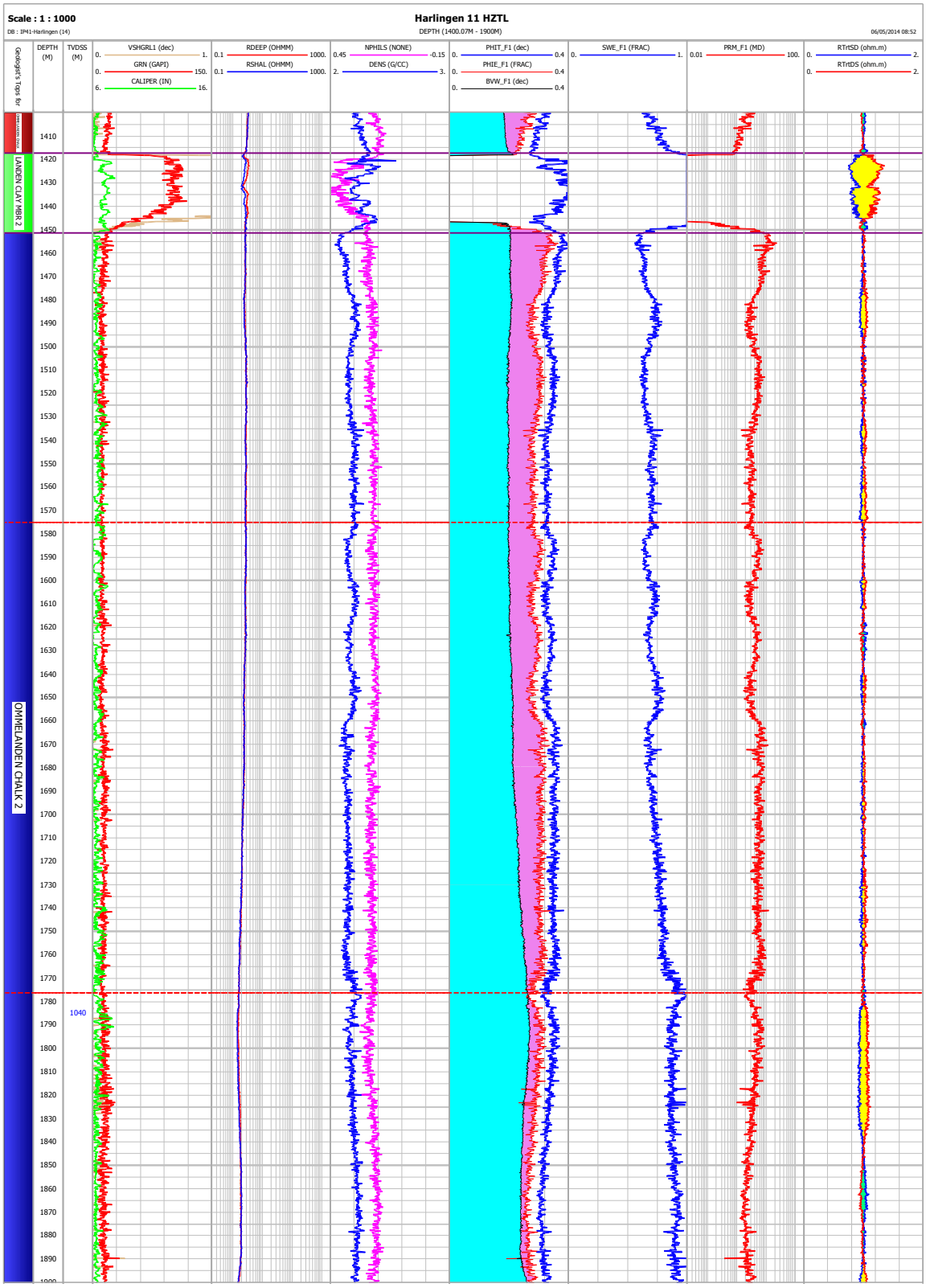

12.2.13 HRL-101

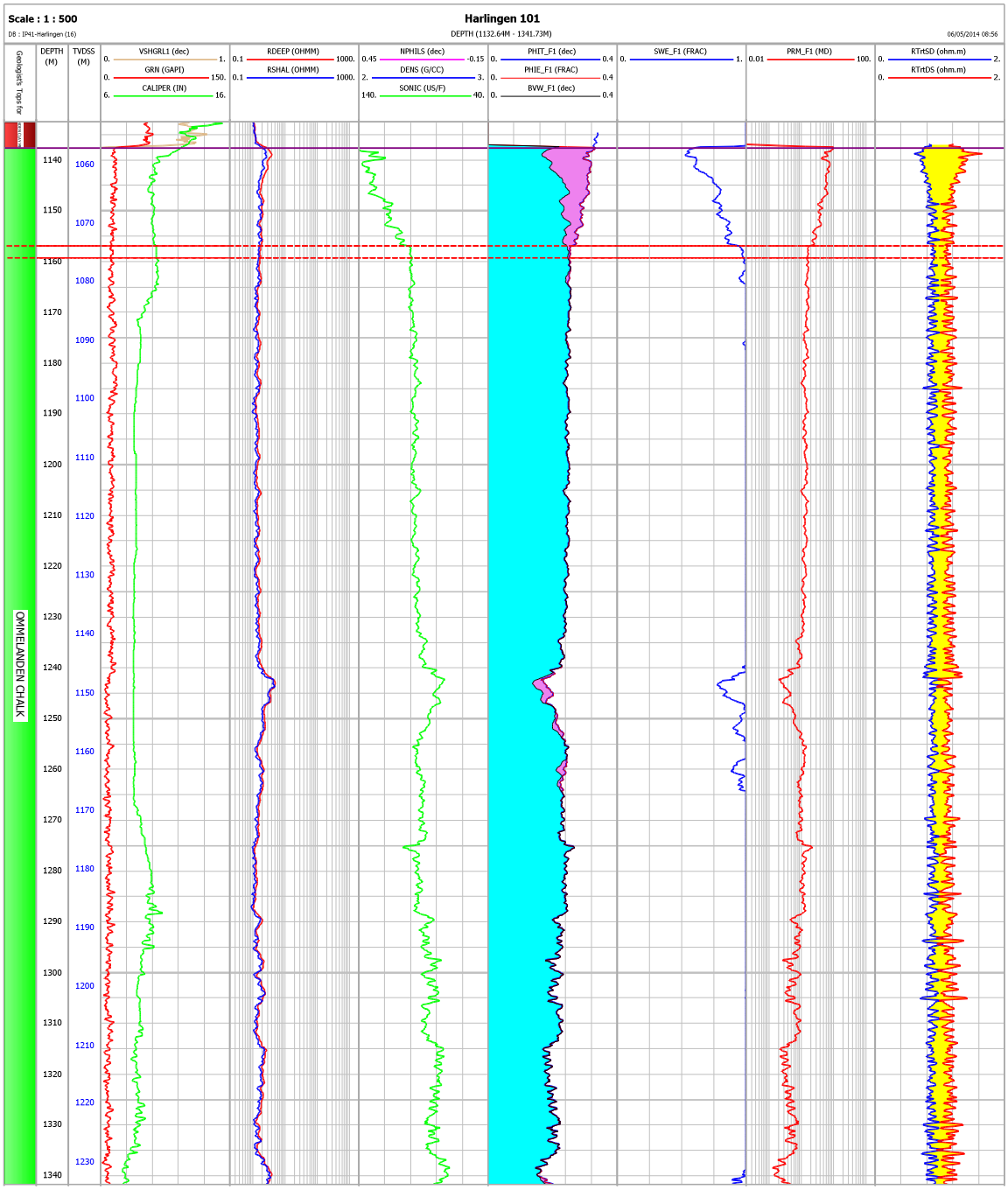

13 APPENDIX 4

13.1 SEISMIC SURVEYS

The tables list the seismic line names per survey that were available for this study.

13.1.1 FR-75 SERIES

FR75-032.STK.0	6
FR75-34.STK.0	
FR-75-15B.STK.0	
FR-75-17.STK.0	
FR-75-36.STK.0	
FR75-021AB.STK.0	

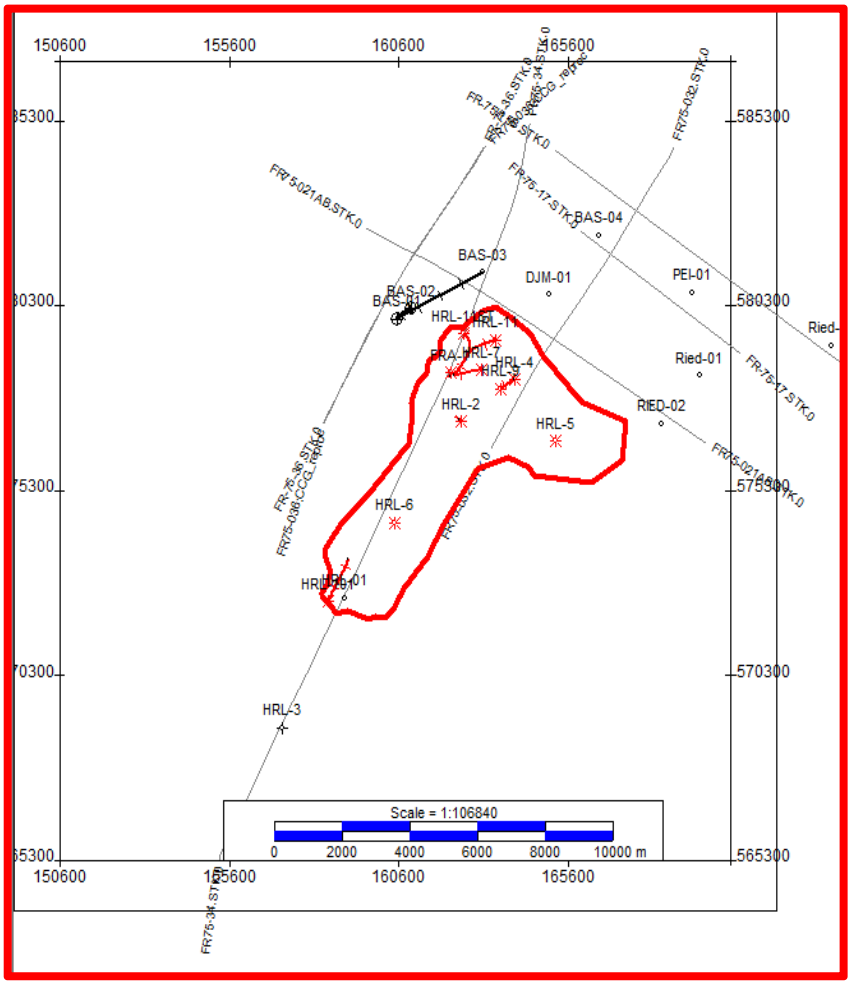

13.1.2 FR-77 SERIES

FR-77-25-3.STK.0	4
FR-77-29.STK.0	
FR77-030-1.STK.0	
FR-77-32-1.STK.0	

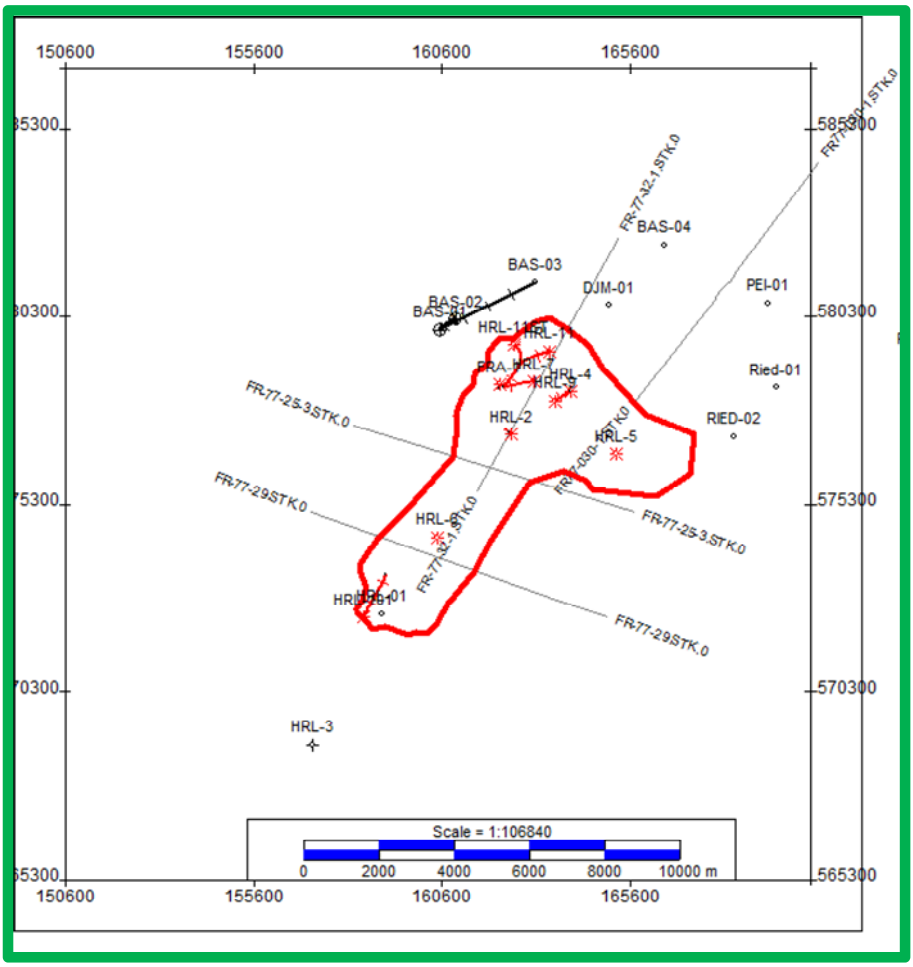

13.1.3 FR-78 SERIES

FR-78-38.STK.0	7
FR-78-34-1.STK.0	
FR78-32-3.STK.0	
FR78-19-1.STK.0	
FR78-030-2.STK.0	
FR78-32-2.STK.0	
FR-78-36.STK.0	

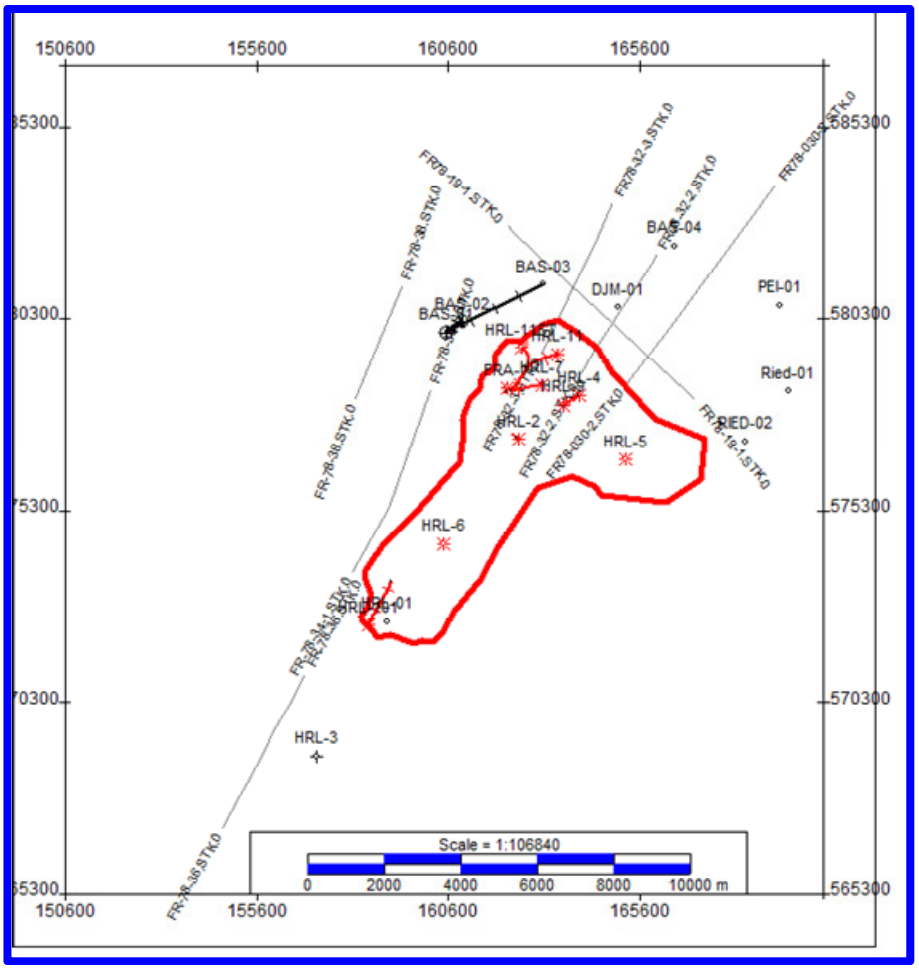

13.1.4 FR-83 SERIES

FR83HR-011.STK.0	4
FR-83-HR-13.STK.0	
FR-83-HR-04.STK.0	
FR-83-HR-06.STK.0	

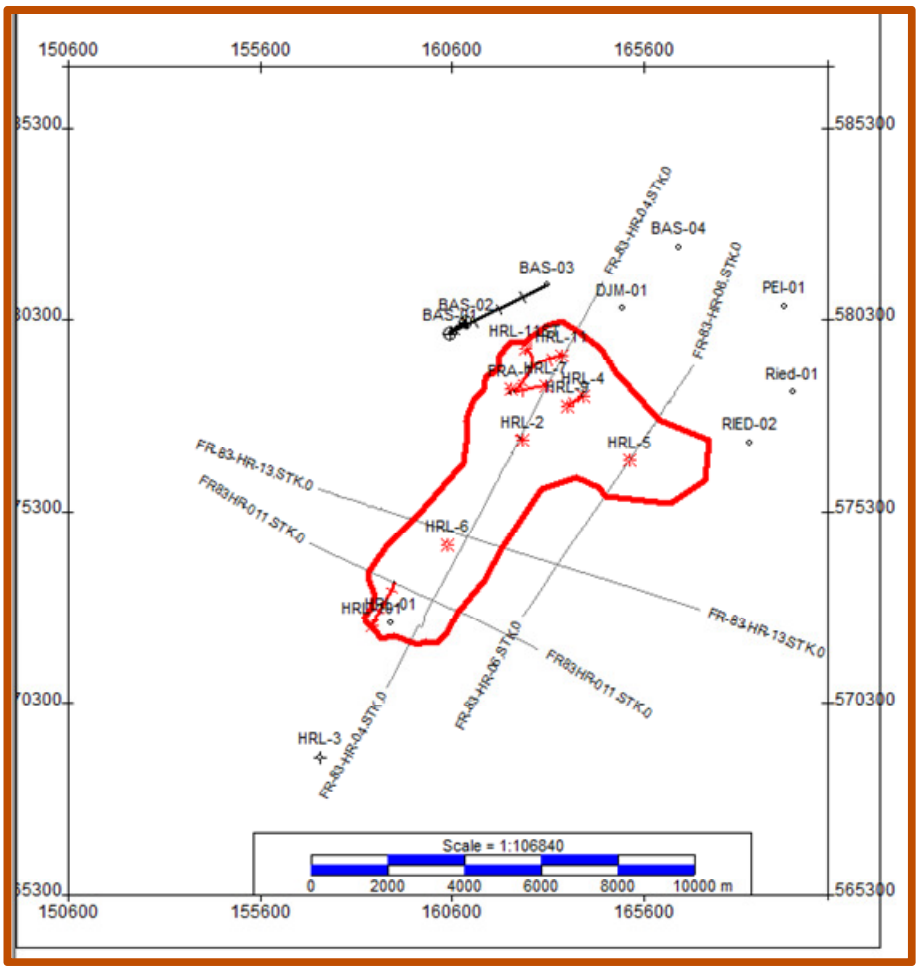

13.1.5 FR-85 SERIES

FR85-10.STK.0	36
FR85-11.STK.0	
FR85-12.STK.0	
FR85-13.STK.0	
FR85-14.STK.0	
FR85-15.STK.0	
FR85-16.STK.0	
FR85-18.STK.0	
FR85-1012.STK.0	
FR85-17.STK.0	
FR85-19.STK.0	
FR85-50.STK.0	
FR85-20.STK.0	
FR85-21.STK.0	
FR85-22.STK.0	
FR85-24.STK.0	
FR85-25.STK.0	
FR85-26.STK.0	
FR85-28.STK.0	
FR85-29.STK.0	
FR85-30.STK.0	
FR85-31.STK.0	
FR85-32.STK.0	
FR85-33.STK.0	
FR85-34.STK.0	
FR85-35.STK.0	
FR85-36.STK.0	
FR85-37.STK.0	
FR85-38.STK.0	
FR85-39.STK.0	
FR85-40.STK.0	
FR85-41.STK.0	
FR85-42.STK.0	
FR85-44.STK.0	
FR85-46.STK.0	
FR85-48.STK.0	

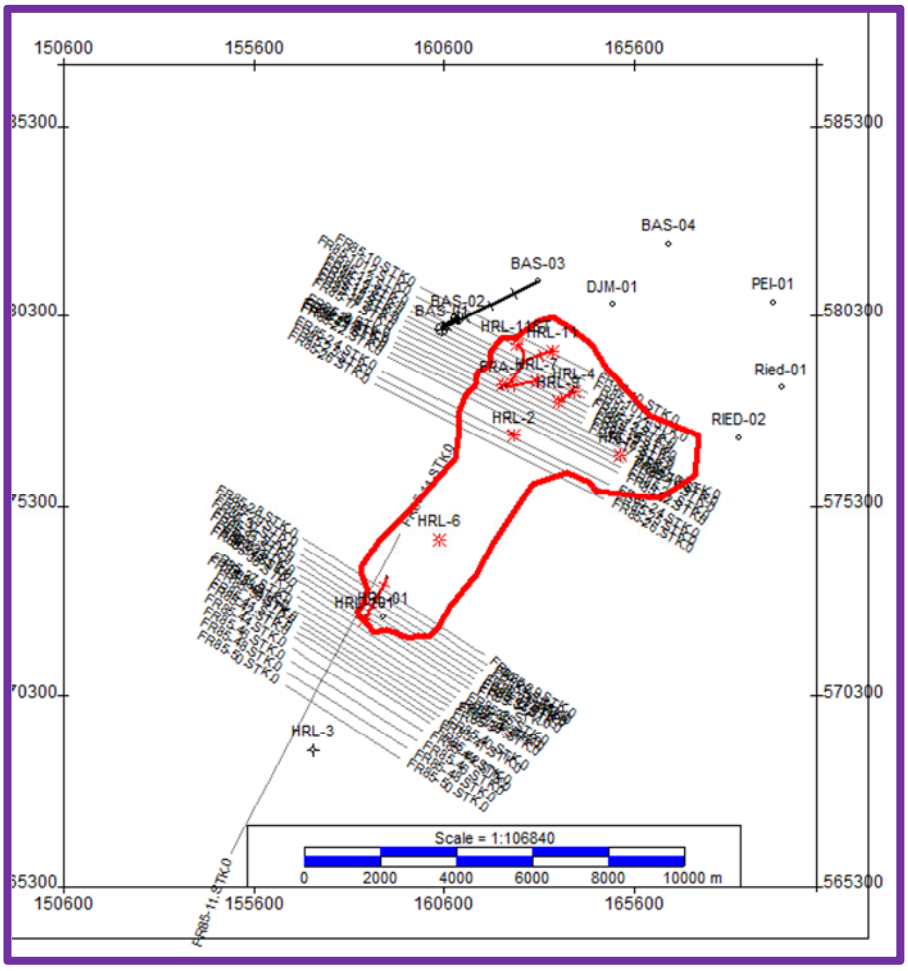
150600
155600
160600
165600
585300
580300
575300
570300
565300
BAS-04
BAS-03
DJM-01
PEI-01
BAS-02
BAS-01
HRL-11
HRL-1
HRL-4
HRL-5
Ried-01
HRL-2
RIED-02
HRL-6
HRL-3
Scale = 1:106840
0
2000
4000
6000
8000
10000 m

13.1.6 FR-89 SERIES

FR89-010.STK.0	5
FR89-14.STK.0	
FR89-12.STK.0	
FR89-15.STK.0	
FR89-13.STK.0	

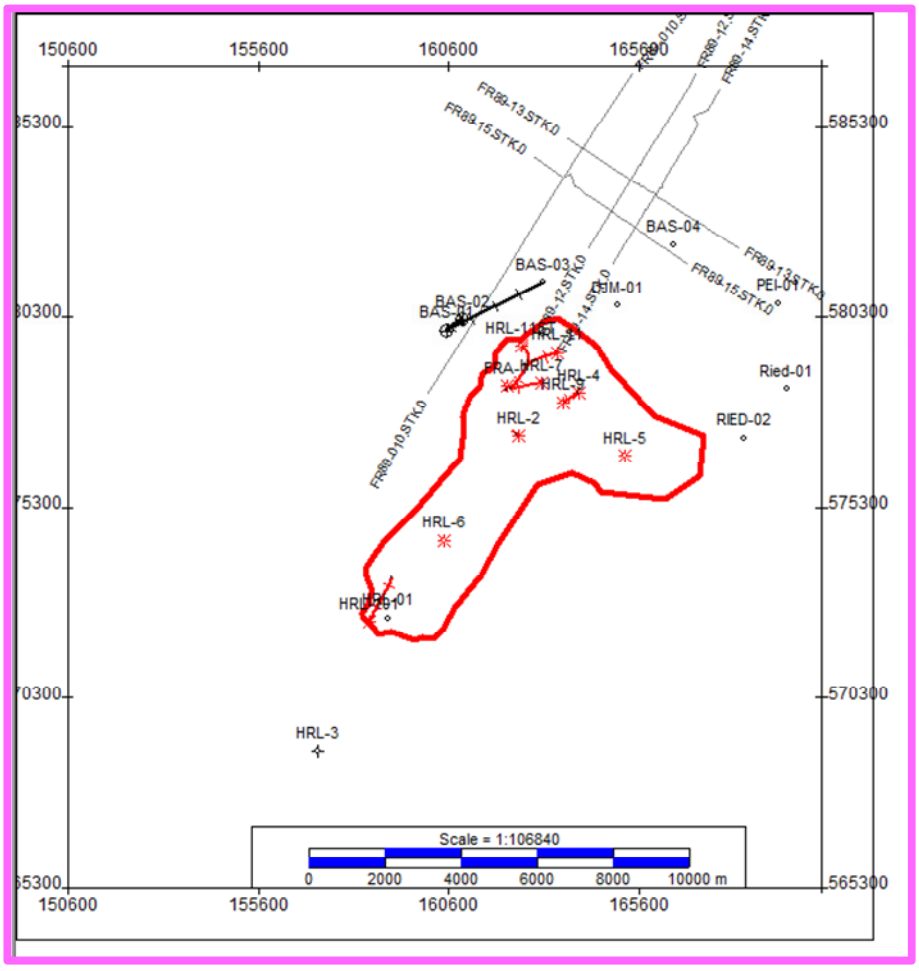

13.1.7 OTHER SEISMIC

437490_002163_0029	**11**
437493_002163_0032	
437491_002163_0030	
437492_002163_0031	
71-W-23	
80-W-25	
80-W-23	
80-W-08	
71-W-24	
72-W-1	
80-W-21.STK.0	

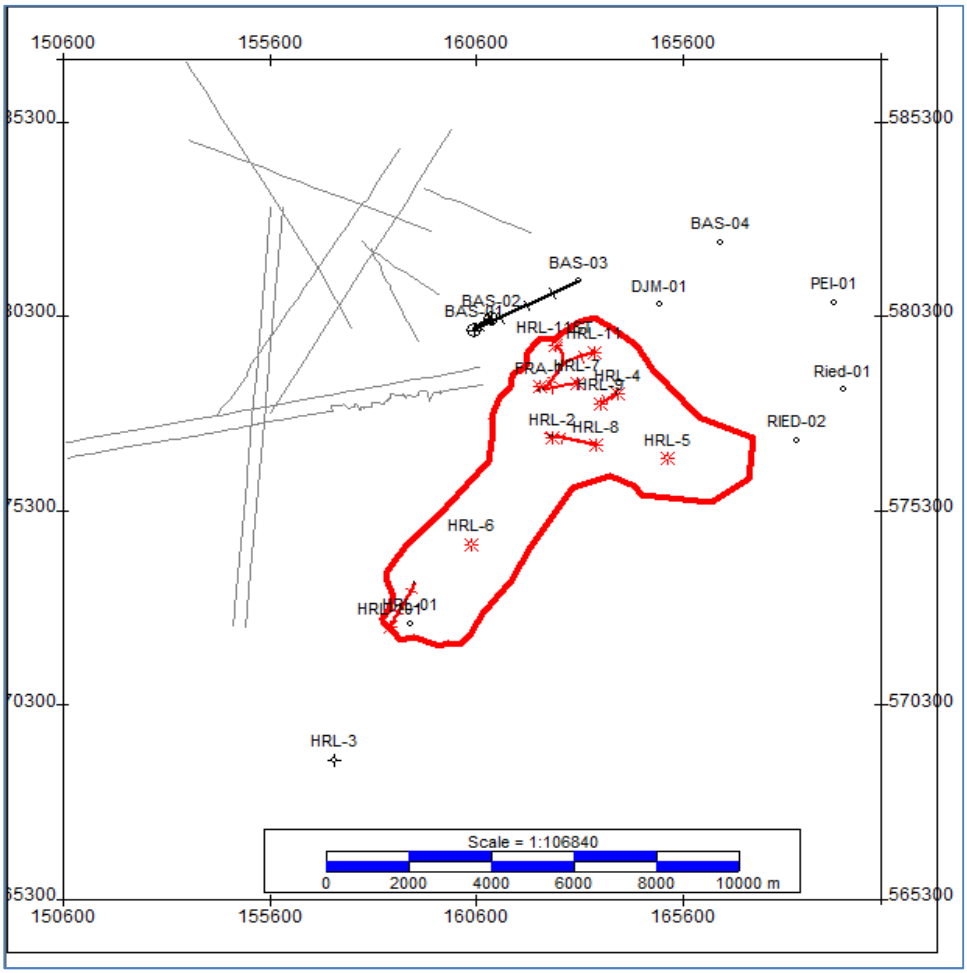

13.2 INTERPRETED SEISMIC HORIZONS – ISOCHRON MAPS

13.2.1 TOP OMMELANDEN CHALK

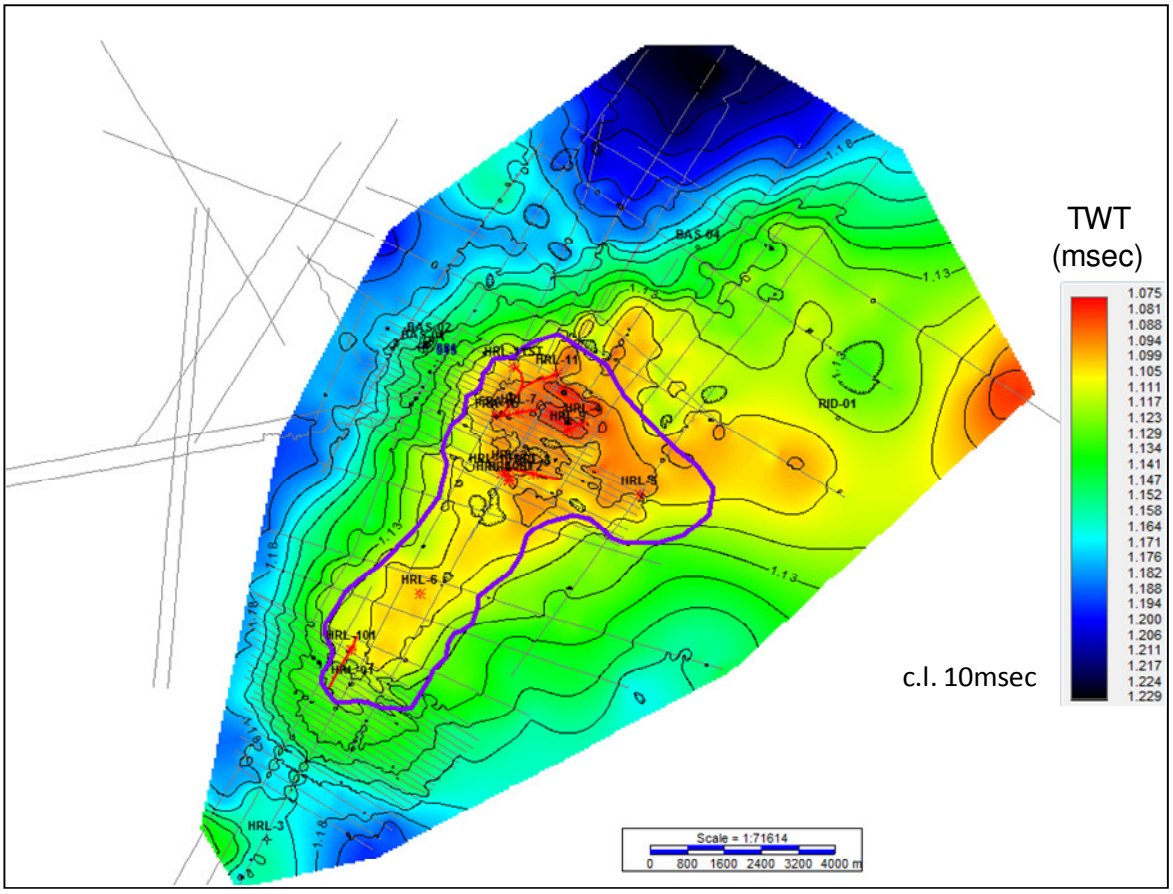

13.2.2 CHALK RESERVOIR BASE

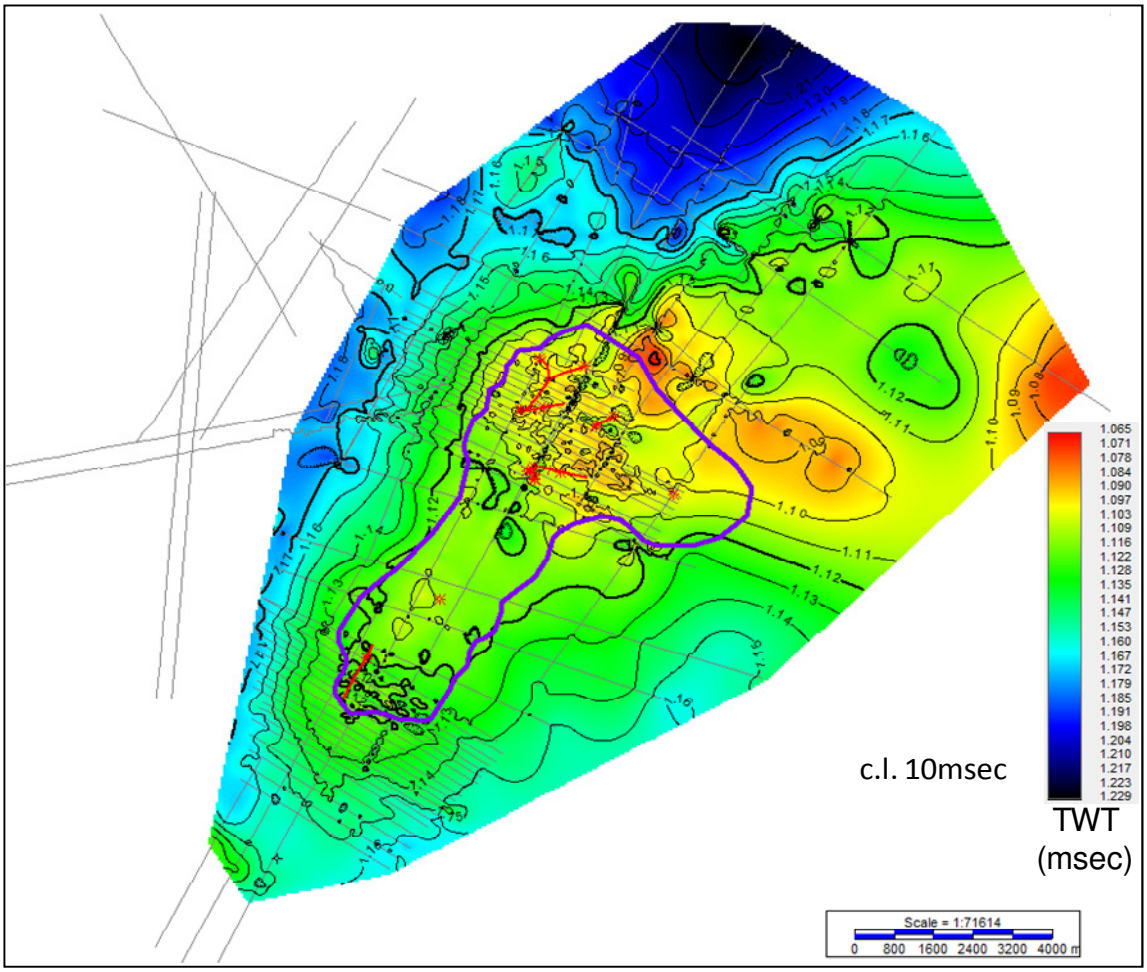

13.2.3 BASE CHALK / TOP HOLLAND MARL

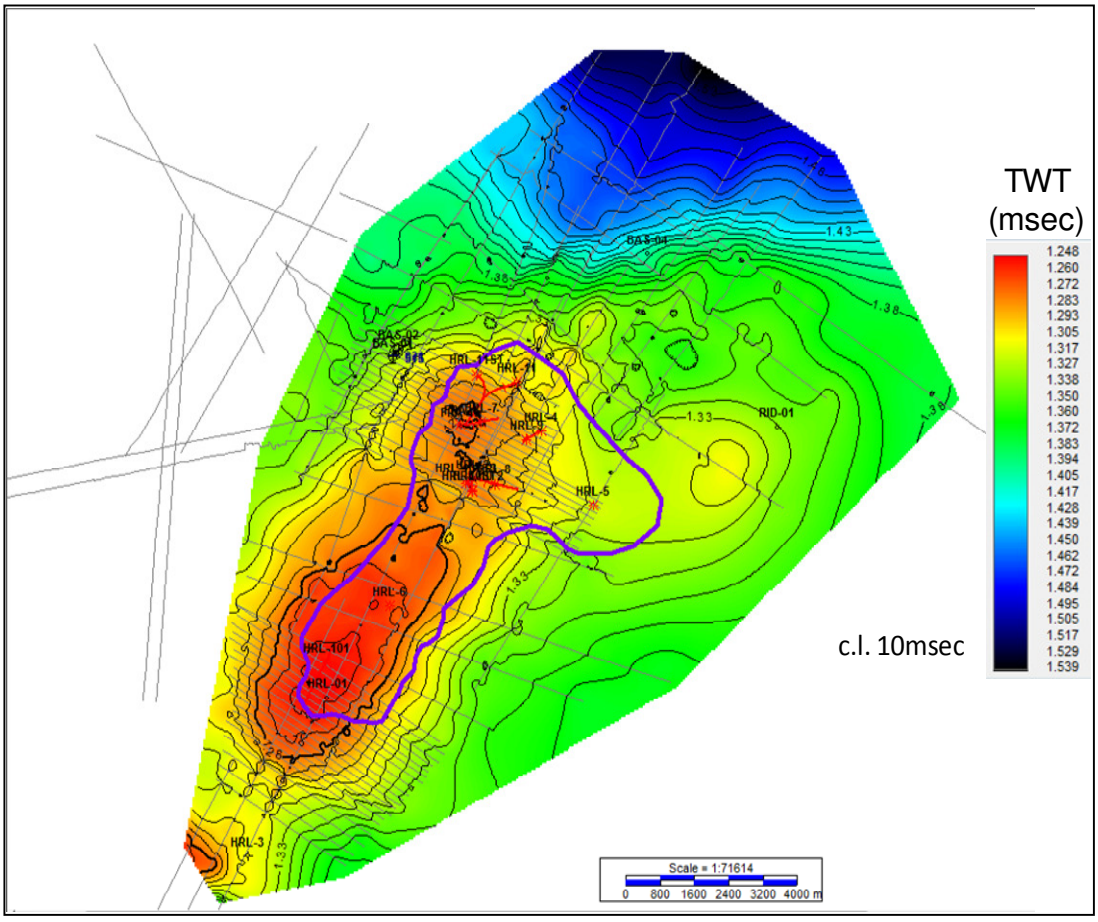

13.3 DEPTH MAPS

13.3.1 TOP OMMELANDEN CHALK

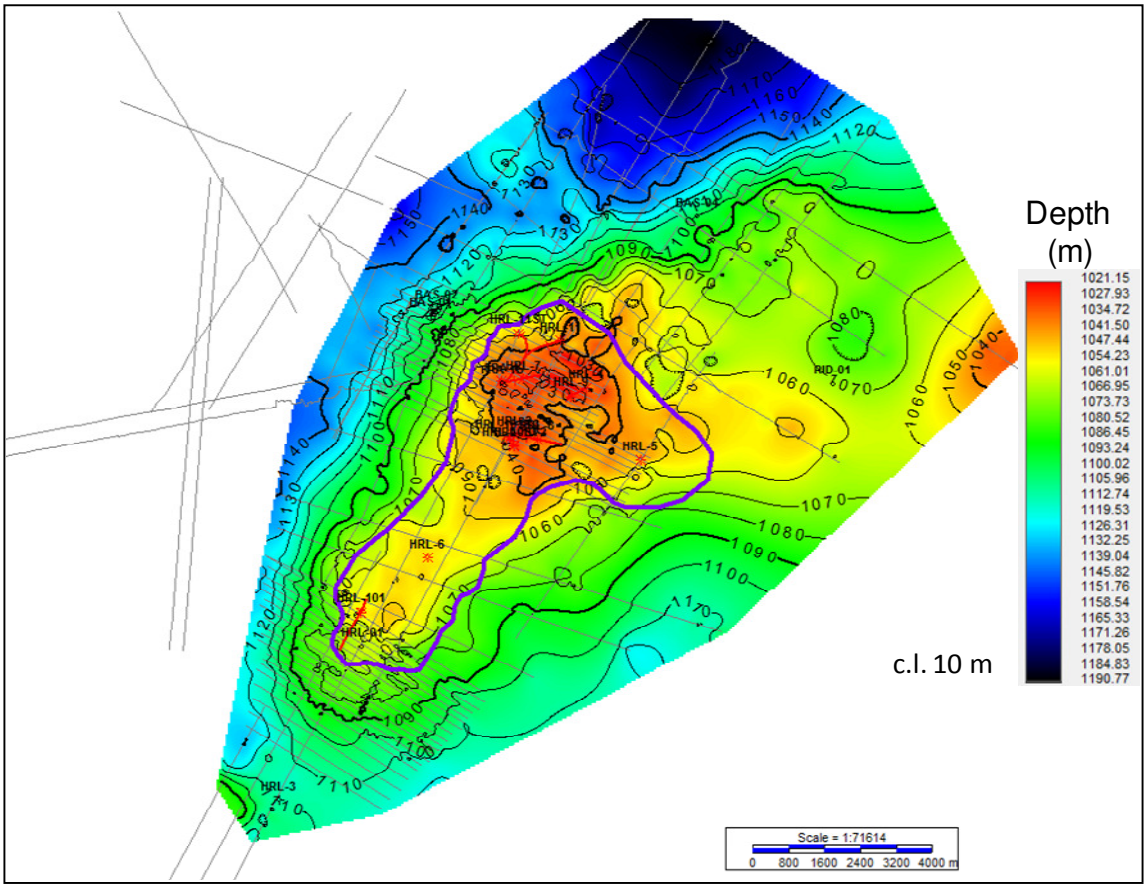

13.3.2 BASE CHALK / TOP HOLLAND MARL

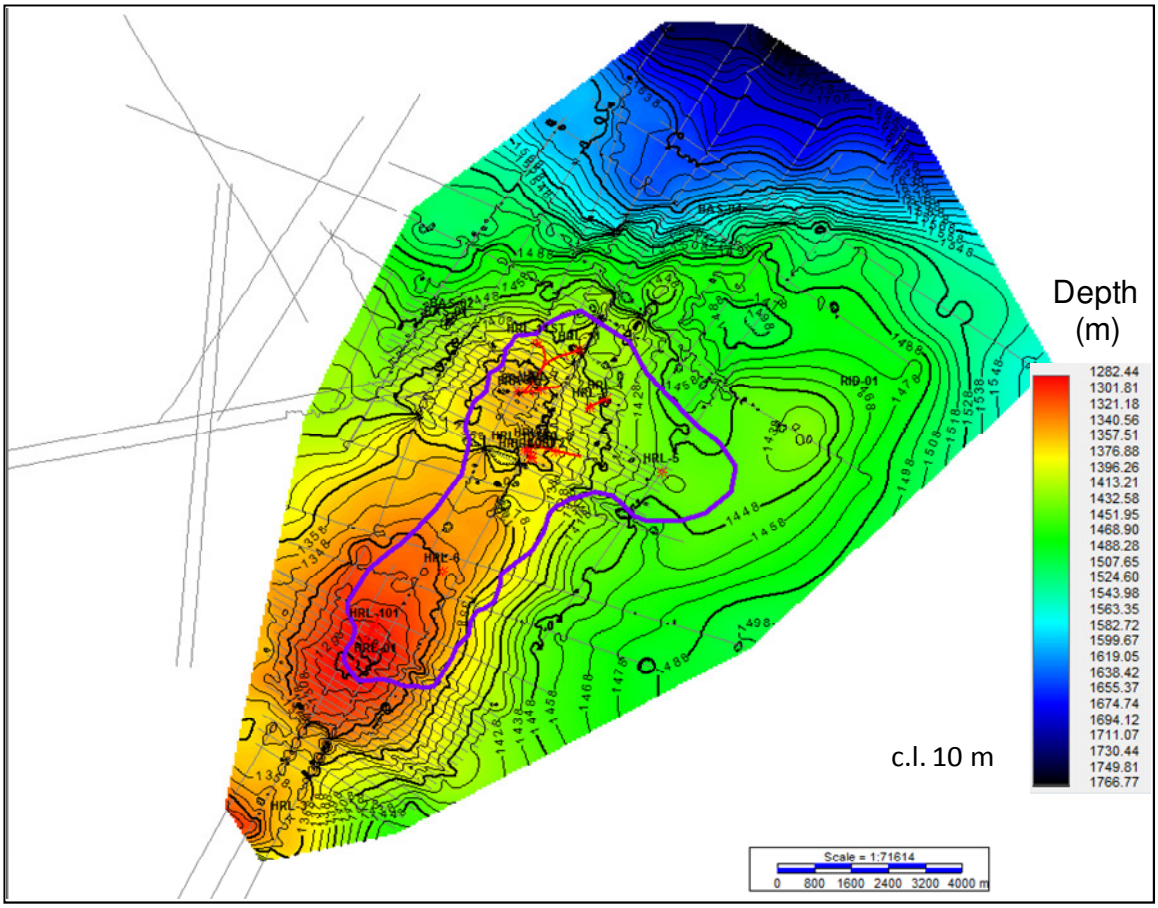

14 APPENDIX 5

VERMILION ENERGY

Vermilion Oil & Gas Netherlands B.V.
Zuidwalweg 2, 8861 NV Harlingen
P.O. Box 71, 8860 AB Harlingen
Tel +31 (0)517 493 333
Fax +31 (0)517 493 330
KvK 34201179
www.vermilionenergy.com

Harlingen-7 Modified Offtake Rate

In the course of history matching the Harlingen Upper Cretaceous field, SGS-Horizon identified Harlingen-7 as having an acceptable history match prior to 2000 and a poor match thereafter. SGS-Horizon proposed that the reservoir model would provide a better match between reservoir pressure and cumulative production if the production rate of that well could be increased by 50%.

A metering and allocation assessment was performed by a third party in November, 2008. While the metering performed provides the required uncertainty band for gas sales, allocation to concessions, and, in most cases, technical work at the individual pool level. The equipment and procedures implemented "provide only a rough estimate of the gas volume produced from each well". This review concluded that there was +/- 20% uncertainty in the flow rate estimates for any given well. To further improve metering at the concession level, three of the four recommendations for Leeuwarden West concession referred to improvements in the gas metering at wells Harlingen-4 and Harlingen-7 (the fourth recommendation referred to sampling and analyzing gas samples that was not done on the previous scheduled time due to the Harlingen Upper Cretaceous Field being shut-in).

The specific gravity cell, used at Harlingen Treatment Center to allocate production between Leeuwarden and Zuidwal Concessions, was removed in 1999 and default gas characteristics were used in the calculation. A review in 2002 concluded that the gas balance between concessions was incorrect, and the gas produced by the Leeuwarden Concession (which the Harlingen Upper Cretaceous Field is included) was underestimated. A recalculation was performed in 2002 and additional gas energy was allocated to the Leeuwarden Concession from the Zuidwal Concession to ensure all partners were treated fairly on a commercial basis, but there is no evidence that this correction was further allocated to the well level. This may have manifested itself as a further under-prediction of Harlingen-7 production (Harlingen-7 was the highest rate producer in the Harlingen Upper Cretaceous Field at that time).

Harlingen-7 has a 100mm (4 inch) Vortex meter to measure gas flow. The output of the meter is captured by an analog stripchart which is collected weekly by the production operator. The minimum flowrate required for the Model E83 Foxboro Vortex meter according to the vendor provided calculation sheet from 1986 is 1215 Nm3/h which is approximately 29 kNm3/d. Harlingen-7 did not see flow rates this low until 2003, but data below this flow rate should certainly be treated as suspect. Also, the lack of an electronic method to integrate the analog stripchart introduces uncertainty in interpretation of this data (the use of a flow computer is common in modern wells to eliminate this error).

It is reasonable to conclude that, in light of the difficulty of obtaining a good history match, there could be enough error in the Harlingen-7 production data to support modifying the offtake rate later in the life of the well. Applying a factor of 50% appears to provide a better history match, and while the actual error in the production rate may not be exactly this amount (i.e., the accuracy may have had different causes and the percentage error may have changed over time), it is entirely plausible that this is within the measurement error of the production data being recorded for this particular well.

Kind Regards,

Rod Gibbons
Technical Team Lead Reservoir & Exploitation Engineering

15 APPENDIX 6

15.1 DYNAMIC MODEL INPUT

15.1.1 WELL TESTS

Table 15-1 Well test interpretation: summary of results

Well	Type	Properties	1984	1987	1991	1996	2005	2006	2008	Comments
FRA-01	vertical, acidized	k*h h [m] k [mD] s [-] ϕ [%]			3.70 22.50 0.17 -3.75 29.00					
HRL-02	vertical, acidized	k*h [mD*m] h [m] k [mD] s [-] ϕ [%]				7.17 19.00 0.38 -3.08		6.54 19.00 0.34 -3.27	7.22 19.00 0.38 -2.15	fractured
HRL-04	vertical, acidized	k*h h [m] k [mD] s [-] ϕ [%]	24.00 15.00 1.60 -4.50 26.00			22.59 17.00 1.33 -2.55	18.83 17.00 1.11 -2.97		24.77 17.00 1.75 -2.27	fractured, scattered derivative towards the end of the test in 1996
HRL-05	vertical, acidized	k*h h [m] k [mD] s [-] ϕ [%]	11.40 9.00 1.27 -4.70 26.00			10.80 15.00 0.72 -4.50	10.44 17.00 0.61 -2.62		10.78 15.00 0.72 -1.38	fractured, derivatives scattered in 2005 anad 2008
HRL-06	vertical, acidized	k*h h [m] k [mD] s [-] ϕ [%]		11.26 6.00 1.88 -2.50 25.00			64.80 10.00 6.46 96.19		2.80 10.00 0.28 -0.04	fractured; 1996: very scattered derivative, interpreted skin unreasonably high
HRL-07	horizontal, acidized	k*h h [m] k [mD] s [-] ϕ [%]						23.00 20.00 1.15 -1.85	28.93 20.00 1.45 -3.15	fractured, scattered derivative
HRL-08	deviated, acidized	k*h h [m] k [mD] s [-] ϕ [%]				22.00 10.00 2.20 -2.71		4.00 10.00 0.40 -4.21	4.00 10.00 0.40 -3.63	fractured; 1996: scattered derivative, interpreted k significantly differs from consecutive tests
HRL-09	deviated, acidized	k*h h [m] k [mD] s [-] ϕ [%]						7.56 27.00 0.28 -1.40	7.56 27.00 0.28 -0.78	fractured
HRL-10S3	deviated, acidized	k*h h [m] k [mD] s [-] ϕ [%]							5.38 19.00 0.28 -2.50	fractured

15.1.2 PRESSURES

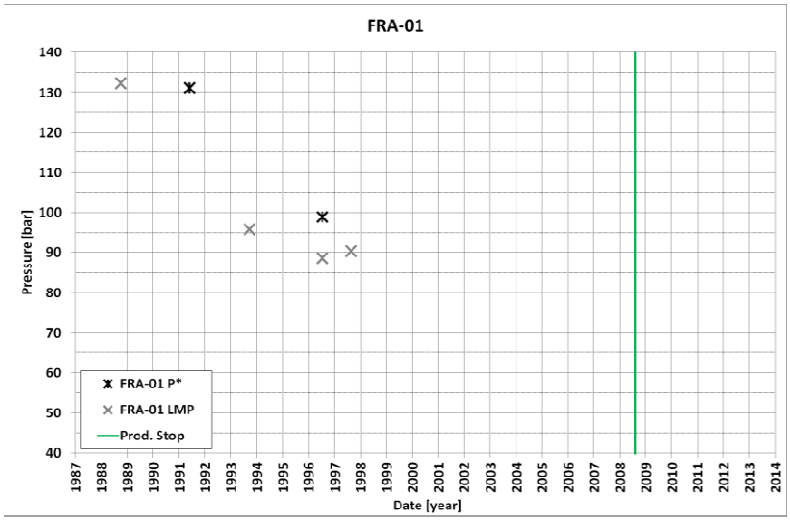

Figure 15-1 **FRA-01 static bottom-hole pressures (p* black, LMP grey, unreliable red, production stop green)**

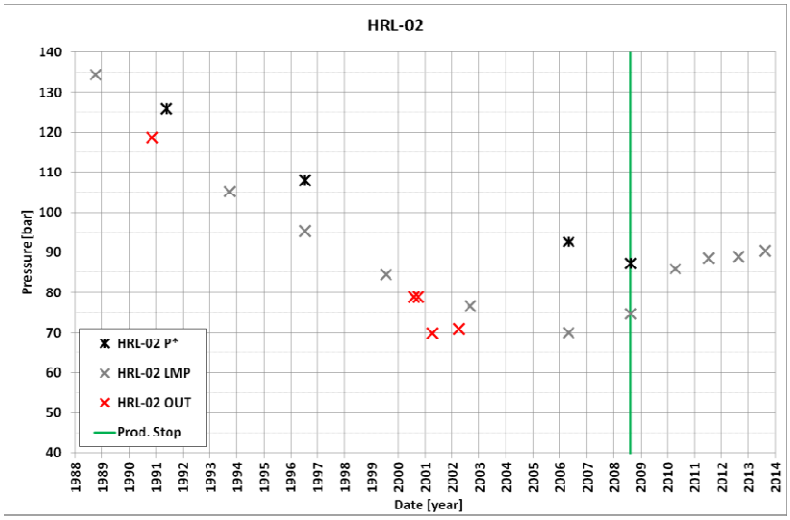

Figure 15-2 **HRL-02 static bottom-hole pressures (p* black, LMP grey, unreliable red, production stop green)**

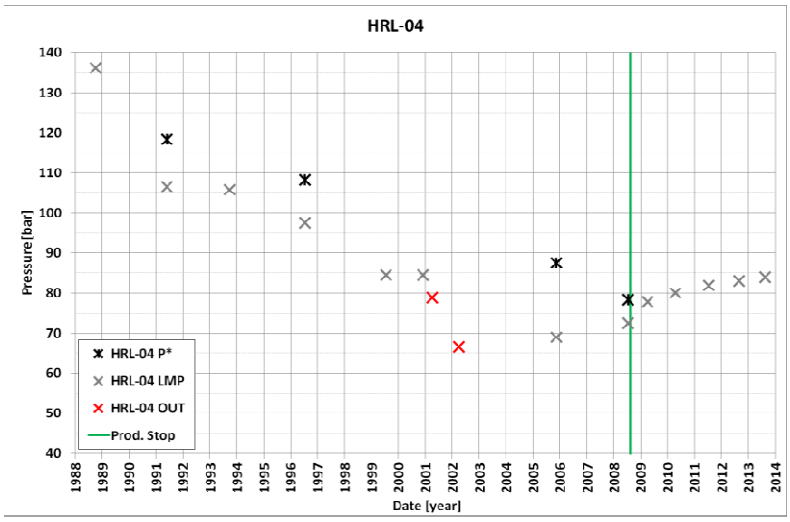

Figure 15-3 **HRL-04 static bottom-hole pressures (p* black, LMP grey, unreliable red, production stop green)**

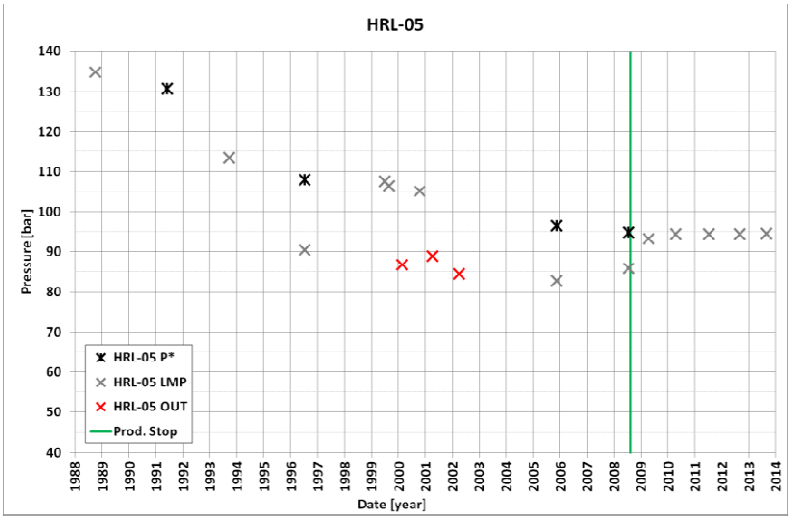

Figure 15-4 **HRL-05 static bottom-hole pressures (p* black, LMP grey, unreliable red, production stop green)**

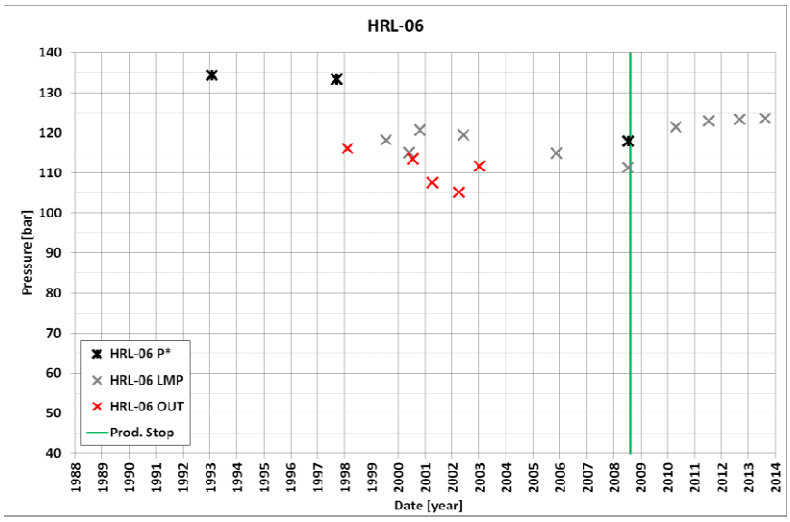

Figure 15-5 **HRL-06 static bottom-hole pressures (p* black, LMP grey, unreliable red, production stop green)**

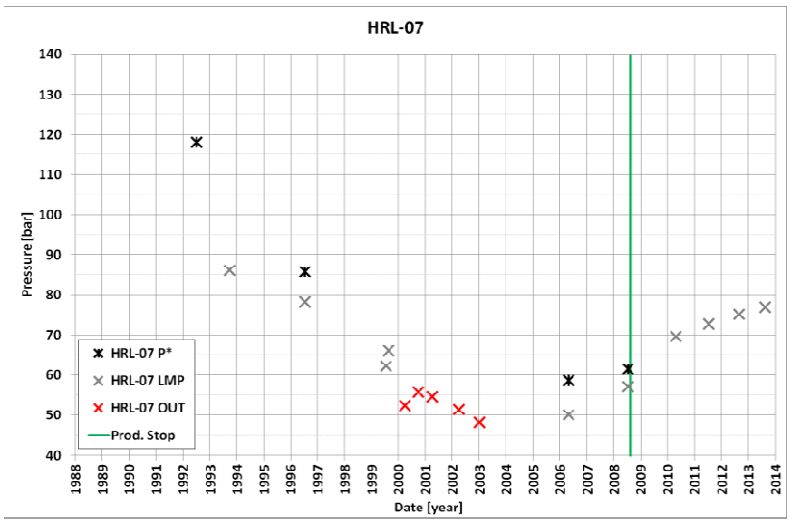

Figure 15-6 **HRL-07 static bottom-hole pressures (p* black, LMP grey, unreliable red, production stop green)**

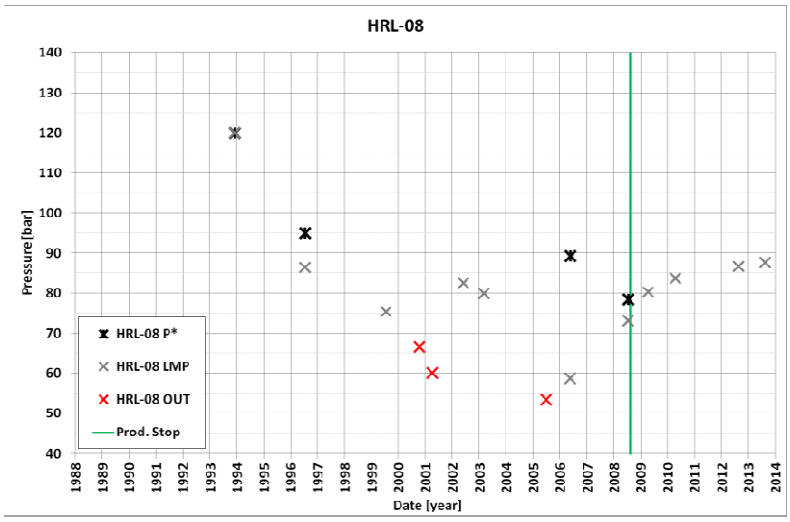

Figure 15-7 **HRL-08 static bottom-hole pressures (p* black, LMP grey, unreliable red, production stop green)**

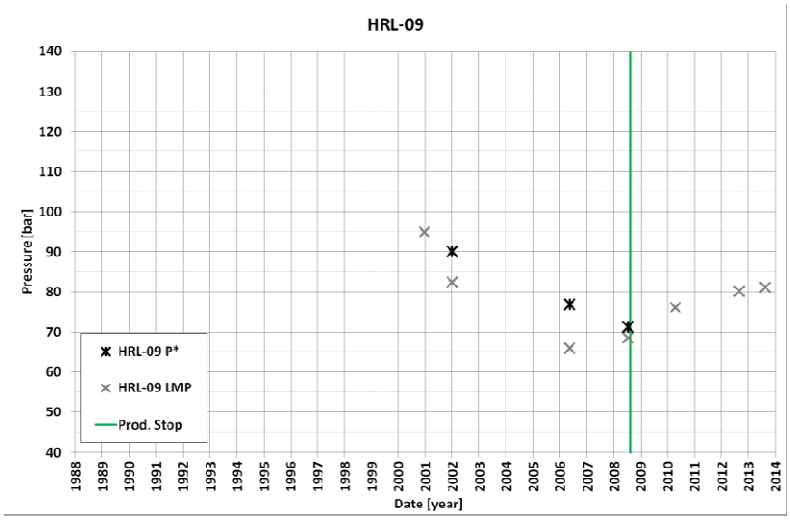

Figure 15-8 **HRL-09 static bottom-hole pressures (p* black, LMP grey, unreliable red, production stop green)**

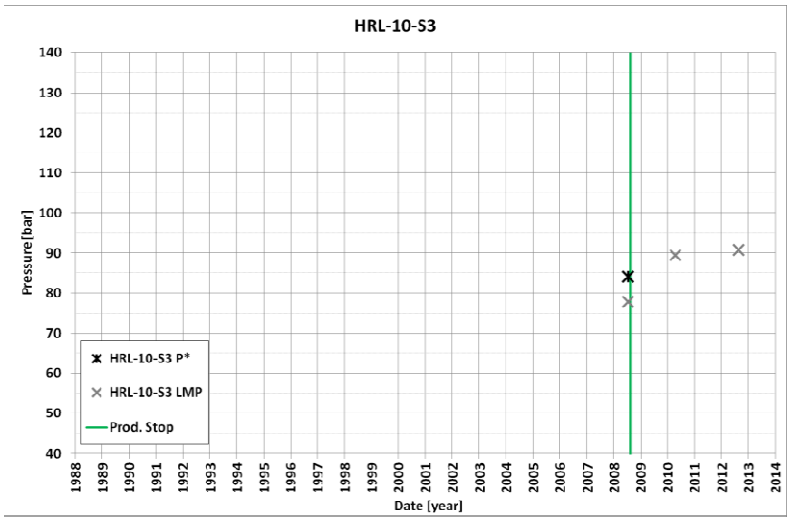

Figure 15-9 **HRL-10-S3 static bottom-hole pressures (p* black, LMP grey, unreliable red, production stop green)**

15.1.3 FLUID PROPERTIES

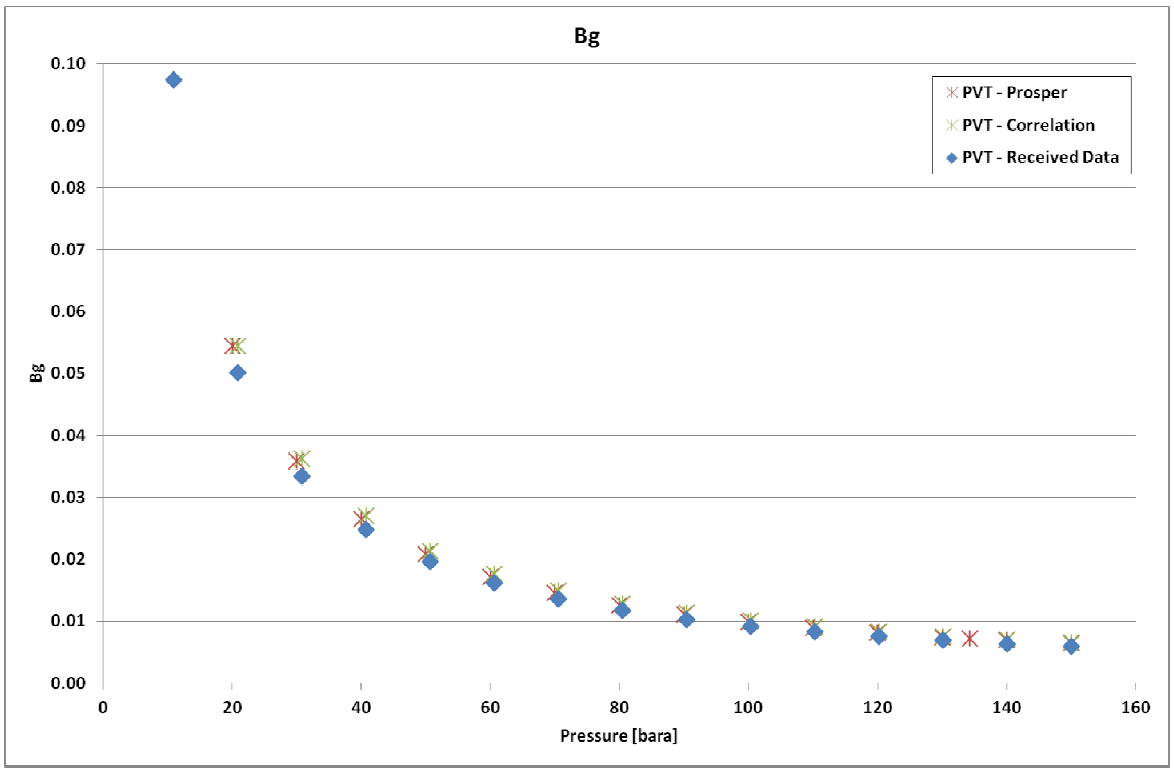

Figure 15-10 **Gas properties: formation volume factor B_g**

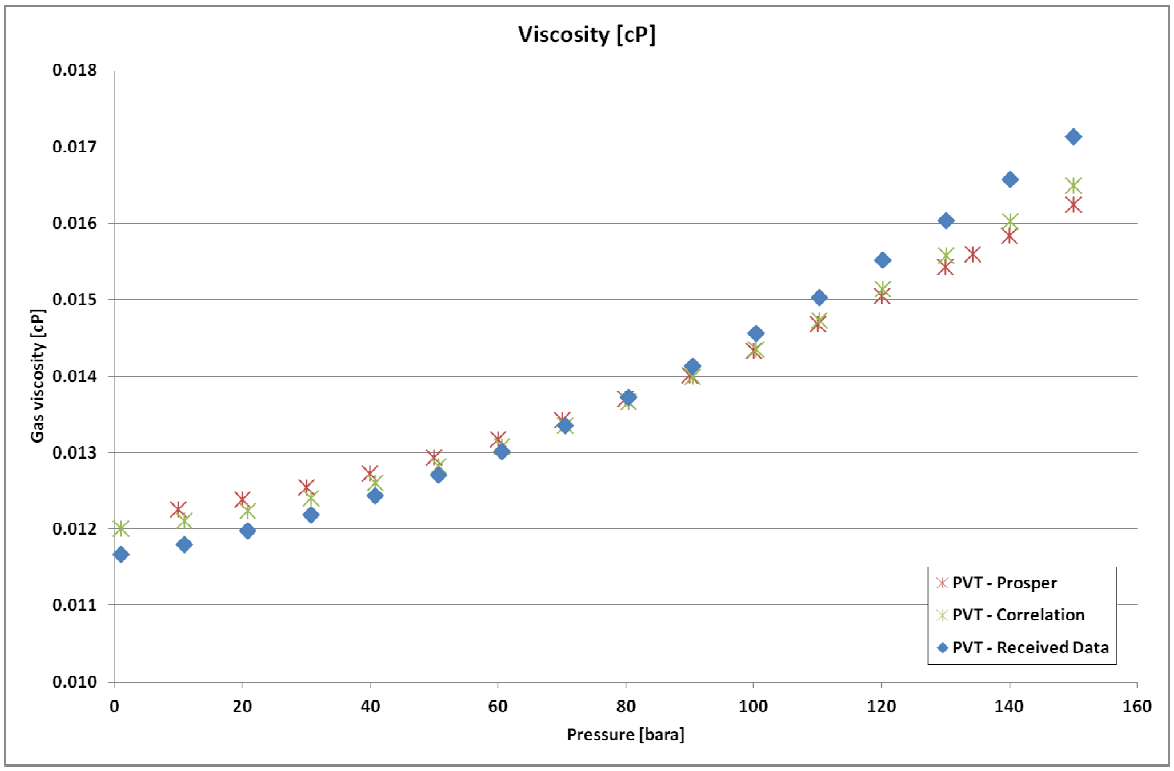

Figure 15-11 Gas properties: viscosity μ_g [cP]

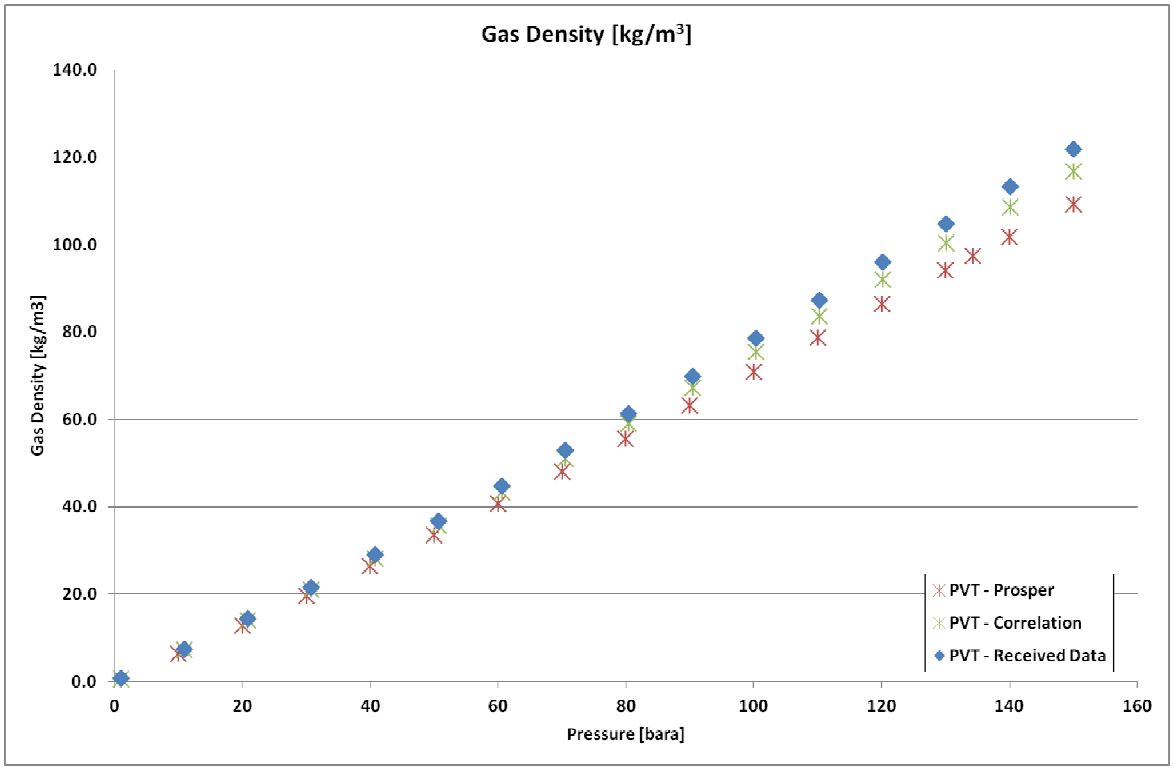

Figure 15-12 Gas properties: density ρ_g [kg/m^3]

15.2 HISTORY MATCH

The average reservoir pressure development for the original history match, i.e. without applying the adjusted offtake in well HRL-07, is shown in Figure 15-13.

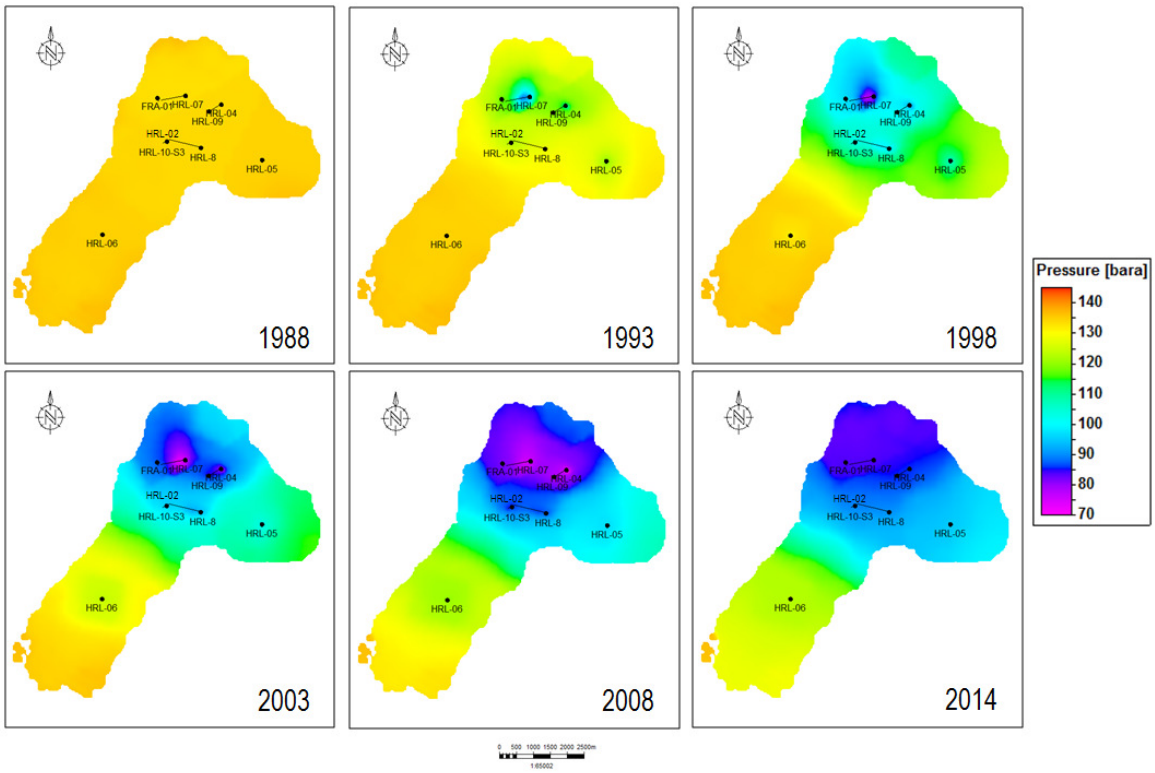

Figure 15-13 Reservoir pressure development: original history matched model

15.2.1 WELL BY WELL RESULTS

In this appendix the history match results for the fine grid history match, including the original and adjusted offtake scenario, and the Franeker area sensitivity are shown.

The original history match is shown as black line, the history match based on the adjusted offtake, which is being carried as final history match, as green line and the history match for the Franeker area sensitivity as red line. The historical pressure are shown as black dots (p*) and grey dots (LMP). Historical production data are shown as black crosses. Note, the historical water production was zero.

In case lines are on top of each other the final history match is displayed (green line).

15.2.1.1 FRA-01

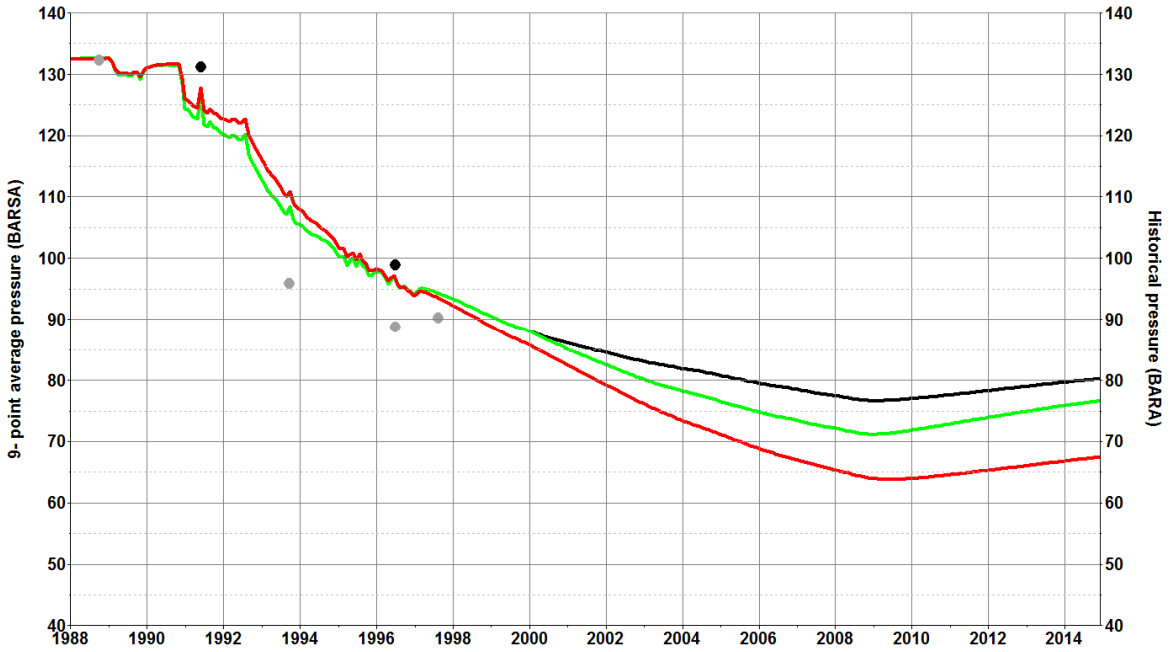

Figure 15-14 FRA-01 HM, pressure (green line = history match, black line = original history match, red line = Franeker sensitivity, black dots = p*, grey dots = LMP reliable, red dots = LMP unreliable)

Figure 15-15 FRA-01 HM, gas production rate (green line = history match, black line = original history match, red line = Franeker sensitivity, black crosses = historical data)

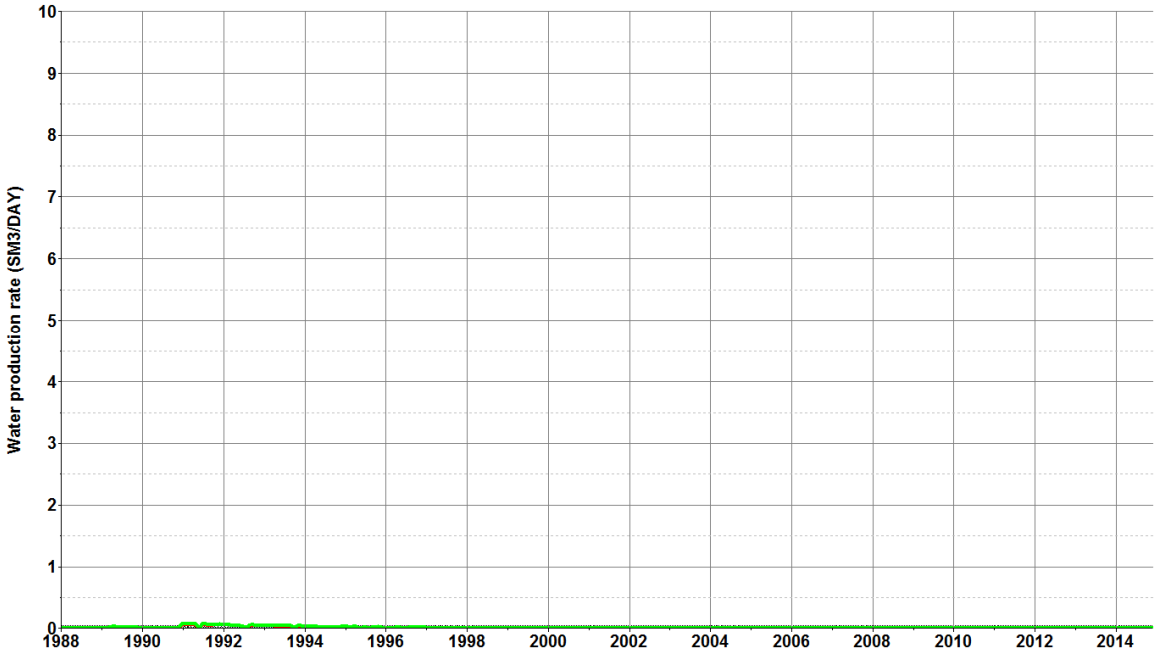

Figure 15-16 **FRA-01 HM: water production rate (green line = history match, black line = original history match, red line = Franeker sensitivity, black crosses = historical data)**

15.2.1.2 HRL-02

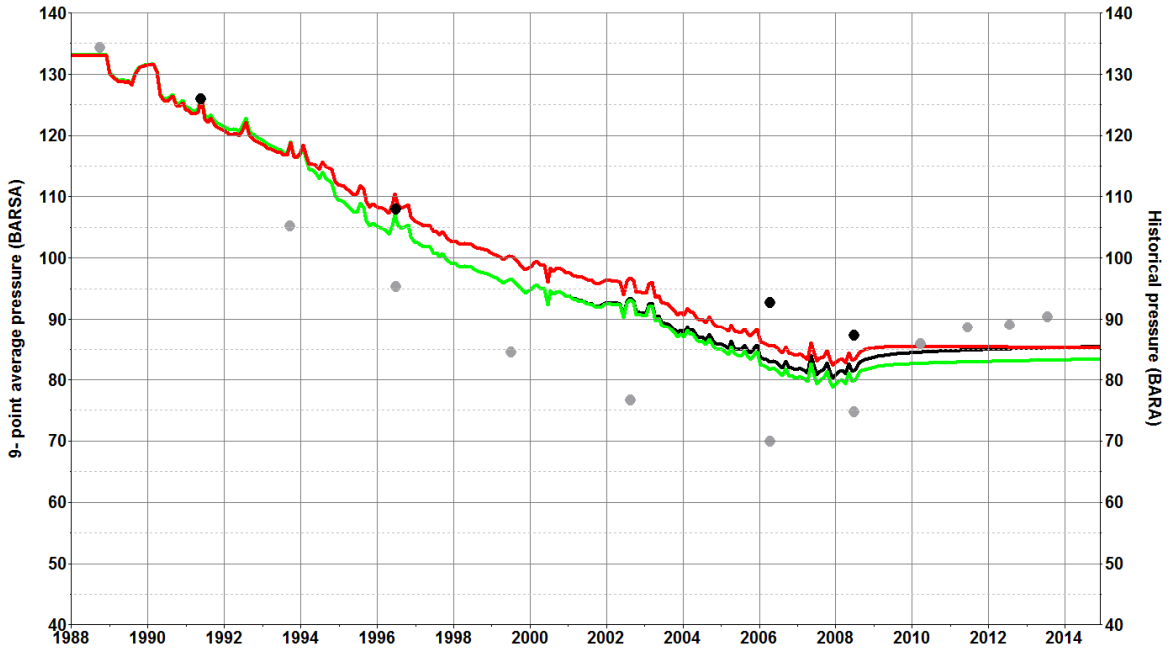

Figure 15-17 **HRL-02 HM, pressure (green line = history match, black line = original history match, red line = Franeker sensitivity, black dots = p*, grey dots = LMP reliable, red dots = LMP unreliable)**

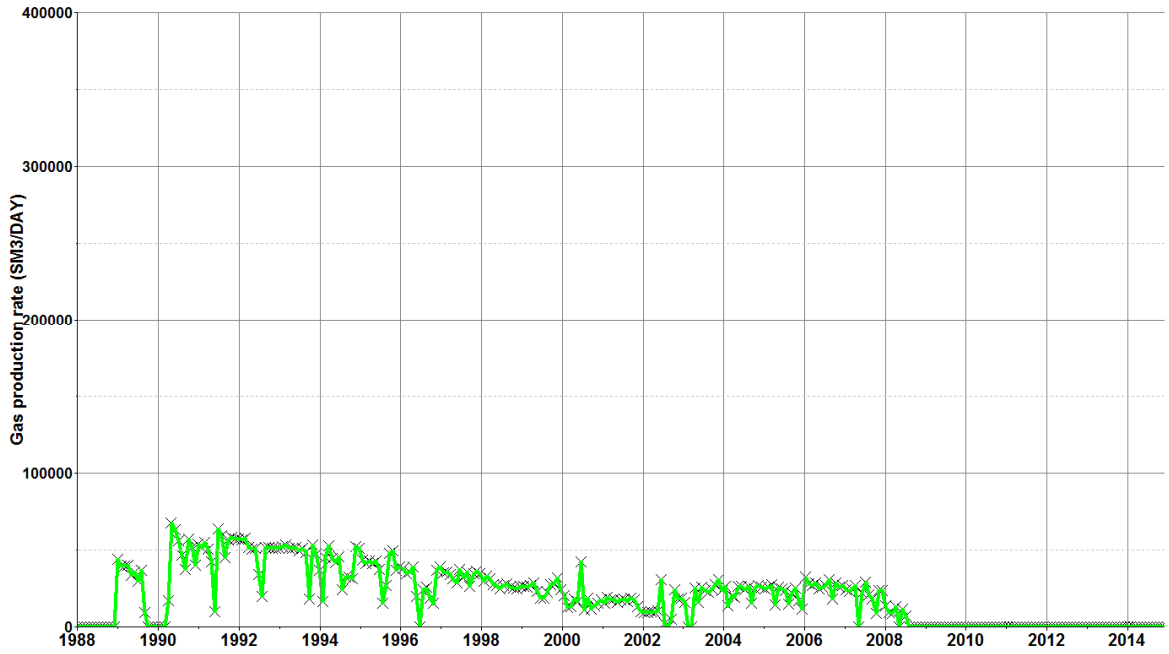

Figure 15-18 HRL-02 HM, gas production rate (green line = history match, black line = original history match, red line = Franeker sensitivity, black crosses = historical data)

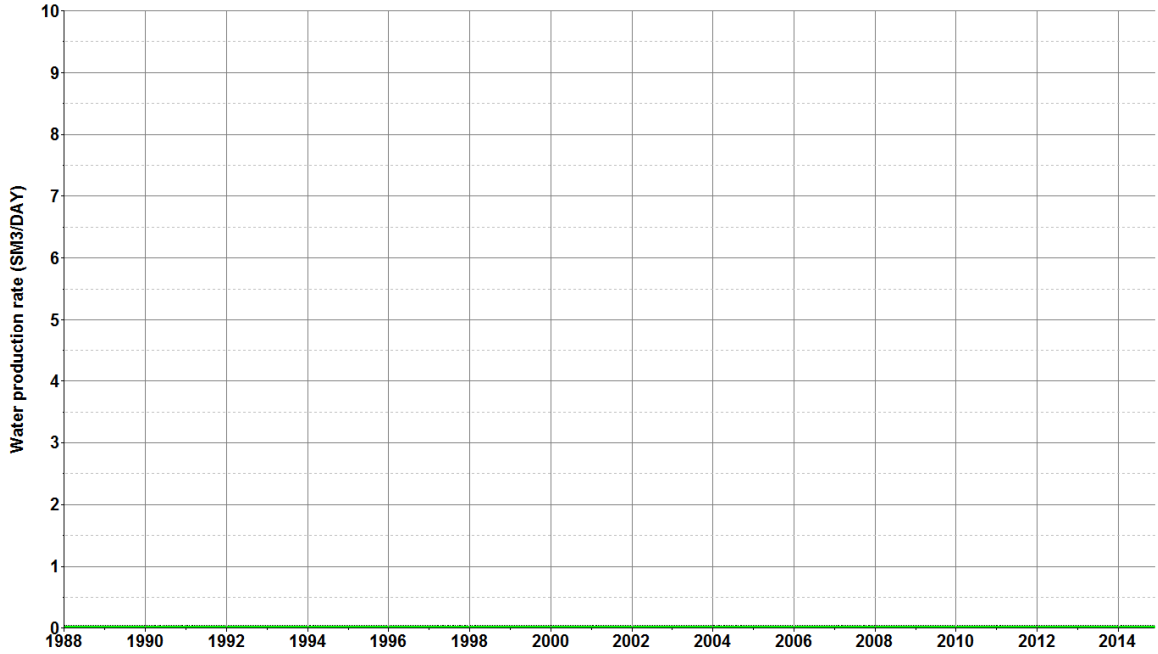

Figure 15-19 HRL-02 HM, water production rate (green line = history match, black line = original history match, red line = Franeker sensitivity, black crosses = historical data)

15.2.1.3 HRL-04

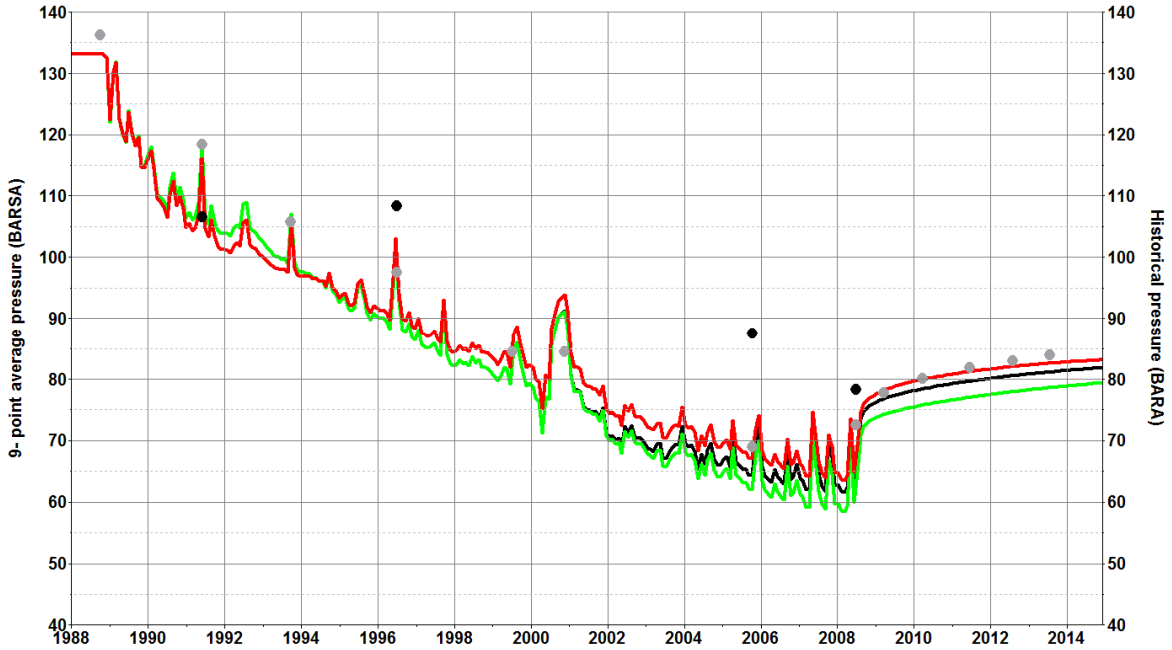

Figure 15-20 **HRL-04 HM, pressure (green line = history match, black line = original history match, red line = Franeker sensitivity, black dots = p*, grey dots = LMP reliable, red dots = LMP unreliable)**

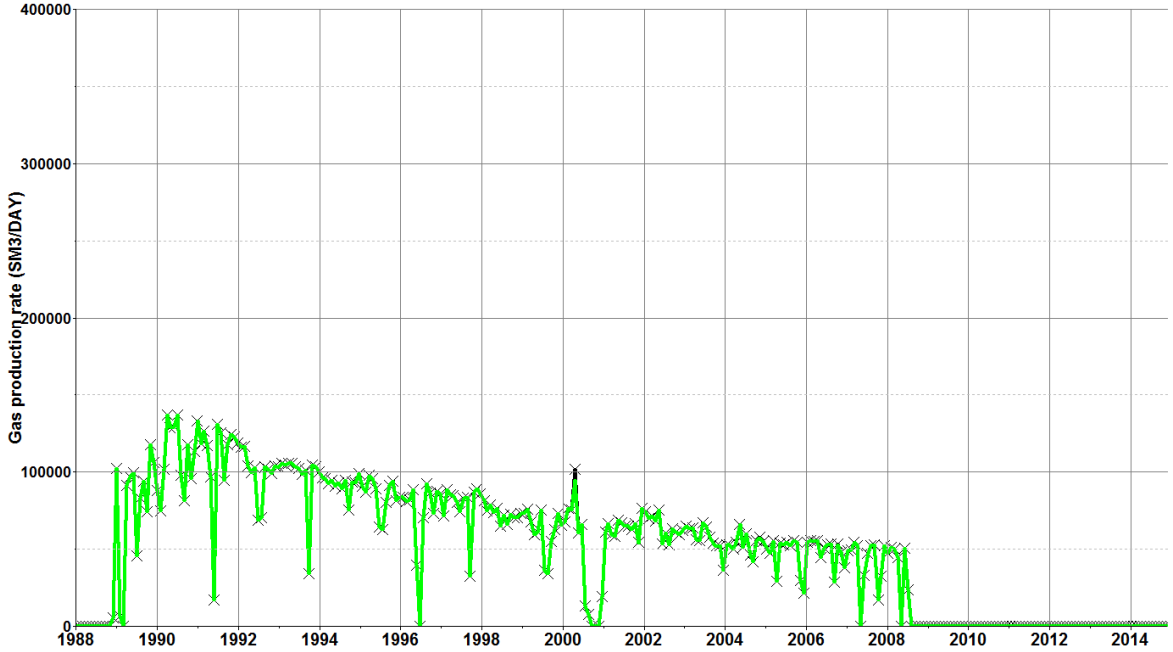

Figure 15-21 **HRL-04 HM, gas production rate (green line = history match, black line = original history match, red line = Franeker sensitivity, black crosses = historical data)**

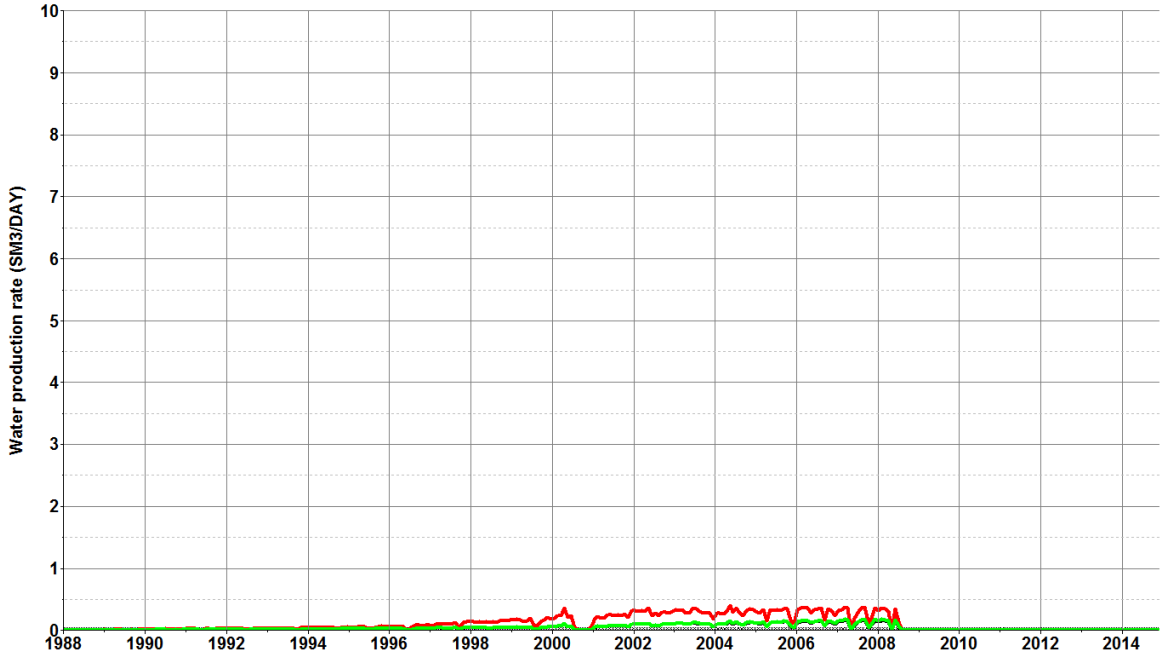

Figure 15-22 **HRL-04 HM, water production rate (green line = history match, black line = original history match, red line = Franeker sensitivity, black crosses = historical data)**

15.2.1.4 HRL-05

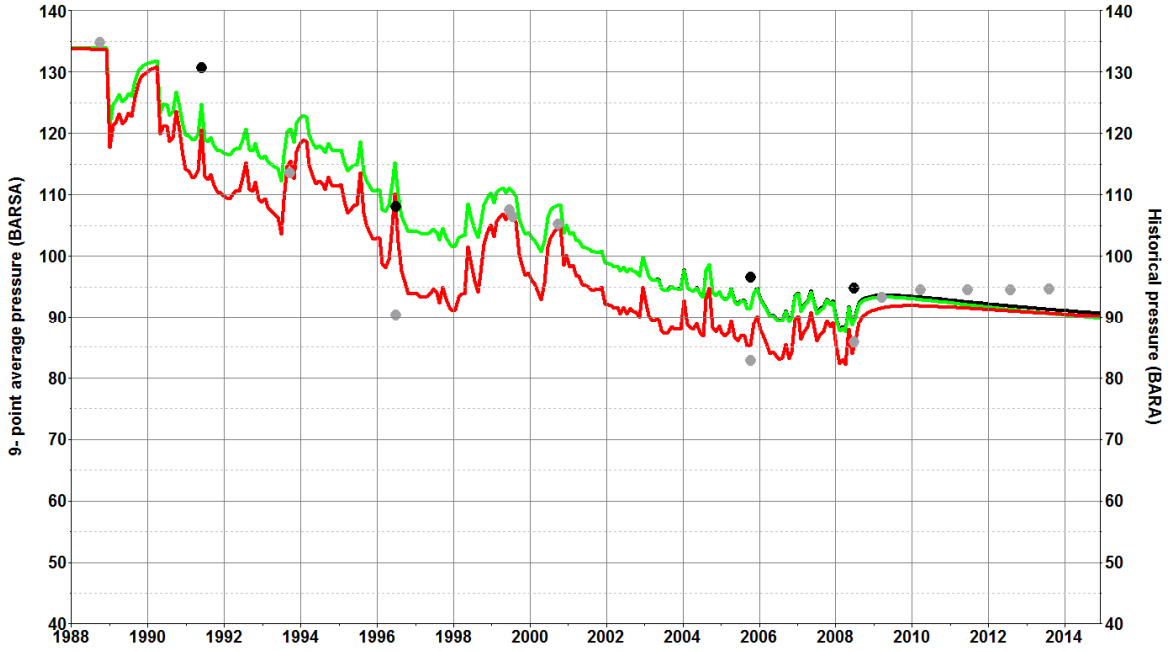

Figure 15-23 **HRL-05 HM, pressure (green line = history match, black line = original history match, red line = Franeker sensitivity, black dots = p*, grey dots = LMP reliable, red dots = LMP unreliable)**

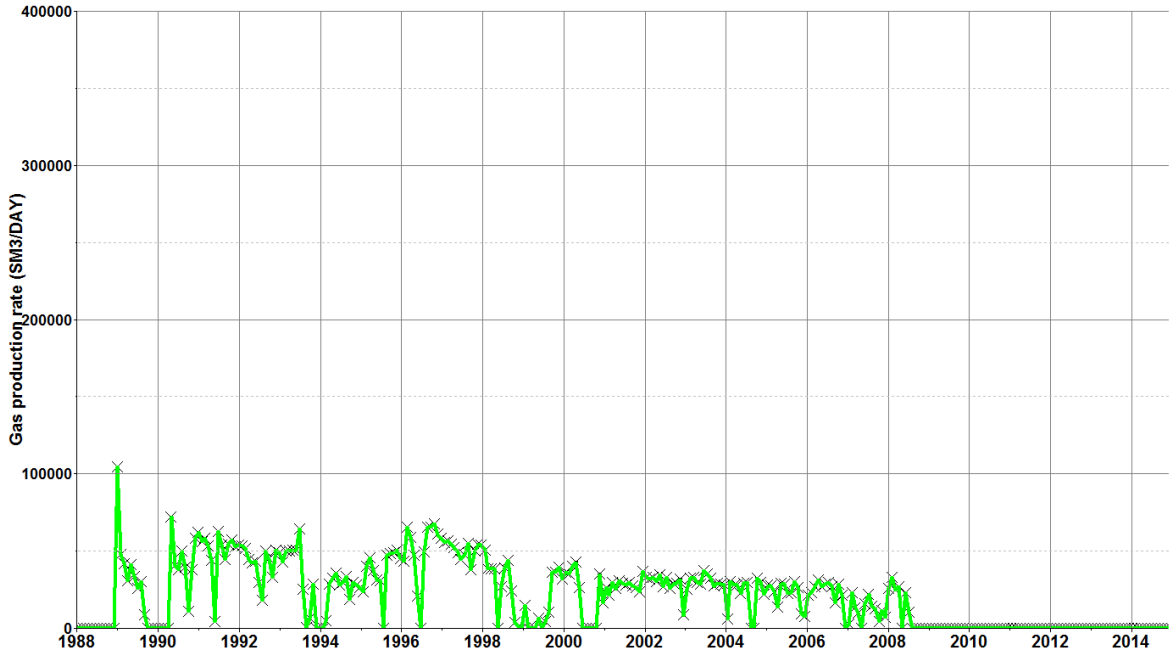

Figure 15-24 **HRL-05 HM, gas production rate (green line = history match, black line = original history match, red line = Franeker sensitivity, black crosses = historical data)**

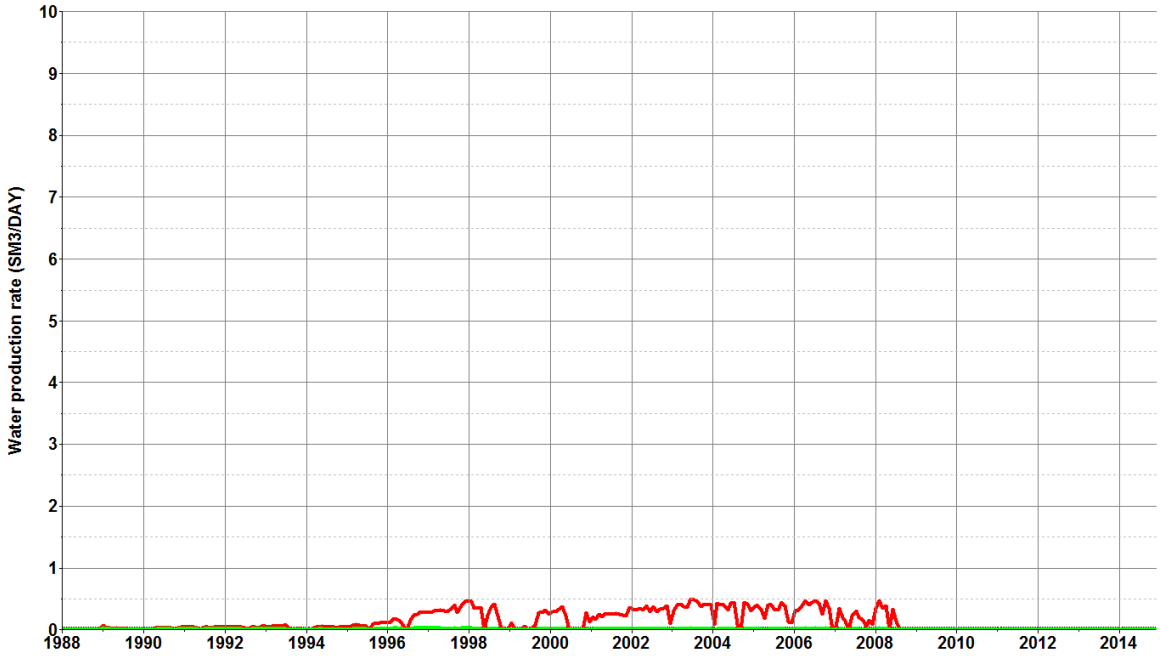

Figure 15-25 **HRL-05 HM, water production rate (green line = history match, black line = original history match, red line = Franeker sensitivity, black crosses = historical data)**

15.2.1.5 HRL-06

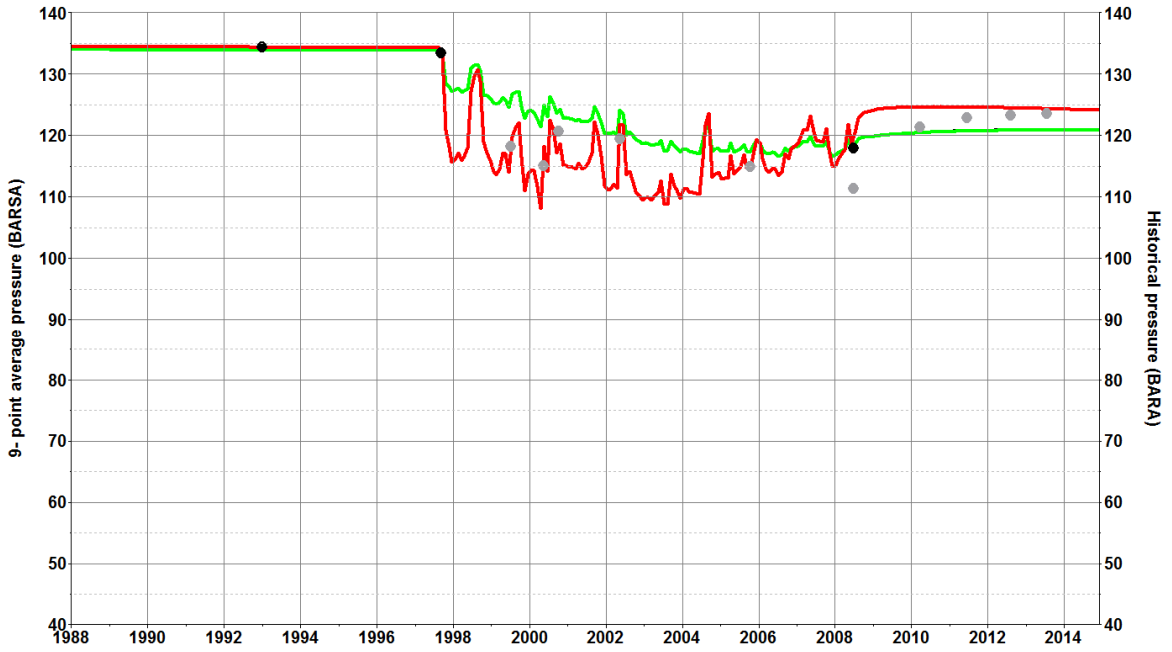

Figure 15-26 **HRL-06 HM, pressure (green line = history match, black line = original history match, red line = Franeker sensitivity, black dots = p*, grey dots = LMP reliable, red dots = LMP unreliable)**

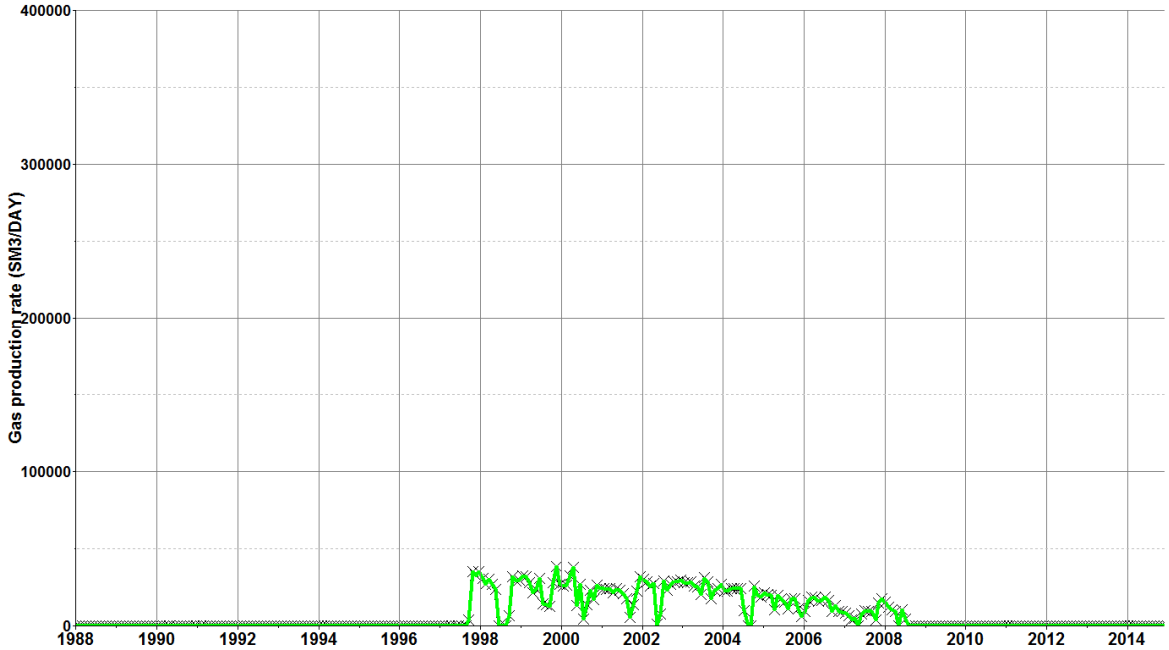

Figure 15-27 **HRL-06 HM, gas production rate (green line = history match, black line = original history match, red line = Franeker sensitivity, black crosses = historical data)**

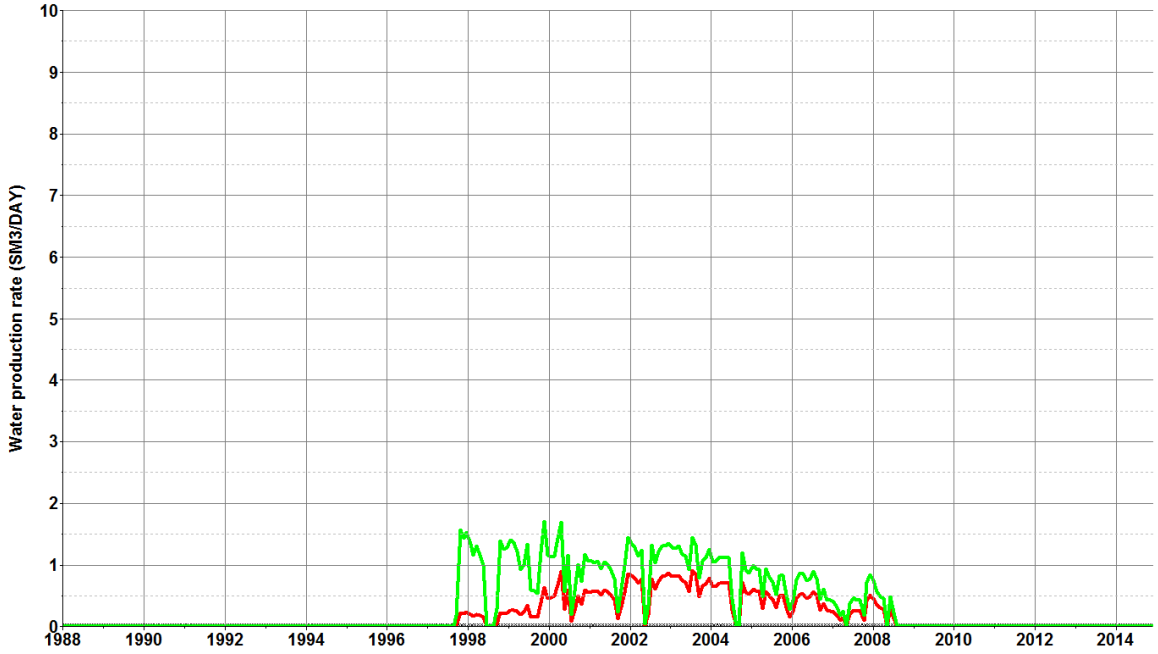

Figure 15-28 **HRL-06 HM, water production rate (green line = history match, black line = original history match, red line = Franeker sensitivity, black crosses = historical data)**

15.2.1.6 HRL-07

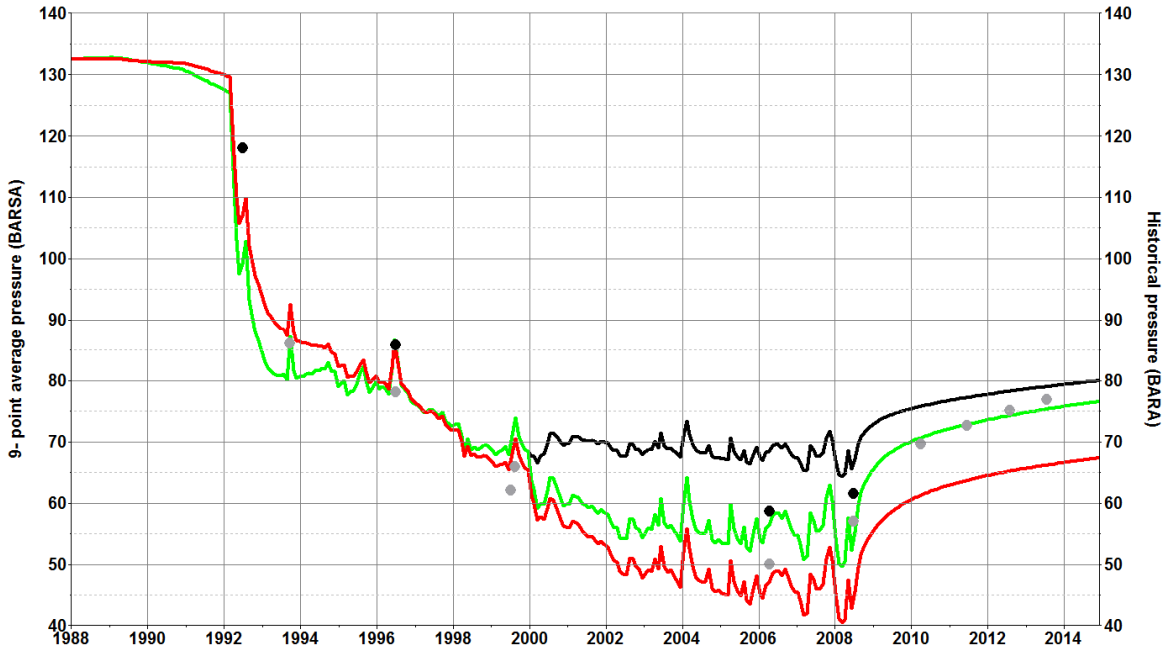

Figure 15-29 **HRL-07 HM, pressure (green line = history match, black line = original history match, red line = Franeker sensitivity, black dots = p*, grey dots = LMP reliable, red dots = LMP unreliable)**

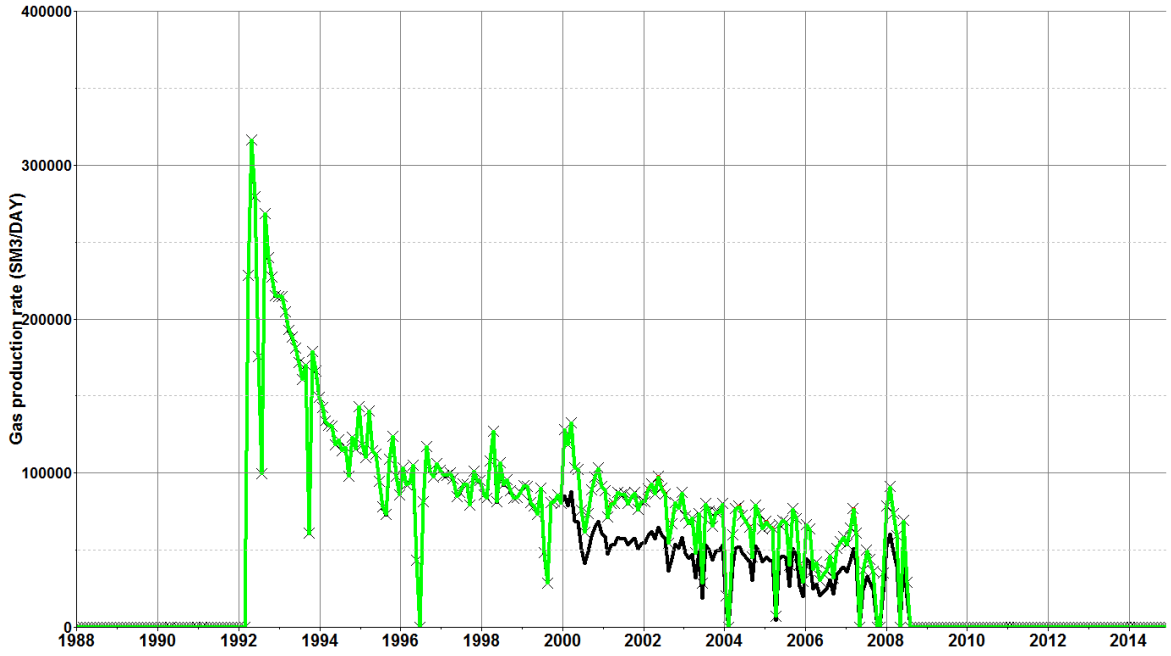

Figure 15-30 **HRL-07 HM, gas production rate (green line = history match, black line = original history match, red line = Franeker sensitivity, black crosses = historical data). Note, the historical data in this plot refer to the modified offtake rate.**

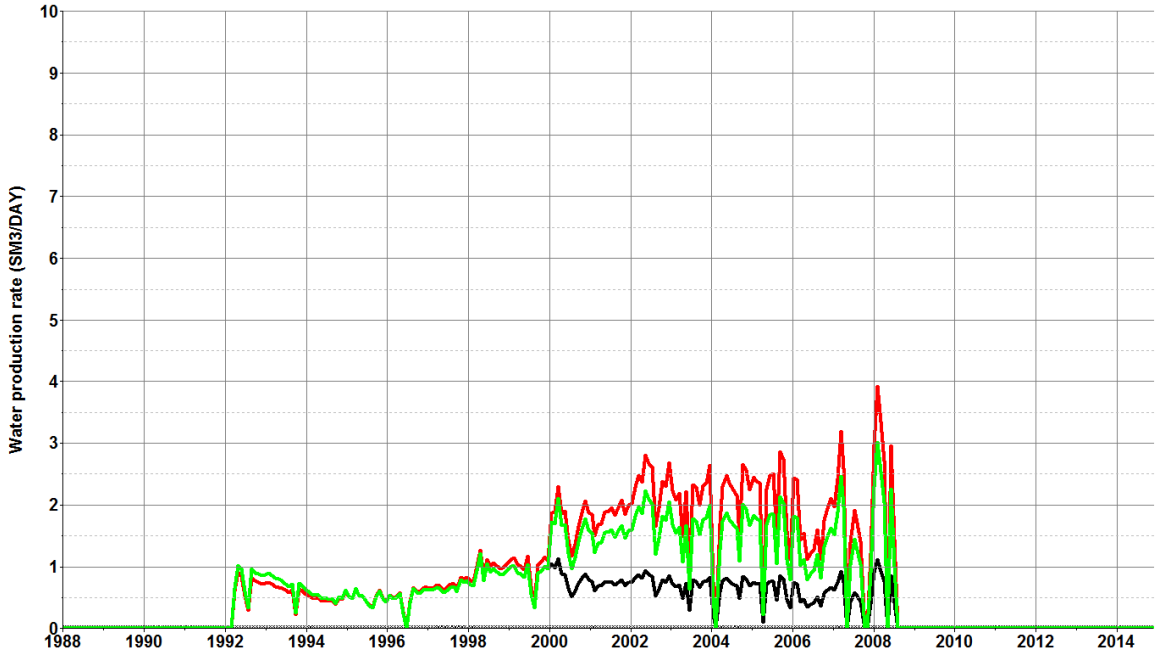

Figure 15-31 **HRL-07 HM, water production rate (green line = history match, black line = original history match, red line = Franeker sensitivity, black crosses = historical data)**

15.2.1.7 HRL-08

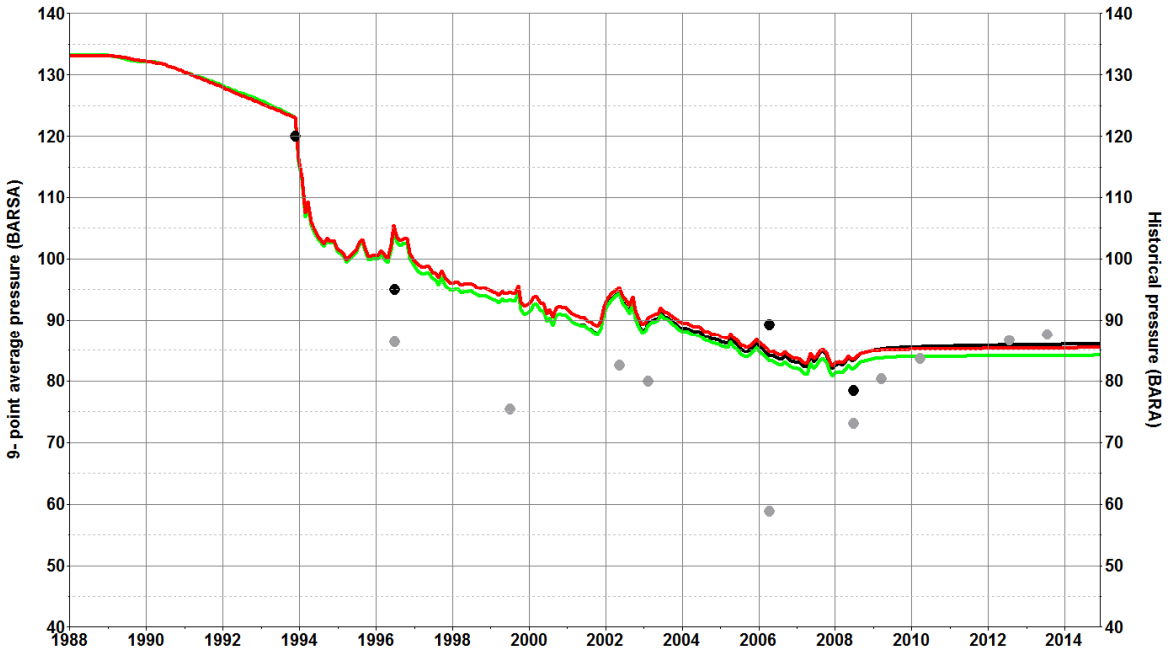

Figure 15-32 **HRL-08 HM, pressure (green line = history match, black line = original history match, red line = Franeker sensitivity, black dots = p*, grey dots = LMP reliable, red dots = LMP unreliable)**

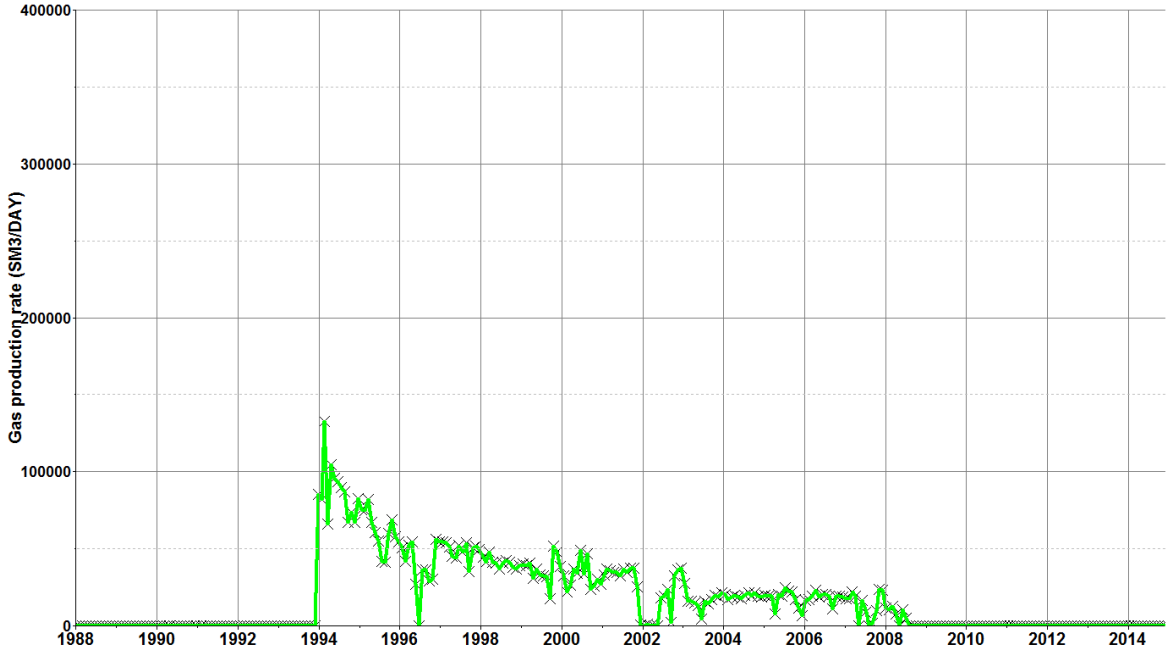

Figure 15-33 **HRL-08 HM, gas production rate (green line = history match, black line = original history match, red line = Franeker sensitivity, black crosses = historical data)**

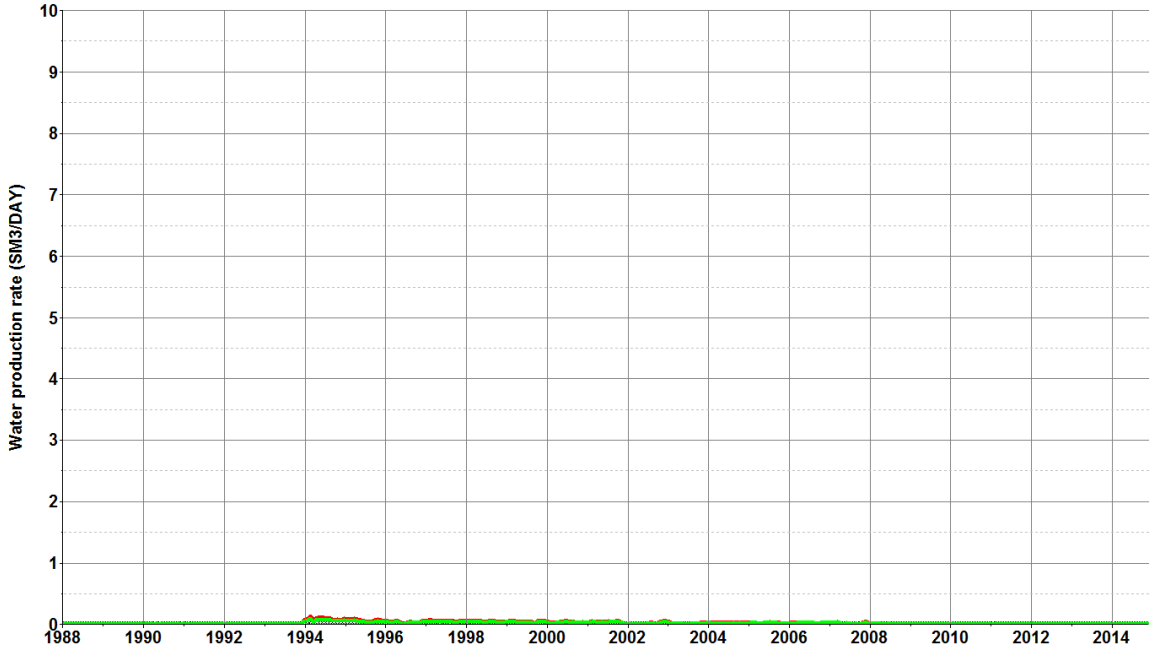

Figure 15-34 **HRL-08 HM, water production rate (green line = history match, black line = original history match, red line = Franeker sensitivity, black crosses = historical data)**

15.2.1.8 HRL-09

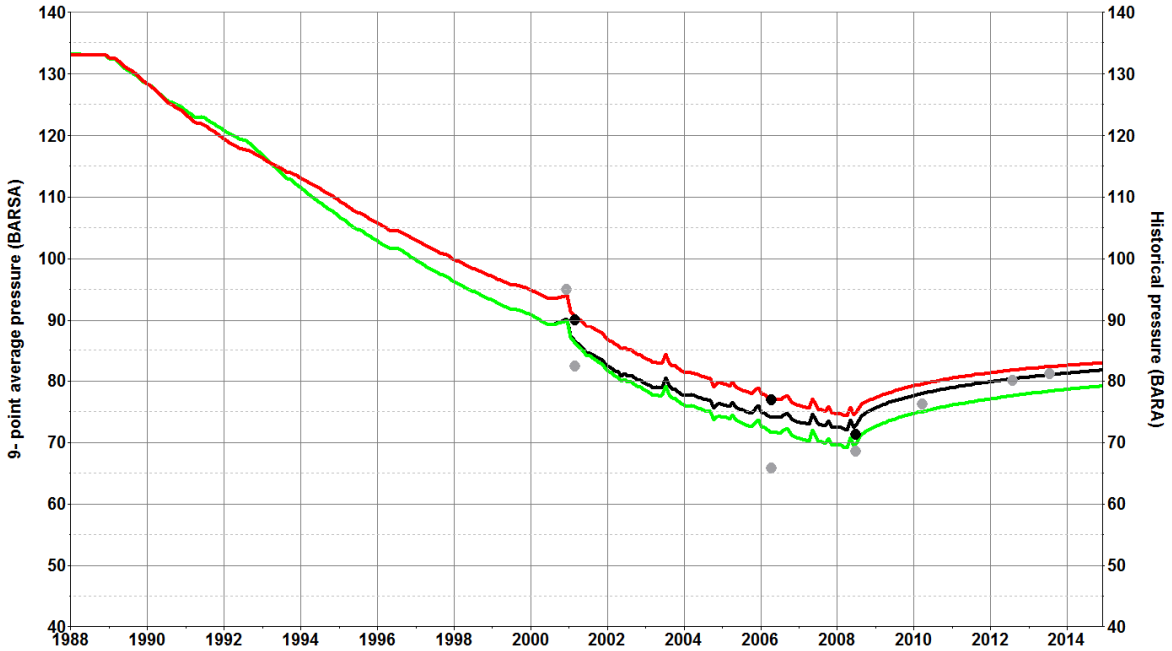

Figure 15-35 **HRL-09 HM, pressure (green line = history match, black line = original history match, red line = Franeker sensitivity, black dots = p*, grey dots = LMP reliable, red dots = LMP unreliable)**

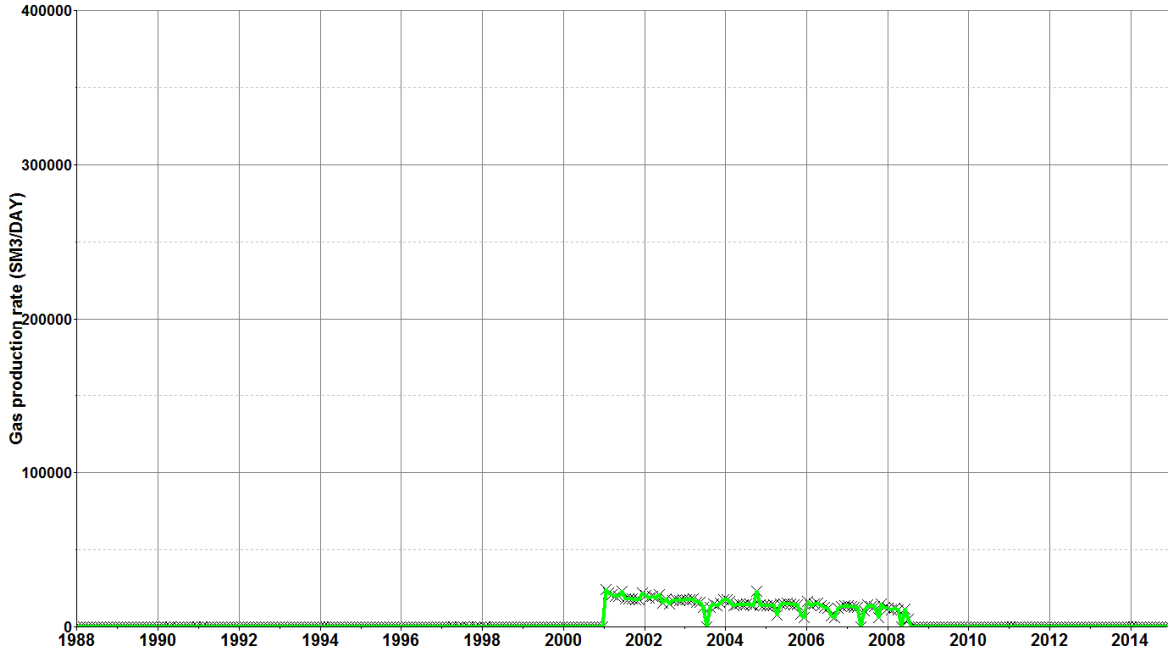

Figure 15-36 **HRL-09 HM, gas production rate (green line = history match, black line = original history match, red line = Franeker sensitivity, black crosses = historical data)**

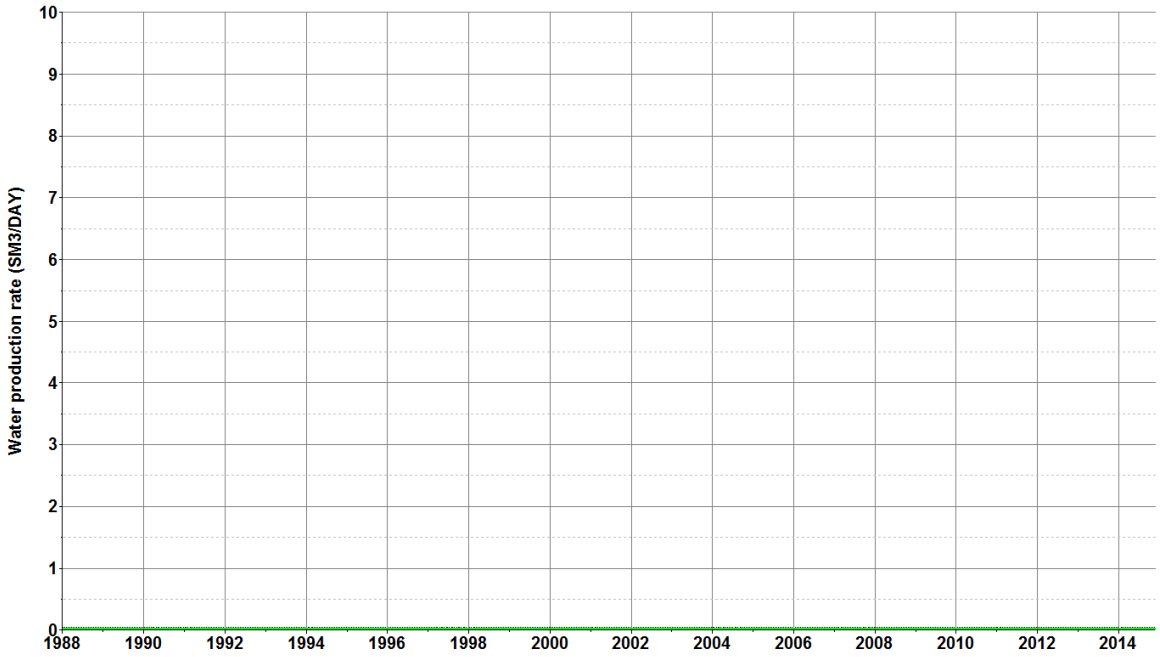

Figure 15-37 **HRL-09 HM, water production rate (green line = history match, black line = original history match, red line = Franeker sensitivity, black crosses = historical data)**

15.2.1.9 HRL-10-S3

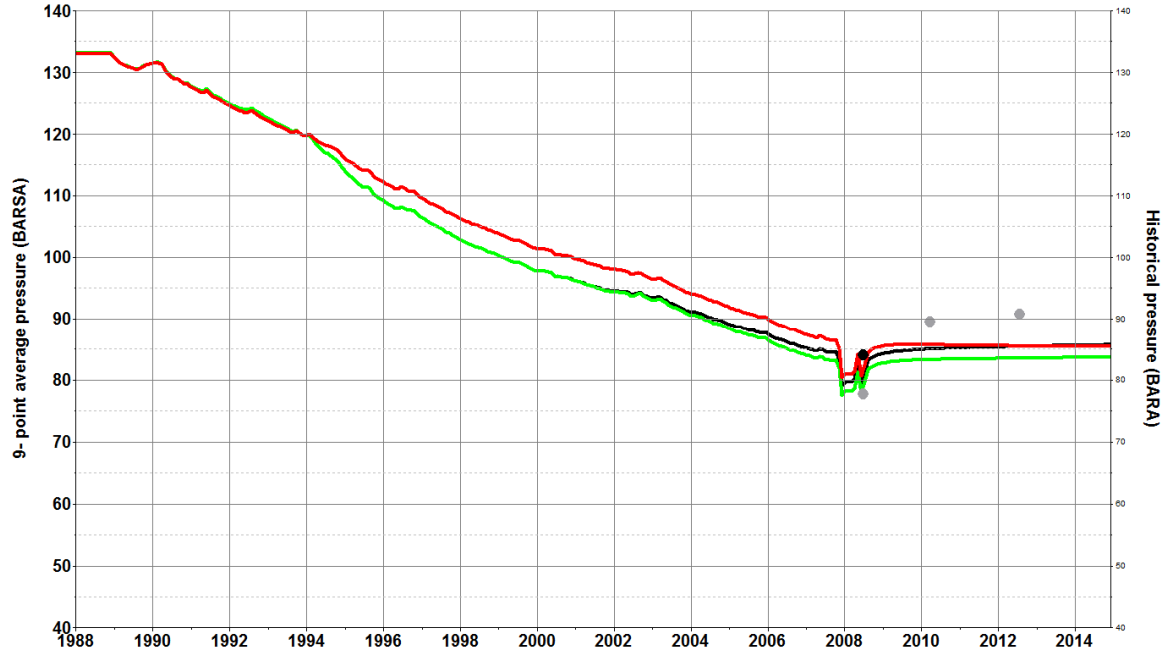

Figure 15-38 HRL-10-S3 HM, pressure (green line = history match, black line = original history match, red line = Franeker sensitivity, black dots = p*, grey dots = LMP reliable, red dots = LMP unreliable)

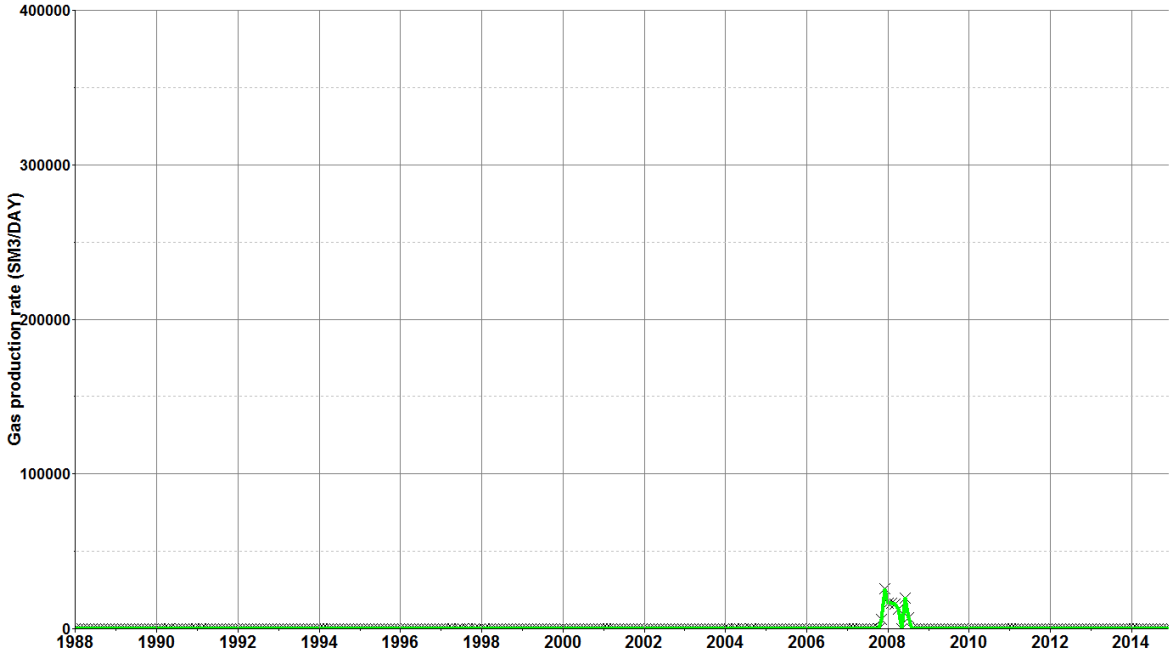

Figure 15-39 HRL-10-S3 HM, gas production rate (green line = history match, black line = original history match, red line = Franeker sensitivity, black crosses = historical data)

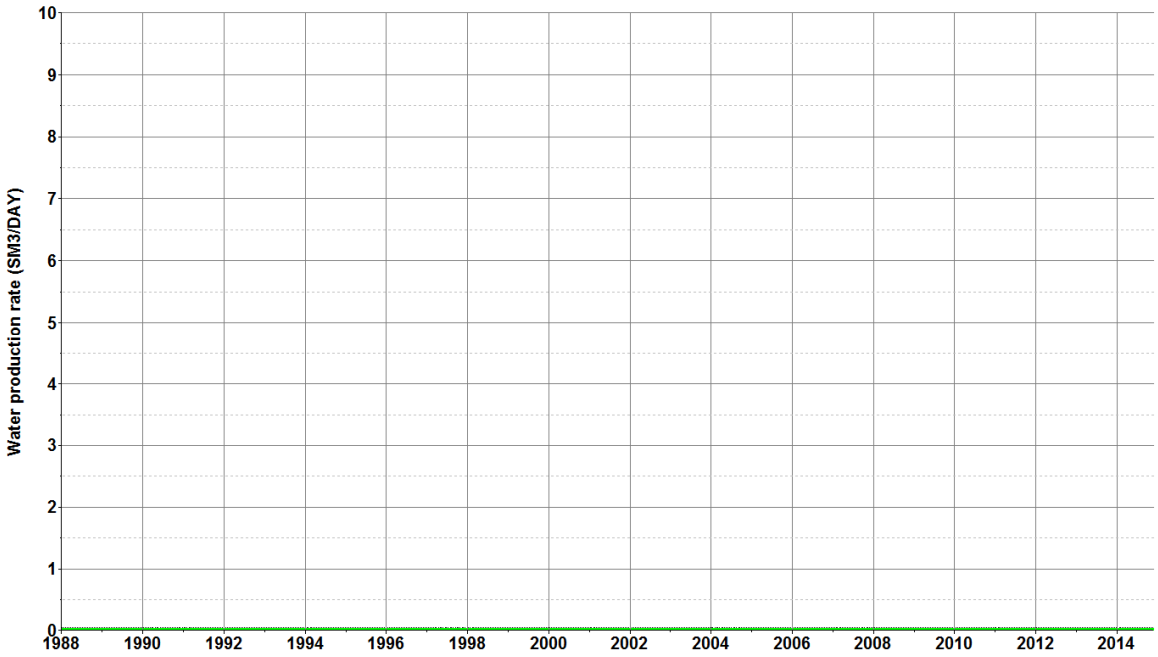

Figure 15-40 HRL-10-S3 HM, water production rate (green line = history match, black line = original history match, red line = Franeker sensitivity, black crosses = historical data)

15.3 FORECASTS

This appendix shows the results of the dynamic model forecast calculations performed on the following models:

- History match with modified offtake rate
  - Field remains shut-in (light green lines)
  - Field remains on production at late historical rates (dark green lines)
- Franeker area sensitivity
  - Field remains shut-in (red lines)

15.3.1 WELL LEVEL

15.3.1.1 FRA-01

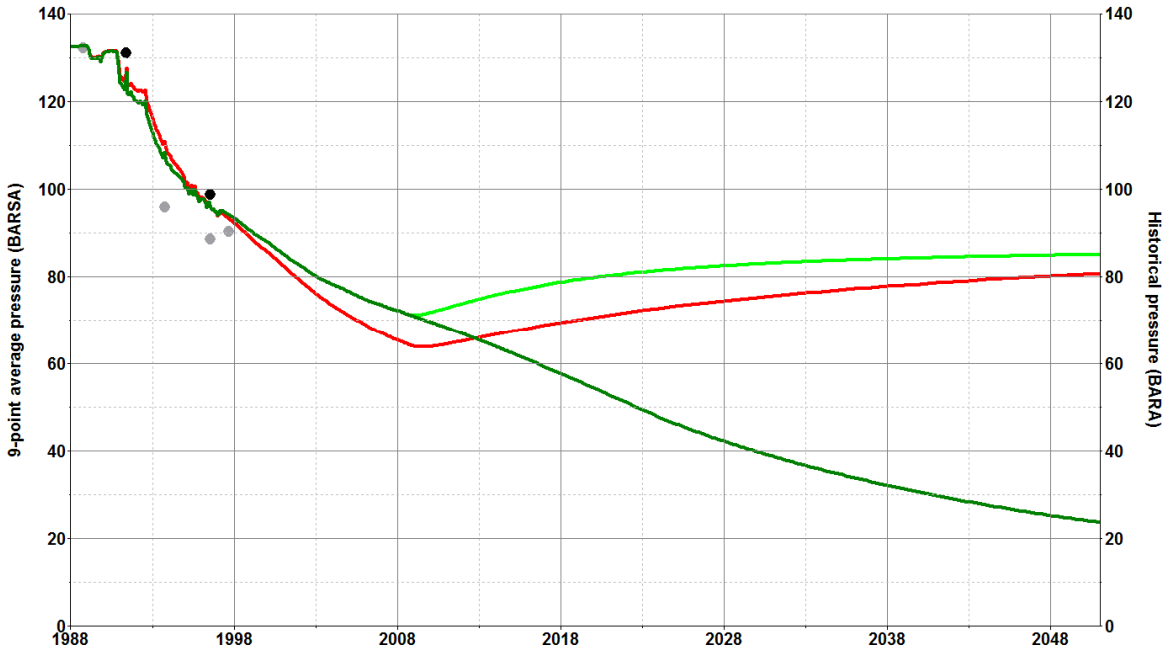

Figure 15-41 FRA-01, pressure (green line = NFA modified offtake, dark green line = continued production modified offtake rate, red line = NFA Franeker area sensitivity, black dots = p*, grey dots = LMP reliable)

15.3.1.2 HRL-02

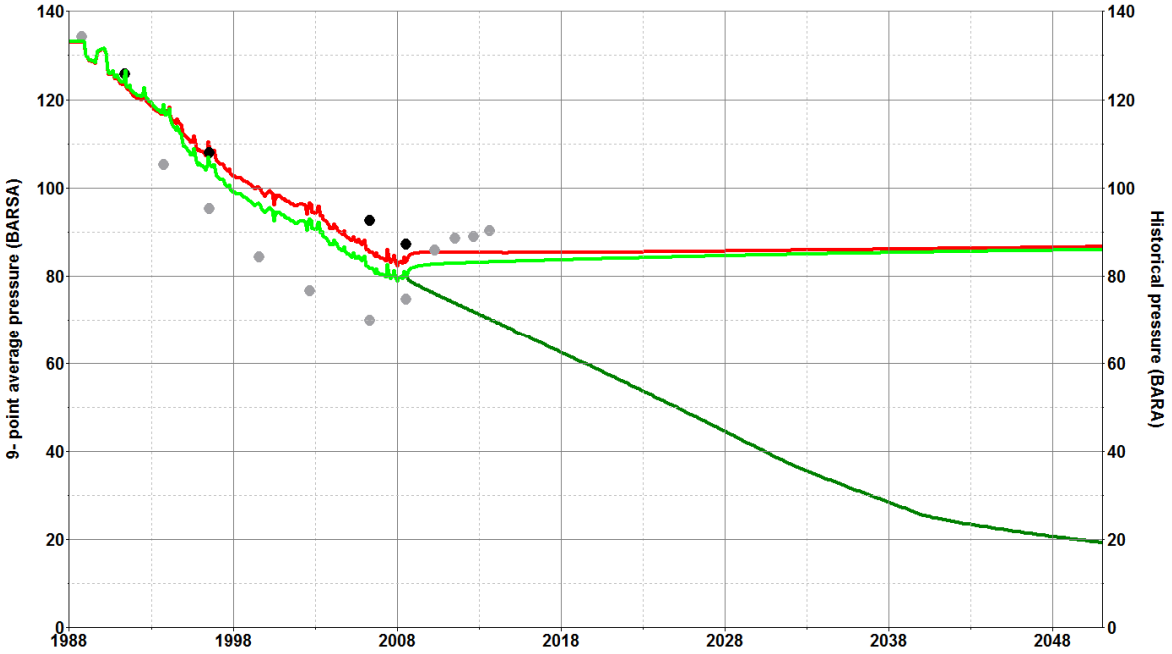

Figure 15-42 HRL-02, pressure (green line = NFA modified offtake, dark green line = continued production modified offtake rate, red line = NFA Franeker area sensitivity, black dots = p*, grey dots = LMP reliable)

15.3.1.3 HRL-04

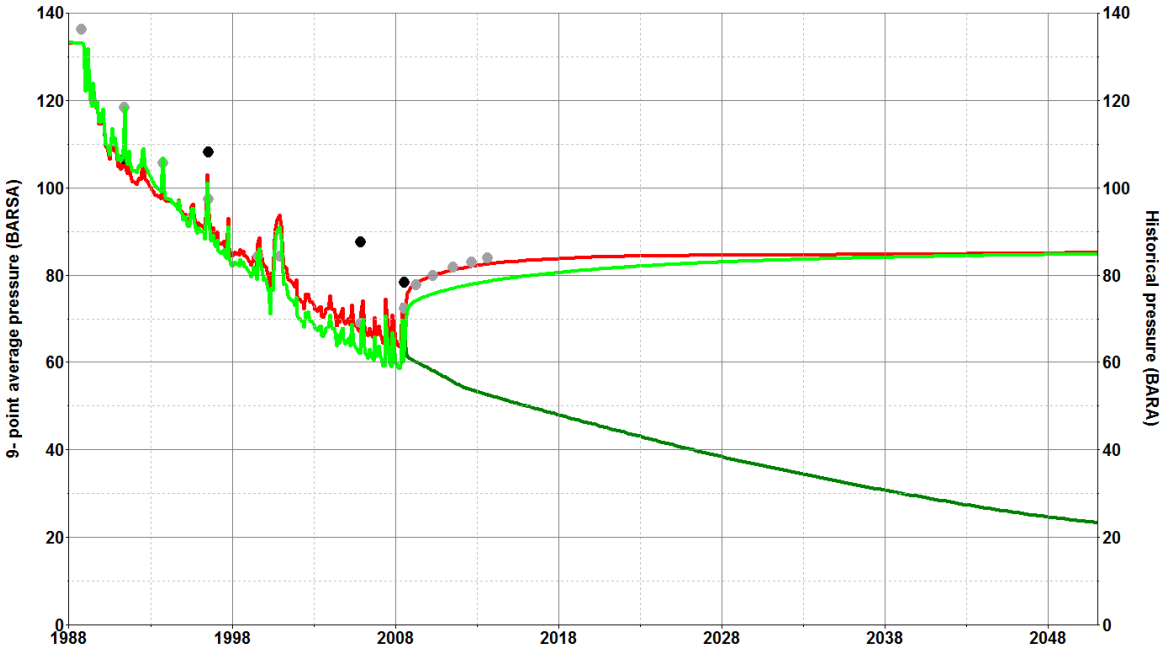

Figure 15-43 HRL-04, pressure (green line = NFA modified offtake, dark green line = continued production modified offtake rate, red line = NFA Franeker area sensitivity, black dots = p*, grey dots = LMP reliable)

15.3.1.4 HRL-05

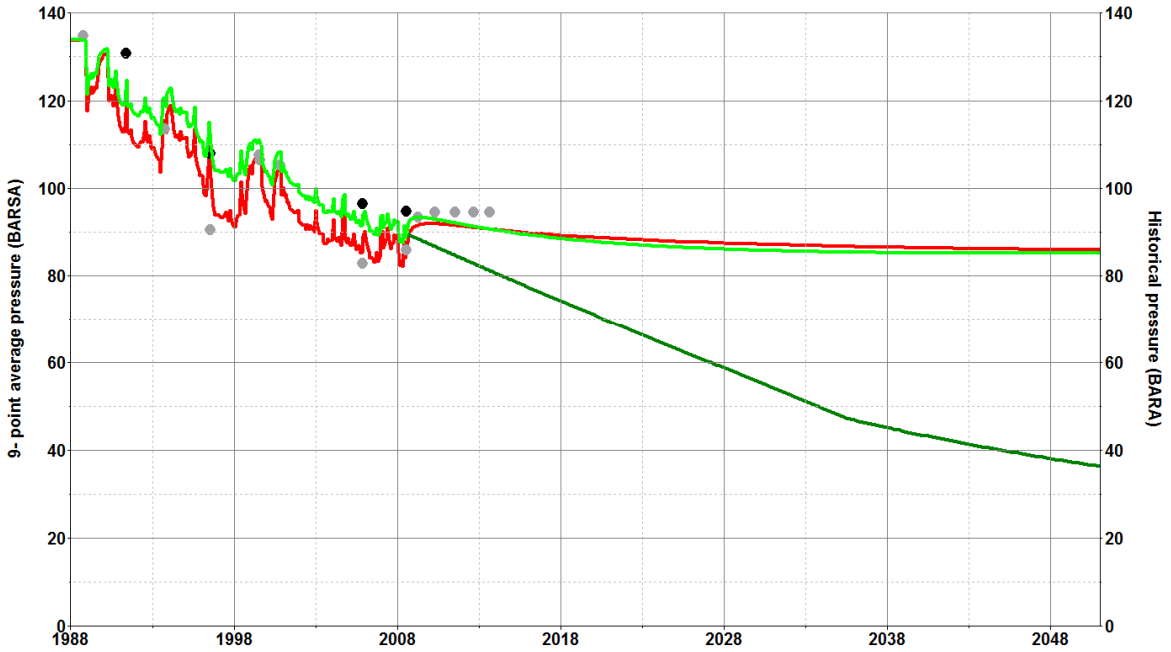

Figure 15-44 HRL-05, pressure (green line = NFA modified offtake, dark green line = continued production modified offtake rate, red line = NFA Franeker area sensitivity, black dots = p*, grey dots = LMP reliable)

15.3.1.5 HRL-06

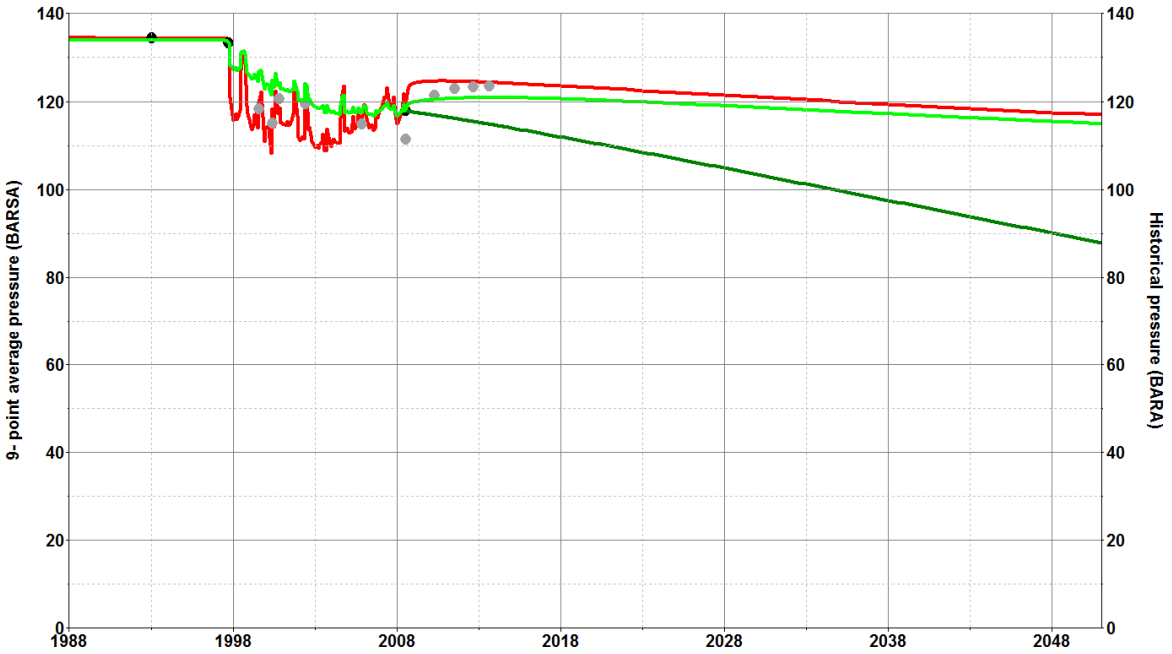

Figure 15-45 HRL-06, pressure (green line = NFA modified offtake, dark green line = continued production modified offtake rate, red line = NFA Franeker area sensitivity, black dots = p*, grey dots = LMP reliable)

15.3.1.6 HRL-07

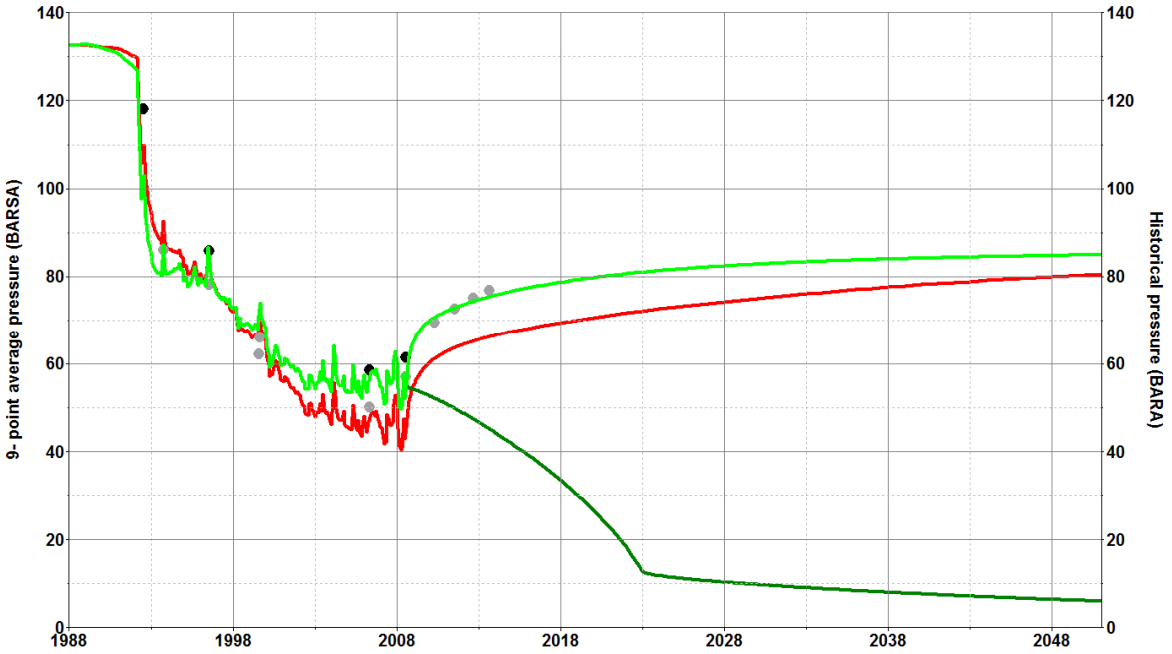

Figure 15-46 HRL-07, pressure (green line = NFA modified offtake, dark green line = continued production modified offtake rate, red line = NFA Franeker area sensitivity, black dots = p*, grey dots = LMP reliable)

15.3.1.7 HRL-08

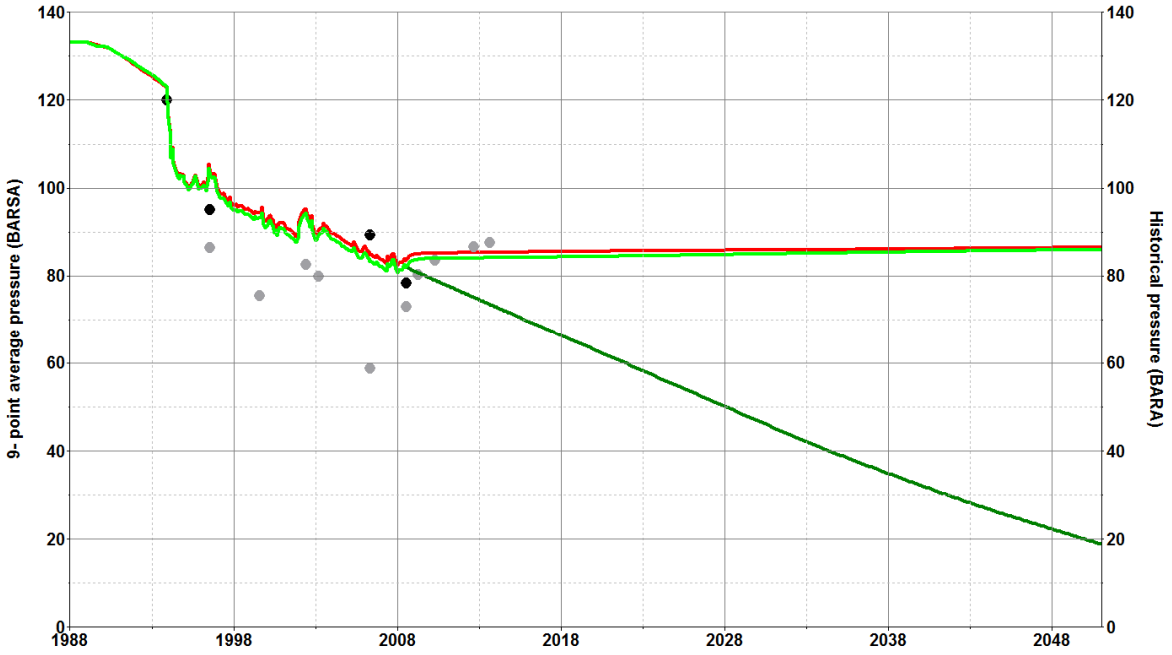

Figure 15-47 HRL-08, pressure (green line = NFA modified offtake, dark green line = continued production modified offtake rate, red line = NFA Franeker area sensitivity, black dots = p*, grey dots = LMP reliable)

15.3.1.8 HRL-09

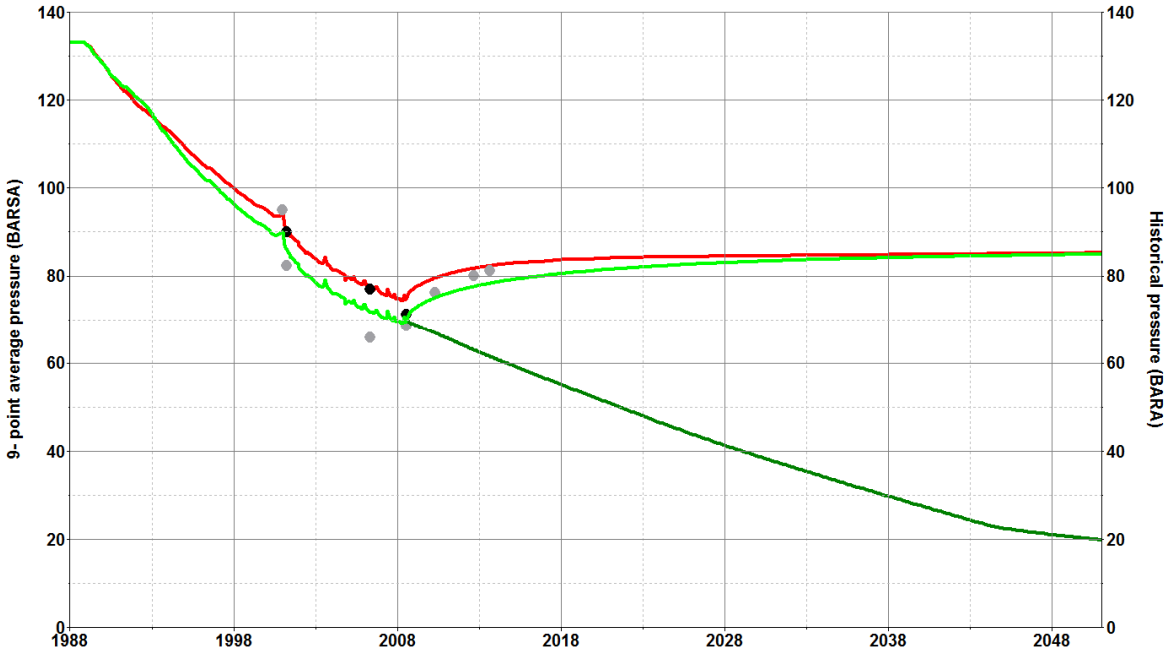

Figure 15-48 HRL-09, pressure (green line = NFA modified offtake, dark green line = continued production modified offtake rate, red line = NFA Franeker area sensitivity, black dots = p*, grey dots = LMP reliable)

15.3.1.9 HRL-10-S3

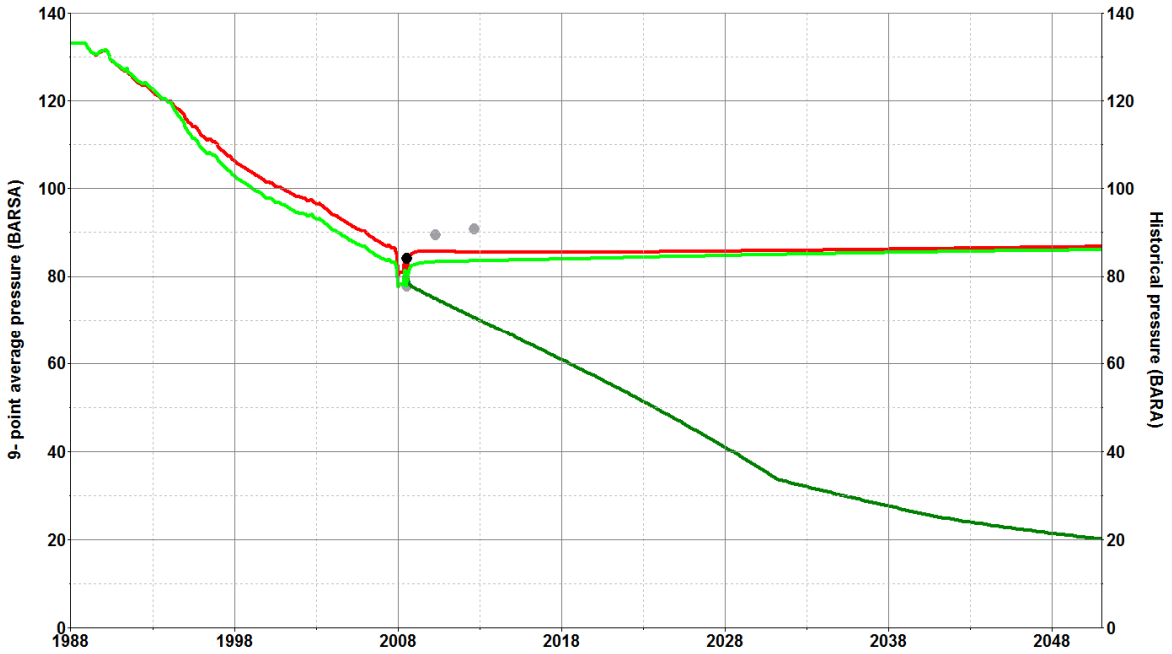

Figure 15-49 **HRL-10-S3, pressure (green line = NFA modified offtake, dark green line = continued production modified offtake rate, red line = NFA Franeker area sensitivity, black dots = p*, grey dots = LMP reliable)**

16 APPENDIX 7

16.1 SUBSIDENCE MISFIT USING ORIGINAL HISTORY MATCHED PRESSURE MODEL

a

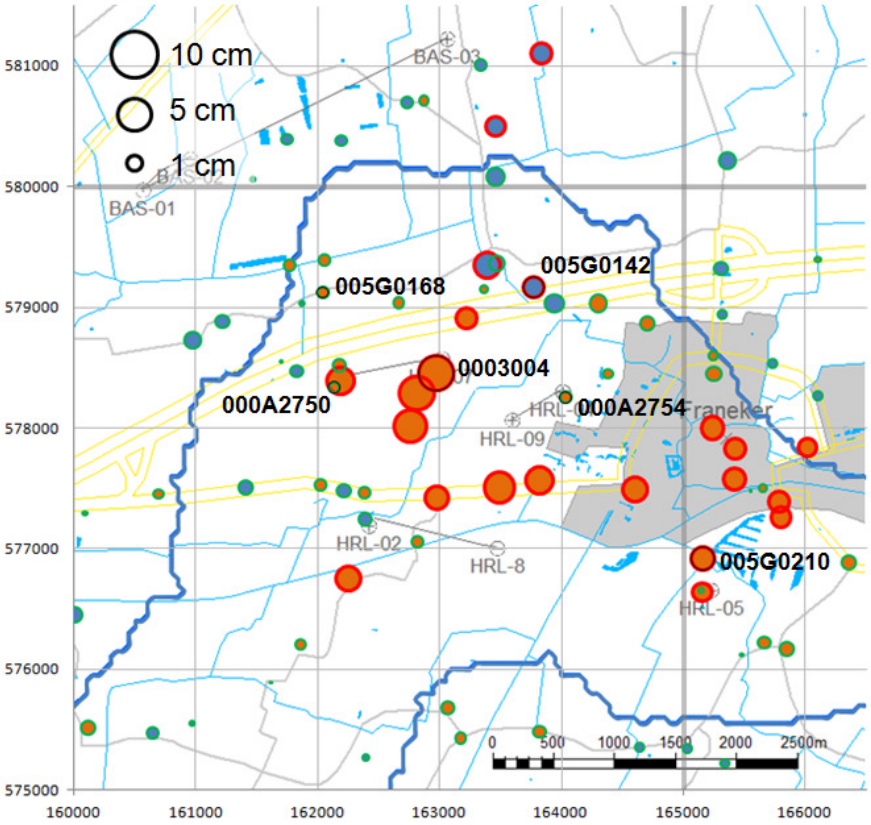

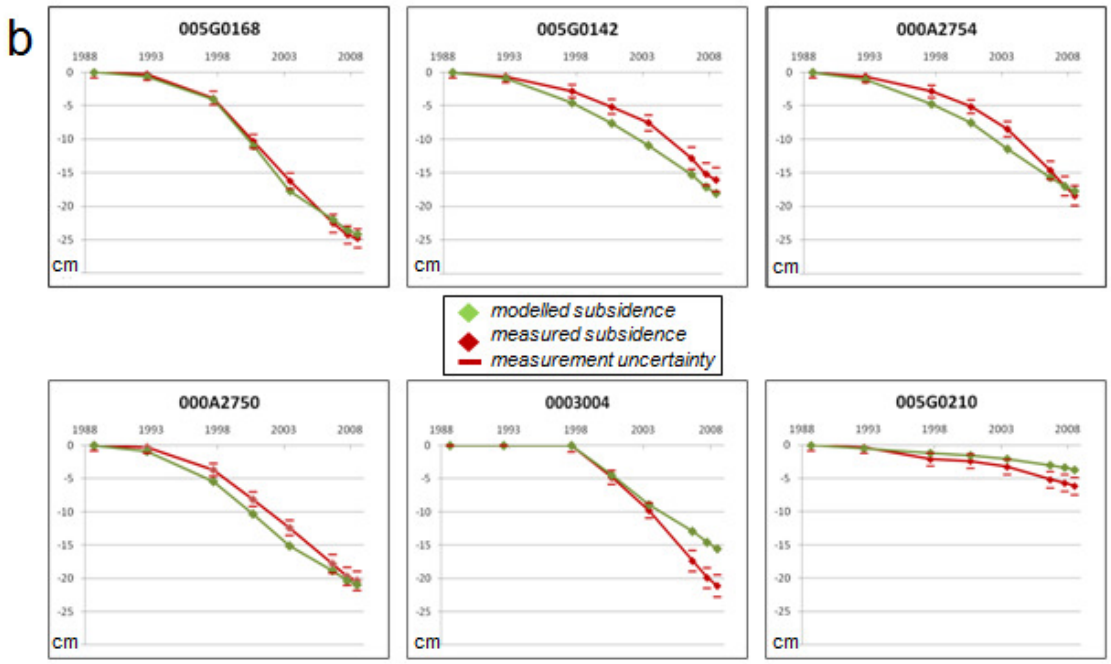

Figure 16-1 **a) difference between modelled and measured subsidence in 2008 indicating if the model exceeds measured subsidence (blue), falls behind (orange), size is proportional to the amount; b) Modelled versus measured subsidence at selected benchmark locations since the start of measuring**

Figure 16-1a shows the misfit between modelled and measured subsidence at the benchmark locations in 2008. The symbol colours indicate where modelled subsidence is more (blue) and where less (orange) than observed and whether the misfit is larger (red) or smaller (green) than the uncertainty on the 2008 measurement. The size of the symbols is proportional to the size of the misfit and because the symbols at locations with a good fit (small misfit) are small this figure highlights the areas with large misfits. Cumulative subsidence between 1988 and 2008 for the named benchmark locations is shown in Figure 16-1b.

16.2 POST SHUT-IN MODELLED SUBSIDENCE VS. GPS MEASUREMENTS

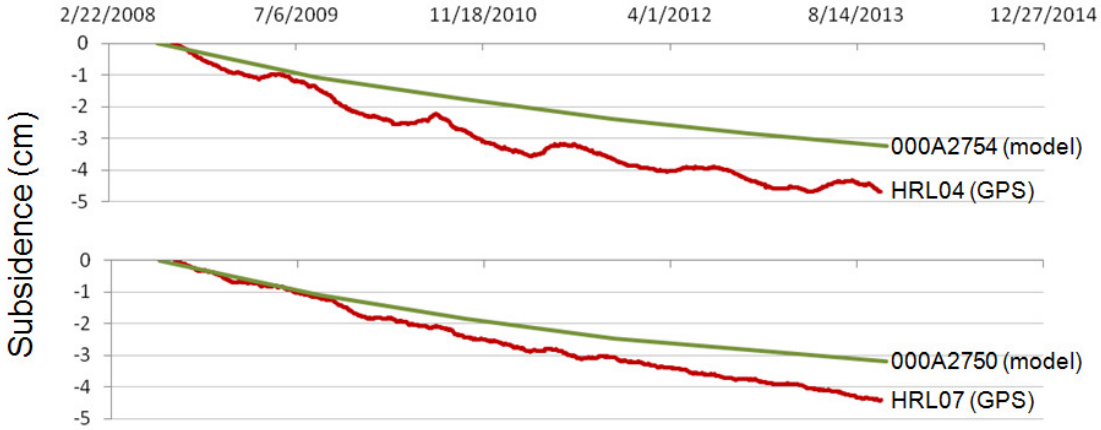

Figure 16-2 **Subsidence post 2008 as measured at two GPS station above the Harlingen gas field (red) and as modelled at two nearby benchmark locations (green)**

Modelled subsidence at two nearby benchmark locations has been compared with measured subsidence at the GPS stations in Figure 16-2. Modelled subsidence at the exact GPS stations

cannot be used here because the model for salt induced subsidence is only provided at the benchmark locations. The two benchmark locations however are very close to the GPS stations, 40 and 125 meter for HRL-04 and HRL-07 respectively, and any error due to this distance is too small to be significant for the comparison presented here.

17 APPENDIX 8

17.1 FITTING PROCEDURE

The main goal of the fitting procedure consists of developing an approach applicable to generate alternative and independent subsidence estimates (over a short/mid-term time period) using the subsidence values measured since the field shut-in (2008). At this aim, a physically plausible subsidence decline curve was defined coherently with the geomechanical laws used in the forward model (Chapter 6), and such a curve was used to fit the measured data while describing the time-dependent decline behaviour of the subsidence at each of the benchmark locations. Based on the assumption that main driver of the post production subsidence is the compactional creep, the time-dependent function of Eq. 17-1 was used to derive the subsidence evolution (NGI, 2009b [19] and NGI, 2011a [20]):

Eq. 17-1
$$\varepsilon(t) = C_C \ln\left(1+\frac{t}{\tau}\right)$$

with:

- $\varepsilon(t)$ equal to the strain rate at time t
- $C_C = b \cdot c_{b,0} \cdot p$, where b is the rate sensitivity parameter, $c_{b,0}$ the bulk compressibility and p the mean effective stress level (at the instant of creep onset $t = 0$)
- $\tau = C_C / \dot{\varepsilon}_0$, where $\tau = C_C / \dot{\varepsilon}_0$ and where $\dot{\varepsilon}_0 = \dot{\varepsilon}(t=0)$ is the volumetric strain rate

As a first step of the fitting procedure, the inverse strain rate of Eq. 17-1 was considered:

Eq. 17-2
$$\frac{1}{\dot{\varepsilon}(t)} = \frac{1}{C_C} t + \frac{1}{\dot{\varepsilon}_0}$$

and the parameters $C_C = C'_C$ and $\dot{\varepsilon}_0 = \dot{\varepsilon}'_0$ were estimated by fitting the measured data with Eq. 17-2 via a least-squares method. An example of the obtained convergence is given in Figure 17-1, where are depicted the data acquired at the benchmark station 0003004 (i.e. the closest location to the deepest point modelled at 2008, and shown in Figure 17-4).

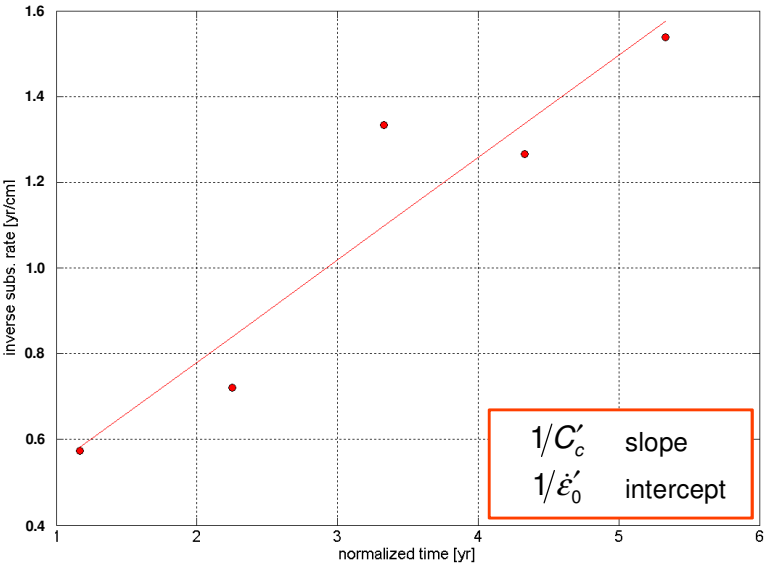

Figure 17-1 Linear regression obtained for the inverse strain rate. Measured data (from benchmark location 0003004) are indicated with dots. On the horizontal axis the time is normalized to the moment the first data were acquired in the post production period.

As a second step, the estimated C'_C value was inserted in Eq. 17-1, obtaining:

Eq. 17-3 $$\varepsilon(t) = C'_C \ln\left(1 + \frac{\dot{\varepsilon}_0}{C'_C} t\right)$$

and the parameter $\dot{\varepsilon}_0 = \dot{\varepsilon}''_0$ was estimated by using a non-linear least-squares procedure. This second step was necessary since a function (Eq. 17-1) is defined by its derivative (Eq. 17-2) as a unique solution up to an additive constant. An example of the obtained final convergence is given in the subset (a) of Figure 17-2.

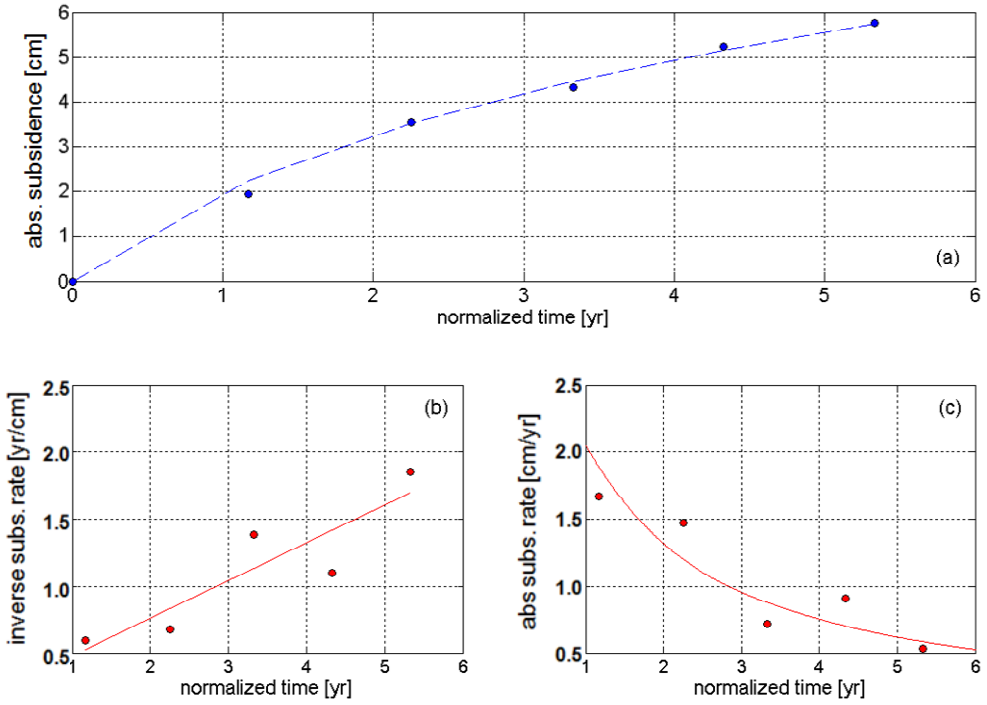

Figure 17-2 Measured points (dots) and the final time-dependent subsidence function obtained by applying the fit procedure (subset (a)). Results of Figure 17-1 (subset (b)) and results for the subsidence rate are also shown (subset (c)). Measured data refer to benchmark location 0003004.

The fitting procedure was successful and was found applicable for the whole field. This allowed the definition of a time-dependent subsidence model for almost all the benchmark locations. Non-convergent fit solutions were only encountered in case of anomalous benchmark measurements (e.g., showing constant or decreasing subsidence values over time). Such issue should be easily overcome once new additional data will be available.

To evaluate the impact of the measurement errors on the fitting procedure and to estimate the uncertainties associated to the fit outputs, the measure-related (σ_{meas}) and the least square-related (σ_{ls}) standard deviations were computed as follows:

Eq. 17-4 $$\sigma(t)_{meas} = \sqrt{{\sigma_{inst}}^2 + {\sigma_{bmk}}^2 + \left((t - t_0) \cdot \sigma_{ref}\right)^2}$$

Eq. 17-5 $$\sigma_{ls} = \sqrt{\frac{1}{(N-2)}\sum_{i=1}^{N}\left(y_i^{meas} - y_i^{ls}\right)^2}$$

where the terms in the time-dependent Eq. 17-4 represent:

- the standard deviation related to the instrument error used for the measurements ($\sigma_{ins} = 3mm$)
- the standard deviation related to the benchmark reference position ($\sigma_{bmk} = 3mm$)
- the time dependent standard deviation related to the drift of the benchmark network since its initiation at $t_0 = 1988$ ($(t - t_0)\cdot\sigma_{ref}$, with $\sigma_{ref} = 0.25mm/yrs$)

while the terms in the location-dependent Eq. 17-5:

- the subsidence measured at the specific benchmark location at the *ith* acquisition time (y_i^{meas})
- the subsidence fitted at the specific benchmark location at the *ith* acquisition time (y_i^{ls})
- the number of measured data available for the specific benchmark location (N)
- the degrees of freedom of the system (i.e. the number of the measured data minus the number of the fitted parameters)

In accordance with common practice (for example Taylor, 1982 [31]), two times the standard deviations of Eq. 17-4 and Eq. 17-5 were used to define an interval of confidence equal to 95%. More precisely, such values were added and subtracted to the measured data and the fitting procedure was repeated, for all the benchmark location, over the datasets: $y^{meas} - 2\sigma_{meas}$, $y^{meas} + 2\sigma_{meas}$, $y^{meas} - 2\sigma_{fit}$ and $y^{meas} + 2\sigma_{fit}$.

Also in this case the fitting procedure resulted convergent for all the reliable benchmark data of the field (as shown as an example in Figure 17-3) providing high-case ($y^{ls+\sigma_{meas}}$ and $y^{ls+\sigma_{fit}}$) and low-case ($y^{ls-\sigma_{meas}}$ and $y^{ls-\sigma_{fit}}$) subsidence predictions. Finally, high- and low-case subsidence scenarios ($y^{ls_{MAX}}$ and $y^{ls_{\min}}$) were created according to the criteria:

Eq. 17-6 $$y^{ls_{MAX}} = \max\left(y^{ls+\sigma_{meas}}, y^{ls+\sigma_{fit}}\right)$$

Eq. 17-7 $$y^{ls_{\min}} = \min\left(y^{ls-\sigma_{meas}}, y^{ls-\sigma_{fit}}\right)$$

As a general remark for the fitting procedure, it must be noted that the fitted coefficients (C_C and $\dot{\varepsilon}_0$) must be considered more as “effective” than “physical” parameters since not directly related to the reservoir compaction but obtained by using the subsidence values measured at the surface.

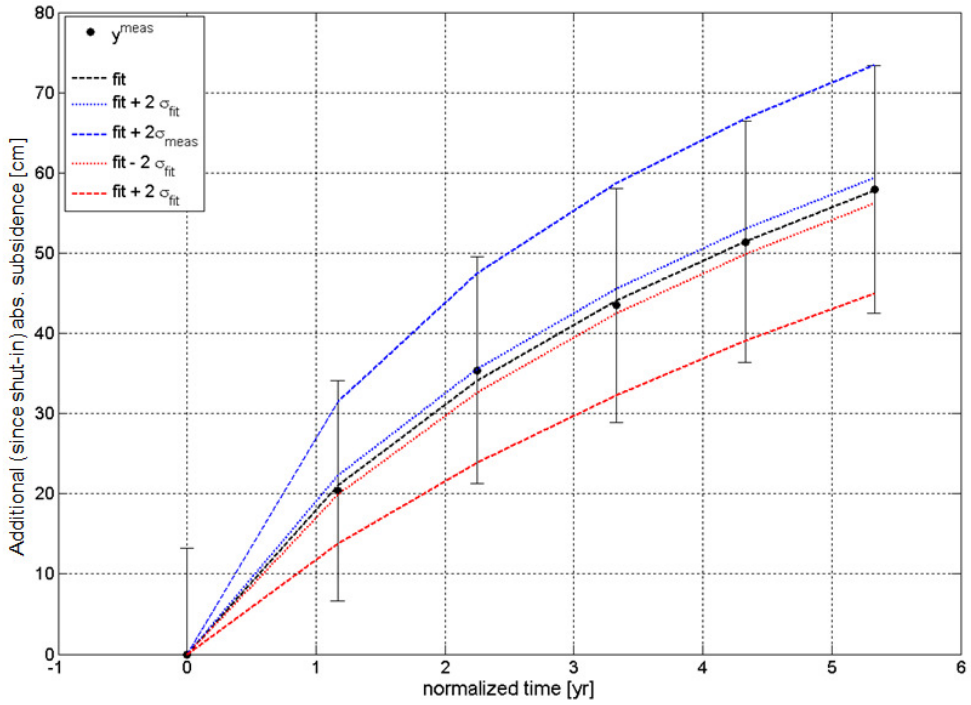

Figure 17-3 Measured points with the associated error bars (dots) and the high- and low-case time-dependent subsidence functions (obtained by taking in account the standard deviations related to the measurements and the fitting-procedure). Measured data refer to benchmark location 0003004.

As a further exercise, a possible parametrical dependence of the fitted coefficients (retrieved for all the different benchmark locations) on a meaningful and physically-based variable was investigated. To this extent, the following quantities were assumed as "state" variables for each of the benchmark point:

- Depletion pressure at field shut-in. Defined as the difference between the pressure at the start and the pressure at end of the production period (1988 – 2008), with values taken from dynamic modelling (as stated in Section 6.1.4);
- Distance from the deepest point of the subsidence bowl modelled at field shut-in (2008), defined using the results described in Section 6.3.2 (summarized in Figure 17-4).

The main purpose of developing such a parametrical approach was to make an attempt to extend the results of the fitting procedure to the whole field, with the aim to forecast the subsidence also away from the benchmark locations.

The retrieved dependencies of C_C and $\dot{\varepsilon}_0$ on the pressure and the distance are shown, respectively, in Figure 17-5 and Figure 17-6, along with the calculated linear interpolation lines. Distance resulted to be a more robust criterion than depletion pressure for building a parametrical regression (for the depletion pressure outliers had to be manually removed to find a meaningful convergence), but in both cases the significant spread that characterizes the data values must be taken in account when considering the goodness of the linear regressions obtained.

Preliminary results appeared consistent by a physical point of view (as shown in Figure 17-7 and Figure 17-8) but the low correlations observable in Figure 17-5 and Figure 17-6 indicate that the parametrical approach cannot be considered statistically rigorous.

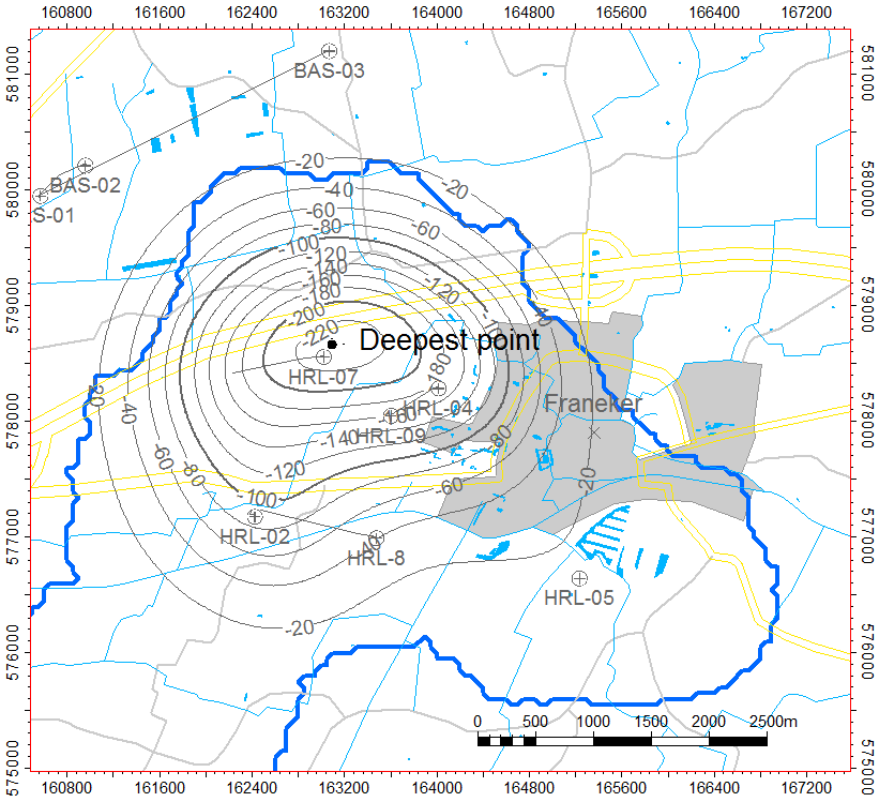

Figure 17-4 **Modelled gas induced subsidence at 2008. Subsidence values are reported via contour lines (in mm). The deepest point is also indicated, showing a subsidence of about 23 cm at the position defined by the coordinates X = 163100 and Y = 578600 (± 100 m).**

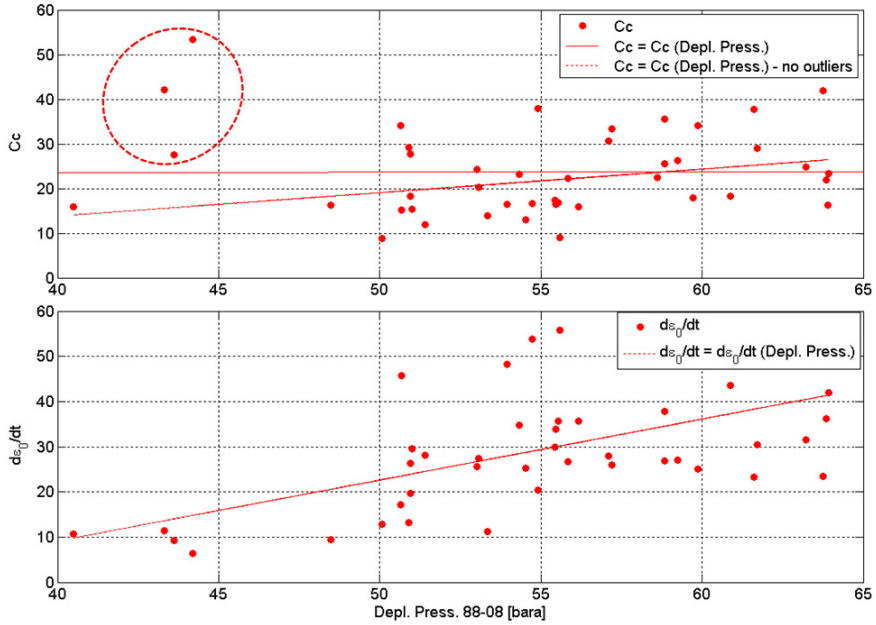

Figure 17-5 C_C **and** $\dot{\varepsilon}_0$ **as functions of the depletion pressures coming from the dynamic model. Values at the different benchmark locations are indicated with dots. The obtained linear interpolation lines are shown for both subplots. In the upper plot, outliers removed to find a meaningful regression are indicated with a dotted circle**

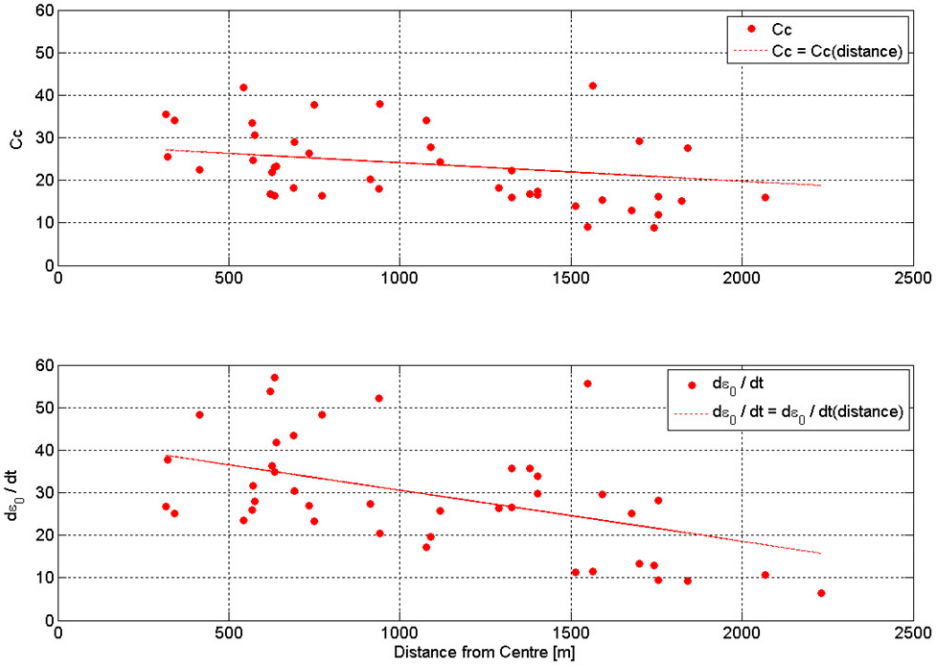

Figure 17-6 C_C **and** $\dot{\varepsilon}_0$ **as functions of the distance from the deepest modelled gas induced subsidence point at 2008 (Figure 17-4). Values at the different benchmark locations are indicated with dots and the obtained linear interpolation lines are shown for both subplots.**

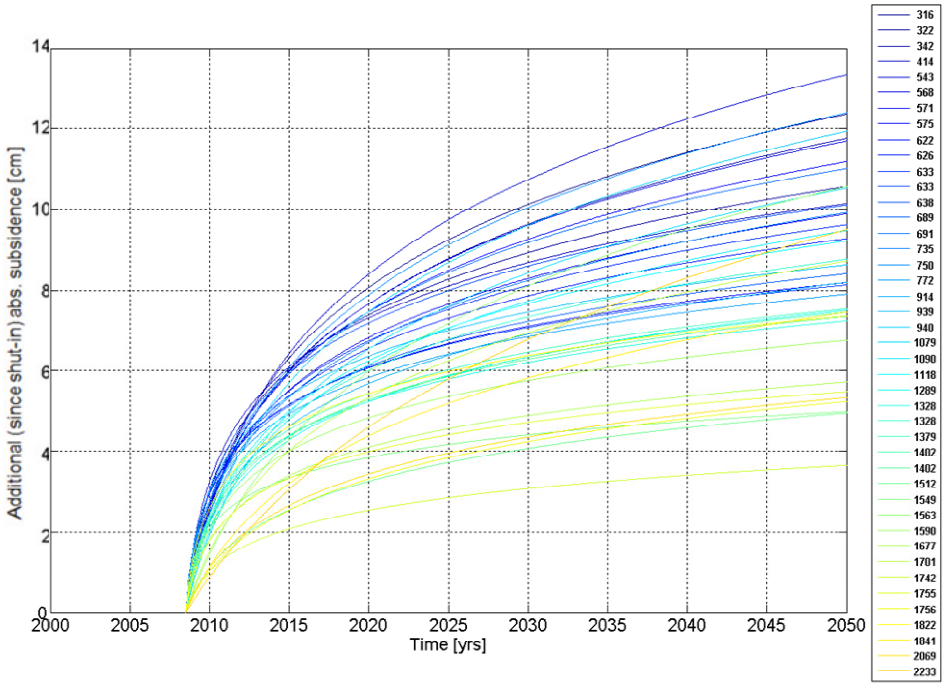

Figure 17-7 **Subsidence as a function of the depletion pressure. The colour code is indicating the distance between the different benchmark locations and the deepest modelled gas induced subsidence point at 2008 (benchmark location 0003004). Benchmark distances (in meters) are reported in the side bar.**

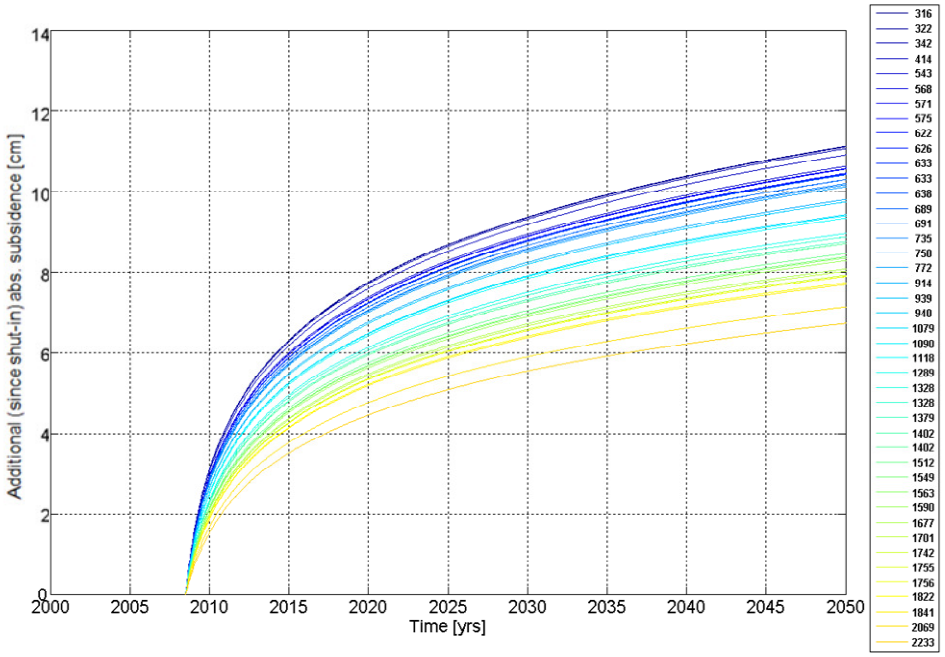

Figure 17-8 **Subsidence as a function of the distance from the deepest point of the 2008 modelled gas induced subsidence bowl (benchmark location 0003004). Distances (in meters) are indicated, for the different benchmark locations, with the colour code reported in the side bar.**